UNIVERSITY OF SOUTHAMPTON

FACULTY OF NATURAL AND ENVIRONMENTAL SCIENCES

School of Chemistry

Particle Size and Support Effects in Electrocatalysis and Photoelectrochemical Water splitting

by

Sandy Kerr

Thesis for the degree of Doctor of Philosophy

November 2015

UNIVERSITY OF SOUTHAMPTON

ABSTRACT

FACULTY OF NATURAL AND ENVIRONMENTAL SCIENCES

Doctor of Philosophy

Particle Size and Support Effects in Electrocatalysis and Photoelectrochemical Water Splitting

By Sandy Kerr

The continued decline in fossil fuel reserves dictates that alternative energy production methods must play an increasing role in our overall energy usage. The generation of hydrogen from photoelectrochemical water splitting has proven itself to be a particularly attractive prospect towards this end. At present, commercial viability of this technology has not been realised due to the large number of stringent material requirements that must be satisfied. One method to improve the efficiency of these cells is through the use of catalysis. The overall effect of catalysts on photoelectrode materials is still relatively unknown. Furthermore, studies of particle size effects and support interactions in this application are seldom reported.

An existing high-throughput methodology [A] was extended towards the synthesis and photoelectrochemical characterisation of metal oxide supported nanoparticles. Pt particles ranging from approximately 1.5 – 6.5 nm in diameter were deposited on both anatase TiO_2 and α-Fe_2O_3. Pt particles reduced the photoelectrochemical performance of TiO_2 towards oxygen evolution and methanol photooxidation, with the effect being greater as the Pt particle size increased. Pt had little effect on the photoevolution of oxygen on α-Fe_2O_3. However, it did bring a significant improvement towards methanol photooxidation, with a specific activity maximum at a particle size of approximately 3 nm. The effects appeared to stem from increased charge separation brought about by Pt. Pt is also ubiquitous as a fuel cell electrocatalyst, in which Pt particle size may have a dramatic effect on cell efficiency. The ORR and MOR were also studied, where in both cases a reduction in specific activity was found as the Pt particle size decreased on both supports. This was particularly apparent on the anatase TiO_2 support due to the increased level of rectification and poorer conductivity.

[A] Guerin, S., Hayden, B., Physical Vapour Deposition Method for the High Through-put Synthesis of Solid-State Material Libraries, *J. Combi. Chem*. **2006**, 8, (1), 66-73

Contents

List of Tables

List of Figures

Figure 6.26. First cathodic sweep of selected Pt particle sizes (Given in the inset) on anatase TiO_2. The electrolyte was O_2 saturated 0.5M NaOH and a potential scan rate of 5 mV s^{-1} was used. The substrate material was ITO. **(169)**

Figure 6.27. Mean onset potential for the oxygen reduction reaction and ferrocyanide reduction. The onset was defined as the voltage to generate -0.028 mA cm^{-2} with respect to the geometric surface area of the electrode. Data was derived from the first cycles where a scan rate of 5 mV s^{-1} was used. **(170)**

Figure 6.28. Mean ORR onset potential as a function of Pt particle size. The onset potential was defined as the point where a specific current density (with respect to the estimated Pt surface area) of -0.028 mA cm^{-2} was reached. **(170)**

Figure 6.29. The effect of metal particles on the interfacial barrier height (B) of a semiconductor in contact with a solution redox couple of energy E_{redox}. The situation is shown for the semiconductor in contact with the solution (B_{SC}), inc ontact with a metal contact with a large spatial area (B_M) and a metal contact with a small area (B_{eff}). Figure adapted from ref [21] **(172)**

Figure 6.30. CVs of a polycrystalline Pt electrode in 6M KOH + 1M MeOH at a scan rate of 25 mV s^{-1}. Figure taken from ref 160 **(173)**

Figure 6.31. CVs of selected Pt particle sizes supported on anatase TiO_2. The measurements were carried out at room temperature in both 0.5 M NaOH and 0.5 M + 1 M NaOH. Data shown in 0.5 M NaOH was collected immediately priot to those with the addition of methanol. The first cycles in methanol containing solution are shown and a scan rate of 50 mV s^{-1} was used in all cases. The apparent MOR onset is marked with an arrow. **(174)**

Figure 6.32. Mean methanol oxidation current density as a function of Pt particle size at 0.8 V vs. RHE. The methanol oxidation current was calculated by subtracting the value obtained in 0.5 M NaOH from that obtained with the addition of 1 M methanol. All measurements were performed with a potential scan rate of 50 mV s^{-1}. **(175)**

Figure 6.33. The first 4 cycles of a Pt/TiO_2 electrode (estimated particle diameter: 5.91 nm) in 0.5 M NaOH + 1M MeOH. The sample was deposited on an ITO substrate and all measurements were conducted at a potential scan rate of 50 mV s^{-1}. **(177)**

Figure 6.34. Illuminated and dark Cvs of selected particle sizes. All measurements were conducted in 0.5 M NaOH with a potential scan rate of 50 mV s^{-1}. The first illuminated cycle is shown. The dark measurements were those conducted immediately prior to the illuminated measurements. The measurements are

uncorrected with respect to irradiance variation. A B and C in the bottom right Figure represent key areas which are referred to in the text. **(178)**

Figure 6.35. Uncorrected geometric current density (mA cm^{-2}) at 0.3 V vs. RHE as a function of array position. Results are shown for the plain TiO_2 calibration array (left) as well as an array of TiO_2 supported Pt particles (right). Data from the first anodic sweep under illumination are shown in each case. Note that 10 randomly placed TiO_2 electrodes are present on the right hand sample. Also shown (Bottom) is the relative intensity distribution across the beam area (relative to the most intense region). **(180)**

Figure 6.36. Intensity normalised CVs of selected Pt particle sizes on Anatase TiO_2 under illumination. The substrate material was Au and measurements took place in 0.5 M NaOH with a potential scan rate of 50 mV s^{-1}. The first cycles are shown. **(181)**

Figure 6.37. Intensity corrected photocurrent density at 0.25 V vs. RHE during the first three illuminated cycles. Measurements were conducted in 0.5 M NaOH with a potential scan rate of 50 mV s^{-1}. Current densities were calculated from the anodic scans. **(182)**

Figure 6.38. Estimated Pt surface areas of Pt nanoparticles supported on anatase TiO_2. Data is shown for the electrodes before and after the photoelectrochemical screening process. Surface areas we estimated from the charge passed in the hydrogen adsorption region.**(183)**

Figure 6.39. Intensity normalised geometric photocurrent density at 0.25 (left) and 0.8 V (right). Data is derived from the first positive going sweep under illumination. The response from the blank TiO_2 electrodes are also shown at the position of 0 nm on the x axis. **(184)**

Figure 6.40. Mean photocurrent onset potential from the illuminated CV measurements. The onset was defined as the voltage to generate geometric current density of 0.24 mA cm^{-2}. Measurements were conducted in 0.5 M NaOH with a potential scan rate of 50 mV s^{-1}. **(185)**

Figure 6.41. Mean illumated OCP values as a function of particle size in both Ar and O_2 purged 0.5 M NaOH. OCP values were caluclated as the average voltage over a 200 s period of illumination. **(186)**

Figure 6.42. Mean ORR onset potential of anatase TiO_2 supported Pt nanoparticles for the first 3 cycles under illumination. Data was collected at 50 mV s^{-1} in 0.5 M NaOH. **(187)**

Figure 6.43. Mean ORR onset potential of anatase TiO_2 supported Pt nanoparticles before and after cycling under illumination. Measurements were carried out in O_2 saturated 0.5 M NaOH at a scan rate of 5 mV s^{-1}.

smallest particle size on each array (Right – Estimated particle diameter = TiO_2: 2.91 nm, Fe_2O_3: 3.15 nm). The first cycle of CVs recorded in Ar purged 0.5 M NaOH are shown. **(263)**

Figure 8.2. Mean ORR onset potential for Pt particles supported on Fe_2O_3 (#8135) and TiO_2 (#8107). The onset was defined as the potential required to generate a geometric current density of -0.028 mA cm^{-2}. Data is shown for the first negative going sweep in O_2 saturated 0.5 M NaOH at a scan rate of 5 mV s^{-1}. **(264)**

Figure 8.3. The 15th cycles of the largest particle diameters deposited on TiO_2 (Estimated particle diameter = 5.90 nm) and Fe_2O_3 (estimated particle diameter = 6.40 nm) supports. Data is shown for sample prepared on Au substrates and screened in Ar purged 0.5 M NaOH at a scan rate of 50 mV s^{-1}. **(265)**

Figure 8.4. Mean photocurrent onset potential of TiO_2 supported nanoparticles and the mean anodic photocurrent peak potential of Fe_2O_3 supported Pt nanoparticles. Measurements were carried out in Ar purged 0.5 M NaOH at a scan rate of 50 mV s^{-1}. Data is shown for the first illuminated cycles of arrays #8075 and #8135. **(267)**

DECLARATION OF AUTHORSHIP

I, Sandy Kerr

declare that the thesis entitled

Particle Size and Support Effects in Electrocatalysis and Photoelectrochemical Water Splitting

and the work presented in the thesis are both my own, and have been generated by me as the result of my own original research. I confirm that:

- this work was done wholly or mainly while in candidature for a research degree at this University;
- where any part of this thesis has previously been submitted for a degree or any other qualification at this University or any other institution, this has been clearly stated;
- where I have consulted the published work of others, this is always clearly attributed;
- where I have quoted from the work of others, the source is always given. With the exception of such quotations, this thesis is entirely my own work;
- I have acknowledged all main sources of help;
- where the thesis is based on work done by myself jointly with others, I have made clear exactly what was done by others and what I have contributed myself;
- none of this work has been published before submission

Signed: …….

Date:…….

Acknowledgements

Firstly I would like to thank my supervisor Brian Hayden for his overall support and guidance throughout the course of this project. Also I would like to thank him for his continued positivity at times when things didn't seem to be going anywhere.

I would also like to thank all past and present members of the Hayden group who have all helped in some way as well as making the lab a more enjoyable place to work in. I would like to extend a particular thanks to Dr Jovine Emmanuel and Fiona rogers for their help preparing the samples used in this work. I also thank the current and previous postdocs of the group who kept the lab running, which everyone who has passed through the group would agree is no easy task.

I am also grateful for the help of all at Ilika technologies, who are always patient and willing to share their expertise in the experimental techniques. I would like to thank Dr Sam Guerin and Dr Denis Pasero in particular for helping out with XRD measurements when our system was down.

Finally I thank all my friends and family for their support and encouragement throughout the course of my studies. Particular thanks to Charlotte for putting up with my stressed state of mind for the latter stages of my studies.

Abbreviations

AFM	Atomic force microscopy
CB	Conduction band
DMFC	Direct methanol fuel cell
DSA	Dimensionally stable anode
E_{CB}	Conduction band edge energy
E_{VB}	Valence band edge energy
E-gun	Electron gun
K-cell	Knudson cell
MBE	Molecular beam epitaxy
MOR	Methanol oxidation reaction
OER	Oxygen evolution reaction
ORR	Oxygen reduction reaction
PEC	Photoelectrochemical cell
PVD	Physical vapour deposition
QCM	Quartz crystal microbalance
RF	Radiofrequency
SMSI	Strong metal support interaction
TEM	Transmission electron microscopy
VB	Valence band
XPS	X-ray photoelectron spectroscopy
XRD	X-ray diffraction

1. Introduction

1.1 Motivation for solar energy conversion research

1.1.1 The Importance of Sustainable Energy

In order to maintain current standards of living and to continue to facilitate economic growth, the world is hugely dependant on a low cost and on demand supply of energy. Currently the worlds annual energy usage stands at approximately 4.5 x 10^{20} J,[22] the vast majority of which being supplied by fossil fuels.[23,1] This figure will inevitably increase in accordance with population growth, as well as the rapid economic expansion currently experienced in developing nations. This level of growth is expected to double the current global population by the end of the century and to at least double the current global energy usage by 2050.[24] In spite of the resulting depletion of the world's primary energy resources (coal, oil and gas), many sources indicate that sufficient reserves exist to meet the needs for the 21st century.[25] Mounting evidence however suggests that continued energy usage even at present day levels may have significant financial and environmental implications for future generations.

Emissions of CO_2 have risen rapidly ever since the dawn of the industrial revolution, which saw widespread implementation of heat and steam based engines powered by fossil fuels. The increased levels of atmospheric CO_2 associated with this significant change in lifestyle, have in turn been accompanied by an increase in the average global surface temperature (Figure 1.1).

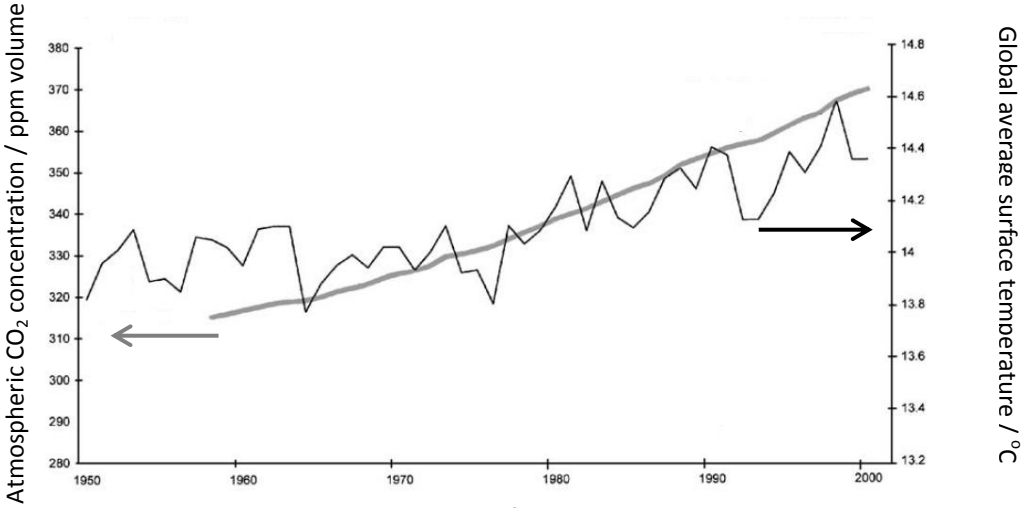

Figure 1.1. Atmospheric CO_2 concentration from 1958 – 2000. Also shown is the average surface temperature of the earth from 1950 - 2000. Figure taken from ref [1].

The observed relation between global temperature and CO_2 emissions serves as compelling evidence for the impact of human activities on the environment for many. The global surface temperature has also closely correlated with atmospheric CO_2 concentration for several hundred thousand years prior to the significant growth in human influence (Figure 1.2).

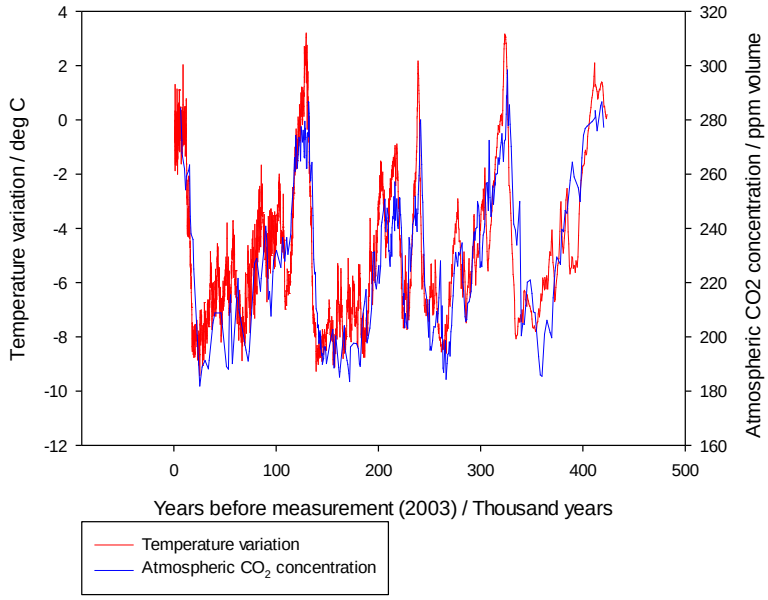

Figure 1.2. Temperature variation and atmospheric CO_2 concentrations over the past 420 000 years derived from the Vostok ice core.[2,3] Figure reproduced from ref [4].

Over the previous several hundred thousand years, the atmospheric CO_2 concentration did not rise much above 300 ppmv (parts per million by volume). With the onset of the industrial revolution this parameter has however increased from approximately 280 to the present day value of approximately 380 ppmv.[26] Furthermore, the rate of rise of both atmospheric CO_2 concentration and global temperature has increased markedly over the previous half century.[26]

In spite of the largely unabated rise in energy usage and CO_2 levels, the average energy intensity (Energy consumed per unit GDP) has steadily decreased over the past century.[27] This results from technological advances in how efficiently fuels are utilised and transported, and may offset to some extent the effects of increasing population growth. Additionally, the proportional usage of the different fossil fuel classes has changed dramatically throughout history. Slowly, there has been a transition to fuels with higher H to C ratio. With the movement from coal to oil to gas, this ratio has increased by 6 times from 1860 to 1990.[28]

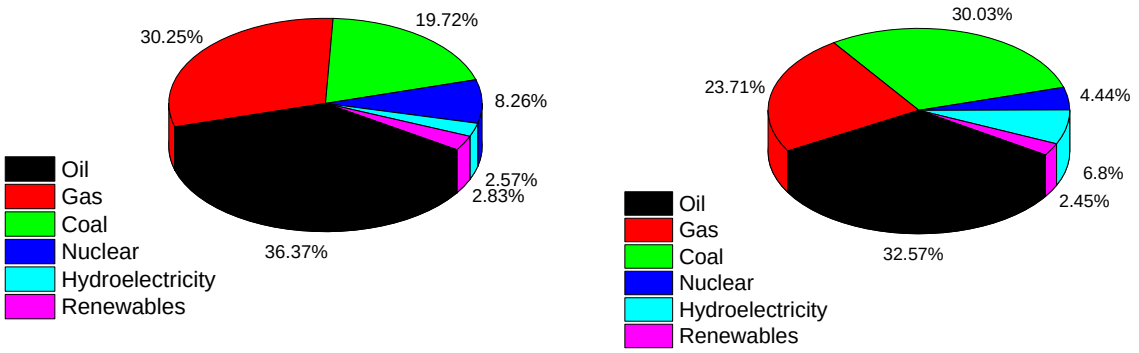

Figure 1.3. Energy consumption by fuel in 2014. The case for both the USA (left) and the global total are shown (right). Data taken from ref [5].

The current proportional usage of the different fuel classes are shown in figure 1.3.[5] It is apparent that the energy production in the U.S. is similar to the global scenario. Being a world leading economy, it also contributes to more usage per capita than any other country. The case is similar for other developed nations,[5] and as such, the level of energy production is considered to be intimately linked to standard of living. In fact, the wealthiest 25% of the population consume approximately 75% of global energy.[29] This standard is not however without cost, and despite a growing realisation of our impact on the terrestrial environment, it has not been matched with a cultural shift from our reliance upon heavily polluting activities.

In addition to rising CO_2 levels, a number of other anthropogenic emissions are a cause of significant concern. Pollutants such as SO_2, NO_x and CO are also produced in large quantities by industrial activities and transportation. As well as the widely documented greenhouse effect, such activities contribute to other damaging processes, such as acid rain, stratospheric ozone depletion and photochemical smog.[30] In order to mitigate such effects, it is clear that an alternative carbon-free energy supply is required to play an increasing role in global energy production. This supply is ideally required to operate with the absence of harmful emissions in both production and the point of end use. A solar – hydrogen economy is widely accepted as the most promising means through which to achieve these demands.[1,27]

1.1.2 Solar Hydrogen Production

The sun represents by far the most abundant natural energy resource, upon which all life is either directly or indirectly dependant. The energy from the sun that strikes the earth's surface can be equated to 150,000,000 x 500 MW power plants at any one time.[22] Efficient utilisation of solar energy could therefore easily supply our current and projected energy requirements many times over. In spite of this, solar energy remains a relatively untapped resource, with the uptake of technologies capturing solar energy being rather limited to date. At present, the usage of energy converted from solar radiation is only roughly 0.5% of the total annual amount consumed.[23] This is largely related to the high costs of the devices employed. The seasonal and daily variability of solar energy yields additional problems, since a stable and constant energy supply is required. Whilst modern solid state photovoltaics convert the suns energy with extremely high efficiencies (with the highest reaching 46% to date)[31] the electrical energy generated in this manner is difficult to store efficiently. Instead, technologies which convert the suns energy into an inherently more storable form are required. Ideally this will be in the form of fuels, whereby energy from the sun is captured and stored efficiently in chemical bonds.

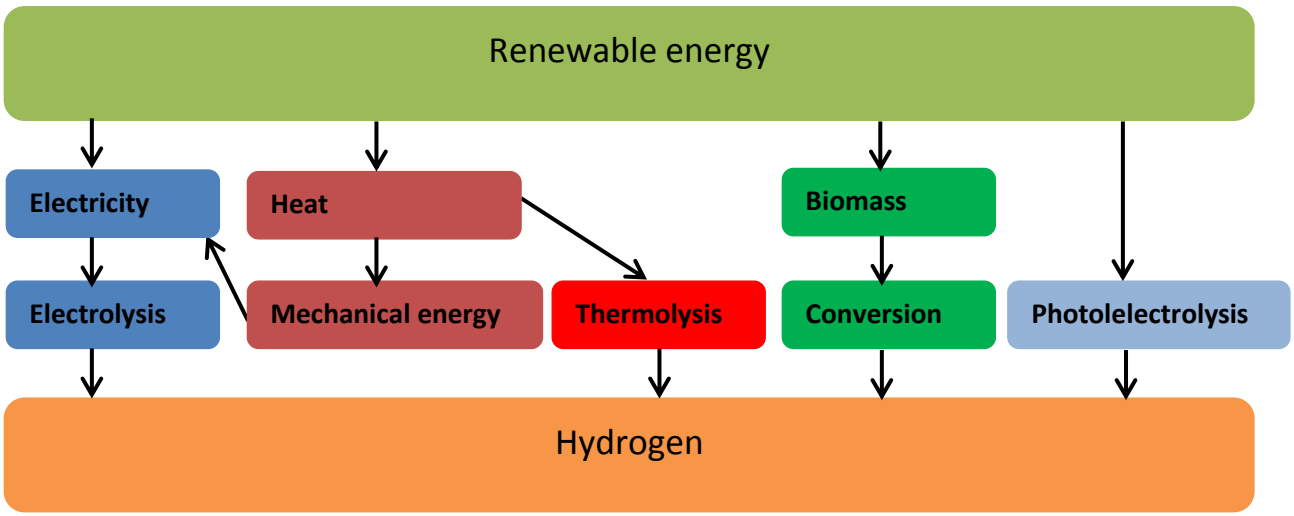

Figure 1.4. Schematic representation of the main sustainable routes to hydrogen production. Reproduced from ref [1]

A relatively large number of techniques can be employed to produce hydrogen from renewable sources (Figure 1.4). Hydrogen is also largely believed to be the most suitable fuel for storage of solar energy, since it possesses extraordinarily high gravimetric energy density, which equates to roughly three times that of oil.[32] In addition, it may be also produced from abundantly available sources (e.g. H_2O) in the absence of harmful emissions. Hydrogen is also a highly versatile fuel suitable for both mobile and stationary applications through combustion or electrochemical reaction. The current favoured production method is from methane via steam reforming, a method which results in further CO_2 emissions.[33] Although electrolytic hydrogen production makes up a small proportion of the current global supply, it is mainly limited to applications where a high purity of hydrogen is required, e.g. the food industry.[34] Nevertheless, such an approach cannot be considered as sustainable if the required electrical energy input is sourced by non-renewable means. Of the sustainable production methods in Figure 1.3, those involving electrochemical conversion of water to hydrogen are considered among the most attractive and potentially offer superior conversion efficiencies over other methods.

Two main solar electrolytic hydrogen production methods are considered feasible,[35] involving either an electrolyser coupled with a PV device, or an integrated device (photoelectrochemical cell, or, 'PEC') in which light absorption and electrochemical reaction occurs at a semiconductor – electrolyte interface. The latter is particularly pertinent, since it may operate at a significantly reduced cost. Cost reductions come in the form of elimination of one of the key components from the former method, as well as less stringent and money intensive processing conditions to fabricate such devices. The ease of electric field formation at a semiconductor – electrolyte junction is particularly attractive,[36] since inexpensive materials may be used without the need for such pristine surface quality as required in the case of p-n junction formation in solid state devices.

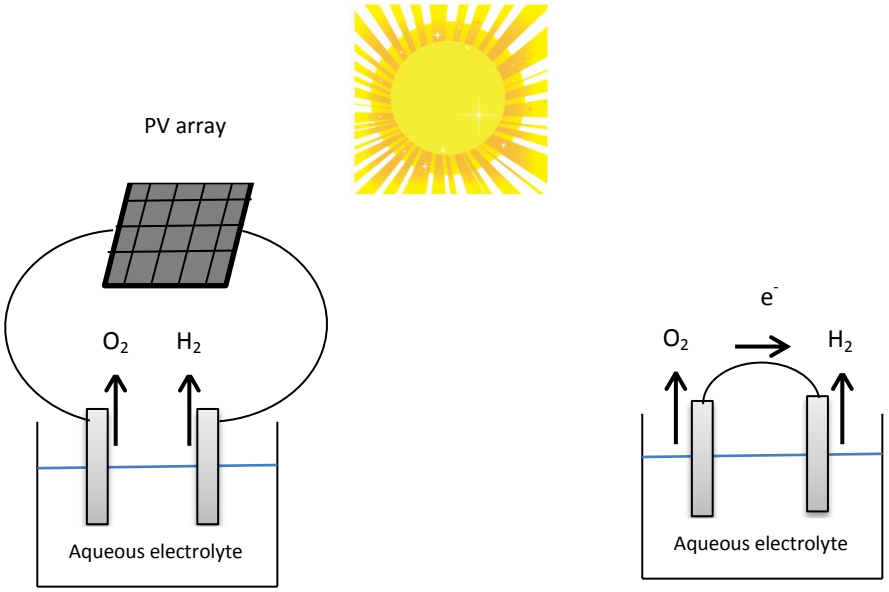

Figure 1.5. Graphical representation of two potential solar hydrogen production methods. Left: PV coupled electrolyser comprising a PV array and an anode and cathode pair immersed in an aqueous electrolyte. Right: Photoelectrochemical cell comprising of either one or two photoactive semiconductor electrodes immersed in an aqueous electrolyte. Where only one semiconductor electrode is employed, a metal (commonly Pt) serves as the counter electrode.

1.1.3. Materials Related Challenges in Energy Applications

The primary factor relating to large-scale viability of solar hydrogen production ultimately resides within the cost of the devices employed. In addition to minimising the initial capital cost, it is important that these devices maintain sufficient fuel production rates over a long period of time and with minimal maintenance to remain economical. The constraints imposed on candidate materials severely limit the number of options, since they are required to be highly active, chemically stable and low cost.

Presently, no single material exists which adequately satisfies the multitude of requirements demanded for a successful device.[37] The basic requirements can be rationalised by splitting the photoelectrochemical water splitting process into its constituent parts. First is the absorption of solar energy to generate electron – hole pairs. To this end, a candidate material is expected to absorb as much of the solar spectrum as possible, a large proportion of which being in the visible light region (~ 400 nm $\leq \lambda \geq$ 700 nm).

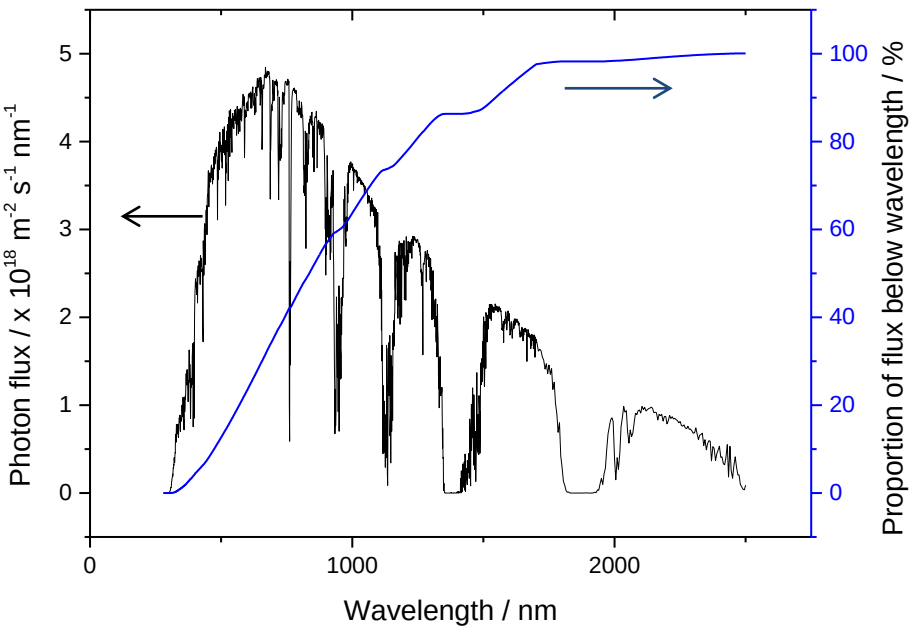

Figure 1.6. Spectral photon flux for solar radiation (AM 1.5 G – Standardised solar spectrum) between 280 and 2500 nm. Shown also are the proportions of the total flux that lie above the energy at the specified wavelength (i.e. at lower wavelengths).

It therefore follows that the optical properties of a material ultimately dictate the maximum achievable efficiency level of the device. Furthermore, a number of energetic requirements must also be met in order to facilitate the water splitting reaction, which will be discussed in more detail in a later section. The important overall factor in materials development is of course the overall efficiency of photoelectrolysis under solar illumination, which clearly will be dependent on the materials ability to satisfy the necessary requirements. In general it is considered that a solar to hydrogen conversion efficiency equal to or greater than 10 % is necessary for commercial implementation of such devices.[38]

1.2. Electrochemistry at Semiconductors

1.2.1. Energy Levels in Semiconductors

The optical, electrical and electrochemical properties of semiconductor electrodes are dictated by their electronic structure, which is most often discussed in terms of, 'energy bands'. This band-type structure is derived from an extension of molecular orbital theory, albeit with the distinction

that an essentially infinite number of atoms are considered in the context of semiconductors.[39] Owing to the large number of atoms composing the solid in this case, the energy spacing between individual energy levels is sufficiently low such that they may be considered as a continuous band as opposed to individual discrete energy states. In the figure below, a hypothetical material composed of n atoms is considered.

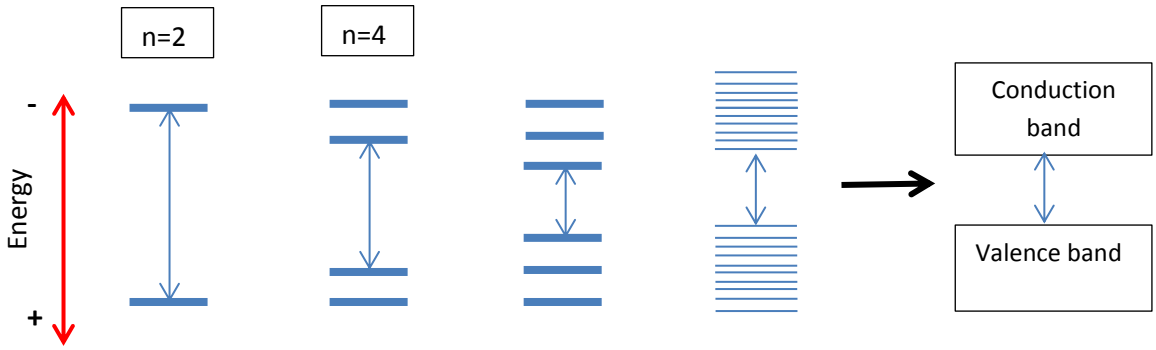

Figure 1.7. Schematic representation of the molecular orbital and band structure creation in a hypothetical solid. Discreet molecular orbitals are formed which are separated by a gap (HOMO-LUMO) on the left hand side. With large numbers of atoms the energy spacing becomes small, and is approximated by denoting the vacant and filled levels as a continuous band (right).

As with most aspects of chemistry, it is the highest occupied and lowest unoccupied levels that are of primary interest. Where a material has an odd number of valence electrons, the valence band will be only partially occupied, effectively allowing delocalisation of electrons through promotion into neighbouring levels which are close in energy. In the case of a material in which there is an even number of valence electrons, the valence band will be fully occupied, with the next lowest unoccupied level (i.e. the conduction band edge) being separated from the valence band edge by a material dependent parameter known as the band gap (E_g). This is analogous to the HOMO – LUMO energy spacing in molecular systems. Typically the valence band is a few eV wide, however due to greater degree of orbital overlap; the conduction band is significantly broader. Furthermore, the bands relating to higher excited states usually overlap with the conduction band and thus there are considered to be unoccupied energy states from the conduction band edge to infinity.

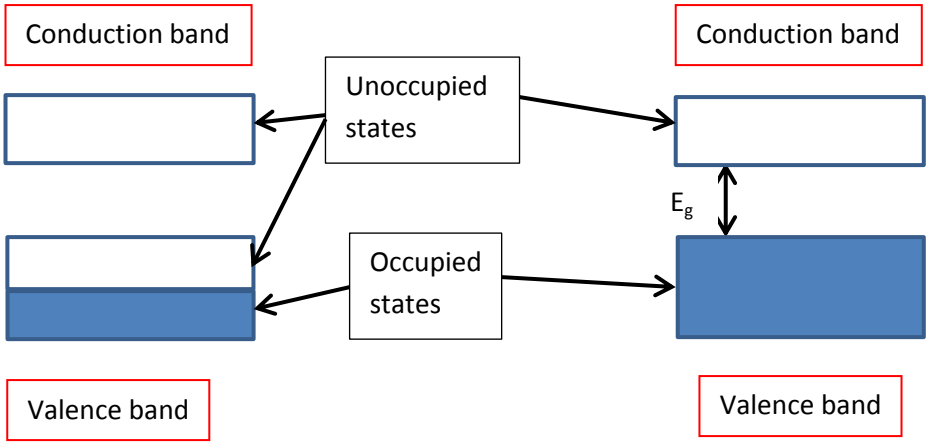

Figure 1.8. Typical band structure diagrams for a hypothetical conductor (left) and semiconductor (right). Solid blue colour represents filled energy levels whereas unfilled areas represent unoccupied levels. Note that in the case of the semiconductor, the highest occupied and lowest unoccupied levels are separated by an energy gap (E_g).

The band gap parameter represents a region in which no energy levels exist, and is largely dependent on the nature of the atoms from which the material is composed, as well as the orbitals that contribute to the bonding. Generally speaking, materials that have higher bond strengths tend to exhibit larger band gap values as well as increased stability towards the operating environments found in photoelectrochemical cells.[10] The band structures found in semiconductors as outlined above are also similar to the case of insulating materials. Insulators too feature a fully occupied valence band separated from the next available energy states by a gap in which no such states exist. The assignment of whether a material is said to be semiconducting or insulating resides within the magnitude of the band gap, with materials considered as semiconductors generally possessing band gaps between the region of 1 – 4 eV.[40,41,42] In solid materials, the movement of electrons (i.e. conductivity) requires that the electrons occupy orbitals that are not fully occupied. This is clearly not the case in semiconductors, and thus either thermal or optical excitation is required to induce conductivity.

Upon excitation, electrons may be transferred from the valence to conduction band, thus causing partial occupation of the conduction band as well as the presence of positively charged electron vacancies (holes) in the valence band. The dominant form of conduction is encompassed in a further distinction that must be made between the different types of semiconductor (Figure 1.8).

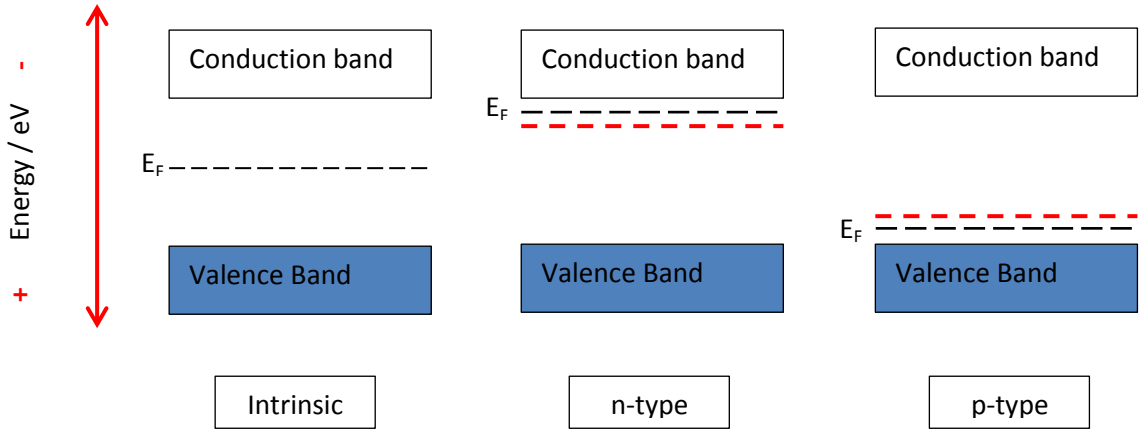

Figure 1.9. Band structure representation of intrinsic, n-type and p-type semiconductors. The position of the Fermi level is represented by E_F. Also shown (Red dotted line), are the positions of the donor and acceptor levels in n and p-type materials respectively.

The concept of extrinsic or 'doped' semiconductors relies on an alternative method through which to generate charge carriers in a semiconductor. In this approach, altervalent elements are introduced into the material to peturb the respective electron and hole carrier concentrations.[39] For example, if phosphorous with 5 valence electrons is incorporated into silicon, an additional valence electron is available from the phosphorous. When the dopant energy is close to that of the conduction band edge (Figure 1.8), electrons may readily be promoted into the conduction band, and as such the concentration of electrons in this instance is greater than that of holes. This can be observed by the negative shift in the Fermi level. Such materials are therefore known as n-type semiconductors. A similar situation exists whereby holes act as the majority charge carrier type. This occurs when acceptor type impurities (e.g. Al in Si) are incorporated into the semiconductor. When the acceptor level lies close in energy to the valence band edge (Figure 1.8), electrons may be promoted into the acceptor thus increasing the concentration of holes relative to electrons. Under such conditions the semiconductor is termed as p-type and the Fermi level moves closer to the valence band.

An additional concept central to the study of semiconducting materials is that of the Fermi level (E_F). This describes the statistical distribution of electrons in a solid and is defined as the energy at which the probability of electron occupation is equal to ½.[6] At all temperatures above absolute zero, the electron distribution is described by Fermi-Dirac statistics. The probability of electron occupation at a given energy and absolute temperature is defined by the Fermi function (f(E):[43]

(1.1) $$f(E) = \frac{1}{1+exp\left(\frac{E-E_F}{kT}\right)}$$

This concept also represents the electrochemical potential of electrons in a given solid electrode. In the case of an intrinsic semiconductor, E_F lies in the centre of the band gap. This is derived with the recognition that all valence band states are occupied and all conduction band states are unoccupied. The consequence of n-type and p-type doping is a displacement of the Fermi level towards the conduction and valence band edges respectively, as shown in Figure 1.8.

The Fermi function clearly shows that the electron occupation depends largely on the temperature of the system, which arises due to thermal excitation of electrons. The associated promotion thereby introduces conductivity in the material by generation of delocalised charge carriers. The relative concentrations of electrons (n_{eq}) and holes (P_{eq}) in the conduction and valence band at equilibrium are described by the equations below:[6]

(1.2) $$n_{eq} = N_c exp\left[-\frac{E_F-E_C}{kT}\right]$$

(1.3) $$p_{eq} = N_v exp\left[-\frac{E_V-E_F}{kT}\right]$$

Where N_v and N_c are the density of states at the valence and conduction band edges respectively.

For intrinsic semiconductors any promotion of electrons must leave behind an equal number of positively charged vacancies. In this case it is apparent that n_{eq} must be equal to p_{eq}. With this in mind, the combination of equations 1.2 and 1.3 can be used to relate the concentration of charge carriers to the band gap (E_g):[44]

(1.4) $$n_{eq}^2 = N_o exp\left[-\frac{E_g}{kT}\right]$$

Where N_0 is N_cN_v.

Equation 1.4 shows that the larger the band gap of a material, the lower the concentration of charge carriers will be. In the case of most materials of interest to photoelectrochemistry, E_g is significantly larger than kT. Consequently, a very small amount of free charge carriers are present

at equilibrium. As a result of this, incorporation of dopants in minute quantities may substantially alter the electric properties of semiconductors.

Whilst the equations above represent the case of an intrinsic semiconductor, the carrier concentrations can also be expressed for doped materials. The total concentration of electrons (n) and holes are simply the sum of those thermally generated and those introduced through doping (N_d), such that in an n-type semiconductor:[44]

(1.5) $$n = N_d + n_{eq}$$

However, since n_{eq} is so small in most semiconductors of interest, equation 1.5 may be further simplified to assume that the total electron concentration is equal to the doping density, N_d.

Where shallow donors are concerned (i.e. those close in energy to the conduction or valence band edge), the concentration of electrons/holes introduced through doping is approximately equal to the doping density.

1.2.2. The Semiconductor Electrolyte Interface

Within the context of electrochemistry, the potential of a given electrolyte is defined by the Nernst equation:[45]

(1.6) $$E_e = E_e^0 + \frac{RT}{nF} Ln \frac{[C_{ox}]}{[C_{red}]}$$

This potential is commonly referred to as the electrolyte Fermi level such that both sides of a semiconductor – liquid interface can be compared in the same terms. The first model of the semiconductor-liquid interface popularised the now widely accepted consideration of the electrolyte in terms of occupied and unoccupied states, referring to the reduced and oxidised species respectively.[46] The model gives rise to a Gaussian relationship between the redox states and electron energy. The model states also that solvent shell fluctuations are described by harmonic oscillations and the energy distributions of both the oxidised and reduced (D_{ox} and D_{red}) species are expressed in Equations 1.7 and 1.8:[46]

(1.7) $$D_{ox} = exp\left[\frac{(E - E_F - \Lambda)^2}{4kT\Lambda}\right]$$

(1.8) $$D_{red} = exp\left[\frac{(E - E_F + \Lambda)^2}{4kT\Lambda}\right]$$

In the equations above Λ represents the electron transfer reorganisation energy and typically falls within the range of 0.5 – 2 eV.[47]

Prior to contact of the two phases, the electrochemical potential of the semiconductor (denoted by the Fermi level) will vary from that of the electrolyte. Consequently a net flow of charge must occur in order to reach equilibrium such that $E_{F(semiconductor)} = E_{F(solution)}$. The direction of charge transfer clearly will depend on the relative positions of the Fermi levels on each side of the interface.

The result of the initial equilibration process is depicted in figure 1.9 for both n and p-type semiconductors.

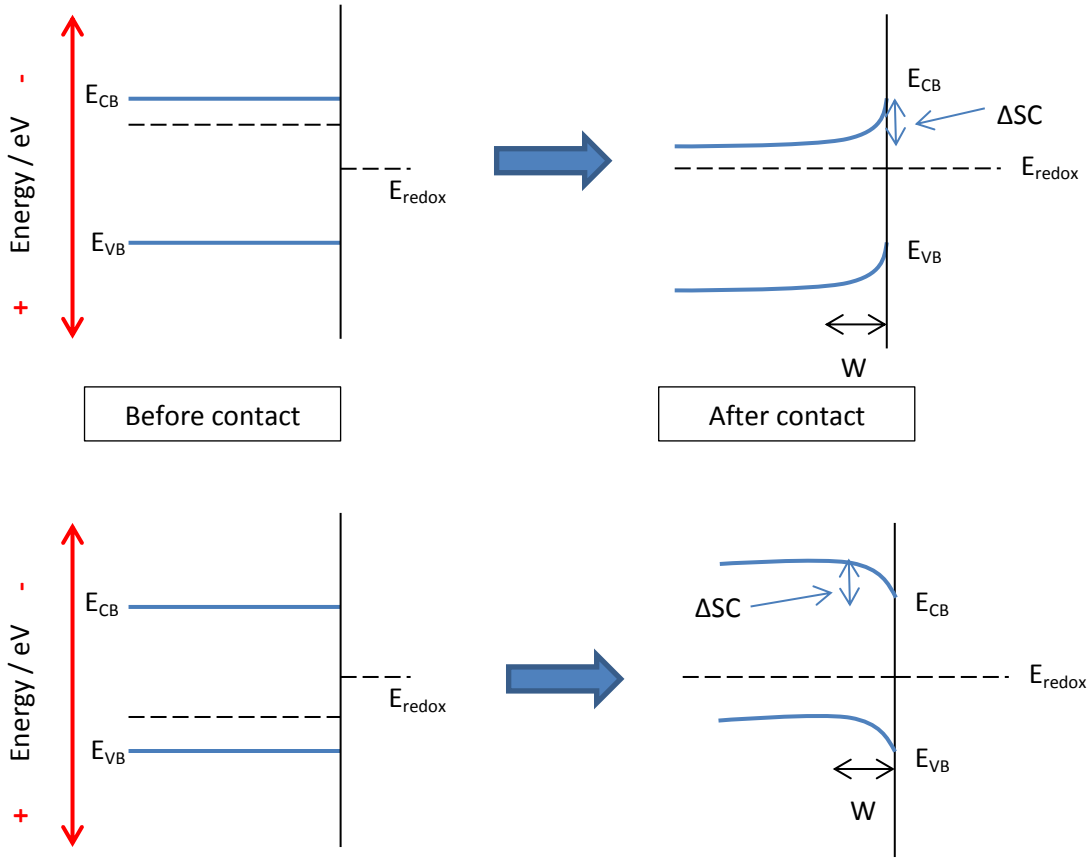

Figure 1.10. A simplified schematic of the equilibration process between semiconductors and a liquid electrolyte. The situations for n and p-type semiconductors are shown in the top and bottom of the diagram respectively. Also shown is the characteristic space charge region voltage ΔSC and its corresponding width W, which forms inside the semiconductor surface.

In the case of an n-type semiconductor, electrons flow from the semiconductor to solution. The ionised donors thereby create a build-up of positive charge which balances the initial potential difference between the two phases. The opposite can be seen to occur in p-type materials. The result of this is the establishment of an internal potential difference known as the space charge region (defined by ΔSC and W in Figure 1.9). The corresponding direction in which the bands are bent at equilibrium is also of key importance in dictating whether a material behaves as a photocathode or photoanode. During the equilibration process, it is also assumed that the electrolyte Fermi level shift is negligible on account of the variation in the density of states between the two sides of the interface.[44] Additionally it is apparent, that the degree of band bending at equilibrium will depend heavily on the potential of the solution.

In addition to the space charge region, a double layer exists at the surface analogous to the situation at metal electrodes. Similarly to metal electrodes, this layer is derived from adsorption of ions in the electrolyte. Bond formation with electrolyte species may also occur. Consequently the total potential drop across the interface is equal to:[47]

(1.9) $$\Phi_{tot} = \Phi_{SC} + \Phi_{H}$$

The previous discussion relates to semiconductors at equilibrium; however the effects of externally applied voltages are of considerable importance in understanding the electrochemical behaviour of semiconductors. At metal electrodes, by varying the applied potential the Fermi level is altered. On account of the much higher electron density, the potential is dropped almost exclusively over the Helmholtz layer at the electrolyte, since an appreciable internal field cannot be sustained inside the metal surface. Semiconductors on the other hand generally maintain a constant potential drop across the Helmholtz layer and the variation in potential is taken up by the space charge layer. This action has significant implications on charge transfer reactions in both dark and light conditions, and will be discussed in the subsequent sections.

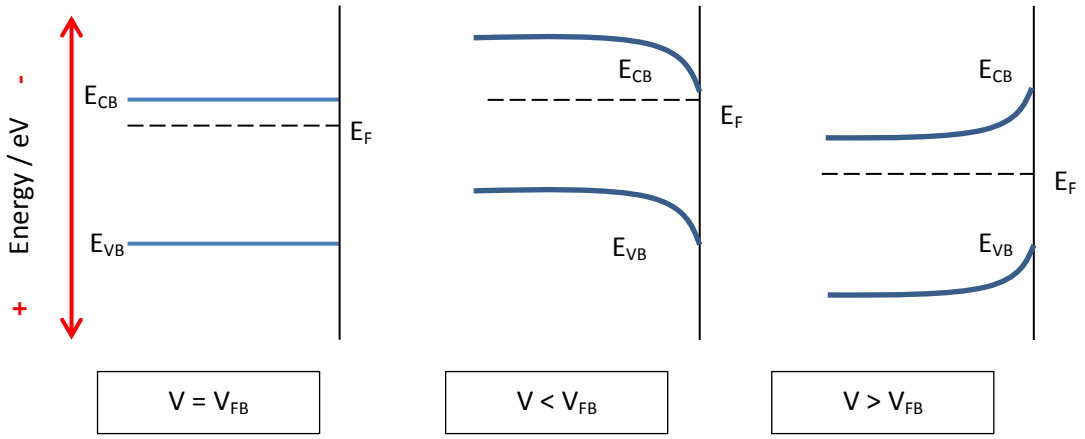

Figure 1.11. Band structure of an n-type semiconductor under differing applied bias. Where V_{FB} denotes the flat band potential (left) i.e. the potential required to remove all band bending.

When potentials are applied that are negative to that of the flat band potential, an accumulation layer forms at the surface. Under these conditions the electric field is such that majority charge carriers are directed toward the semiconductor surface. Conversely, at potentials positive of the FBP, electrons are driven towards the bulk of the semiconductor. Note that in the ideal case as depicted in Figure 1.10, the position of the CB and VB edges remain fixed in place.

1.2.3. Surface States

So far the behaviour of the ideal semiconductor-electrolyte has been described; however the presence of surface states may cause a significant deviation from the expected behaviour. Surface states arise from the sudden termination of the bulk semiconductor structure and may arise from a number of factors such as surface reconstructions, coordinative unsaturation and bonding with electrolyte species.[6] As a result, the electronic structure of the surface differs to that in the bulk, with additional energy levels often present in the band gap region[6]. It is known that these states are able to transfer charge between the semiconductor bands as well as the solution.[48] In the initial equilibration process, charge transfer from surface states can therefore limit the degree of band bending that occurs within the semiconductor. In extreme cases, the equilibration process may involve only transfer from surface states such that the potential difference is instead primarily distributed over the Helmholtz layer.[49] In such situations, any change in the solution

redox potential or the applied potential simply imparts a variation in the Helmholtz layer rather than V_{SC}. This concept is referred to as 'Fermi-level pinning'.

Additionally, the presence of illumination may alter the population of surface states, which may change the band edge positions relative the position in the dark. It has also been shown that where slow interfacial kinetics are present, a build-up of surface trapped holes may alter the interfacial properties such that the level of band bending is reduced.[50]

The magnitude of the potential drop over the Helmholtz layer has also been modelled in respect to different doping levels.[6] It can be seen in Figure 1.12 that the contribution of the Helmholtz layer may make up a significant proportion of the total potential drop across the interface under certain conditions.

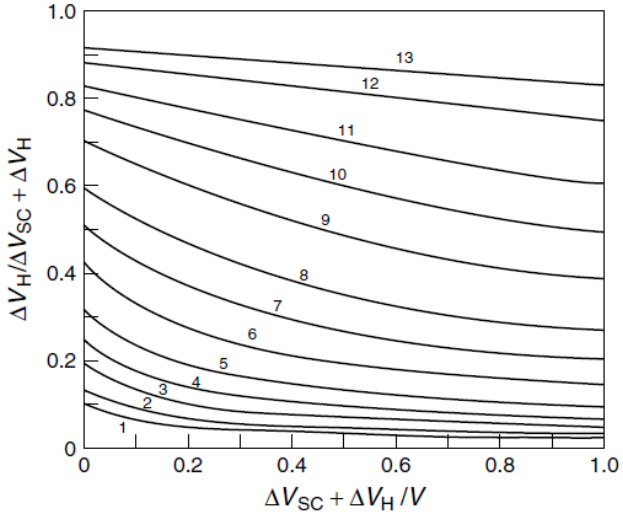

Figure 1.12. The proportion of the potential drop over the Helmholz layer as a function of the total interfacial potential difference. The typical static dielectric constant of TiO_2 (173) was used as well as a Helmholz capacitance of 10 µF cm^{-2}. The different lines represent differing doping densities from 10^{16} (1) to 10^{20} cm^{-3} (13). Figure taken from ref [6].

1.2.4 Dark Charge Transfer Behaviour

Charge transfer between a semiconductor and solution occurs only via the conduction and valence bands (In the ideal scenario). Additionally, the action of a varying the potential at a semiconductor electrode varies to that seen at their metallic counterparts. As such, a separate model to the well-known Butler-Volmer and Tafel relationships is required for a quantitative treatment of electron transfer at semiconductor electrodes.[51]

Unlike metallic electrodes, changes in potential have little to no effect on the potential difference over the Helmholz layer of semiconductors. Instead, the bands bend while remaining fixed in position at the surface.[47] The resulting variation in electric field therefore changes the driving force to direct electrons to or from the surface. Unlike metals, this leads to a situation where the concentration of electrons in the bulk and the surface are not equal. The surface electron concentration is related to the doping density (N_d) and applied bias (V) by equation 1.10:[51]

(1.10) $$n_s = N_D exp\left(-\frac{e_o(V_{SC}+V)}{kT}\right)$$

Where e_0 is the electron charge, k is the bolzmann constant and T is the absolute temperature. Ultimately the concentration of electrons at the surface represents the driving force for the reaction, as opposed to changes in the Helmholz distribution and therefore activation energy at metallic electrodes. The driving force can also be compared to the concentration of surface electrons relative to the equilibrium state, at which the net current is zero. At equilibrium, the surface electron concentration is represented by equation 1.10 but with a replacement of the(V_{SC} + V) term with V_{SC}. The rates of cathodic and anodic electron flux have previously been shown to equal equations 1.11 and 1.12 respectively.[52]

(1.11) $$Cathodic\ electron\ flux = k_{et} n_s [A]$$

(1.12) $$Anodic\ electron\ flux = k_{et}^{-1} [A^-]$$

K_{et} and K_{et}^{-1} represent the forward and reverse rate constants respectively whereas [A] is the concentration of acceptor (oxidised) species and [A^-] is the concentration of donor (reduced) species in solution. At equilibrium where the net current is zero, the two fluxes are equal and can be expressed as:

(1.13) $$k_{ht} n_{se} [A] = k_{ht}^{-1} [A^-]$$

Where n_{se} is the surface electron concentration at equilibrium. The expression for k_{ht}^{-1} can then be obtained and substituted in to the expression for the net electron flux, which is simply the forward flux minus the reverse. The resulting expression for the net electron flux is therefore:[52]

(1.14) $$net\ electron\ flux = k_{et}[A](n_s - n_{se})$$

It is clear from the previous expressions that at potentials more negative of that at equilibrium, an exponential increase in the surface electron concentration occurs, thus greatly increasing the magnitude of cathodic current. Conversely the electron concentration becomes very small when the potential is more positive of the equilibrium value. Little to no anodic current is therefore

expected since the concentration of valence band holes required for anodic current generation is very small in the dark. This however represents the ideal case of a defect free semiconductor, which is rarely the case in reality. The aforementioned surface states may also play a part in dark charge transfer reactions.[53] At this point, the kinetic equations become more complex, and a number of alternatives have been suggested.[54] Many of these still include the n_s (surface electron concentration) term, which becomes problematic when the density of surface states is high enough to introduce Fermi level pinning. This is due to the dependence of n_s on the level of band bending (V_{SC}), which may be altered significantly by the inclusion of surface states.

1.2.4. The Effects of Illumination

The photogeneration of electron-hole pairs occurs when a semiconductor is illuminated with light of energy equal or greater than the band gap energy. These optical transitions can be split into two types; indirect and direct. Direct transitions occur when the conduction band minimum and valence band maximum are at the same wave vector, denoted as k. If the wave vectors are different however, an indirect transition occurs, which requires a change in momentum by a phonon.[7]

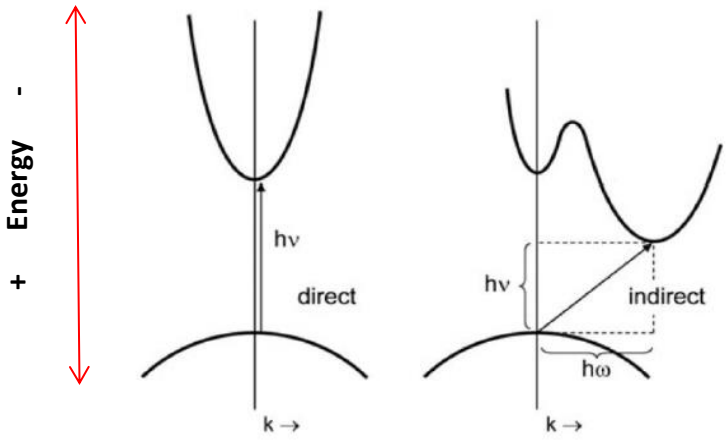

Figure 1.13. Direct and indirect optical transitions in a semiconductor (Left and right respectively). Image taken from ref [7]

The absorption coefficient (α) for these transitions is given by equation 1.15.[7]

(1.15) $\alpha = A(hv - E_g)^x$

Whereby A is a proportionality constant, *h*v is the photon energy and E_g is the band gap. The value of x is equal to 2 and ½ for indirect and direct transitions respectively. Upon promotion of electrons to the conduction band, the electron Fermi level moves upwards (i.e. more negative). Unlike the equilibrium situation in the dark, a single Fermi level is no longer appropriate to describe the carrier distributions. Instead, both the hole and electron populations are described by quasi Fermi levels:[13]

(1.16) $$E_{F,n(x)} = E_C - kTln\left(\frac{N_c}{n(x)}\right)$$

(1.17) $$E_{F,p}(x) = E_v + kTln\left(\frac{N_v}{p(x)}\right)$$

In the equations n(x) and p(x) represent the electron and hole concentrations at point x respectively. Also N_v and N_c refer to the density of states at the valence and conduction band edges respectively. At an n –type semiconductor, the concentration of electrons in the dark is much higher than that of holes. Consequently the electron Fermi level shifts to a much lesser degree than that of the hole Fermi level under illumination. It is also generally assumed that the electron quasi-Fermi level lies at the same value under both illuminated and non-illuminated conditions. Outside of the space charge region, holes will typically recombine and thus the hole quasi Fermi level changes with distance in the semiconductor (Figure 1.14).

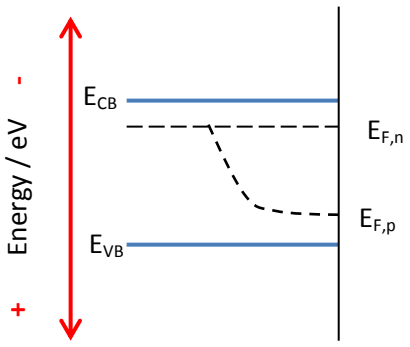

Figure 1.14. Quasi-Fermi levels of an n-type semiconductor under illumination.

Due to the greatly enhanced concentration of holes in the valence band under illumination, the charge transfer characteristics are altered considerably. Now anodic current may take place due to migration of holes towards the interface under influence of the electric field. A similar

approach to the dark electron flux can be used to derive the net hole flux, which relates to the surface concentration of holes (p_s) relative to at equilibrium (p_{se}):[52]

(1.18) $$net\ hole\ flux = k_{ht}[A^-](p_s - p_{se})$$

Electron hole pairs may however be generated inside the space charge region as well as regions in which no appreciable electric field exists. Consequently many optically generated charge carriers will simply recombine. The ratio of charge carriers which contribute to the overall current against those generated under illumination is known as the effective quantum yield. The number of holes collected from outside the depletion layer is dictated by the hole diffusion length L_p, given by:[7]

(1.19) $$L_p = \sqrt{kT\mu_p\tau_p}$$

The hole mobility and hole lifetime are denoted by μ_p and τ_p respectively. The surface hole concentration must also be defined in terms of illumination intensity and the applied voltage. This is a relatively complex process, and as such some simplifications are made. Lewis adopted the approach of denoting the hole flux as the product of illumination intensity and quantum yield, which makes the assumptions that interfacial electron transfer is sufficiently fast that p_s=p_{se}.[52] In the majority of early models it is also assumed that all charge carriers generated in the space charge region are transported to the surface without recombination.[55,56] The most common model was proposed by Gärtner,[57] which again makes the assumption that all photogenerated charges in the depletion layer contribute to the current. It also assumes that all holes at the surface react with the redox species in the electrolyte. The overall equation is:[57]

(1.20) $$Hole\ flux = I_0\left(1 - \frac{\exp(-\alpha W)}{1+\alpha L_p}\right)$$

Where I_o is the incident light intensity.

Typically the relationship is relatively accurate at high levels of band bending and less so at low to moderate band bending. A number of refinements have since been made,[58,59,60] which include the effects of recombination at the surface and in the depletion layer. As is always the case, the net current (i) is represented by the forward current minus that of the reverse, which was previously given in Equation 1.14. The equation therefore becomes:[6]

(1.21) $$i = nF[Hole\ flux - (k_{et}[A](n_s - n_{se})]$$

1.3. Photoelectrochemical Cells

1.3.1. Photoelectrochemical Cell Configurations

The photoelectrochemical splitting of water was first demonstrated by Fujishima and Honda in 1971.[61] In this publication a chemically biased n-type TiO_2 photoanode was shown to produce oxygen upon irradiation, with hydrogen formation at a Pt cathode. Since this initial investigation, the field of photoelectrochemistry has expanded to the design of increasingly complex photoelectrochemical cells and a range of novel improvement techniques. Regardless of the cell configuration employed, the overall water splitting reaction remains the same:

(1.22) $H_2O_{(l)} \rightarrow H_{2(g)} + \frac{1}{2}O_{2(g)}$ ΔG =+ 237.2 kJ mol^{-1}

The positive Gibbs free energy change denotes that the reaction is thermodynamically uphill and consequently a relatively large energy input is required to drive the reaction. The energy band structure of a simple photoelectrochemical cell of the type described above is depicted in figure 1.13. An alternative single photoelectrode system is also possible, where a p-type photocathode is employed in addition to a metallic anode.[62] Additionally, the possibility of using two photoelectrodes is possible, with an n-type photoanode and p-type photocathode.[63]

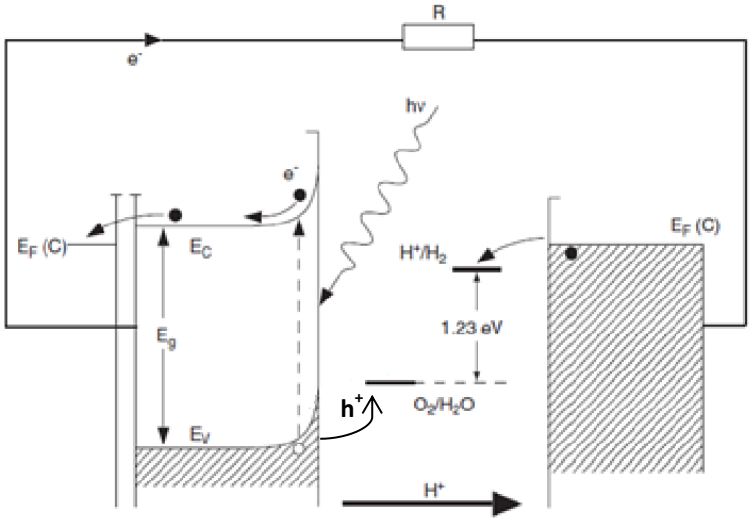

Figure 1.15. Band diagram of an n-type photoanode connected to a Pt cathode in an aqueous electrolyte. The relative positions of the H^+/H_2 and H_2O/O_2 redox couple are also shown with respect to the conduction and valence band edges. Figure taken from ref [8]

In the situation depicted above, photogenerated holes are swept towards the interface by the internal electric field where they react to evolve oxygen from the electrolyte. Electrons are subsequently driven towards the semiconductor bulk and into the external circuitry to the cathode. At the cathode water is thereby reduced to form hydrogen. The associated reactions occurring in the cell depicted above are outlined for both acidic and alkaline electrolytes in equations 1.23 – 1.26.[7]

(1.23) Cathode: $2H_2O + 2e^- \rightarrow H_2 + 2OH^-$ (Alkali)

(1.24) Cathode: $2H^+ + 2e^- \rightarrow H_2$ (Acid)

(1.25) Anode: $2OH^- + 2h^+ \rightarrow \frac{1}{2}O_2 + H_2O$ (Alkali)

(1.26) Anode $H_2O + 2h^+ \rightarrow 2H^+ + \frac{1}{2}O_2$ (Acid)

A configuration also exists whereby both the anodic and cathodic reactions may take place at a single semiconductor.[64] These systems employ finely dispersed semiconductor particles and are known as photocatalysts. They effectively behave as a miniature short circuited cell, whereby the occurrence of both the water splitting reactions dictates that no net current flow occurs in the particle. Systems of this type have been extensively investigated with respect to degradation of organic pollutants as well as water splitting.[64,65] Generally, the cell type depicted above is most prevalent in the literature, partly due to the lack of appropriate photocathode materials that have adequate stability.

Single absorber systems are also attractive due to their versatility. In addition to water splitting, an appropriate reversible redox couple may be interconverted to allow the photoassisted conversion of chemical energy to electrical energy.[66] Cells of this type are typically referred to as regenerative photoelectrochemical cells. An additional increasingly popular concept is that of dye sensitised solar cells (DSSCs) or, 'Gratzel cells'.[67] In this instance a dye is anchored to a semiconductor electrode (typically TiO_2) which undergoes an optical transition under illumination to produce an excited species. Electrons are subsequently injected into the semiconductor conduction band before reducing a simple mediator at the cathode that in turn regenerates the dye. State of the art dyes are typically ruthenium complexes with various organic ligands.[68] However, use of chlorophyll derivatives, related natural porphyrins and other natural dyes are also reported.[67]

Several, 'hybrid' cell designs have also been reported which include multiple stacked semiconductors.[69,70] This hybrid approach may include solid state photovoltaic cells simply wired to conventional electrolysers or monolithic devices with 'buried' junctions. The latter approach

has been trialled with both Si solar cells as well as those based on group III/V semiconductors, reaching solar to hydrogen conversion efficiencies of approximately 7 and 12-20% respectively.[71,72] These relatively modest levels of efficiency are however unlikely to warrant the significant costs incurred with this method. Particularly promising was a cell reported by Gratzel,[73] which used a DSSC of the type described above to bias a WO_3 photoanode. Such materials feature only metal oxide materials and therefore come at relatively low cost. An additional prospect is the use of a single semiconductor of opposite conductivity type behind a photoanode/photocathode.[74] These devices have also shown promising levels of efficiency. Furthermore, use of two stacked n-type absorbers has also been reported. In this case it was shown that n-type Si placed behind a n-type TiO_2 electrode altered its conduction band position in a favourable way for water splitting.[74] Multiple semiconductor junctions have also been successfully applied in other applications, whereby buried p-n junctions were utilised to produce H_2 and Br_2 from HBr solutions.[75]

In spite of the relatively good performance of multiple semiconductor junctions, it remains unclear whether this is enough to offset the higher costs associated with the increased level of device complexity.

1.3.2. Material Requirements for Photoelectrochemical Water Splitting

A large number of requirements are necessary to be satisfied simultaneously to give a viable photoelectrode material. Due to the stringent requirements, an appropriate photoelectrode material has so far remained elusive. Some of the key requirements have already been implied, however they may briefly be summarised as follows:

1. A band gap which maximises absorption of solar energy (i.e. visible light active).
2. Band edges that straddle the H_2O/H_2 and OH^-/O_2 redox couples (i.e. more negative and positive positions of the conduction and valence band edges than the afore mentioned reactions respectively)
3. A significant degree of photovoltage production under illumination to drive the water splitting reaction (1.23 V).
4. Good charge separation/transport ability.

5. A catalytically active surface to reduce the required overpotentials for the water splitting half reactions.
6. Good stability towards photocorrosion and chemical corrosion.

The various requirements are depicted in Figure 1.16.

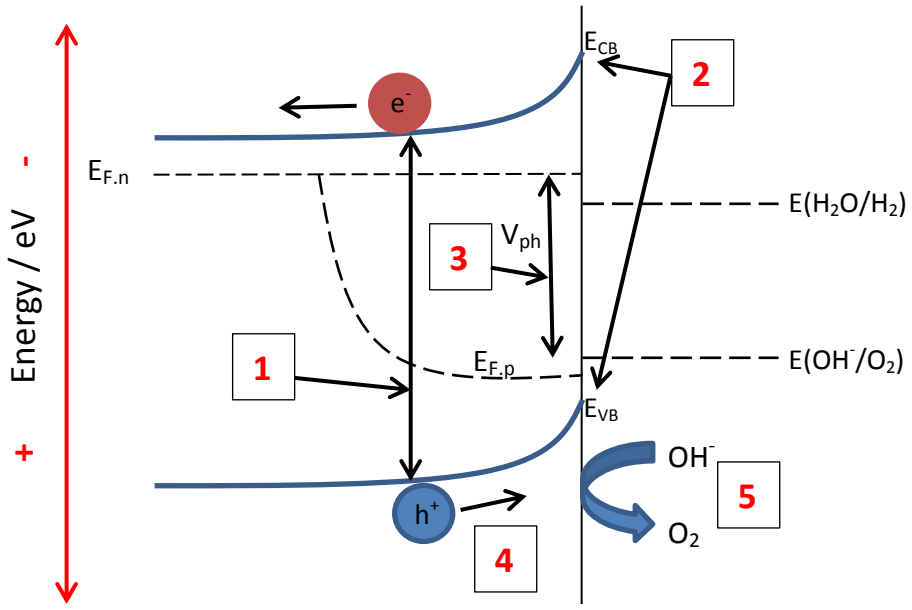

Figure 1.16: Diagrammatic representation of the key requirements for an efficient photoelectrode material. The case shown is that of an n-type photoanode. The band edge positions are shown in relation to the potentials for water splitting half reactions. Also shown is the photovoltage (V_{ph}) given by the different between $E(OH^-/O_2)$ and the majority carrier quasi fermi level.

Perhaps the most important requirement is that of the band gap, since this ultimately dictates the proportion of solar irradiation which may be absorbed. This parameter therefore limits the maximum attainable efficiency of solar energy conversion at a given semiconductor. Typically it is stated that the ideal band gap size will fall in the range of 1.6 – 2.4 eV in order to account for losses associated with the kinetic overpotentials required to drive the reaction.[76] Few of the known stable semiconductors have band gaps between this range, and those that do often suffer from poor alignment of the band edges with respect to the water splitting reaction. The band gaps of a number of well-known semiconductors are presented in table 1.1.

Table 1.1

Semiconductor	Band gap (E_g) / eV	Approximate absorption threshold / nm
Si	1.11[77]	1117
GaAs	1.42[78]	873
CdS	2.42[9]	512
Fe_2O_3	2.20[9]	563
TiO_2 (Anatase)	3.20[79]	388
TiO_2 (Rutile)	3.00[79]	413
WO_3	2.70[9]	459

The band edge positions are also important, since charge carriers enter the solution at fixed energies dictated by the positions of the conduction and valence band edges. The position of the valence band edge in most oxide semiconductors easily meets the conditions required and is significantly positive of the OH^-/O_2 potential. On the other hand, very few materials have sufficiently negative conduction band energies to drive the hydrogen evolution reaction. In such cases an additional bias is required to raise the Fermi level of the cathode more negative, thus greatly reducing the overall efficiency of the device. The band edge placements for several known semiconductors are depicted in Figure 1.17, in addition to some hypothetically ideal materials.

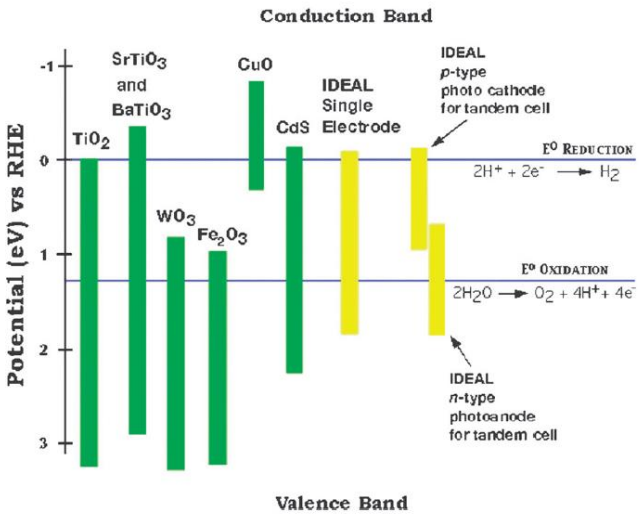

Figure 1.17. Band edge positions of several known semiconductors in relation to the water splitting half reaction potentials. Also shown are the hypothetical ideal band edge placements for a single photoelectrode configuration in addition to a system featuring two absorbers. Figure taken from ref [9]

It is clear from Figure 1.17 that CdS is in closest agreement with the requirements for an ideal single photoelectrode material. However CdS is unstable in the operating environments of a photoelectrochemical cell.[80] Additionally whilst the band edge conditions are met by $SrTiO_3$, its large band gap limits its sensitivity to light within the UV range of the spectrum. Consequently it operates with very low solar to hydrogen conversion efficiency.[81]

The third requirement of photovoltage is theoretically defined as the difference between the conduction band edge and the potential of the OH^-/O_2 couple for an n-type semiconductor. Once again however a much larger value than the predicted 1.23 V is required in order to overcome the required kinetic overpotentials. Even in the case of materials that show good semiconducting properties, the maximum attainable photovoltage is only approximately two thirds of the band gap value.[82] More accurately, the photovoltage is defined as the difference between the electron and hole quasi-Fermi levels.[83] This in turn is dictated by the kinetics of the processes which determine the charge carrier concentrations in the material. Lewis et al. classified the five main fates of photogenerated charge carriers which affect the magnitude of the photovoltage as follows:[82]

1. Recombination in the bulk of the semiconductor
2. Recombination in the depletion layer
3. Tunnelling through the potential barrier at the semiconductor surface
4. Thermionic emission
5. Recombination at defects or trap states at the semiconductor – liquid interface.

The relative magnitudes of such processes are relatively independent of the semiconductor band edge positions and band gap. This draws further emphasis that all the photoelectrode material requirements must be satisfied simultaneously. Appropriate band edge placement and catalytic ability are therefore irrelevant if insufficient photovoltage is produced to drive the reaction of interest.

The requirement of good charge separation ability is intimately linked with photovoltage, since poor separation will lead to increased levels of recombination accompanied by lower photovoltage production.[82] Whilst the space charge layer is generally extremely efficient at separating charges, recombination may readily take place at defects.[84] Consequently, appropriate processing methods must be employed to minimise such effects. Additionally, the physical dimensions of the semiconductor are important, since this can hugely influence both the magnitude of the internal electric field in addition to the length over which holes must

travel to reach the surface.[19] The addition of dopants has been previously found to greatly increase the rate of recombination in a number of different materials.[85] Dopant addition has also been suggested to improve charge separation by the passivation of grain boundaries in Fe_2O_3.[86] Additionally, the inhomogeneous distribution of dopant species has previously been shown to alter the strength of the internal electric field.[87] This has previously been shown to alter the charge separation ability of metal oxide materials.[88]

The fourth requirement of a catalytically active surface is seldom met with the semiconductors of interest towards photoelectrochemical water splitting. Owing to the extremely positive valence band energies in many oxides, this is often an area which is over looked. The principle techniques to improve this parameter are identification and imposition of surface active sites for water splitting as well as the addition of appropriate HER/OER catalysts.[89,90,91] The exact function of these catalysts is not well understood and it is often cited that catalysts function by improving charge separation performance rather than increasing the rate of interfacial electron transfer.[92] This area is discussed in greater detail in Section 1.4.2.

The final requirement which is of extreme importance is that of corrosion and photocorrosion resistance. Gerischer previously stated the requirements for the stability of photoanodes and photocathodes for water splitting respectively as:[93]

$E(OH^-/O_2) < E_{p,d}$

$E(H_2O/H_2) > E_{n,d}$

$E_{p,d}$ and $E_{n,d}$ denote the anodic and cathodic decomposition potentials respectively. The decomposition potentials and band edge positions with respect to the water splitting potentials are shown for several semiconductors in Figure 1.18.

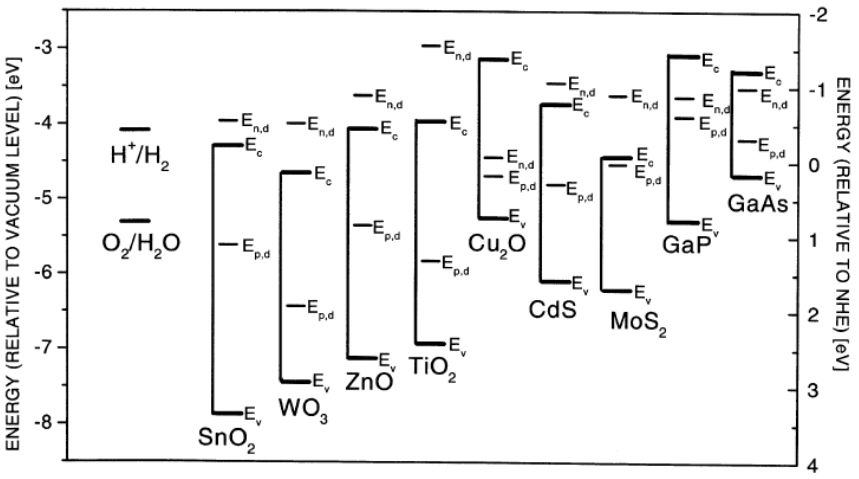

Figure 1.18. Anodic and cathodic decomposition potentials for a range of well-studied semiconductors. Figure taken from ref [10]

In spite of their promising characteristics, non-ionic semiconductors readily undergo corrosion in aqueous environments.[80,] A number of methods have sought to stabilise these materials, such as incorporation of protective layers as well as catalyst addition to compete kinetically with the decomposition processes.[94]

1.3.3. Metal Oxide Photoelectrode Materials

Metal oxides are so far the only material class in which the stability issues inside PEC operating environments have been solved. The majority of oxides have valence bands comprised of O (2p) orbitals and thus it can be seen from Figure 1.17 that the valence band energies vary very little.[9] The metal d orbitals typically form the conduction band and thus vary to a greater degree.

By far the most studied photoelectrode material is TiO_2, mainly due to its excellent stability and reactivity towards water.[8] TiO_2 exists as three main structures, Rutile, Anatase and Brookite, although Anatase has consistently emerged as the most promising towards water splitting.[95] TiO_2 has also found use in a number of other technologies, such as mineralisation of organic pollutants, self-cleaning glass, anti-cancer treatments, gas sensing and fuel cell catalyst supports.[65,96,97,98,99]

The bulk unit cells of the two most commonly studied TiO_2 structures are presented in Figure 1.19:[11]

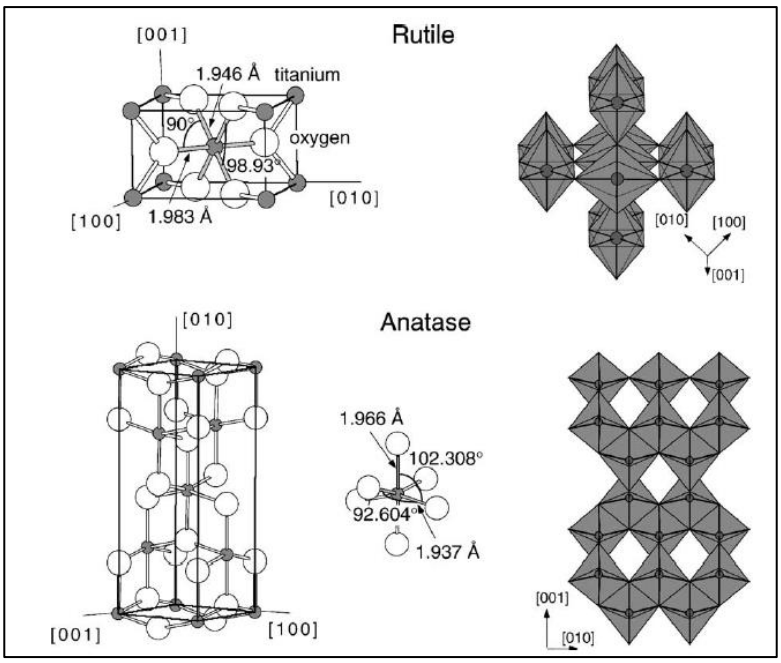

Figure 1.19. Bulk unit cell structures of anatase and rutile TiO_2. Figure taken from ref [11]

All of the structures consist of $[TiO_6]^{2-}$ octahedra which vary in the nature of corner and edge sharing whilst maintaining an overall stoichiometry of TiO_2. The rutile form is the most thermodynamically stable, and the only phase stable at elevated temperatures.[100] Typically a substrate temperature of approximately 350 ^{o}C is reported to be required for anatase formation during deposition.[101] At temperatures of 600 – 700 ^{o}C anatase is known to irreversibly transition to the rutile form.[102,103,104] The interstitial spaces between the component octahedra is comparatively larger in anatase than rutile, which has been shown to reduce the recombination of electron-hole pairs and lead to greater water splitting ability.[95,105] Furthermore the rutile phase has been shown to exhibit a higher level of resistivity and lower charge carrier mobility.[106] Also the lower band gap of rutile is caused by less negative conduction band energy, which is detrimental to water splitting performance.[79]

The mechanism of water splitting on TiO_2 is not well understood, however a number of studies have suggested that defects are important.[20] It has previously been shown that ideal defect free TiO_2 surfaces are unreactive at room temperature.[107] Generally it is reported that oxygen vacancies represent sites at which water molecules dissociatively adsorb.[108] Additionally a decrease in the number of Ti^{3+} sites has been observed upon adsorption of water.[109]

A commonly proposed mechanism for water splitting involves oxidation of surface hydroxyl (OH_s) groups by photogenerated holes:[110]

(1.27) $Ti - OH_s + h^+ \rightarrow [TiOH]_s^+$

The involvement of surface hydroxyl groups has been supported by the observation of decreased water splitting activity with lower surface hydroxyl density.[111] This has also been suggested as a reason for the decreased activity of rutile, since the higher temperatures employed during synthesis imparts a lesser surface hydroxyl density. Additionally the rehydroxilation of Rutile in contact with water occurs to a much lesser degree.[112] Additional theories involve initiation by nucleophilic attack of water on a surface trapped hole at a lattice oxygen site.[110] Nowotny et al. have also suggested that a more recently discovered defect type of Ti vacancies represent the surface active sites.[91]

Due the large band gap of TiO_2, alternative oxide materials have also been sought for photoelectrochemical water splitting. Fe_2O_3 has been extensively studied on account of its much smaller band gap, which allows it to harvest a greater proportion of solar energy.[113] This material is however severely limited in performance, due to a combination of low hole diffusion length and sluggish kinetics in the oxygen evolution reaction.[114] These characteristics are manifested in a 300 – 400 mV positive shift in the photocurrent onset with respect to the flat band potential.

A number of solutions have ameliorated these deficiencies to some extent, such as surface bound catalysts and optimised electrode morphology.[114,] The hole diffusion length in haematite is approximately 3 – 5 nm,[114,115] and thus novel morphologies have sought to reduce the path length of holes to reach the semiconductor surface. A number of catalysts have also brought about increased efficiency, although it is often unclear whether charge separation or electron transfer performance is increased.[116,117]

It is often implied that the short hole diffusion length dictates that bulk recombination is the primary cause for the poor performance. However others have suggested that surface states located 0.9 and 1.8 eV below the conduction band in conjunction with poor catalytic ability is the cause.[118] Surface states are thought to be more important in the case of Fe_2O_3 compared to TiO_2. In TiO_2 the Ti is in its highest oxidation state and thus the reaction pathway is assumed to involve peroxo and superoxo species. Conversely, Fe may transition to a number of other higher oxidation states as well as form peroxo or superoxo species.[50] Clearly the activation energy for one or more of the processes is relatively high on Fe_2O_3. Peter et al. recently suggested the involvement of

higher valent iron species in the water splitting mechanism, and showed the reduction in band bending obtained when holes accumulate at the surface due to poor charge transfer kinetics.[50,119]

A number of studies have also been reported on other moderate band gap oxides, including WO_3, NiO and Cu_2O.[120,121,122] Several perovskite materials such as $SrTiO_3$ and $BaTiO_3$ are also often reported,[123,124] which are limited in performance by excessively large band gap energies. CuO has also been investigated and unlike many oxides, its valance band is not sufficiently positive to oxidise water.[9] Furthermore it is prone to corrosion in the PEC operating environment.[9] More complex layered perovskite structures were also reported by Akihiko et al.[125] Despite offering promising performance, the band gaps of these materials are even larger than that of TiO_2, thus placing a limit on the maximum achievable efficiency. $YAlO_3$ was also identified via a combinatorial approach, and was found to be sensitive to visible light.[126]

Several alkali and alkaline earth tantalates have also proved to be active towards water splitting. These include $K_3Ta_3Si_2O_{13}$, $BaTa_2O_6$, $NaTaO_3$ and $SrTa_2O_6$. [127,128] Structures such as $K_2La_2Ti_3O_{10}$, $Sr_2Ta_2O_7$ and $Sr_2Nb_2O_7$ have also proved to be promising.[125,129]These materials adopt a layered perovskite type structure.

Furthermore, a vast number of composite and solid solutions of metal oxides have been trialled, which are discussed in the following section.

1.3.4. Strategies for Increasing the Efficiency of Photoelectrochemical Cells

The large band gaps of many suitable photoelectrodes have focused a large amount of attention in reducing this parameter. TiO_2 has been doped with a wide range of both metals and non-metals in attempts to achieve this aim. Incorporation of Cr, Mo, V and Mn were all shown to alter the spectral dependence of TiO_2 and induce visible light response.[130,131,132] Samples of TiO_2/Ta, Mo, W, Nb, Re, Cr, V, Fe, Mn, Ni and Co were also investigated by Aroutounian et al.[130] Any improvements in efficiency are generally minimal. Whilst Cr and Al doping has increased the efficiencies to 0.44 and 0.6 % relative to the undoped level of 0.4 %,[133] other materials such as Y, V, Cu and Ta had no clear effect.[134] Some scepticism however exists concerning whether doping may adequately increase the efficiency of large band gap materials. For example, high level doping with Cr leads to a substantial reduction in the band gap, although this is accompanied by a greatly increased recombination rate and concomitant reduction in photovoltage.[85] Doping of many other oxides has also been carried out. In the case of WO_3, Cr, Mn and Fe addition was found to sensitise the

semiconductor most effectively.[120] However the positive conduction band edge position still remains a significant problem. Similar approaches have been applied to Fe_2O_3, with Si doping affording the greatest improvement.[135] Often however the method of improvement upon dopant addition is poorly understood. Possible suggested improvement methods are:[136]

1. Decreased electrical resistance
2. Improvements in electrocatalytic activity by imposition of surface active sites
3. Passivation of grain boundaries
4. Morphological changes

Glasscock et al. also investigated the effects of Ti and Si addition on Fe_2O_3, with the conclusion that Ti showed the greatest level of improvement.[86] A similar approach using a combinatorial method was reported by Jianghua and Parkinson.[136] In this case, synergistic effects of Si and Ti co-doping were observed.

A wide range of non-metal dopants have also been investigated. Particularly effective was incorporation of C into TiO_2 though annealing of TiO_2 in a natural gas flame. A reduction in band gap to approximately 2.32 eV was recorded, with an energy conversion efficiency of 8.35 % under UV illumination.[137] Further investigation of this technique by Barnes et al. could not however reproduce these effects.[138] Attempts have also been made to incorporate sulphur and nitrogen into a number of materials. Examples of such materials reported in the literature include, $Sm_2Ti_2S_2O_5$, TaON, $Y_2Ta_2O_5N_2$, Ta_3N_5 and $LaTiO_2N$.[139,140,141,142,143] A number of these materials offer promising characteristics, however such materials are usually screened in the presence of sacrificial reagents. These act to scavenge holes and reduce the occurrence of corrosion reactions at the semiconductor surface. It is therefore likely that these materials suffer from corrosion due to the more positive placement of the valence bands formed upon inclusion of S, N and C.

In addition to addition of small quantities of dopant atoms, synthesis of solid solutions of metal oxides with varying characteristics has been trialled. In this case, semiconductors with large band gaps are combined with those with smaller band gaps in the hope to combine the favourable characteristics of each material. Once again this approach is typically aimed at reducing the band gap of a material. The way in which this method contrasts from dopant addition is depicted in Figure 1.20:[12]

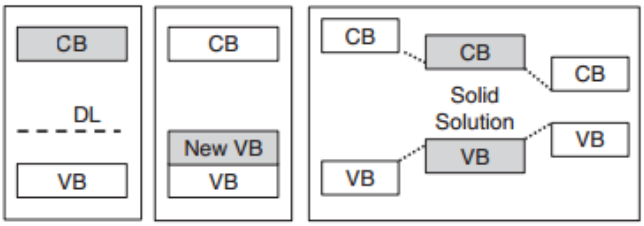

Figure 1.20. The effects of doping and formation of solid solutions on the band structure of semiconductors (left and right respectively). The donor level (DL) is shown as the dashed line in the left hand figure. Figure taken from ref [12]

A relatively large number of Ti based solid solutions have been reported in the literature, including TiO_2-MnO_2, TiO_2-Cu_2O, TiO_2-WO_3 and TiO_2-CdO.[130] Aroutounian et al. found that increasing Cd concentrations in TiO_2-CdO brought about a dramatic increase in visible light sensitivity, although a reduction in activity was found at high Cd concentration by formation of a less photosensitive phase.[130] Additionally it was found that TiO_2-Nb_2O_5 produced twice the photocurrent of pure TiO_2.[144]

The combination of large and small band gap semiconductors has also been used to construct semiconductor composites.[145] Unlike the previously mentioned solid solutions, the component materials are in electronic contact although are not mixed on an atomic level. These materials are attractive in the way that they may facilitate interparticle charge separation. In the case of TiO_2/WO_3, photogenerated electrons from the TiO_2 may be transferred to the more positive conduction band of WO_3, thereby significantly decreasing electron-hole recombination.[146]

Additional improvement efforts have included optimisation of electrode morphology. This seeks to both increase the electrode surface area, as well as alter the diffusion path of electrons or holes. Such effects are discussed in more detail in chapter 6. Additionally, noble metal addition is commonly employed in photocatalyst suspensions (e.g. Pt/TiO_2). In this case, electrons from the conduction band of TiO_2 transfer to Pt, which is considered to supress the recombination of electron-hole pairs. Pt may also act as a catalyst for H_2 generation, or facilitate production of O_2^- species which take part in the degradation of organics.[147] Several reviews have been published in order to further the understanding of the effects relating to noble metal addition in such systems.[148,149]. In a photoelectrode, the behaviour and nature of any improvement may differ significantly. The effects of noble metal particles on photoelectrodes are discussed in more detail in Section 1.3.3. An additional use of noble metals is doping of semiconducting materials. Several

researchers have reported the doping of materials with Pt in an effort to extend the visible light response of a semiconductor.[150,151]

1.4. Catalysis

1.4.1. Electrocatalysis and Particle Size Effects

Catalysts for electrochemical reactions generally seek to lower the activation energy and/or increase the selectivity of a certain reaction.[152] The quantification of catalysts ability is typically given in terms of specific activity at a given overpotential (i.e. current per unit area of platinum) in order to facilitate comparison. This is similar to the case of gas phase reactions, where activities are referenced to the occurrence of a reaction at a catalyst site per unit time (Turnover frequency or TOF). It is advantageous to maximise the surface area of a catalyst, which therefore requires the catalyst to be dispersed as finely as possible. However it has been found that a number of reactions are sensitive to particle size and are said to be structurally sensitive. This classification was originally made by Boudart, who popularised the classification of structurally sensitive and structurally insensitive reactions.[153] In the case of structurally sensitive reactions, the activity of a given process may be changed dramatically with alteration to particle size.

One of the most obvious examples of this behaviour is that of the oxygen reduction reaction on Pt, which is deactivated at particle sizes below approximately 3 nm in diameter.[154] An important characteristic of small nanoparticles is their greatly increased proportion of surface atoms. Assuming that particles are configured in their lowest energy form, a possibility exists for drastically different geometries at small particles.[155] Kinoshita later suggested that the variation in distribution of the different Pt crystal faces could account for the observed oxygen reduction particle size trends.[156] It was also suggested that the increased prevalence of corner and edge sites at smaller particles was unfavourable for oxygen reduction performance.

Hardeveld and Montfoort previously implemented a model to show the variation in coordination of particles between the sizes of 1.5 – 7 nm.[157] Their work showed that a large number of surface sites with a coordination number of 5 were found for particles within this range. Kinoshita utilised the same mathematical model to determine the number of 5 coordinated sites in different sized platinum particles with octahedral and cubo octahedral shapes. A maximum of these sites was found for particles with diameters of ~2nm. Only very small numbers of such sites were found below 1.5 nm or above 8 nm.

In addition to the widely studied geometric effects, it is proposed that the electronic structure of Pt may also change with particle size.[158] At very small particle sizes, the behaviour of metals becomes more molecule-like on account of the quantum size effect. In this case the valence band is considered to have individual discreet energy states as opposed to the continuous band structure of bulk materials. At room temperature, the spacing of energy levels may therefore be greater than the thermal energy kT.

Additionally, it has been proposed that the nature of the support may alter the characteristics of supported metal nanoparticles. It has previously been shown that the adsorption properties of Pt are altered when supported on TiO_2.[159] Additionally, metals such as Au exhibit anomalously high catalytic activities towards gas phase CO oxidation when supported on TiO_2.[160]

TiO_2 has gained increasing attention as a catalyst support due to its increased stability towards corrosion when compared with carbon in fuel cell operating environments. The effects of an interaction between metal oxide supports and Pt was first observed by Tauster on the Pt/TiO_2 system which gave rise to the term of SMSI (strong metal support interaction).[161] It was observed that the capacity of a number of metals towards H_2 and CO adsorption was lessened significantly when supported on metal oxides that were reduced in H_2. An initial explanation for the effects viewed, was the sintering of the metal particles, however this was later discounted upon viewing evidence obtained from XRD and electron microscopy.[161] A more likely explanation for the observed decrease in adsorption capacity has been proposed by several researchers. These suggest encapsulation of the metal particles by the support material. Pesty et al. employed in-situ low energy ion scattering during the annealing process, which showed a noticeable decrease in Pt signal before it eventually disappeared.[162] This is consistent with an encapsulation process; so too is the observed dependence of the Pt signal disappearance on temperature and Pt coverage. In other studies of low Pt coverages, there is still an observed decrease in desorption temperature in the absence of encapsulation, suggesting that electronic interaction is important also in the study of SMSI.[163] Another consideration is the metal-support boundary. Researchers have commented that there are special sites between the metal and the support known as, 'catalytic ensembles'.[163] These sites can be important factors in particle size effects, due to the increased number of boundary sites as the particle size decreases.

In the vast majority of experimental results, a decrease in specific activity towards the ORR was observed with decreasing particle size.[154, 164] The majority of such studies are carried out in acidic media, however the limited number of studies carried out in alkaline media have shown similar trends.[165] Typically the ORR proceeds with lower overpotential in alkali, which is often attributed

to the lack of strongly adsorbing counter ions.[166] In single crystal studies the activities of the low index faces increase in the order (100) < (110) < (111).[167] In the case of measurements carried out in $HClO_4$ the activity increased in the order of (100) < (110) < (111). In the alkaline case, the exact opposite trend was observed in terms of OH adsorption strength, which suggests an increase in OH coverage may hinder the ORR.[167]

The adsorption of OH is suggested to play a key role in particle size effects with respect to a number of different reactions. The oxide formation behaviour has been shown to be notably different at small particle sizes when compared to bulk Pt.[168] Additionally a negative shift in the oxide stripping peak is almost always observed as the particle size decreases.[169] The position of the oxide formation peak is much more variable, with some authors observing a negative shift at smaller particle sizes and others reporting no clear variation.[170] Some suggest that smaller particles adsorb oxygen containing species more strongly, and X-ray absorption studies have indeed shown that particles below 5 nm adsorb OH more strongly than bulk Pt.[171] This theory of more strongly absorbed oxygen containing species at smaller particle sizes has also been suggested to account for the observed particle size trends towards methanol and CO oxidation.[168]

In addition to the aforementioned effects, Watanabe et al. suggested a different explanation to particle size effects in the ORR.[172] They suggested that the activity was in fact independent of particle size and instead dependent on the interparticle spacing.

1.4.2. Catalysis of the Oxygen Evolution Reaction (OER)

In both photoelectrochemical cells and electrolysers, the oxygen evolution reaction contributes significantly to the overall catalytic overpotential requirements.[173] A considerable amount of research has therefore been undertaken in the quest to find catalysts with adequate activity and durability. However even the best known catalysts are known to exhibit exchange current densities significantly lower than those for the HER.[174] The significantly lower activities of OER catalysts are typically attributed to the more complex mechanism and the inclusion of an oxide phase in the overall kinetics.[175] For oxide formation on noble metals, it is generally accepted that OH^- first adsorbs to the electrode surface, before a subsequent place exchange where oxygen migrates into the uppermost layers of the metal surface.[176] A number of detailed mechanistic studies are reported for the oxygen evolution reaction on noble metals, in which the authors speculate on the nature of the rate limiting steps.[177] A proposed mechanism for the OER is shown in equations 1.29 – 1.31, where M represents a metal surface site.[178]

(1.28) $OH^- + M \rightarrow M - OH + e^-$

(1.29) $2M - OH \rightarrow M - O + M + H_2O$

(1.30) $2M - O \rightarrow 2M + O_2$

Much of the understanding of the OER activities and mechanism is derived from Tafel slopes[13] (Figure 1.21) and current voltage behaviour. Typically an increase in the Tafel slope gradient appears at high overpotential, which is generally attributed to catalyst degradation and changes to the mechanism.[174] As can be seen from the nature of the materials in figure 1.19, oxides are among the most popular OER catalysts. These materials gained popularity after the DSA (dimensionally stable anode) was patented by Henry Beer in 1965.[179] Among the most active catalysts in alkaline media are $NiCo_2O_4$, RuO_2 and doped lanthanum oxides.[13] Some stability issues are present with RuO_2 however, which is often lessened by the incorporation of IrO_2.[180] Stable non-noble metal oxides are also commonly employed to aid in stabilising catalyst materials (e.g. TiO_2, SnO_2).[180]

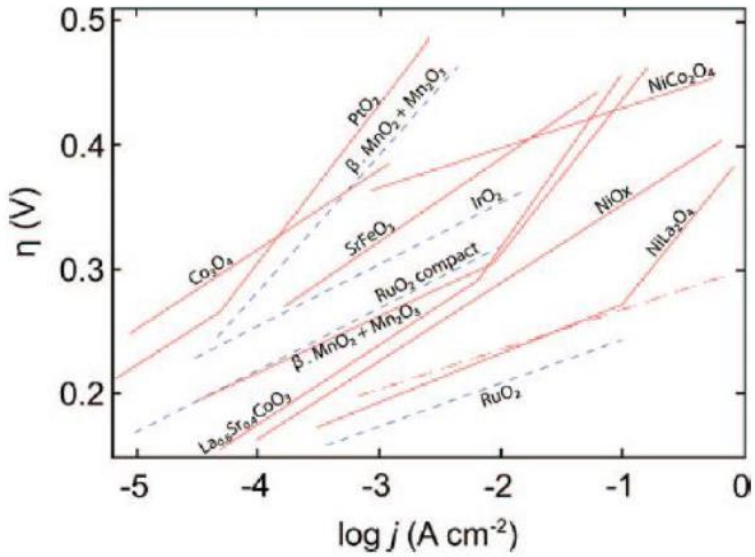

Figure 1.21. Tafel plots for a range of known OER catalysts. Solid and dashed lines represent measurements in alkaline and acidic media respectively. Figure taken from ref [13]

Initially the variation in catalytic activity between different materials was rationalised by the ability of a catalyst to transition between different oxidation states.[181] It was suggested that the proximity of this redox transition to the potential required for the OER was the cause of the activity variation.[181] Subsequently a similar theory to that introduced for the hydrogen evolution reaction was suggested.[14] In this case, the oxygen bond strength was thought to be the primary

factor in dictating a catalysts ability. This gives rise to a familiar volcano-type plot (Figure 1.22) as presented for the hydrogen evolution reaction.

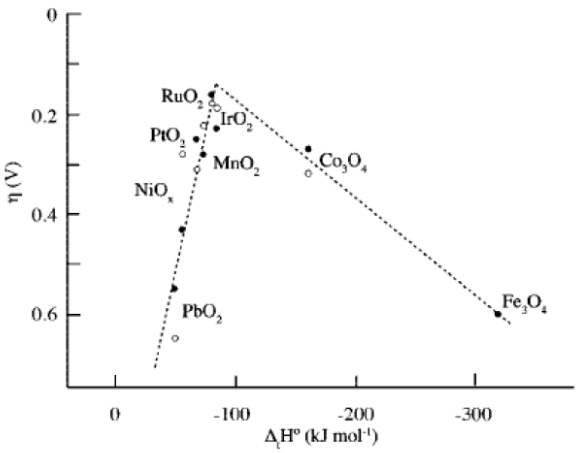

Figure 1.22. Volcano relationship for a range of metal oxide OER catalysts. Figure taken from ref [14]

As in the HER case, the intermediate bond strengths give the best activity, on account of a balance between stabilising adsorbed intermediates and allowing desorption of the products. Simple metal dioxide catalysts form only a small part of the reported OER catalysts, and several spinel, perovskite and pyrochlores have also been reported.[13]

The study of OER catalysis is primary limited to metal-air batteries and electrolysers, and comparatively few studies investigate the effects of catalysts on photoelectrode materials. This is in part due to the strongly positive placement of the valence band edge in oxide semiconductors, allowing the reaction to proceed with relative ease at the bare semiconductor surface in many cases. However in order to meet the band gap and efficiency requirements, it is necessary to produce materials with smaller band gaps. Since the conduction band edge of most metal oxides is close to the H^+/H_2 redox potential, any band engineering will require movement of the valence band edge. As a result of moving the valence band edge more negative in potential, the 'built in' driving force for the OER will be lessened. The role of catalysis will therefore become increasingly important as efficient semiconductors are optimised for photoelectrochemical water splitting.

1.4.3. Catalysts in Photoelectrochemical Cells

The vast majority of studies relating to catalysing reactions at semiconductor surfaces have been biased towards the mineralisation of organic pollutants.[147-149] In addition to understanding charge transfer behaviour, a number of other factors require investigation and optimisation at semiconductor surfaces. Firstly, the optical properties of a catalyst are of importance since they may limit the absorption by the semiconductor layer. Secondly, the nature of the interface must be considered. The level of band bending in a semiconductor is dependent on the nature of the contacting phase,[182] meaning that a catalyst may strongly affect the driving force to transport electrons/holes to the semiconductor surface. As a result of these effects, the best catalysts for the OER in the dark do not necessarily yield the best activity in a photoelectrochemical cell.[183] In spite of these stringent requirements, the stability requirements of catalysts may be reduced to some degree compared with dark electrolysis. Typically stability issues are encountered due to the requirement of long term operation at high current densities, however the current density will be much smaller in a PEC since the active surface area will be comparatively higher to facilitate light absorption.[13]

Typically catalysts are loaded as finely dispersed particles to maximise light absorption. If the particles are smaller than the wavelength of the incident light then they will effectively be optically transparent and have little effect on the electrodes absorption properties.[184] Additionally, small particles limit the barrier height reduction that is seen when a continuous metal layer is applied to a semiconductor surface.[185] The pinch-off theory was suggested to account for this behaviour.[13] This theory suggests that when particles are of a comparable or smaller size than the depletion layer width, the semiconductor band bending is dominated by the nature of the solution instead of that of the metal. Detailed studies of the size dependence of metal contacts have been carried out for the case of Si/Ni/liquid interfaces by Lewis.[21]

Generally the action of noble metal particles is thought to increase the ability of an electrode to separate photogenerated charges. Studies have shown that this effect occurs due to metal particles acting as an electron sink on account of their lower Fermi level than TiO_2.[186] This effect is also known to depend on the metal work function, which was shown to significantly affect the generation of NH_3 from azide ions.[187] Anpo and Takeuchi have also previously shown that electron transfer occurs to Pt particles with electron spin resonance.[188] This accumulation of electrons on metal particles has also been found to raise the Fermi level of the semiconductor to more

negative potentials.[189] A particle size dependence was also observed, in which smaller particles brought about a more negative Fermi level shift.[189]

In the majority of cases, smaller sized nanoparticles have shown the best photoelectrochemical activity.[189-190] However a limit in efficiency is reached, whereby a further decrease in particle size results in a loss in activity. This has been explained by a poorly matched work function at smaller particle sizes, which makes electron transfer to the nanoparticles less facile.[190b] The loss in activity at larger particle size is most commonly attributed to the formation of recombination centres or a reduction in absorption due to higher surface coverage.[191]

The majority of studies are carried out on nanostructured semiconductors, in which a very small space charge voltage may form. In this case it is feasible for electrons to transfer to the particles. In cases where a significant space charge voltage forms, the built in field will however direct electrons away from the surface. Studies were undertaken to elucidate the effects of catalysts towards water splitting and photocatalytic decomposition reaction. It was found that Pt addition to TiO_2 facilitated hole transfer to the Pt and TiO_2 surface due to large interfacial band bending.[192] This is because the Fermi level of bulk Pt lies approximately in the band gap of TiO_2 which also gives a similar probability of hole or electron transfer to the metal. Conversely the addition of Ag, who's Fermi level is lower than that of TiO_2 (-4.26 compared with -4.2 eV) prevented transfer of electrons to the substrate contact.[192]

The addition of Au has also been shown to greatly enhance the water splitting ability of TiO_2. In this case it was suggested that the varying catalytic ability of the metal particles caused this effect due to the conventional dark particle size effects.[193] Additionally, it has been shown that the addition of catalysts can in fact be detrimental to PEC performance.[182] This was rationalised by the formation of surface states which reduced the interfacial band bending in the semiconductor.

Although the study of catalysis is relatively well developed in semiconductor suspensions, their action on photoelectrodes is still relatively unknown. In addition to being catalytically active for the OER, it is important that catalyst imposition balances this with photovoltage production while maximising the absorption of solar illumination.

1.5. High-throughput Techniques in Electrochemical Energy Applications

High-throughput combinatorial methods essentially involve the synthesis of large number of materials in a rapid manner. The material libraries may then be screened for properties of interest, and activity trends can be rationalised in terms of structure, composition, etc. These methods were originally developed in the pharmaceutical industry for medicinal applications; however they have become increasingly possible for a number of other areas including, electrocatalysts, battery materials and corrosion resistant alloys.[194] Typically the rapid acquisition of data is performed with either automated serial measurements or by parallel screening in which a large number of materials are screened simultaneously.

The first example of combinatorial electrochemistry was reported by Reddington et al.[195] In this method, metal salt solutions of Pt, Ru, Ir, Os and Rh were printed onto carbon paper with a modified inkjet printer. The library of 645 varying compositions was then reduced in sodium borohydride before subsequent screening for methanol oxidation. The activities of the various catalysts were evaluated by use of quinine as a fluorescent pH indicator.

A number of similar methods have been applied to photoelectrochemical reaction, in which a fluorescent pH indicator is used.[126, 196] Since an indirect quantification of activity is employed, the information gained from such techniques is relatively limited. Furthermore, such studies are only possible in a relatively narrow pH region. Other indirect quantification methods have also been reported, including imaging of bubble formation resulting from the evolution of H_2 and O_2 from HER and OER catalysts.[197]

Gregoire also reported the screening of catalysts for photoelectrochemical water splitting through use of an automated scanning droplet cell.[198] In this instance, a standard 3 electrode droplet cell was moved over a combinatorial library while carrying out electrochemical screening at each one. This method enhances the quality of electrochemical data obtained, however this is accompanied by an increased complexity of the system and a lower overall throughput compared to parallel methods. In this effort, both the dark oxygen evolution behaviour and the absorption properties of the catalysts were examined.[198] Whilst the optical measurements prove that the end use in PECs was considered, this route to catalyst optimisation fails to address the effects that catalysts may have on the interfacial energetics of the semiconductor electrodes.

Additional methods for developing photoelectrode materials have included dye discolouration methods.[126] In such approaches the oxidation of a simple dye is used to measure activities, with quantification by the level of dye discolouration.

Typically a common conducting substrate provides simultaneous contact with all materials in a library. Individual assessment of each material is therefore carried out by either scanning a cell over the surface (as described above), or by focusing the light source on the desired spot. In such methods the conducting substrate is often exposed to the electrolyte, meaning that assessment with simple reversible redox couples in not possible due to substrate shunting. More recently Katz and Lewis reported a technique in which the individual electrodes were electronically isolated (In a similar approach to this work).[199] This brought about the possibility to use simple redox couples in characterisation as well as allowing photopotential measurements. This is an extremely important parameter which is often overlooked in other high throughput methods.

In terms of synthesis methods, inkjet printing represents one of the most common approaches.[199-200] Typically the various precursor solutions are held in different cartridges and printed in varying amounts to yield different compositions. A disadvantage to this method is the difficulty in assessing the level of mixing at an atomic level. Takeo et al attempted to improve upon this by mixing the precursor solutions prior to printing electrodeposition synthesis methods,[201] in which a scanning electrochemical probe was used to quantify activities. Jaramillo also employed high throughput electrodeposition as a synthesis method.[202] Activities were subsequently measured by a scanning droplet cell. Electrodeposition methods however suffer from the fact that the number of materials that can be prepared in this way is limited.[203]

Xiang et al also recently described a novel high-throughput screening methodology in which synthesis was carried out by inkjet printing.[204] In this approach, individual electrodes were addressed by a multiplexed counter electrode assembly. By addressing an individual counter electrode the activity of a single photoelectrode could be measured.

At present the application of high-throughput techniques in photoelectrochemical water splitting is rapidly expanding. However the majority of systems must make a compromise on either the speed of data acquisition or the quality of the electrochemical data obtained. In light of the high number of material requirements for water splitting, the perfect material has so far proved elusive. It is generally accepted that a complex metal oxide material will be required in order to satisfy the requirements relating to cost and stability. The challenge remains to develop

multicomponent materials which adequately satisfy the other requirements. A huge number of materials are possible in this approach and thus high-throughput methods may prove to be of significance. In order to narrow down the search as much as possible, Parkinson has loosely classified a number of materials into their different roles:[9]

- Structural: Materials which form stable oxides (e.g. Ti, W, Ta etc.)
- Light absorbing: Materials which help absorb light at higher wavelengths (e.g. Ni, Cr, Mo, Mn etc.)
- Catalytic: Materials which help catalyse the interfacial charge transfer reactions (e.g. Pt, Ru, Pd, Rh etc.)
- Charge balance: Materials which balance the charge of the O^{2-} atoms present in the structure (e.g. Ca, Ba, Na, K etc.)

With the above in mind, the key to finding suitable materials lies within an intelligent search of material libraries. Additionally a number of areas such as catalysis require more thorough investigation in order to determine their method of action. The approach employed herein is particularly useful in this regard, since materials may be synthesised and screened simultaneously in an identical environment. This is extremely important since subtle differences in preparation conditions can considerably alter the characteristics of semiconducting materials. Therefore in addition to exploratory research, a number of fundamental aspects of semiconductor electrochemistry may benefit from appropriate high-throughput studies. The PVD synthesis method used in this work has a number of benefits towards this goal. Firstly, materials do not require annealing, and as a result a number of non-eqilibrium phases can be obtained. This factor, combined with the ability to deposit at temperature and post anneal allows a significant level of control over the crystalline structure obtained. Deposition of metals may also be combined with either atomic or molecular oxygen, thus allowing control of the overall stoichiometry.

2. Experimental Techniques

2.1. High-throughput Physical Vapour Deposition

2.1.1. HT-PVD System

All samples prepared in this work were synthesised in an ultrahigh vacuum (UHV) physical vapour deposition system (DCA instruments).[15] The system features two growth chambers which allow simultaneous co-deposition of multiple elements across the substrate. The layout of the system as a whole is shown in Figure 2.1.

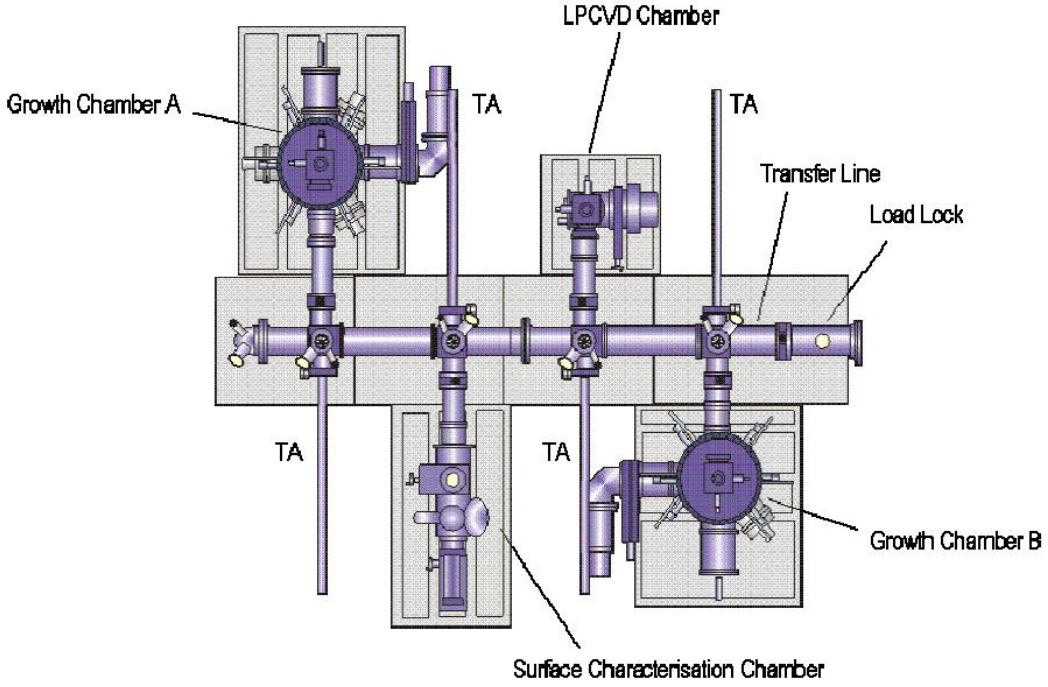

Figure 2.1. Schematic diagram of the HT-PVD system. Shown also are the transfer arms (TA) used to insert and remove samples from the chambers. Figure taken from ref [15]

In addition to the two PVD growth chambers, the system features a surface characterisation chamber (XPS) and a sputtering chamber. All samples prepared in this work were carried out in growth chamber A. All of the chambers are interconnected by a series of buffer lines, which houses a trolley system to allow movement of samples throughout the system. The whole of this system is also maintained under UHV. Samples are inserted and removed from the system via the load lock, which can be vented to atmospheric pressure and pumped down to UHV in a relatively

short space of time. This load lock is pumped with a turbomolecular pump (Pfieffer) backed by an oil free rotary pump (Pfeiffer). The vacuum in the deposition chambers is maintained with cryo-pumps (Helix tech corp) and turbomolecular pumps (Pfeiffer) as well as a Ti sublimation pump (Varion) for intermittent use. Both the sputtering chamber and XPS chamber are also pumped with turbomolecular pumps backed by oil free rotary pumps. A combination of ion (Varian) and Ti sublimation pumps (Varian) maintain the vacuum in the buffer lines.

The two deposition chamber feature multiple sources for evaporation, however only the layout of growth chamber A is shown since this was the only chamber utilised within this work (Figure 2.2).

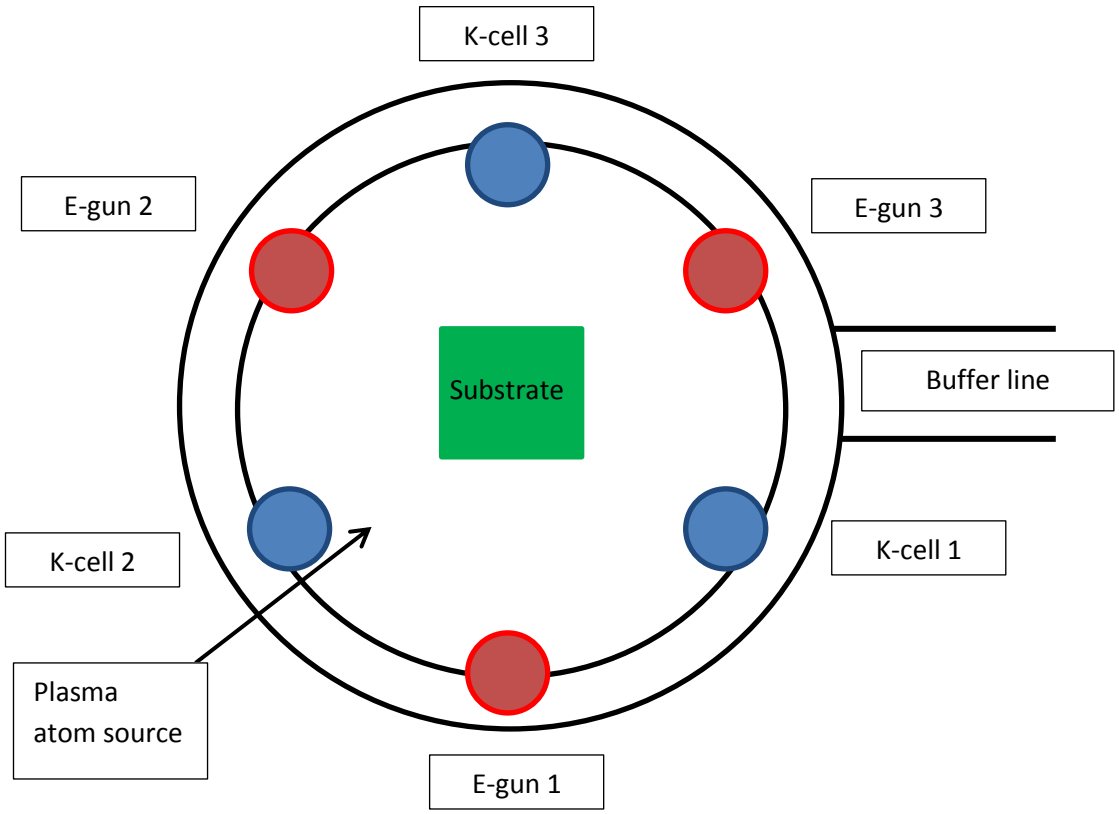

Figure 2.2. Top down view of growth chamber A showing the positions of the e-gun and K-cell sources relative to the substrate. The arrow by K-cell 2 represents the atomic oxygen source, which is positioned in place of K-cell 2 when used.

The chamber features six off axis sources including three Knudson cells (K-cells (DCA)) and three electron beam guns (E-guns (Temescal)). The electron beam guns are used to evaporate materials with high melting points. In this technique, electrons are emitted from a tungsten filament which

is then directed by a permanent magnet under the source material in to the crucible (typically graphite). Additionally, a series of electromagnetic coils operate to sweep the electron beam over the entire of the crucible in a reproducible and controlled manner. This ensures uniform heating of the entire source material. In addition to offering heating to higher temperatures, e-guns give an added level of control over the deposition process. This is due to the placement of a quartz crystal microbalance (QCM) in close proximity to the vapour flux from each e-gun. As such, the deposition rate may be monitored throughout the deposition process, which is particularly important in the low rates of deposition required for particle formation. It should be noted however, that due to the discrepancy between the source – QCM and source-substrate distances, the measured rate is not equal to the true deposition rate at the substrate. The rate measured at the QCM is however directly proportional to the real deposition rate, and may therefore be calibrated to obtain the true rate of deposition.

The K-cells in the chamber are of two different types. Both function in a similar way, whereby a tungsten filament is used to heat the crucible in which the source material is located. The first K-cell type is a low temperature K-cell, in which materials may be heated up to 1400 ^{o}C. The high temperature K-cells may however be used to heat source materials up to 2000 ^{o}C.

Finally, a plasma atom source (Oxford Applied Research), may be located in position of K-cell 2. This was used in order to produce reactive atomic oxygen species which is then directed at the sample face during deposition. In this technique the desired gas is introduced into the discharge tube (Al_2O_3) where a plasma is formed by introduction of inductively coupled RF excitation. Charged atoms are retained in the discharge zone by a plasma confinement plate while neutrally charged atomic species diffuse to the substrate surface. An automated impedance matching system was used to minimise power loss. In addition to oxygen, other gases may be used such as nitrogen and hydrogen to extend the synthesis capabilities of the system to nitrides/ oxynitrides/hydrides etc.

In addition to the various sources, a number of different shutter types are employed in the system. Each individual source features a source (on/off) shutter, which either fully blocks the vapour flux from the source to substrate or allows complete passage of the vapour. These are actuated by compressed air and allow precise definition of the start and finish of the deposition, thus allowing controlled and reproducible deposition times.

Each source also incorporated a ‘wedge shutter’. The operation of this for a single source is depicted in Figure 2.3 and is discussed in more detail by Guerin and Hayden elsewhere.[15] These

are again located above each source and allow for a controllable and variable gradation in material composition or thickness across the substrate area.

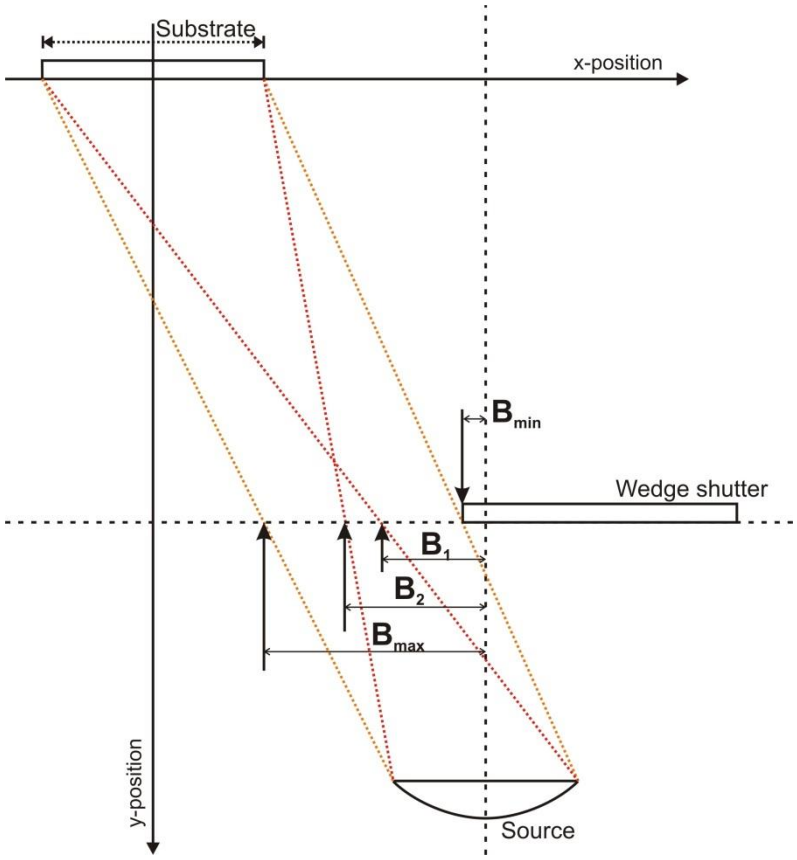

Figure 2.3. Schematic diagram of the wedge shutter effect on a single off-axis source with respect to the substrate. Figure taken from ref [15]

It can be seen from Figure 2.3 that at the position of B_{min}, the vapour flux is unhindered and the substrate is fully exposed to the vapour emanating from all areas of the source material. At positions B_1 and B_2 the substrate is however partially shielded from some areas of the source material. This shadowing effect means that the left hand side of the substrate 'sees' more of the flux and a concomitantly larger amount of material of material is deposited at the left hand side of the substrate. The action of the wedge shutter dictates that an increasingly small amount of material is deposited when moving to the right across the substrate. As a result of these effects, a gradient in material thickness is produced.

When deposition occurs from a source opposite, the thickness profile of the second element across the substrate is reversed. Upon simultaneous co-deposition of the materials, these opposing thickness gradients create a gradient (Figure 2.4) in material composition.[15, 205] By independent movement of the wedge shutters, the nature of the composition gradient may be altered to produce the desired range of composition. The simultaneous evaporation of multiple sources has a number of benefits. Firstly is that this ensures mixing of the constituent elements on an atomic level. Additionally this removes the requirement of a post-annealing step. In this manner it is therefore possible to form metastable phases.

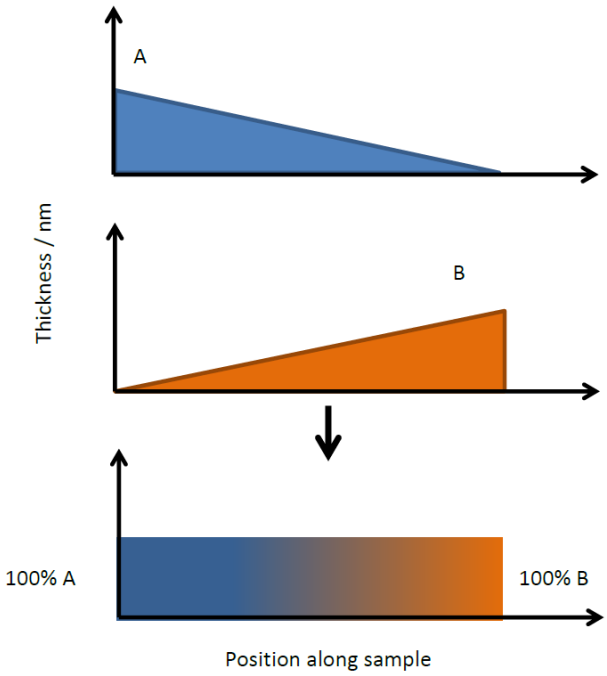

Figure 2.4. Hypothetical deposition profile of two oppositely positioned off axis sources. A and B show the constituent thickness profiles of the two elements, which combine when deposited simultaneously to yield the thin film at the bottom of the figure. Figure taken from ref[16]

In addition to the source shutters and wedge shutters, a single 'main shutter' is located close to the sample face. This obscures a variable amount of the substrate material from all sources in the chamber. In this work, the main shutter was used for particle formation, which is described in more detail in the next section. Where a uniform coating of a material is required, the wedge shutters and main shutters are not used. Additionally, a motor allows the substrate to be rotated during deposition thus ensuring an even film thickness across the substrate area. This approach was used for all of the support material depositions in this work.

2.1.2. Deposition Calibration

In order to achieve the desired thickness and compositional range of thin films, it is first necessary to calibrate the sources. Where a compositional gradient is required, calibration must be carried out for the deposition rate, deposition time and wedge position. In this work however, calibration was only required for deposition rate and time for the uniform films of the support material. A different approach is however required for particle calibration, which is described in more detail later. The TiO_2 and Fe_2O_3 layers prepared in this work were carried out by evaporation of Fe (Alfa Aesar 99.97 %) and Ti (Alfa Aesar 99.995 %) from e-gun sources. During deposition, high purity oxygen (BOC 99.999 %) was leaked into the chamber via the plasma atom source at a constant rate. The oxygen flow rate was maintained at 1 sccm for all samples presented in this work and the plasma source was operated with an RF power of 300 W.

Initially the rate was calibrated, by depositing for a fixed duration at a variety of different rates (as measured at the QCM). Figure 2.5 shows that a linear relationship exists between deposition rate and film thickness.

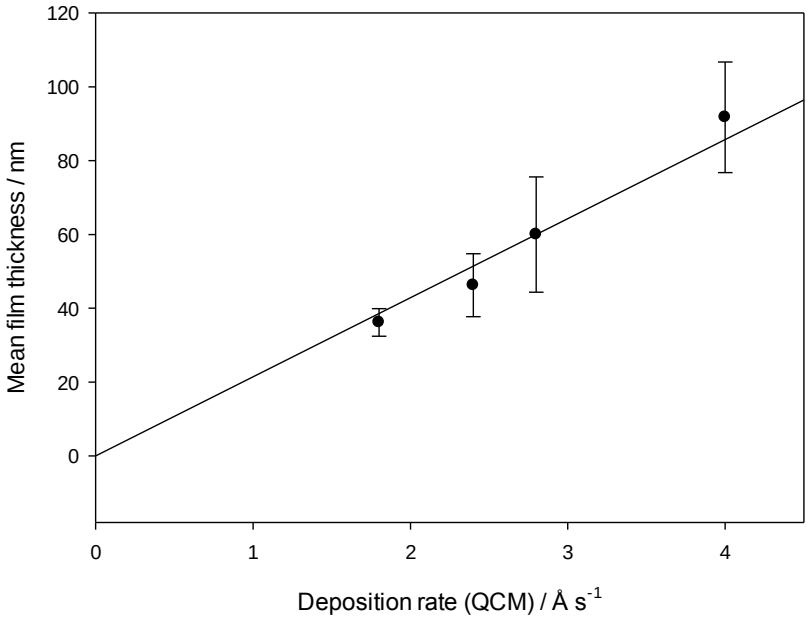

Figure 2.5. The effect of deposition rate (measured by the QCM) on the thickness of TiO_2 films. A constant deposition time of 30 mins was used in each case with an oxygen flow rate of 1 sccm and P_{RF} = 300 W. Thickness measurements were determined by AFM, whereby 6 locations were measured from two different sides each.

After selection of an appropriate deposition rate, the deposition time for the desired thickness was calculated. The thickness was measured of several samples where a fixed deposition rate was used and the deposition time was varied.

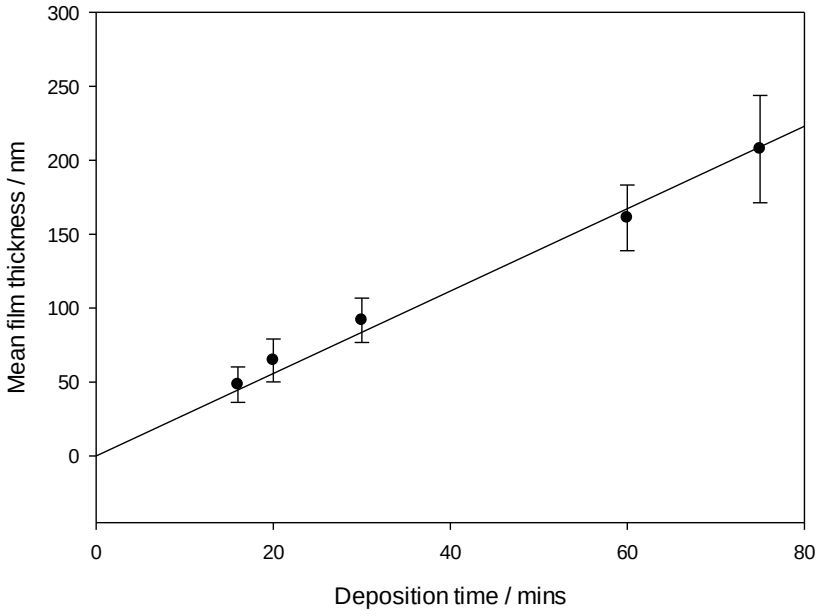

Figure 2.6. The effect of deposition time on TiO_2 film thickness at a constant deposition rate of 4 Å s^{-1} (measured by the QCM). All other deposition parameters and film thickness measurement parameters were the same as those in Figure 2.5.

Calibration of the deposition parameters for Fe_2O_3 was performed in an identical manner to that described above.

After support material deposition, calibration was subsequently performed for particle deposition using the same method reported by Davies et al.[206] Deposition of platinum was carried out from an e-gun source, with use of the chambers main shutter to control a variation in particle size across the sample. The main shutter functioned by selectively masking a defined portion of the array, which allowed for different deposition times to be imposed at each row of electrodes on the array. Figure 2.7 illustrates the action of the main shutter position in masking the array.

The required position of the main shutter for uncovering the desired number of electrode rows was dependent on the location of the source used for deposition. Additionally, any change in the sweeping pattern of the electron beam in the crucible also had an effect on the shutter positions.

Consequently, it was necessary to calibrate the shutter positions each time the beam profile was modified or where a different source was used. This was carried out by depositing relatively thick films at varied shutter positions such that it was possible to visually identify the number of electrode rows that had been deposited on.

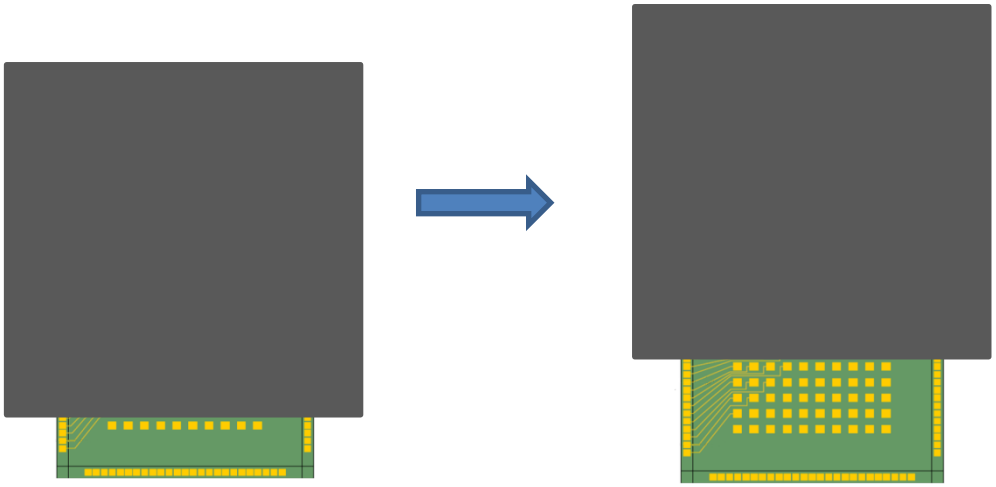

Figure 2.7. Diagram to represent main shutter movement during the deposition process. At the beginning of the deposition (t=0) only one electrode row is exposed to the elemental flux. The shutter is then moved to sequentially uncover the electrodes at fixed time increments until all rows are uncovered. The right hand diagram shows the shutter position midway through the deposition.

After the shutter positions had been determined, a calibration sample was prepared at a higher deposition rate than that used for the screening arrays. Deposition was also carried out over a long time period, such that the film thickness at the different electrode rows could be measured by AFM. In this case a deposition rate of 0.4 Å s^{-1} was used with the shutter being moved every 24 mins over a period of 2 hours. This yielded 5 different Pt thicknesses that could be used to create a calibration plot of thickness against time (Figure 2.8).

From this graph, a plot of thickness against time was then generated for the lower deposition rate used for particle deposition (0.15 Å s^{-1}). This could also be used to determine the thickness in terms of monolayers as a function of time. Typically equivalent thicknesses of between approximately 0.5 and 3.5 ML were required for particle deposition of the desired size range in this work. The lower rate was chosen for particle formation in order to allow time for movement of the main shutter throughout the deposition process.

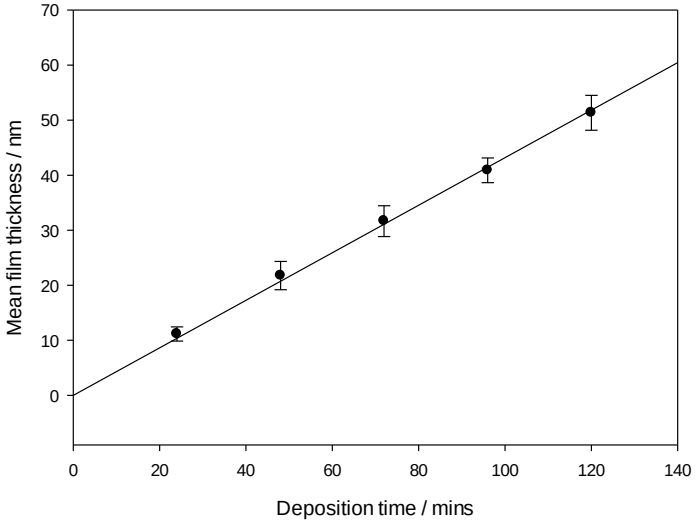

Figure 2.8. Calibration graph of thickness vs. time for Pt particle deposition. The total deposition time was 120 mins, with the various deposition times imposed by movement of the main shutter. A rate of 0.4 Å s^{-1} was used and thickness measurements by AFM were carried out at two different sides of four squares for each electrode row.

From the various calibration graphs, the deposition times required at each row were calculated. The deposition times used as well as the calculated equivalent monolayer thicknesses are shown in Figure 2.8.

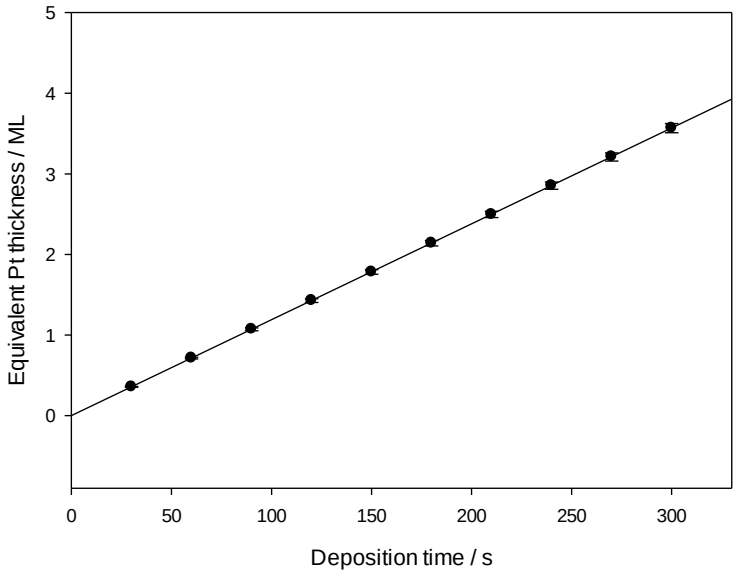

Figure 2.9. Calculated parameters for particle deposition, The deposition times used are presented in addition to the expected Pt equivalent thickness in terms of monolayers. The thickness of a platinum monolayer was calculated to be 0.227 nm.

In order to characterise the sizes of the deposited particles, deposition was subsequently carried out on TEM grids. These were held in a special TEM grid holder where the grids are arranged in a 4 x 4 pattern. The array positions to which the TEM locations are placed are at rows/columns 1, 4, 7 and 10. This thereby allowed mapping of the particle sizes to the various array locations (Figure2.10). Prior to particle deposition, a thin film (approximately 20 nm) of TiO_2 or Fe_2O_3 was deposited on the grids in order recreate the growth properties on the arrays as closely as possible. In each case the support material was deposited under identical conditions to those used for the screening arrays, albeit with shorter deposition times.

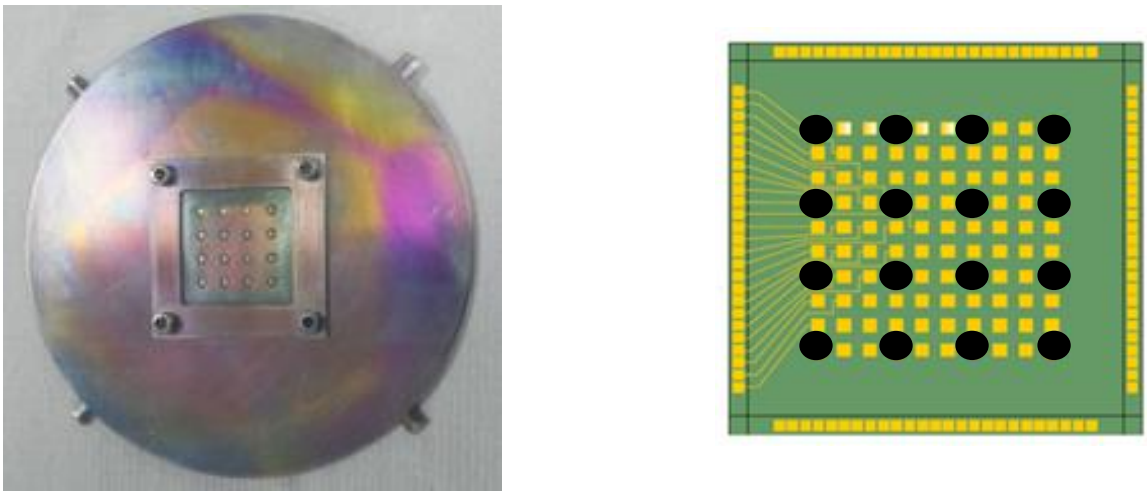

Figure 2.10. TEM grid holder (left) for use in the PVD system. The grids are held in a 4 x 4 array of holes in the center of the holder. Also shown (right) are the equivalent array locations to which the TEM locations correspond.

2.1.3. Substrates

A number of different substrate materials were employed throughout this work. The selection of which was dictated by the intended screening or characterisation application of the sample. Ideally, the samples would be screened and characterised on a single chip, however the varying constraints of the measurements often require synthesis on different substrates or formats.

Si substrates (Nova electronics) were used for all compositional measurements (since a conductive material is required for SEM/EDX) and were suitable also for thickness measurements

carried out by AFM. A 10 x 10 contact mask was used on such substrates to allow deposition of 100 different squares equivalent to the dimensions of the screening array.

SiN substrates (Nova electronics) were used for all structural characterisation by XRD. These substrates were also used for conductivity measurements, whereby a non-conducting substrate is required. The choice of mask depended on the application of the sample, with a 10 x 10 mask used for XRD measurements. A larger mask producing a continuous film was employed for conductivity measurements due to the large probe size on the four point probe used for such measurements. The larger than usual film area is also used to mitigate edge effects resulting from inhomogeneous current distribution near the sample edge.

For thickness measurements and the calibration of shutter position, **SiO_2** substrates were used.

The electrochemical screening array used within this work is depicted in Figure 2.11 and is described in detail elsewhere.[205] The array (supplied by Ilika technologies) features 100 individually addressable Au electrodes onto which the sample is deposited. The same 10 x 10 contact mask described above constrains the deposition to only the Au electrodes. Electrical contact to the array is made by Au contact pads (0.8 x 0.8 mm) around the periphery of the array. These are electrically connected to the electrodes via Au tracks. The entire array excluding the contact pads and electrodes is coated by a thin layer of SiN. This is to remove any contribution of Au to the voltammetric studies and is used due to its stability in the acidic and basic electrolytes employed.

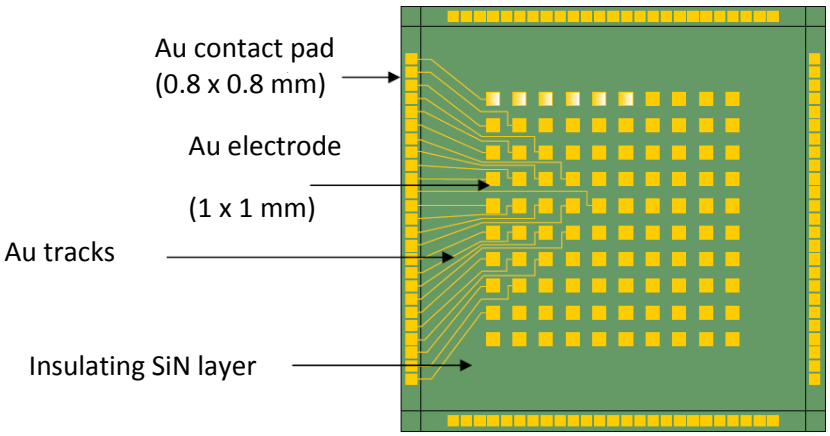

Figure 2.11. Schematic of the electrochemical screening arrays used within this work. The chip features 100 electrodes which are connected to contacts around the edge of the sample by Au tracks.

2.2. Characterisation Methods

2.2.1. Atomic Force Microscopy (AFM)

Atomic force microscopy is a type of high resolution scanning probe microscopy. Only topographical information was obtained in this study; however AFM may also be used to measure voltages and currents at the surface of a sample.

The AFM features a cantilever on which a small tip is located. When the tip is brought within close proximity of the sample, the atomic forces acting between the two results in a deflection of the cantilever, which is described by Hooke's law.

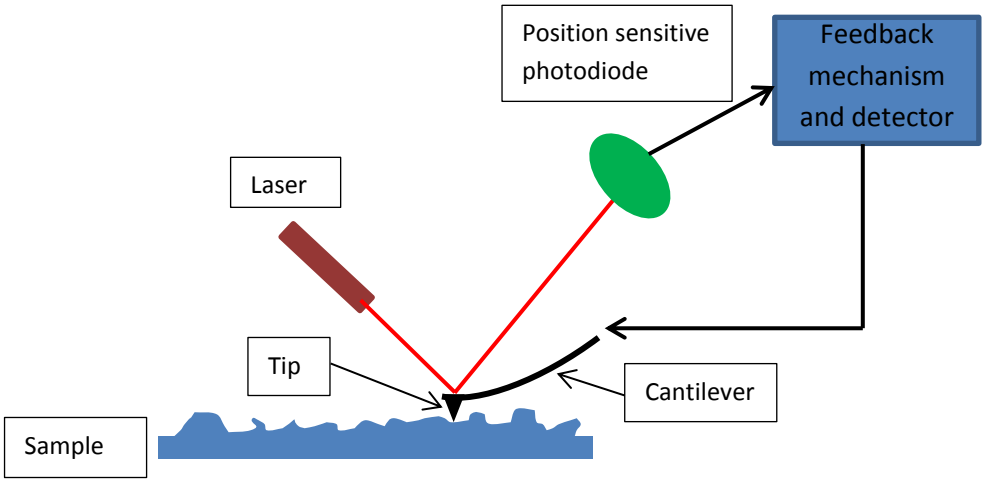

Figure 2.12. Schematic of the key components of an AFM and the mechanism of operation.

The deflection of the cantilever in turn deflects a laser spot which is focused on the top of the cantilever. A piezoelectric scanner is used to move the tip over a small area of the sample whereby the structure of the surface deflects the cantilever to varying degrees. A feedback mechanism is employed during this process in order to maintain a constant distance between the tip and the surface. The cantilever deflections are picked up by a position sensitive photodiode, which in turn aids in generating the image of the surface. Thickness measurements were carried out on samples on which a 10 x 10 array of $1mm^2$ films were deposited. The AFM tip was scanned over a small area of the substrate and onto the film, where the difference in height between the two was assigned as the film thickness.

In this work a Veeco Autoprobe M5 was used for thickness measurements, with a Si tip (Micromasch, tip radius 10 nm, spring constant 0.15 N m^{-1}). An Agilant 5600LS was also used for thickness measurements as well as topographical imaging. Imaging and thickness measurements were performed in tapping mode, whereby the tip is oscillated at its resonant frequency. The force between the tip and the sample results in a variation in the oscillation amplitude. This is dependent on the tip – substrate distance and thus can be used to generate an image of the sample surface.

2.2.2. Energy Dispersive X-ray Spectroscopy (EDX)

Energy dispersive x-ray spectroscopy is a technique which allows analysis of the elemental composition of materials. The instrument measures the x-ray emission spectrum of a sample, which distinguishes between elements by the unique characteristic x-ray energies of each constituent element in the material.

The system functions by focusing a beam of high energy electrons on the sample of interest. A core electron of an atom may then be ejected, leaving behind an electron hole. Higher energy electrons in outer shells may then fill this hole, at which point x-ray emission occurs. The energy of the x-rays is dependent on the energy difference between two shells involved in the aforementioned processes. Since all elements feature a unique atomic structure, the collections of x-ray emission peaks are unique to each element. An energy dispersive spectrometer then measures the energies and intensities of the emitted x-rays which may then be used for elemental analysis. Qualitative analysis can be carried out simply by identifying the energies of the peaks in the spectrum, although quantitative analysis is possible when the intensities of the various x-ray energies are available. The key processes behind the operation of EDX are depicted in Figure 2.13.

Within this work, EDX measurements were carried out with a JEOL JSM5910 scanning electron microscope equipped with an Oxford Instruments Inca 300 EDX system. A working distance of 10 mm was used in all cases with a spot size of 55. The spot size is proportional to the area of the beam. The composition at each point on the array was carried out with an automated macro where each electrode location was moved under the beam with an x-y stage. At each location the EDX spectra were recorded for 60 seconds using a magnification of x500. In each case an accelerating voltage of 15 kV was employed. After the measurements, the composition in terms of atomic percent (at.%) could be mapped to each electrode location on the screening array.

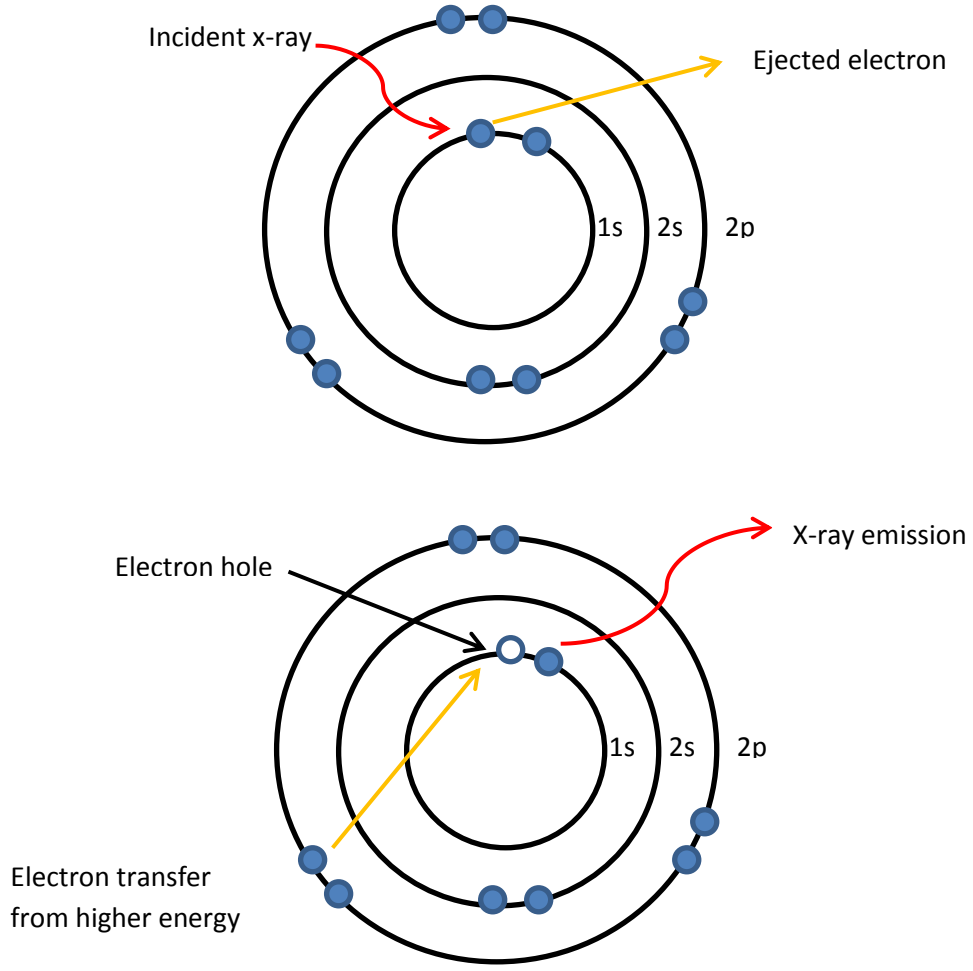

Figure 2.13. Diagram showing the sequence of events leading to x-ray emission in EDX.

2.2.3. Transmission electron microscopy (TEM)

Transmission electron microscopy (TEM) is an imaging technique that allows for creation of extremely high resolution (typically to sub-nanometer levels) images of materials. The basic principle of operation is similar to optical microscopes; however electrons are instead used as the 'light' source. The ability to produce images of much higher resolution stems from the greatly reduced wavelength of electrons when compared to light.

At the top of the column is a Tungsten or LaB_6 filament which is connected to a high voltage source. The filament emits electrons by thermionic emission which is subsequently focused by a series of lenses. The lenses act in a similar way to those in optical microscopes; however they alter

the beam by way of a varying magnetic field. The various TEM components are depicted in Figure 2.14. The electron beam from the emission source is initially focused into a thin beam by the use of a pair of condenser lenses. The first lens determines the size range that the spot incident on the sample can obtain. The second lens however dictates the actual beam size on the sample. The beam subsequently passes through one of the three user selectable apertures on the system, the condenser aperture. This functions by further restricting the beam size and removes electrons that are far away from the optical axis running through the center of Figure 2.13.

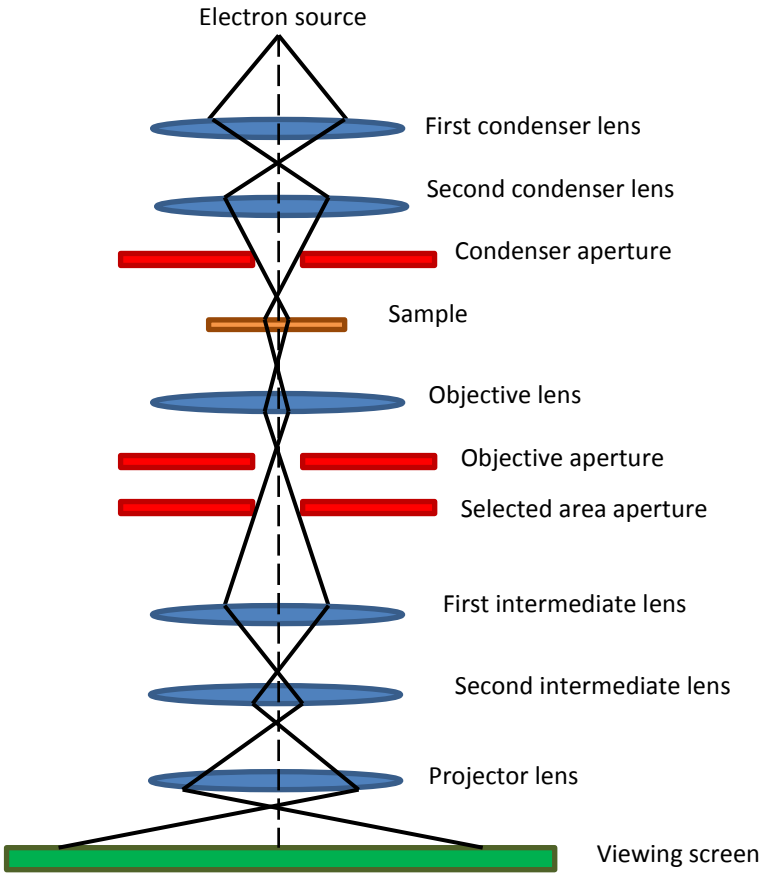

Figure 2.14. Schematic of the key TEM system components. The image axis is represented by the dotted line running throughout the center of the figure.

Upon striking the sample, electrons may be randomly scattered and absorbed or may be transmitted through the material. The degree of transmission is dictated by the density and thickness of the sample, which forms the contrast of the image. The transmitted part of the beam is then focused into an image by the objective lens, before passing through the second variable aperture known as the objective aperture. Once again this aperture may remove electrons far from the optical axis and be used to alter the level of contrast. The selected area aperture functions similarly and allows the examination of electron diffraction. The image is subsequently

enlarged by the two intermediate lenses and the projector lens. The electrons then strike a phosphor viewing screen whereby the image is converted to a form perceptible by the operator. The electrons generate light upon interacting with the screen, the brightness of which dictated by the level of transmission. As a result, darker areas represent thicker areas of the sample where transmission is more limited.

For the purpose of this work, TEM was used to study the size and morphology of the deposited Pt nanoparticles. A JEOL JEM3010 TEM was used with an accelerating voltage of 300 kV. Images were captured by a Gatan CCD (charge coupled device) camera at a magnification of x200k. The particle sizes were analysed using software developed by Ilika Tehnologies, which enabled characterisation of particle size, particle density and the total Pt surface area. A hemispherical model was used which measured the area of the particles before calculating the equivalent diameter of a hemispherical particle.

2.2.4. X-ray Diffraction (XRD)

X-ray diffraction is a technique that can be used to determine the crystalline structures of materials. The system operates on the principle that atoms cause interference of waves resulting in their diffraction in specific ways. The characteristic peaks in XRD represent constructive interference of monochromatic x-rays upon interaction with atoms in a material. This type of diffraction occurs when conditions obey the Bragg equation, whereby ordered atomic arrangement produces constructive interference. The principle of operation is depicted in Figure 2.15.

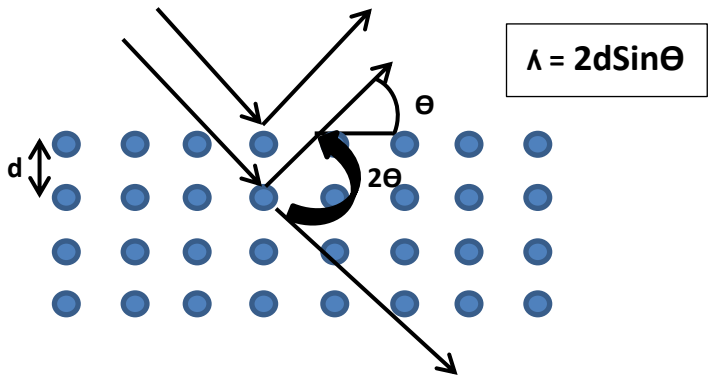

Figure 2.15. Schematic of the x-ray diffraction process according to Bragg's law. Parrallel X-rays are diffracted by the crystal planes, which form constructive interference when 2dSinΘ is equal to the wavelength of the incoming X-rays.

The characteristic angles of diffraction are picked up by a detector, as well as their relative intensities. The diffraction angles are characteristic of the material structure and may therefore be used to determine the crystalline structure of a given material. A two dimensional detector was used in this work, which allows for diffractions of a large range of angles to be measured simultaneously without requiring movement of the detector or source. The instrument employed was a Bruker D8 diffractometer with a C2 general area detector. The x-ray source used was Cu Kα1. In all measurements the source was fixed at 11^{o} while the detector was held at 26^{o}. The data acquisition time was 10 minutes in each case also. Samples were deposited in an identical manner to the screening substrates but instead using SiN substrates. An automated macro was also used in order to collect data for each square on the 10 x 10 film.

2.2.5. X-ray Photoelectron Spectroscopy (XPS)

X-ray photoelectron spectroscopy (XPS) is a surface sensitive spectroscopic technique. It may be used to determine the elements present at a surface as well as their relative compositions. Additionally XPS may be used to detect the chemical state of such elements.

XPS functions by irradiating a surface with x-rays and measuring both the kinetic energy and intensity of ejected electrons that reach the detector. A tungsten filament serves as an electron source which is used to bombard the anode material with electrons. In many systems, including that used in this work, a dual anode arrangement is employed. This features both a magnesium and aluminium anode which subsequently emit x-rays upon bombardment of electrons. The x-rays incident on the sample lead to ejection of a core electron (photoelectron), whos kinetic energy is then analysed by the detector. A schematic of this process is shown in Figure 2.16.

The electron energies are presented as binding energies (E_B), which are calculated from known parameters by Equation 2.1.

(2.1) $$E_B = hv - E_K - \Phi$$

Where *hv* is the photon energy, E_K is the kinetic energy of the ejected electron and Φ is the work function.

The surface sensitivity of the technique stems from the fact that only a limited number of electrons ejected by the sample actually reach the detector to be analysed. Before reaching the

detector the ejected electrons must traverse the depth of the sample dependent on the point of generation. Ejected electrons may undergo inelastic collisions, recombine, excite the sample or become trapped in various states. These effects limit the number of electrons reaching the detector, and result in an exponential attenuation in response to increasing sample depth. As a result, only photoelectrons generated in the top 1 – 10 nm of the sample contribute to the observed spectrum.

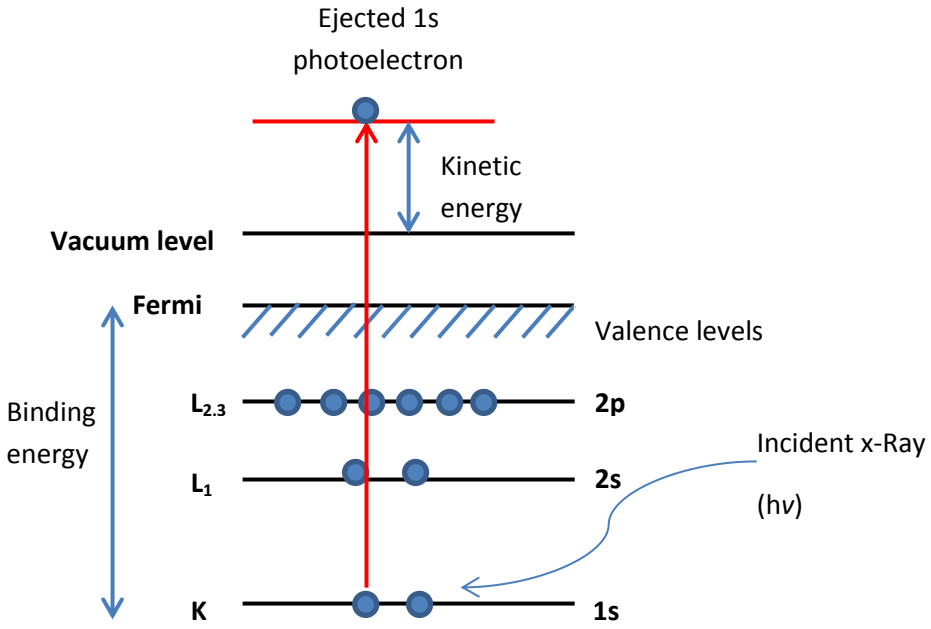

Figure 2.16. Schematic of the photoelectron emission process in XPS. The photoionisation of the sample is shown by the ejection of a 1s core electron.

In this work, the XPS chamber incorporated into the HT-PVD system was used. An Al anodes was used form the measurements within this work. The system featured a PSP multichannel XPS analyser and the acquisition of data was performed using software from PSP vacuum technologies. All subsequent data analysis was performed with CasaXPS software. All samples characterised with XPS required removal from the vacuum chamber prior to undertaking measurements. Some level of sample contamination is therefore likely. Where it was required that samples were stored outside of vacuum, they were placed in vacuum sealed bags.

2.3. Electrochemical Measurements

2.3.1. Instrumentation and Screening Protocol

All the samples prepared during this work were screened using custom built High-throughput electrochemical screening apparatus previously developed in the research group and by Ilika technologies.[207] The method is adapted from a previously reported method in which a pseudo-parallel method was used to screen supported metal nanoparticles. The method involves rapid sequential screening of the array electrodes by use of a single channel potentiostat equipped with a 100 channel current follower. The system operated as a conventional three – electrode cell in which a single counter electrode and reference electrode were also employed. It should be noted however that the screening process operates in parallel and only the acquisition of data is performed in a serial manner. The high throughput potentiostat is depicted in Figure 2.17.

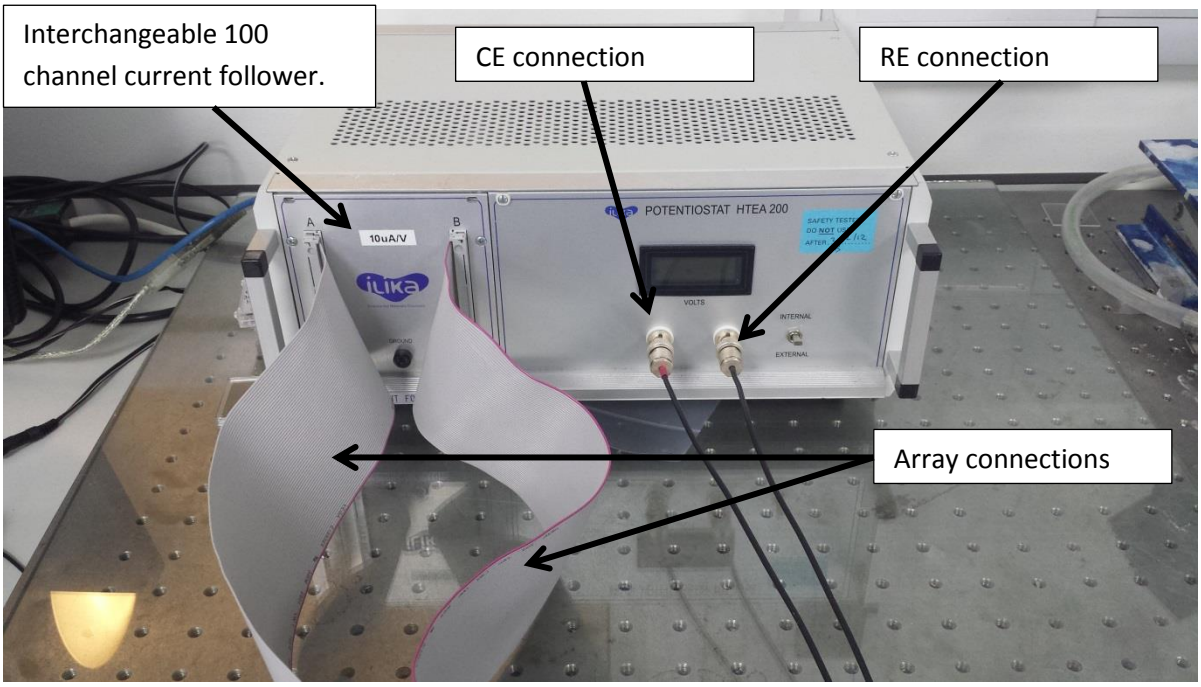

Figure 2.17. Image of the high-throughput potentiostat. The 100 channel current follower is shown in addition to the connections to the array, counter electrode (CE) and reference electrode (RE).

The potentiostat incorporates the current follower where contact is made to the array. Three different sensitivities of current follower may be used (100, 10 and 1 μA V^{-1}) and a current follower of 10 μA V^{-1} was used within this work. Control of the system was carried out by purpose built software developed by Ilika technologies, which allowed for cyclic voltammetry and potential

step experiments to be carried out. Subsequent data analysis was also carried out using software developed at Ilika Technologies.

A custom built electrochemical cell was used to hold the array electrodes used in this work (Figure 2.18), which were stored in vacuum sealed bags prior to testing. All experiments were carried out at room temperature (20 – 25 ^{o}C) with the use of the cell depicted below. In addition to the main cell body, separate compartments were used to house the reference and counter electrodes. The counter electrode was separated from the main cell by use of a glass frit and a luggin capillary was used to hold the reference electrode. An Hg/HgO reference electrode (EC-Lab) with a filling solution of 0.5 M NaOH (fisher scientific) was used in the majority of measurements due to its suitability in alkaline media and lack of chloride containing filling solution. An SCE electrode (Accumet) was however used in experiments in acid. The counter electrode was a platinum gauze (Alfa Aesar, 99.99%).

Additionally, the cell featured both a tap for draining electrolyte as well as a gas inlet in the form of a glass frit. The tap on the gas inlet allowed switching of the gas flow to either through the electrolyte or over the top of the electrolyte surface, which was used during measurements.

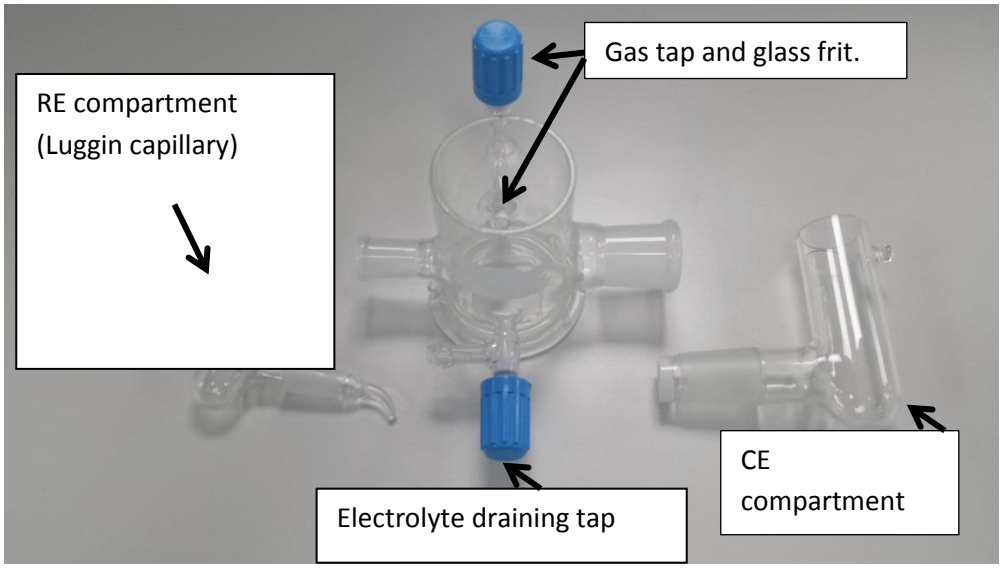

Figure 2.18. Image of the electrochemical cell used within this work. The cell features a tap to select whether gas is blown over the top or through the electrolyte. An electrolyte draining tap is also incorporated. Separate compartments are used to house the counter and reference electrodes.

The working array electrode was placed in a PTFE block. A number of other components depicted in Figure 2.19 completed the cell construction. Electrical contact was made to the array through

the contacts around the edge of the sample by use of a gold gasket. A Viton gasket was then placed after the gold gasket in order to prevent its exposure to the electrolyte. A PCB was clamped to the assembly which made contact with the gold gasket and featured connections to interface with the potentiostat. The cell was then fixed to the assembly by a series of metal clamps.

Typically CV measurements were generally recorded between the limits of -0.05 and 1.4 V vs. RHE, although this was dependent on the experiment. In all cases the electrolyte was purged with a fast stream of argon (BOC) for 30 minutes prior to data acquisition. In oxygen reduction experiments the solution was instead purged with high purity oxygen (BOC) before carrying out measurements. During this time the working electrode was held at a potential more positive than that required for oxygen reduction.

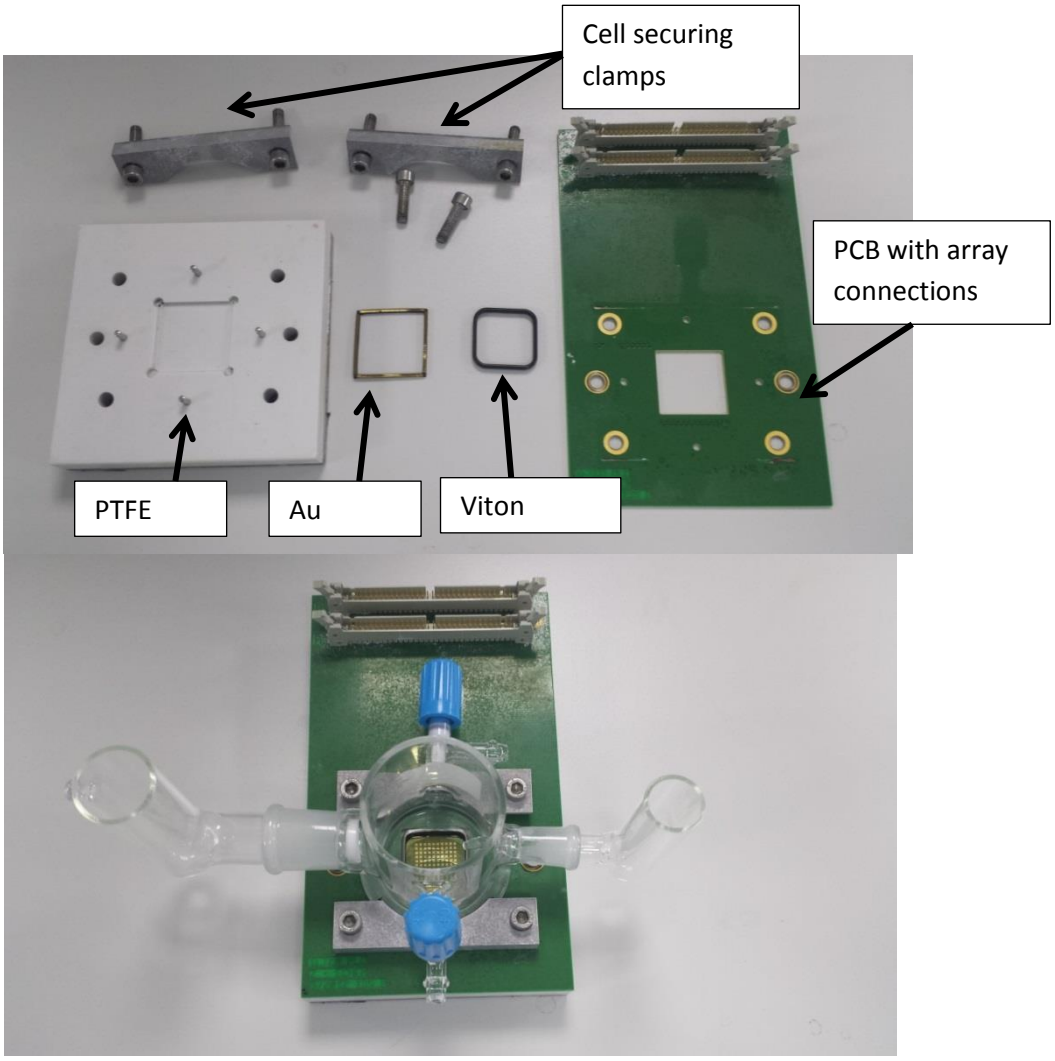

Figure 2.19. Components of the electrochemical cell apparatus (Top), showing the various gaskets used as well as the PCB used to connect the electrode array to the potentiostat. Also shown is the cell apparatus when assembled (Bottom).

This method allowed for acquisition of data for 100 electrodes in a short space of time. Furthermore the simultaneous measurement of all the electrodes means that all data is recorded under identical conditions. Due to the presence of 10 electrodes of the same thickness / particle size across the array, all measurements reported herin are presented as an average for a given thickness / particle size. All errors are also reported as 1 standard deviation.

2.3.2. Solutions and Gases

Electrochemical measurements in alkali were carried out at room temperature using 0.5M NaOH, 0.5 M NaOH + 5 mM $K_3Fe(CN)_6$ and 0.5 M NaOH + 1 M MeOH (Fisher scientific analytical grade). All solutions were prepared with ultrapure water (18.2 MΩ, ELGA). Alkaline media was chosen since few studies to date have reported particle size effects of supported nanoparticles in alkali. Additionally this medium was chosen to facilitate comparison of photoelectrochemical data with that in the literature. Alkaline media is generally preferred in this context due to the greater efficiency of the oxygen evolution reaction.[208] Additionally, the dark electrochemical behaviour is of interest in alkali since it is seldom reported in the literature with regard to particle size effects in supported Pt nanoparticles.

Where screening was carried out in acidic media, 0.5 M $HClO_4$ was used. Additionally, 10 mM $CuSO_4$ was added (Fisher scientific). Prior to measurements, the electrolyte was purged with Ar (BOC) in order to remove dissolved oxygen from the solution. In oxygen reduction experiments, high purity oxygen (BOC, 99.999%) was bubbled through the solution before data acquisition.

2.4. Photoelectrochemical Measurements

2.4.1. Instrumentation

Photoelectrochemical measurements were obtained using the previously described high-throughput potentiostat and electrochemical cell. The cell was previously developed for a scanning DEMS system and features an open top to minimise the attenuation of UV radiation

which normally occurs when using glass cells.[16] Additionally the luggin capillary is shorter than the standard high-throughput cell design in order to ensure unhindered passage of light to the electrode sample face.

In all experiments a constant volume of electrolyte (80 ml) was dispensed into the cell in order to prevent a variation in the degree of optical attenuation by the electrolyte. This results in a near constant optical path length. The estimated error in the amount of electrolyte was estimated as 0.2 ml. This translates to an insignificant variation in optical path length due to the relatively wide diameter of the cell body. The electrolyte height was however allowed to vary by approximately 0.5 cm, which was found to have a negligible impact of the recorded photocurrent (Figure 2.20). No correction was applied for electrolyte attenuation, since this is a key component of any photoelectrochemical cell and any real devices will most likely feature additional windows which further scatter incident irradiation.

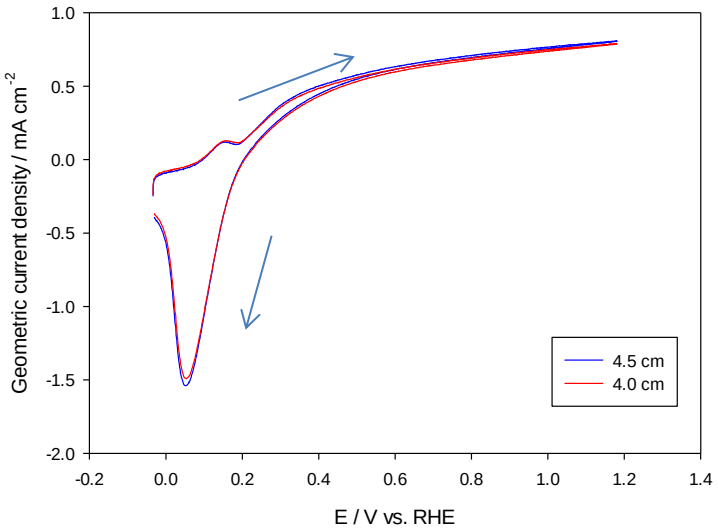

Figure 2.20. Illuminated CVs recorded at 50 mV s^{-1} in 0.5 M NaOH of a Pt/TiO_2 electrode. The height of the electrolyte above the sample (given in the inset) was allowed to vary by 0.5 cm. The arrows show the directions of the scans.

The photoelectrochemical screening apparatus is depicted in Figure 2.21. The system features a 150 W Xe arc lamp (LOT-Oriel) as the illumination source with an overall irradiance uniformity of approximately 15 % after optimisation. An Al beam turning mirror was used to transmit the whole spectral output of the lamp onto the sample from above. The lamp also featured a regulated power supply which ensures a constant current is supplied to the lamp. This is adjustable so that a constant illumination level is achievable throughout the lamps lifetime.

The circular output (Beam diameter approximately 30 mm) of the beam was focused onto the center of the sample. The lamp was also fitted with custom built legs which allowed adjustment of the lamps height with respect to the sample. The lamp was also fixed to an optical bench to ensure a constant placement of the sample with respect to the beam. The cell assembly was fixed to a small scissor jack, which also allowed control of the sample height. The entire assembly was pushed up against a locating block such that the sample was always in the same location with respect to the light beam.

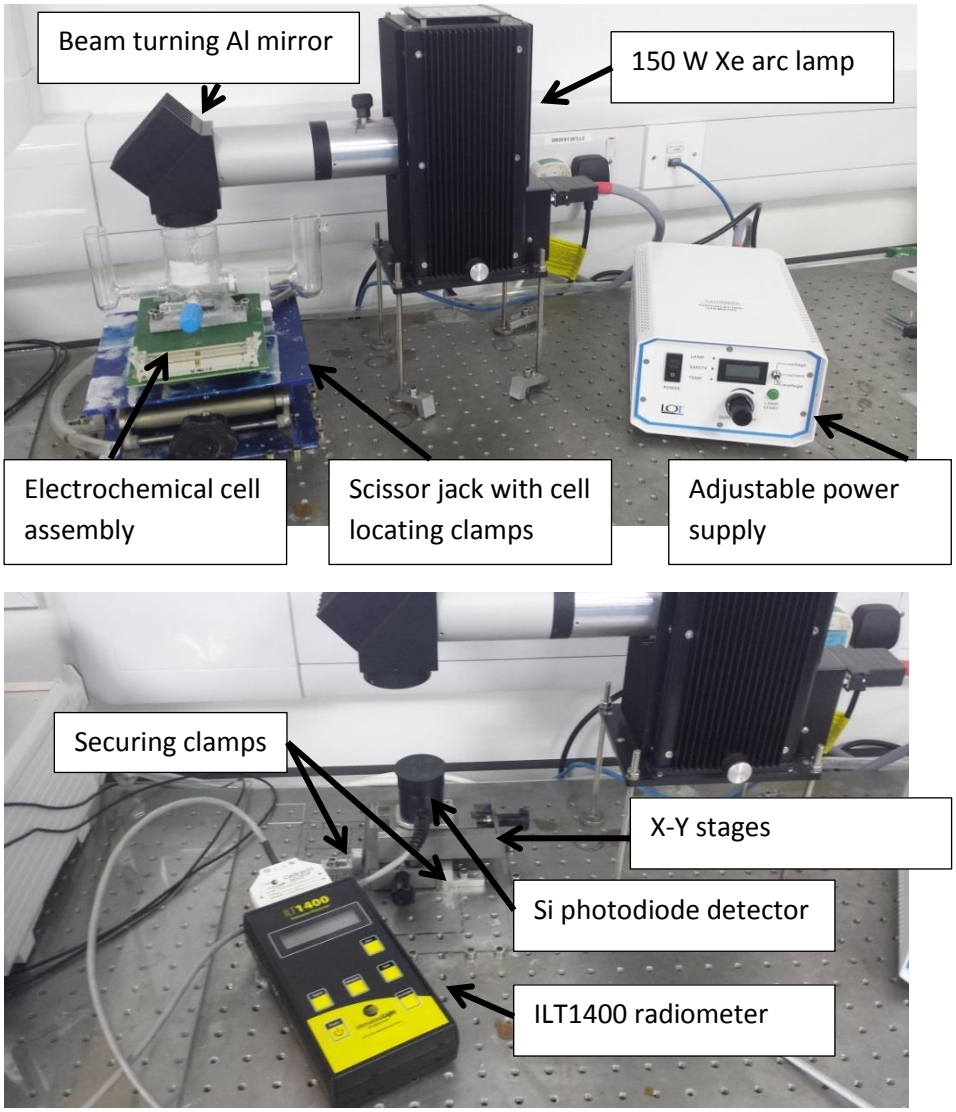

Figure 2.21. Top: Photoelectrochemical screening apparatus, with the high throughput electrochemical cell and Xe arc lamp. The cell is located on a scissor jack for height adjustment and features locating clamps to ensure the sample is at a constant position in the beam. Bottom: Equipment used for measuring irradiance across the beam area. The detector and radiometer are shown as well as the X-Y stages that are fixed to the optical bench.

Where intensity measurements were carried out, a Si photodiode (ILT) was positioned in place of the photoelectrochemical cell. This was fixed to a manually actuated X-Y stage, which was in turn fixed to the optical bench by a series of metal clamps. The assembly was positioned such that the center of the detector was in the same location as the electrode with coordinates (1,1). A long pass filter was also employed in order to estimate the relative proportional UV contribution to the overall irradiance. In order to mitigate the effects of any spatial optical inhomogeneity at the filter, the detector was filtered rather than the source during these measurements. This therefore dictated that the beam passed through the same area of the filter as the detector was moved over the beam area.

2.4.2. Photocurrent Measurement

All photocurrent measurements were performed using the equipment described above. Prior to each measurement a number of irradiance readings were taken to facilitate normalisation to the desired irradiance level. Additionally, photocurrent CVs were recorded for calibration arrays of either uniform TiO_2 or Fe_2O_3 prior to the supported particle samples. This allowed assessment of the effects of irradiance non-uniformity so that the results could be normalised. The calibration arrays showed the lamp output to be relatively stable between experiments, although some subtle variation in the overall intensity occurred. Since calibration was carried out before every array was screened, the results between different arrays remain comparable after the normalisation process. More details on the lamp stability are presented in Chapter 3.

In each case, non-illuminated CVs were recorded immediately prior to those under illumination. Where possible the lamp was turned off during these measurements due to the level of noise produced in the measurements while the lamp was operating. In between measurements, the sample was shielded from the beam by a thin sheet of metal. From the light and dark measurements photocurrents (j_{ph}) were subsequently calculated according to Equation 2.2.

(2.2) $$j_{ph} = j_l - j_d$$

Where j_l and j_d are the currents recorded under illumination and in the dark respectively.

After calculation of the photocurrent at each electrode, a normalisation process was required in order to account for the varying irradiance levels across the sample. In all cases, the electrodes were normalised to the array electrode of coordinates (5,5). The spatial dependence of the

irradiance was found to be non-identical in both the x and y directions with respect to the array coordinates, and as such, normalisation had to be carried out in both the x and Y directions. In the simplest case, the intensity – photocurrent relationship is the same as the blank support material without platinum particles. This was the case of both the α- Fe_2O_3 and anatase TiO_2 supported particles. The normalisation factors ($x_{n(X,Y)}$) for a given electrode of coordinates (X,Y) may then be directly calculated from the calibration sample by Equation 2.3.

(2.3) $$x_{(X,Y)} = \frac{j_{ph,n}}{j_{ph(X,Y)}}$$

Where $j_{ph,n}$ is the measured photocurrent at the electrode to which all others are normalised on the calibration sample. $J_{ph(X,Y)}$ represents the measured photocurrent at the electrode of coordinates (X,Y) which is to be normalised on the calibration. The electrode may then be normalised to the desired electrode according to Equation 2.4.

(2.4) $$j_{ph,2} = j_{ph,1} \times x_{(X,Y)}$$

Where $j_{ph,1}$ and $j_{ph,2}$ are the pre-normalised and normalised photocurrent respectively and $x_{(X,Y)}$ is the calculated normalisation factor for the beam location of the electrode being normalised. Figure 2.22 shows the photocurrent recorded at a typical array both before and after the normalisation process.

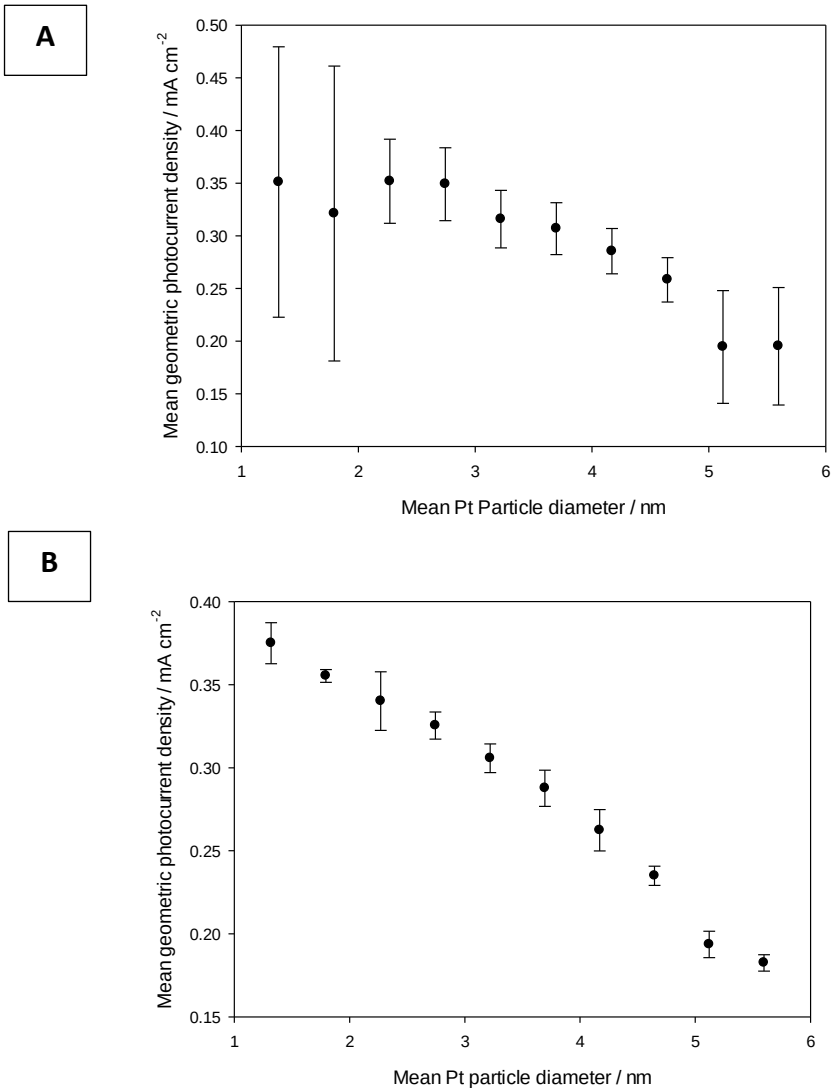

Figure 2.22. Uncorrected (A) and corrected (B) photocurrent density at 0.26 V Vs RHE on an array of Pt nanoparticles on anatase TiO_2. Measurements were recorded at 50 mV s^{-1} in 0.5 M NaOH.

In some cases overall activity trends were observable even before the correction process was implemented. This is the case in the figures above, in that the same general trend exists in both cases. It should be noted also that due to the direction in which the sample is oriented, the activity trend does not simply track the relative intensity across the array (see Chapter 3). The overall level of error is however greatly reduced after the normalisation process. Furthermore, normalisation may have a much greater importance in cases where the overall activity variation is much smaller across the array.

2.4.3. Photovoltage Measurement

Illuminated open circuit potentials were recorded using the same instrumentation as that described above for photocurrent measurements. The potentiostat was however equipped with a 100 channel voltage follower in place of the current follower developed by Ilika technologies. All measurements were recorded directly vs. the reference electrode. Measurement of the illuminated open circuit potential is a widely used and simple way to determine the flat band potential of a material. The method involves measurement of the OCP at various light intensities. The flat band condition is met when the OCP reaches a limiting plateau. This did not appear to occur at any of the samples prepared in this work, although the anatase TiO_2 samples were closer to reaching this limiting plateau compared with α-Fe_2O_3. However, the method still provides useful data on the level of photovoltage production in response to variations in material properties across the sample.

The open circuit was first measured in the dark, before measuring values under illumination. Although the materials employed in this work are well known n-type semiconductors, the direction of voltage shift under illumination is useful in rapidly determining the conductivity type of a material. Typically the illuminated value was measured over a period of 200 – 300 seconds, over which the average value was calculated. The light was periodically blocked and the measurements were repeated in order to assess whether any changes to the material occur that result in a change in the OCP. In order to assess whether the flat band potential had been met, the measurements were also conducted over a range of different illumination intensities. The photoelectrochemical measurement methodology as well as the various normalisation processes are discussed in more detail in Chapter 3. The results of a typical experiment of the type described above are shown for an anatase TiO_2 electrode in Figure 2.23.

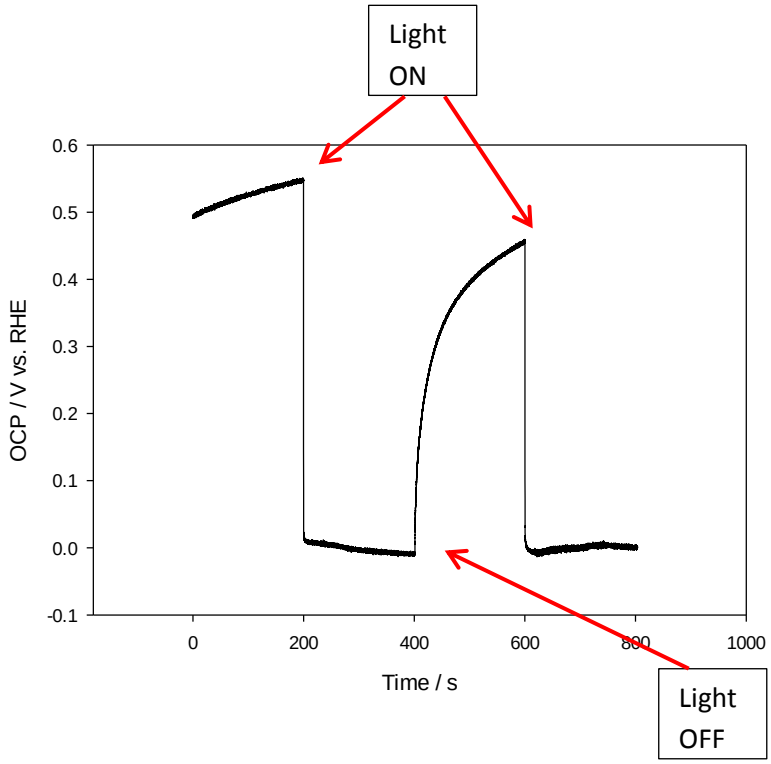

Figure 2.23. Typical voltage response for an experiment measuring the OCP of an anatase TiO_2 electrode. Measurements were conducted in 0.5 M NaOH with an illumination intensity of approximately 60 mW cm^{-2}. The points at which the light was turned on and off are indicated.

In all cases the OCP values were stable (on anatase TiO_2) and repeatable. It is assumed that due to the relatively short timescale of the experiments that the contribution of heating effects from the lamp was insignificant.

3. High-Throughput Photoelectrochemical Screening

3.1. Lamp Calibration

In order to obtain reliable and accurate activity trends across a combinatorial material library it is imperative that the characteristics of the optical system used are understood. By introducing light to augment an electrochemical reaction, one essentially adds an additional reactant, which must be carefully controlled in order to prevent a variation in this parameter from dominating the electrochemical measurements obtained.

In this work, a 150 W ozone free Xe arc lamp (LOT–Oriel) was used as the illumination source. The lamp was operated in a, 'beam down' configuration such that the sample was illuminated from above. This was achieved by use of a 90 degree beam turning Al mirror (LOT-Oriel) which offers transmission for wavelengths between 200 – 3000 nm (i.e. the entire spectral output of the lamp). The lamp housing also contained a condenser lens which could be used to alter the profile of the beam to be diverging, converging or collimated. For the purpose of this work a slightly divergent beam was necessary in order to illuminate the maximum possible number of electrodes on the sample. Additionally, all optics were composed of quartz in order to preserve the UV output of the lamp.

Xe arc lamps of this type closely match the colour temperature of the sun (6000 – 6500 K)[209] and thus offer a good approximation of solar illumination. As such, they are commonly employed in order to assess the behaviours of candidate photoelectrode materials. It is necessary however to acknowledge, that even in the case of high-end solar simulators the characteristics of such lamps do not exactly match that of the solar spectrum. In particular it is difficult to accurately recreate the attenuation properties of atmospheric components such as H_2O, O_3 and CO_2.

For the screening of materials herein, the lamp was operated without any additional filters, since it was of greater interest to preserve the intensity and UV output of the source. Additionally, the primary purpose of this screening methodology was to assess relative trends across the material libraries rather than generation of highly accurate solar to hydrogen conversion efficiencies.

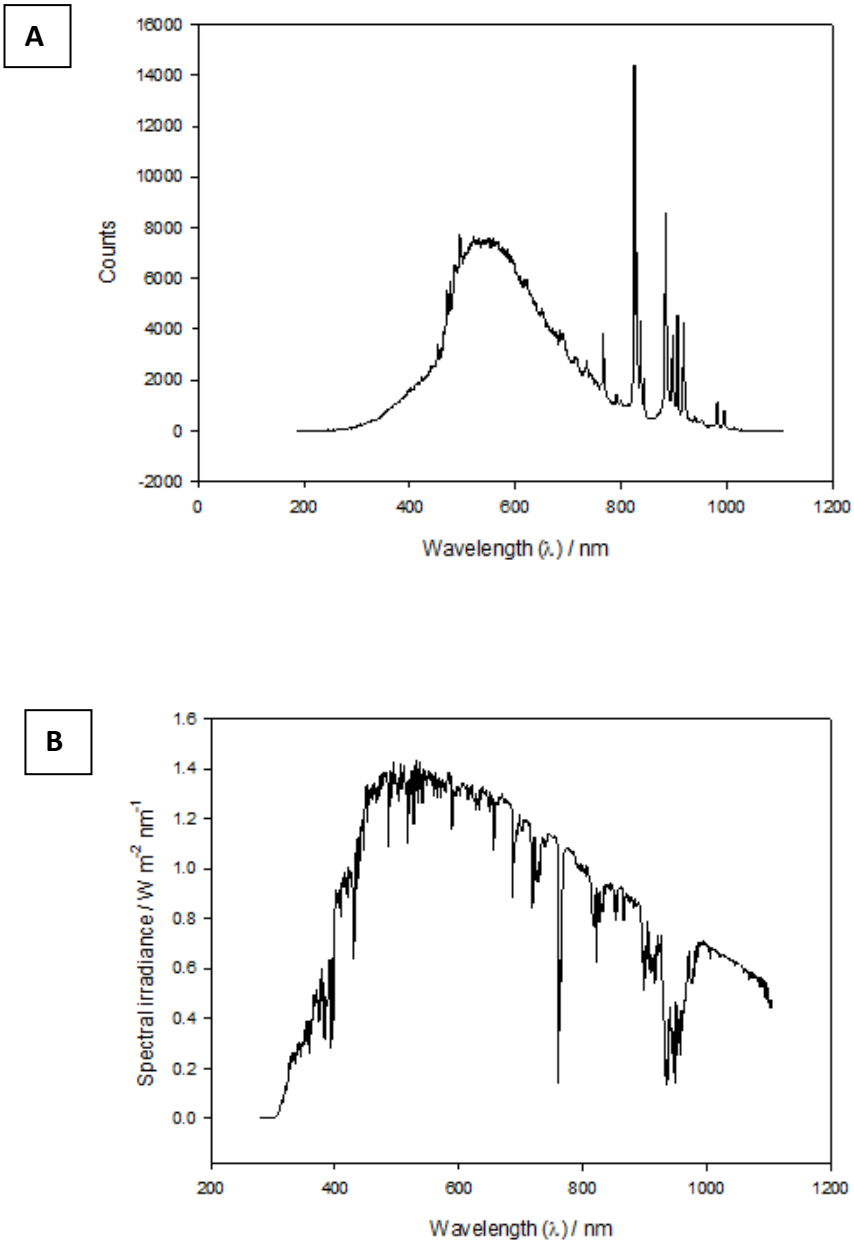

Figure 3.1. Spectrum of the Xe arc lamp used within this work (A) obtained with a UV-vis spectroradiometer (Ocean optics) between the wavelengths of 180 – 1100 nm. The lamp emission current was held at a constant value of 8.5 A and measurements were taken at a distance of 8 cm from the lamp output. Also shown (B) is the AM 1.5 G solar spectrum for wavelengths below 1100 nm. Data taken from ref [17]

In spite of some broad similarities between the spectra over the visible range, arc lamps of this type have a much larger proportional output of UV radiation compared with the solar spectrum. Additionally, the output of Xe arc lamps extends to shorter wavelengths. In the case of the ozone

free Xe lamp used herein, the doped quartz lamp envelope absorbs below 300 nm, with an eventual cut-off at around 250 nm. Although the Xe arc lamp is relatively flat throughout the UV and visible ranges, the characteristic Xenon lines can be seen to dominate from approximately 750 – 1000 nm.

Within this work the primary concern was the relative irradiance level of photons with energy greater than the material band gap across the sample. i.e. the overall irradiance is not important, but rather the proportional makeup of the overall intensity. The irradiance of the experimental light source for wavelengths smaller than 400 nm was calculated by use of a high quality long pass filter, (Andover corp.) which allowed transmission of all wavelengths above 400 nm with an average transmission efficiency of 93%. The difference in irradiance with and without the filter (also with correction for the average transmission efficiency of the filter) was then used to estimate the irradiance associated with wavelengths below 400 nm.

(3.1.) $I_{UV} = I_{tot} - \frac{I_{long}}{E_T}$

This approach was used rather than directly measuring the UV component with the use of a short pass filter for two main reasons. Firstly, the majority of readily available short pass filters begin to transmit at longer wavelengths which are still within the detection limit of the Si photodiode detector. Secondly, the relatively large IR output from the lamp will cause heating effects on the filter, which may cause damage or a variation in optical characteristics with prolonged use.

A further issue with arc lamps is the irradiance uniformity (Figure 3.2), particularly within the context of high throughput measurements of this type.

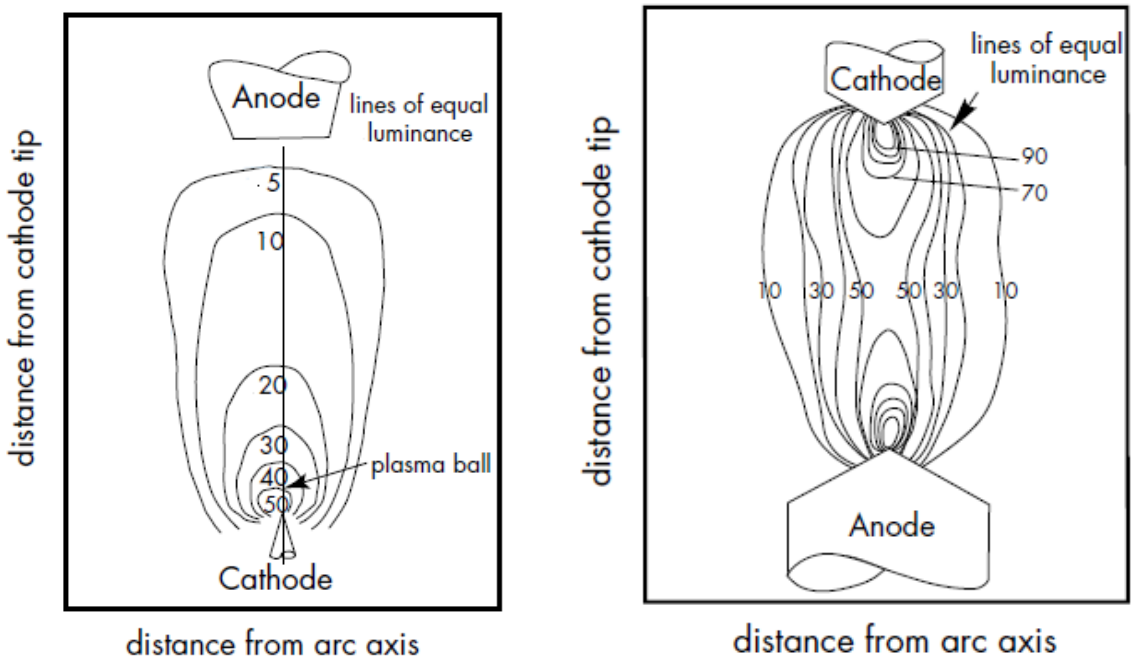

Figure 3.2. Typical contour maps of Xenon (left) and Mercury (right) arc lamps. In both cases there are luminance hotspots, which occur at the cathode in the case of Xenon arc lamps and both the cathode and anode on mercury arc lamps. Figure taken from ref [18]

In view of the fact that the arc in the lamp is non – uniform and non-similar in orthogonal directions, great care must be taken to ensure that any photoelectrochemical activity trends are not simply a result of varying irradiance at the different electrode positions in the sample. Although it is ideal to screen materials under identical optical conditions, it is rarely possible in parallel measurements due to the inherent spatial non-uniformity of such lamps. Even in the case of sequential measurements, the temporal instability of a lamp may have a significant effect on the overall results obtained. Sequential measurements were also found to be unsuitable for the materials investigated herein on account of the significant changes that occurred to the materials in response to electrochemical cycling. Since cycling of all materials occurs simultaneously, the characteristics of the materials vary greatly depending on the order of data collection.

In this case, the lamp was capable of producing a highly uniform beam over only a small region and as such correction for non-uniformity was necessary. This is possible only where a well-defined relationship between irradiance and the photoelectrochemical property to be measured can be obtained.

The photocurrent at a photoelectrode material is a strong function or the irradiance at the sample. As noted in section 1, a linear relationship is expected between irradiance and photocurrent in the Gartner model. In order to assess the effects of intensity on the photoelectrochemical characteristics, photocurrent vs. irradiance measurements were carried out on a uniform anatase TiO_2 film. In these experiments the intensity was modulated by adjustment of the lamps emission current (Figure 3.3).

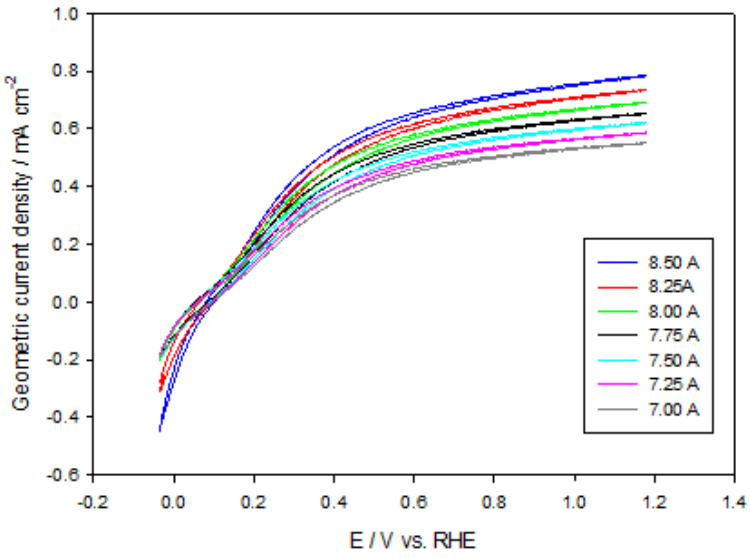

Figure 3.3. The effect of variation of lamp emission current on the photocurrent response of an Anatase TiO_2 thin film (~250 nm thick). Measurements were carried out in 0.5 M NaOH at a sweep rate of 50 mV/s. The 5th cycle is shown in all cases. An Au substrate material was used.

It can be seen from Figure 3.3 that a clear relationship between photocurrent and lamp emission current exists. With the lower emission currents, the irradiance at the sample face is less (Table 3.1), and therefore a lower photocurrent is generated. Previous results which investigated the irradiance sensitivity of TiO_2 found that at lower irradiance levels, the photocurrent was more strongly dependant on the irradiance level.[210] In all cases a sub linear relationship against irradiance was obtained. The relationships against intensity in the literature range from $I^{0.47}$ to $I^{0.63}$.[210] The lack of agreement between the results most likely arises from use of differing applied bias in the generation of the results. It is clear from Figure 3.3 that the voltage used to derive such a relationship has a marked effect on the photocurrent value obtained. In the case of correcting the photocurrent for varying irradiance across the sample it is therefore required that a different

normalisation process be carried out depending on the bias point at which the photocurrent is taken.

By using this approach it is important to ascertain the exact change in intensity as the lamp emission current is altered in order to obtain the intensity dependence. Care must be taken however when using a radiometer towards this goal. A radiometer simply integrates the whole photon flux incident on its surface. This therefore gives no information on the spectral distributions of photons and thus information on the relative proportions of the different wavelength bands cannot be derived with a radiometer alone. The relative UV proportion was therefore calculated at different intensities in the manner described earlier (Equation 3.1), such that the occurrence of any spectral variation could be determined.

Table 3.1.

Lamp emission current / A	Total measured irradiance / mW cm^{-2}	Irradiance measured with filter (λ>400 nm) / mW cm^{-2}	Calculated UV irradiance / mW cm^{-2}	Proportion of UV relative to total / %
7.00	57.3	50.4	3.11	5.43
7.25	60.6	53.3	3.29	5.43
7.50	63.6	55.9	3.49	5.49
7.75	66.6	58.5	3.70	5.55
8.00	69.7	61.3	3.79	5.44
8.25	73.2	64.4	3.95	5.40
8.50	76.9	67.6	4.21	5.47

It is clear from the data above that adjustment of the lamp emission current correlates linearly with the total measured irradiance. Additionally, the UV output changes in a similar fashion, with very little change to the overall proportion of this wavelength band.

A relatively small variation in irradiance was accessible at a single electrode location, due to the unstable behaviour of the lamp below emission currents of approximately 6.75 A. In fact the achievable range of intensities was less than that initially present across the area of the sample area when held at a fixed emission current. The intensity relationship must however be known for the whole range of intensities present across the beam footprint. The existing spatial non-uniformity was therefore utilised to cover a wider intensity range. In this approach, and for

subsequent photocurrent normalisation, the relative content of UV radiation must be known across the beam area. Additionally it is required that the level of intensity variation in response to changes in emission current be known for the different areas of the beam. A number of irradiance measurements were performed across the beam area, at several different different lamp emission current values. (Figure 3.4)

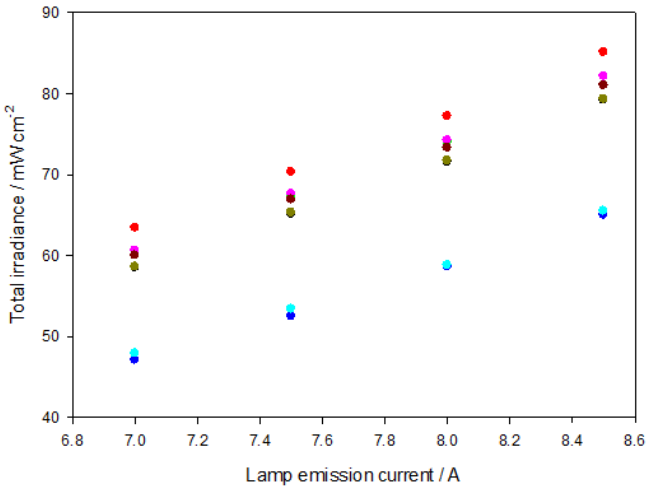

Figure 3.4. The effect of lamp emission current on the total measured irradiance at a variety of locations within the foot print of a 150 W Xe arc lamp.

The intensity was found to vary in a largely homogenous manner upon alteration of the lamp emission current at all locations across the sample area. The average increase in intensity per 0.5 A increase in emission current was found to be 6.46 mW cm^{-2} with an error of +/- 0.81 mW cm^{-2}.

Although the proportional UV content was found to be similar with emission current changes (Table 3.1), it was necessary to determine if this was the case at different locations across the beam. Figure 3.5 shows the relationship between the total irradiance and that measured with the filter ($\lambda \geq 400$ nm) for a range of different intensities acquired at both different areas of the sample area as well as measurement at different lamp emission currents.

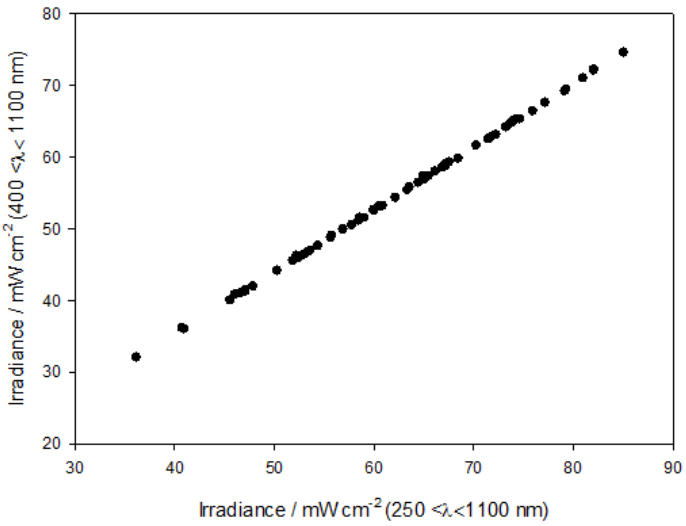

Figure 3.5. The relationship between the total measured irradiance and that recorded with the filter whereby wavelengths of 400 nm and above are transmitted.

A linear relationship existed between the two measurements, and it was clear that the proportional content of UV did not change appreciably. The average percentage contribution of UV relative to the total measured was found to be 5.62 %, with an error of +/- 0.22 %. This level of error would create a variation in intensity of only approximately 0.19 mW cm^{-2} at the highest measured irradiances, which has a negligible impact on the photocurrent over the range of intensities studied.

In light of the measurements above it was determined that the intensity changed in a similar way in response to emission current variation across the entire array. Additionally, changes in intensity brought about by either emission current variation or spatial non-uniformity had no significant impact on the proportional contribution of UV wavelengths to the overall irradiance. It is therefore assumed that any spectral changes to the illumination as the intensity changes are unlikely to have a significant effect on the photoelectrochemical data.

For an accurate assessment of the photocurrent – intensity trend it is necessary to measure the intensity of the whole beam area. Subsequently the photocurrent must be recorded either by translating a single electrode across the beam area or simultaneously recording the photocurrent across an array of identical electrodes.

3.2. Lamp Irradiance Mapping

In order to correct for irradiance non-uniformity, the irradiance at each electrode must be utilised together with a pre –determined relationship between irradiance and photocurrent. The manufacturer's specification stated that the lamp was capable of producing a beam of uniform intensity to +/- 10 %. This was found to be the case only where a relatively small beam diameter was employed. This was not suitable for the measurements carried out in this work, since only a small portion of the 100 electrode array could be illuminated simultaneously. Conversely, the uniformity of the lamp was found to be very poor in the case where all 100 electrodes were illuminated. The non –uniformity of a given lamp can be quantified by measuring the irradiance across the beam footprint and substituting the appropriate values into Equation 3.2.

(3.2) $$Spatial\ non-uniformity\ (\%) = \left(\frac{I_{max}-I_{min}}{I_{max}+I_{min}}\right) \times 100$$

Whereby I_{max} and I_{min} represent the maximum and minimum irradiances measured respectively.

Initially the measurements were carried out using a Si photodiode detector in conjunction with a hand held radiometer. The detector was fixed to a custom made manually actuated x – y stage. The assembly was then fixed to the optical bench in the same location as the sample, with the detector aligned to the same height as where the sample face would sit. The detector height represents an important parameter, since the irradiance exhibits a dependence on the detector-source distance.

The detector was then translated across a 19 x 19 area to match that of the sample such that an irradiance measurement could be taken at each electrode location. Figure 3.6 shows measurements recorded in this manner with a constant lamp emission current of 8.5 A. The non-uniformity of the measured irradiance is immediately apparent.

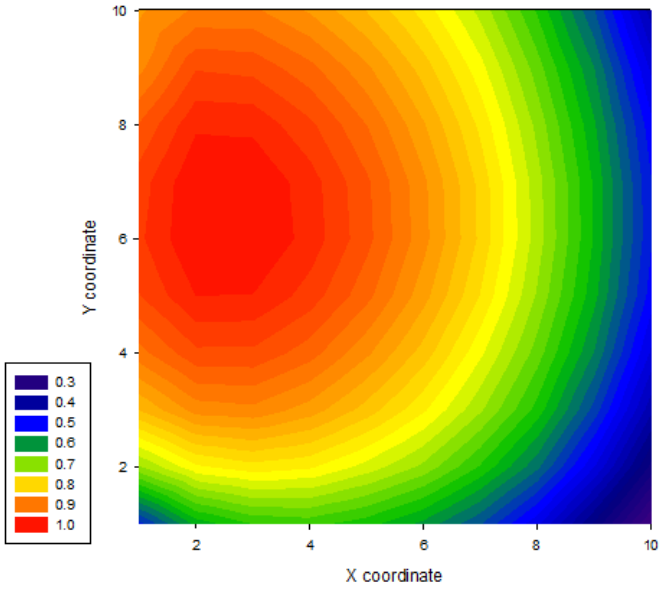

Figure 3.6. Contour diagram to show the relative intensity across the beam footprint relative to the most intense region. Coordinates refer to the equivalent location of the different electrodes on the sample array. Measurements were carried out at a distance of 13.5 cm from the lamp output. The condenser lens was placed fully back towards the lamp to produce the largest beam size possible.

The irradiance distribution shows the characteristic form expected for a lamp of this type. The figure effectively shows an image of the lamps arc, with a region of high intensity close to the cathode. The irradiance then subsequently decreases when moving along either the x or y axis from the hotspot at the cathode.

It is also apparent that the level of non-uniformity is generally higher along the x axis when compared with the y direction. The irradiance profiles for several rows and columns across the x and y directions respectively are shown in Figure 3.7.

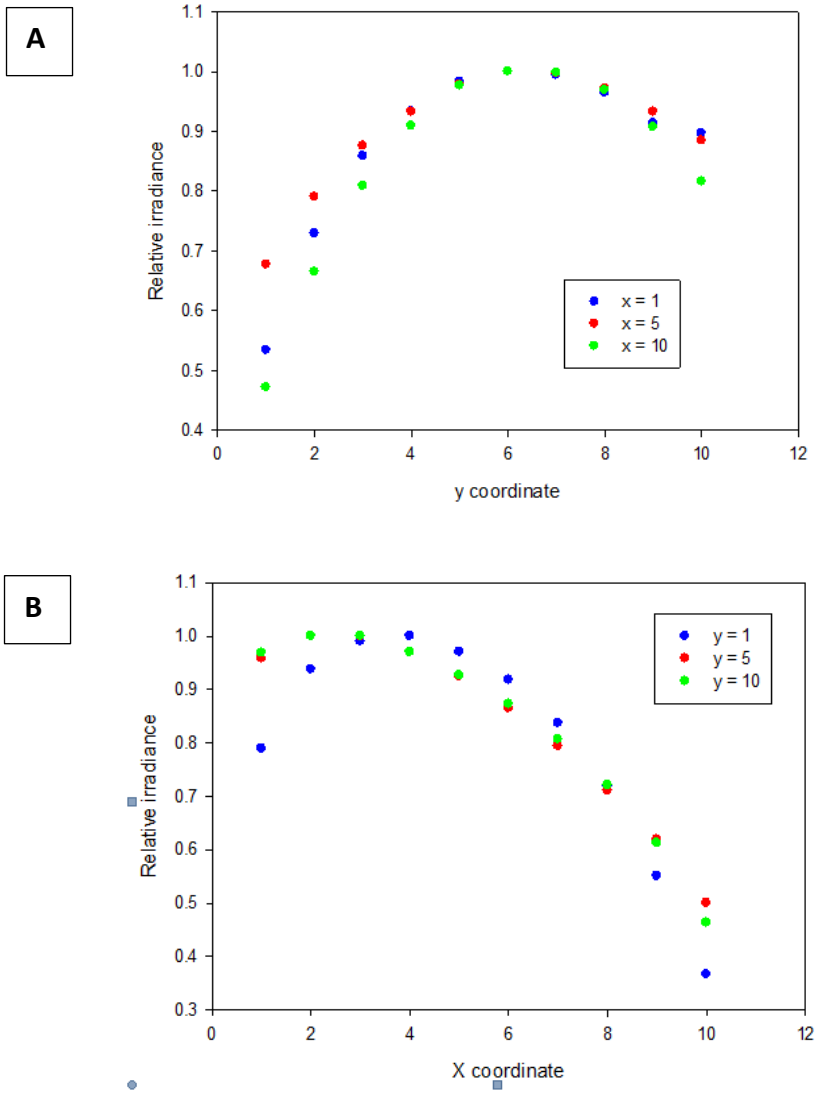

Figure 3.7. Relative intensities with respect to the highest recorded value across a number of rows/columns in the y (A) and x (B) directions as depicted in Figure 3.6.

It can be determined that the level of uniformity is poor in both the x and y axis across the sample area. An image of the lamps arc is produced when the condenser is placed towards the lamp housing, although this effect is lessened when the condenser lens is moved further away. Movement of the condenser lens produces two additional effects. The first is that the overall irradiance level is decreased. This is undesirable, since the lower irradiance values generate lower photocurrents that are more susceptible to noise. This is particularly problematic with the Fe_2O_3 samples which produced very low photocurrents even at the comparatively higher irradiance

levels. Secondly, the beam diameter decreases markedly thus allowing simultaneous illumination of a much lower proportion of the electrodes on the array.

Although it is possible to correct for intensity variation, any errors associated with the intensity measurement and the intensity vs. photocurrent relationship are multiplied when a larger level of correction must be applied. As a result, a compromise had to be made between the proportion of illuminated electrodes and the level of intensity uniformity. Both the position of the condenser lens as well as the height of the lamp output with respect to the detector/array was adjusted to achieve this. The irradiance profile of the optimised setup is presented in Figure 3.8.

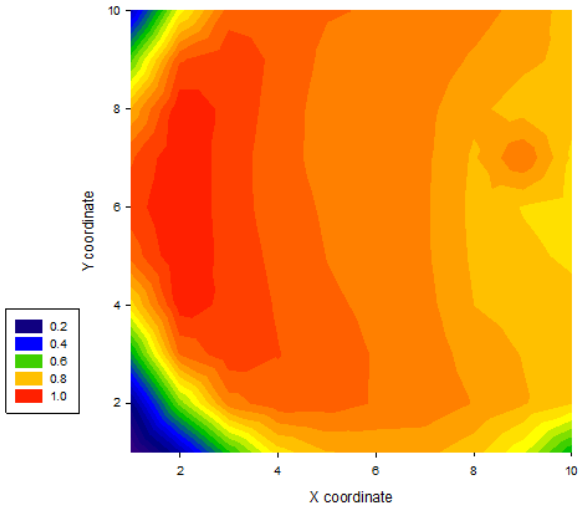

Figure 3.8. Contour diagram to show the relative intensity across the beam footprint relative to the most intense region. Coordinates refer to the equivalent location of the different electrodes on the sample array. Measurements were carried out at a distance of 10.5 cm from the lamp output. The condenser lens was placed in an intermediate location such that the beam diameter was approximately 2.5 cm.

Although a level of non-uniformity still exists, this was generally greatly improved across both the x and y directions. Additionally, due to the smaller size of the beam at this point, some locations at which the detector/electrodes are placed are not fully illuminated and require removal from any subsequent analysis. Due to this restriction in beam size, the overall non-uniformity in the first two columns in the y direction is slightly increased. All others however show a level of improvement. This is apparent from the comparison in Figure 3.9. Since some electrodes were removed in the first two rows, only rows in which all available electrodes were used are shown.

A

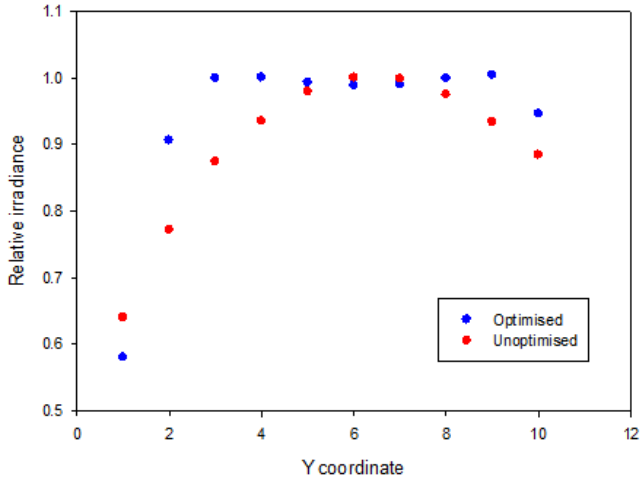

B

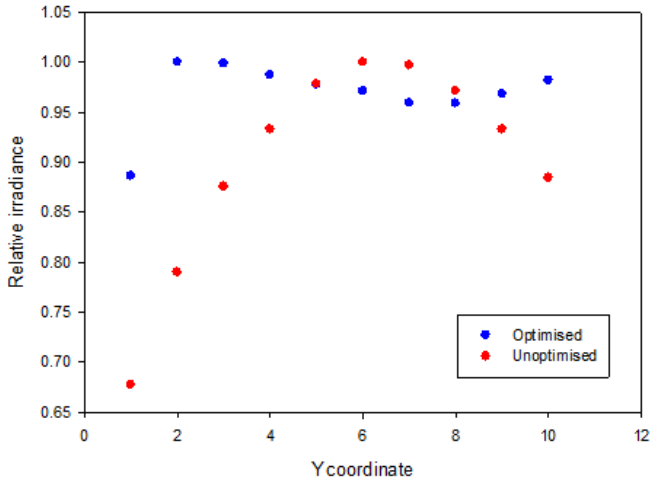

C

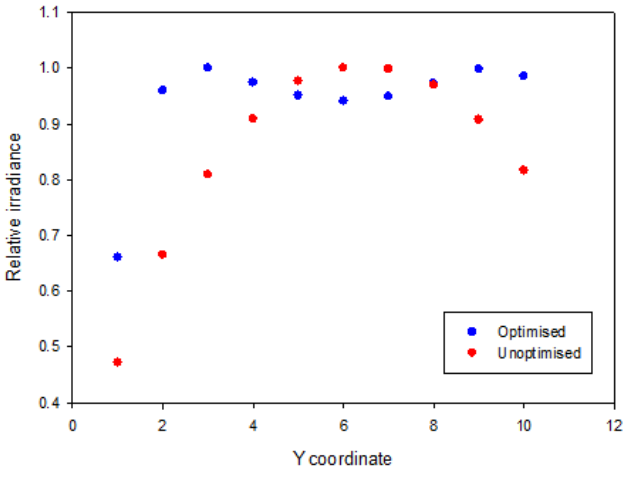

Figure 3.9. Relative irradiance measurements (with respect to the highest recorded value at each row) across the y direction of the beam area. The figures represent the intensity profile at x = 3 (A), x = 5 (B) and x = 10 (C).

With the optimised lamp setup, the average level of non-uniformity across the y direction was 11.23 %. This represents a marked improvement on the initial irradiance profile, whereby the average irradiance non-uniformity across the y direction was 23.76 %. The irradiance was once again found to be slightly more uniform over the y direction; therefore all samples were positioned such that any variations in material characteristics (i.e. particle size or film thickness) were positioned across this direction.

In order to derive the relationship between photocurrent and irradiance, the photocurrent was measured at an array of identically prepared TiO_2 or Fe_2O_3 electrodes. The emission current was also altered, such that the relationship could be determined beyond the range of intensities present across the sample area. Figure 3.10 shows that the photocurrent is extremely sensitive to the illumination intensity, and obeys a very similar trend to that seen in the intensity distribution. The trends did not however show the exact same spatial dependence. It was found that the intensity measurements lacked the spatial resolution to accurately determine the intensity distribution. Attempts to use an automated positioning stage to move the detector also proved largely unsuccessful.

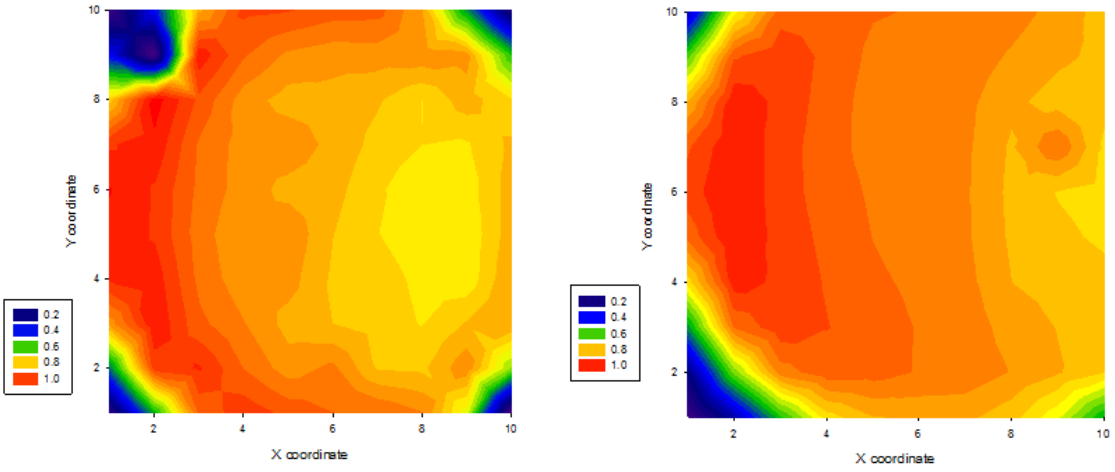

Figure 3.10. Photocurrent density at 1 V vs. RHE (left) (mA cm^{-2}) and relative irradiance with respect to the highest measured value (right) as a function of array position.

Consequently, this approach was found to be inadequate with regard to normalisation of photocurrent. Subsequently, the intensity was measured at a single location and the intensity at each electrode location was calculated from the relative photocurrent response on a uniform TiO_2/Fe_2O_3 film in addition to the previously determined photocurrent vs. intensity relationship.

The photocurrent response of the calibration sample was found to be in excellent agreement with the relative values across rows of the same particle size (Figure 3.11)

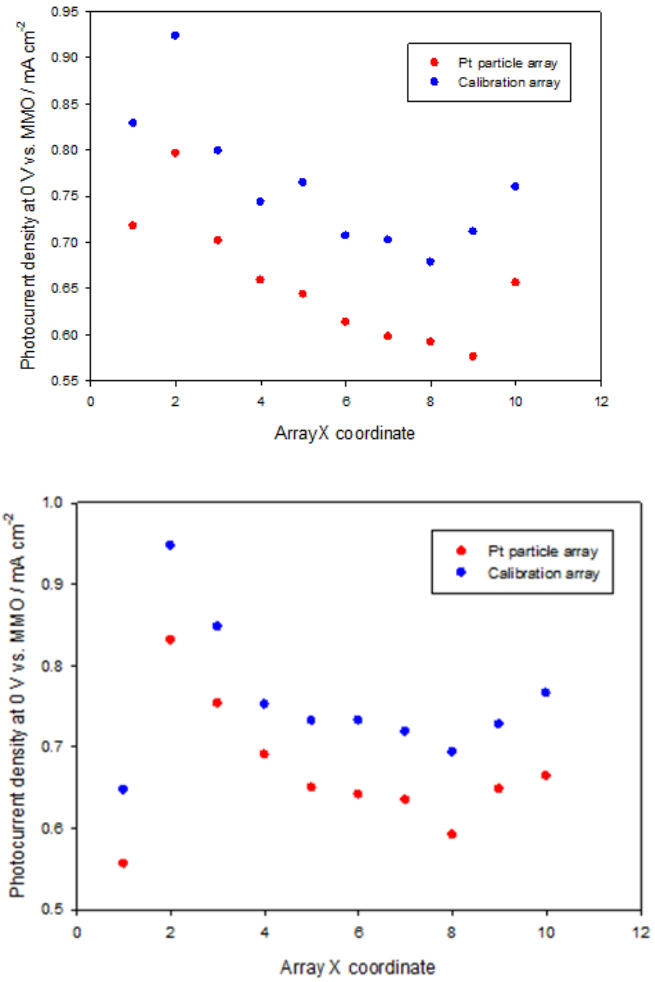

Figure 3.11. Geometric photocurrent densities going across rows of the same particle size at 0 V vs. MMO (1.03 V vs. RHE) (A = 4.40 nm, B = 2.40 nm). The photocurrent densities of the uniform TiO_2 calibration sample at equivalent array locations are also shown. Note that the photocurrents of the two samples are offset by 0.08 mA cm^{-2} for clarity.

In all cases, the photocurrents faithfully tracked the relative values recorded on the calibration sample. As a result an effective correction for spatial non-uniformity could be carried out. The same indirect measurement of intensity (by measurement of the photocurrent on a uniform array) was carried out immediately before all sample measurements. Any drift in the lamps characteristics could therefore be accounted for in the end normalisation process. Any drift was however relatively minor, as can be seen by the photocurrent response of identical uniform TiO_2

arrays presented below. In this case measurements were performed over a period of two months, whereby the photocurrent (which is directly linked to illumination intensity) was measured under illumination at a lamp emission current of 8.5 A.

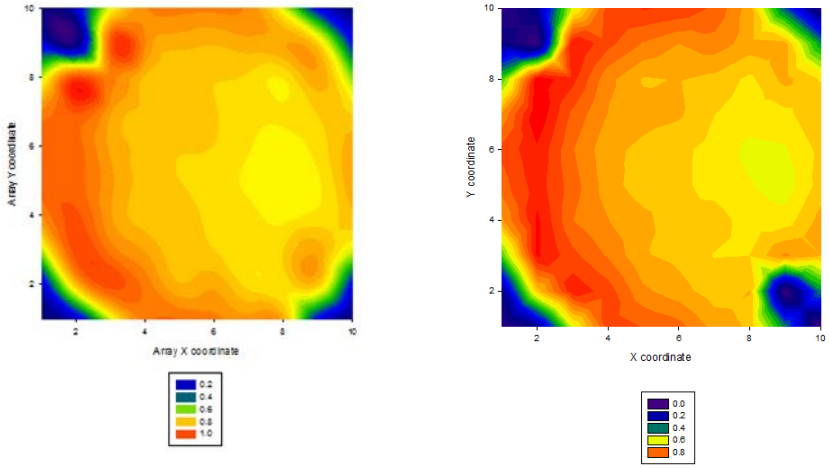

Figure 3.12. Geometric photocurrent density at 1 V vs. RHE of uniform arrays of anatase TiO_2. Data was collected from the first positive going sweep of CVs recorded at 50 mV s^{-1} in Ar purged 0.5 M NaOH. The measurements shown were conducted under identical conditions but two months apart.

3.3. Photocurrent Correction

The correction of the photocurrent requires knowledge of both the relative intensities at the different electrode locations and the relationship of intensity against photocurrent. In the case of a combinatorial library, it is clearly possible that the variation in material characteristics may change the relationship of intensity vs. photocurrent. As a result, it was necessary to first investigate the behaviour of each particle size/film thickness in response to changes in illumination intensity. In the case of the supported nanoparticle samples, changes in intensity appeared to affect each electrode in the same manner, thus simplifying the correction process considerably (Figure 3.13). In this instance the electrodes were normalised by the multiplication of the photocurrent by a normalisation factor calculated for each electrode location. The normalisation factor in this case was simply calculated from the relative photocurrent responses across the calibration array (Uniform anatase TiO_2 or α-Fe_2O_3. Therefore the normalisation factor for a given array location ($N_{X,Y}$) was calculated by dividing the response at the intensity to which

the electrode was being normalised (electrode location (5,5) on the screening array: $j_{ph}^{5,5}$) by that at the location to be normalised ($j_{ph}^{X,Y}$):

(3.4.) $$N_{X,Y} = \frac{j_{ph}^{5,5}}{j_{ph}^{X,Y}}$$

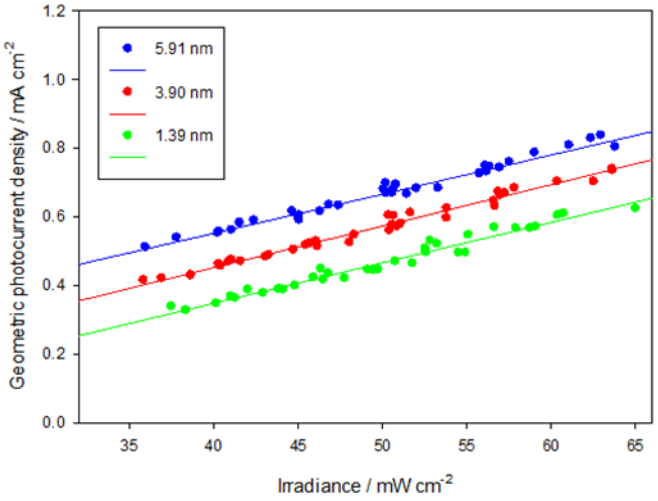

Figure 3.13. The relationship between photocurrent and irradiance at various Pt particle sizes on TiO_2. Measurements represent the photocurrent density at 1.03 V vs. RHE, whereby all measurements were collected with a potential scan rate of 50 mV s^{-1}. Data is shown from the second anodic sweep in each case and each dataset is offset by 0.1 mA cm^{-2} for clarity.

An identical approach was used to that described above for the correction process relating to Fe_2O_3 supported nanoparticles. The level of correction in required in this case however was much smaller. Due to the slow kinetics at the Fe_2O_3 surface, the rate of reaction was primarily dominated by this factor and therefore variation in intensity had very little effect. Figure 3.14 shows illuminated CV measurements of Fe_2O_3 supported Pt nanoparticles across a row of the same particle size (d ~ 5.86 nm) The correction approach described above is however only applicable to situations in which all electrodes on the array exhibit the same relative dependence on illumination intensity, i.e. the gradient of the photocurrent vs. intensity relationship must remain the same.

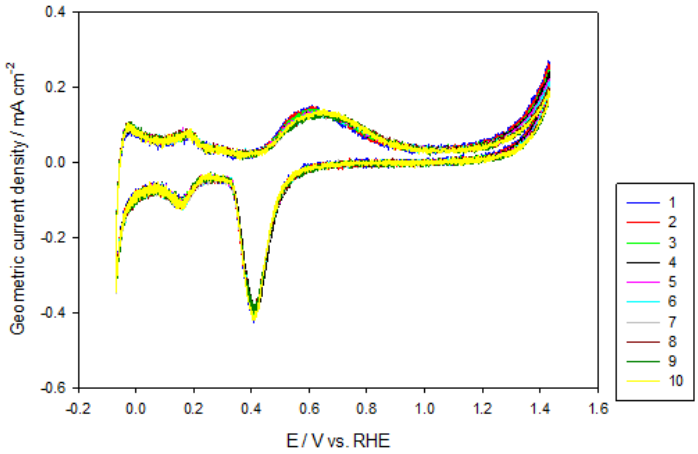

Figure 3.14. Illuminated CVs of α-Fe_2O_3 supported Pt particles (d ~ 5.86 nm) going across the x – direction on the screening array, i.e. a row of constant particle size. Data was collected in 0.5 M NaOH with a scan rate of 50 mV^{-1}. The support material was approximately 156 nm thick, and was deposited on an Au screening array. The first cycles are shown

The photocurrent intensity gradient however was found to change with TiO_2 film thickness (see Chapter 5). In this case, an additional sensitivity factor was required in order to correct to a given intensity. In this approach the normalisation factor was initially calculated in the manner described above. This was subsequently multiplied by the sensitivity factor calculated from the gradient of the intensity vs. photocurrent relationship relative to that of the uniform TiO_2 calibration sample. In this case, the inclusion of the sensitivity factor did not change the overall trends significantly, although it may increase the absolute level of accuracy in the results. The correction procedure was relatively effective, and rows of the same particle size showed close agreement after the normalisation process. This is in spite of the typically larger level of non-uniformity present across rows of the same particle size. The result of the correction process at TiO_2 supported Pt nanoparticles can be seen in Figure 3.15. Both the uncorrected and corrected photocurrent densities are shown across a row of the same particle size on an array of TiO_2 supported Pt nanoparticles.

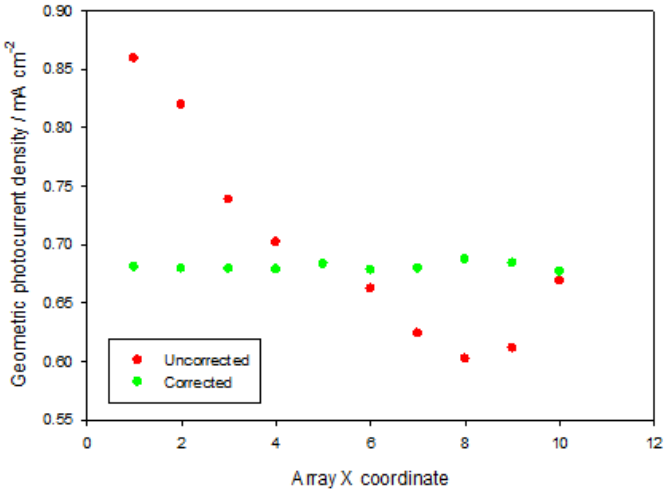

Figure 3.15. Uncorrected (red) and corrected (green) geometric photocurrent density at 1.03 V vs.MMO as a function of array position. In this case the electrodes were normalised to the 5th electrode in the row.

In all corrected photocurrent measurements presented, the electrodes were normalised to the intensity at electrode location (5,5) on the electrochemical screening array. The intensity of this location was measured as 65 mW cm^{-2} +/- 10 mW cm^{-2}. The behaviour of the lamp was stable and repeatable, however the relatively large error stems primarily from the poor spatial resolution of the detector used for irradiance measurements.

3.4. Illuminated Open Circuit Potential Measurements

The measurement of the illuminated open circuit potential was performed in the manner described in the Experimental Chapter. The measurement serves as indication of the quasi-Fermi level of the majority charge carriers under illumination. As a result, the measurements may give information on the relative levels of photovoltage generation in the materials to be screened. The measurement may also indicate the flat band potential of a material, although this is only the case where the measurements reach a limiting plateau against light intensity. This was not the case within this work, and therefore it is apparent that a significant degree of recombination occurs in the materials investigated herein.

The open circuit potential under illumination has a greatly reduced dependence on light intensity. Whereas a linear dependence is observed between photocurrent and intensity, the relationship between the OCP and intensity is logarithmic.[211] This can be observed in the Figure below, where the illuminated OCP and the photocurrent at 1.03 V vs. RHE are shown for a plain anatase TiO_2 array.

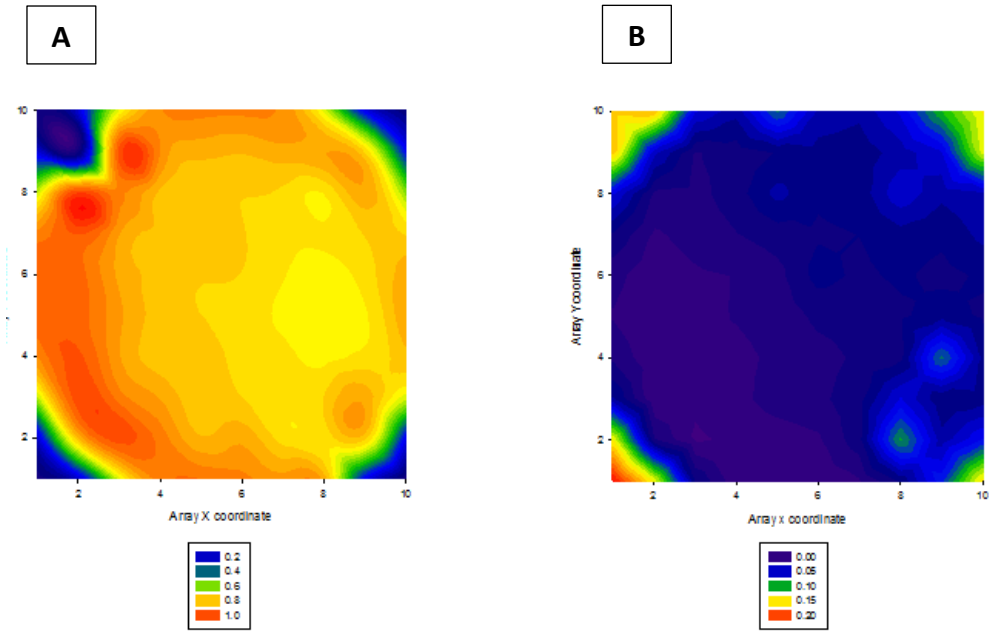

Figure 3.16. Geometric photocurrent density (A) at 1.03 V vs. RHE and the illuminated OCP (B) of a uniform TiO_2 film as a function of array position. Note that in Figure 3.13(B) the electrodes at locations (8,2) and (9,4) did not make electrical contact to the potentiostat.

In general it can be seen that the OCP values are in relatively close agreement across the array, aside from the locations at the corners. Additionally, several electrodes where the electrical contact was poor show values significantly different to the surrounding areas. Any such electrodes were always removed from any subsequent analysis. So too were the electrodes at the corners where no illumination or only partial illumination was present.

In this instance the average values recorded across each row (equivalent to rows of same particle size on the nanoparticle samples) showed extremely good agreement. It was therefore possible to determine relative trends without the need for a correction procedure. Any trends generated were much larger than the level of variation across arrays with uniform electrodes.

3.5. Sample Preparation Considerations

In order to meaningfully assess photoelectrode material performance, it is of extreme importance that the candidate material is prepared and screened in a way that allows analysis only of the intended electrode surface. It is therefore important to remove or minimise any contributions of the surrounding environment. In the case of this work, considerable effort was taken to ensure that only the surface of the electrode itself contacted the electrolyte rather than the substrate. This was particularly challenging due to the effects that the synthesis conditions had on the level of substrate exposure.

Of particular importance in this work, was the stability of the screening arrays to the synthesis process as well as constraining the active surface area to only that of the deposited film. The latter proved particularly challenging due to the exposure of the substrate material upon employing a post annealing approach in the material synthesis. Such an approach was generally required in order to produce highly crystalline films. As described in Chapter 6, arrays were heated to 450 ^{o}C (at a rate of 5 ^{o}C min^{-1}) where a post annealing method was used. Whilst no evidence for substrate exposure was observed before annealing, the films essentially showed electrochemical behaviour analogous to the polycrystalline Au substrate after annealing. Initially it was not clear whether this resulted from damage to the substrate that resulted in exposure of the Au tracks. .

The stability of the screening arrays towards heat treatment also varied slightly between different array batches. In order to check whether the exposure of substrate material occurred by damage to the arrays or cracks in the film, deposition was carried out onto the arrays with a larger mask. In this instance, deposition was carried out on the entire array, excluding the contact pads around the edge of the sample. Note that the area of exposed array without the TiO_2 film was sealed off from the electrolyte during measurements by the rubber gasket explained in Chapter 2.

The voltammetry in this instance appeared identical to the polycrystalline Au substrate (albeit with smaller current densities), which dominated the response. The same was true of the supported nanoparticle samples prepared in a similar way. An example response at a Pt/TiO_2 electrode prepared in this way is shown in Figure 3.17. As such it is likely that cracks in the film contribute at least in part to the occurrence of substrate exposure to the electrolyte. Such exposure of the substrate drastically affected the electrochemical/photoelectrochemical data obtained. In many cases, no photoactivity was observed at all, most likely due to the exposed

substrate behaving in a way analogous to surface states. The area of Au exposed also appeared to vary in a random nature, which rendered the correction process impossible. This was simply due to the inability to accurately determine the level of substrate exposure as well as systematically study the effect of this on the photoelectrochemical response. Additionally it was not possible to ascertain whether photocurrent variation across the array was a result of intensity variation or a variation in the level of Au exposure. Furthermore, the efficiency of the ORR on Au in alkaline media also affected the electrochemical data adversely. Calculation of the electrochemically active surface area was also very difficult in such cases. Once again however the behaviour varied to some degree between different array batches.

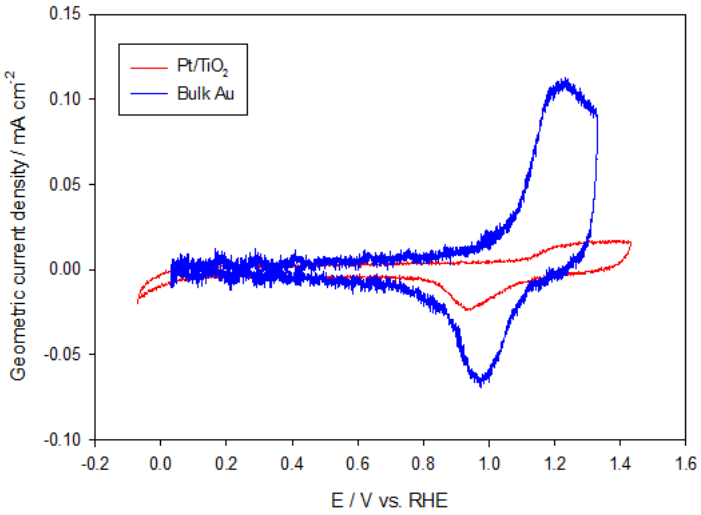

Figure 3.17. Cyclic voltammogram of an anatase TiO_2 supported Pt nanoparticle (mean Pt diameter 1.39 nm) electrode prepared by a post annealing method. Also shown is the voltammetry of an Au electrode on a blank Au screening array. Measurements were conducted in 0.5 M NaOH with a potential scan rate of 50 mV s^{-1}. The first cycles are shown.

Typically where any photoactivity was observed, the open circuit potential measurements were significantly positive of those prepared without post annealing. Additionally the presence of oxygen in solution had an effect on the photocurrent below the potential at which the ORR occurred on Au. This was particularly important in the results discussed herein, whereby the reduction in photocurrent by O_2 reduction obscured any trends in the region of primary interest. On limited occasions, the general trend of the OCP remained, albeit shifted significantly positive, as shown in Figure 3.18. The majority of the time very little change in the OCP occurred under illumination, and showed a limited dependence on Pt particle size (on samples prepared with post annealing).

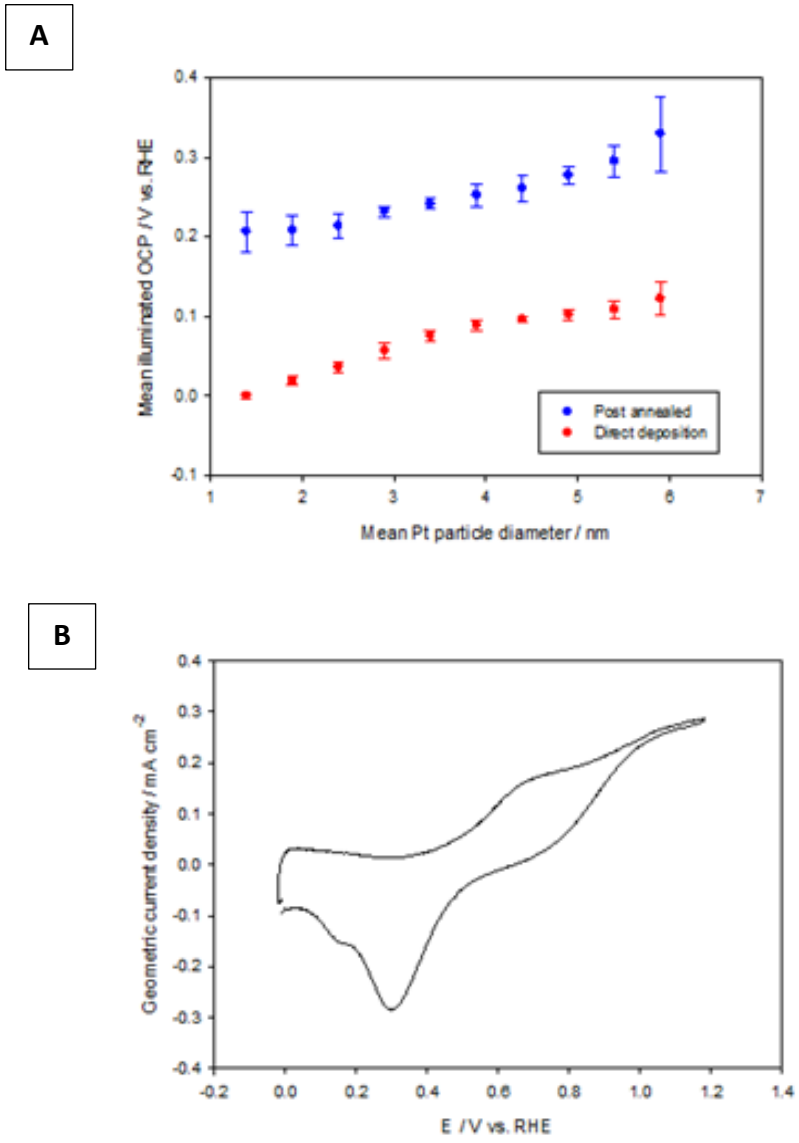

Figure 3.18. Comparison of the illuminated open circuit potential between arrays where anatase was directly deposited and where it was formed via post annealing (A). Also shown (B) is an illuminated CV (first cycle) of a Pt/TiO_2 electrode (Post annealed) with an estimated Pt particle diameter of 5.91 nm. Measurements were conducted in 0.5 M NaOH and a scan rate of 50 mV s^{-1} was used.

It was particularly evident that where the Au substrate was exposed, the photocurrent was markedly decreased at potentials below the ORR onset on Au (approximately 0.9 V). With the above in mind, it was clear that the method relied upon forming the oxides of interest without post annealing.

Throughout the attempts using post annealing, the need for an array which could withstand higher temperatures was identified. A new ITO screening array was developed within the University research group towards this aim. All of the fabrication processes were carried out by Dr. Jin Yao.

ITO was chosen due to its good conductivity, high temperature stability and relatively inert electrochemical response relative to Au. Furthermore it is known to be compatible with the metal oxide materials synthesised in this work as well as those synthesised for other ongoing projects in the research group. The fabrication methods are identical to those used in the Au screening chip, although the materials vary. ITO forms the electrode pads as well as the interconnects and contact pads. Instead of SiN (as on the Au screening arrays), SiO_2 was used as the capping layer. Currently work is still ongoing on the development of these chips. However, at the time of writing this thesis, they have been shown to be stable up to temperatures of 600 ^{o}C.

4. Electrochemistry of the Substrate Materials

The purpose of this Chapter is to briefly summarise the electrochemical responses of the substrate materials. The aim is to facilitate comparison with the responses obtained on the supported nanoparticle samples, such that any contribution to the voltammetry can be identified.

4.1. Electrochemical Response of Anatase TiO_2

The voltammetry of anatase TiO_2 deposited on both ITO and Au substrates is shown in Figure 4.1. Measurements in both cases were performed in Ar purged 0.5 M NaOH at a scan rate of 50 mV s^{-1}.

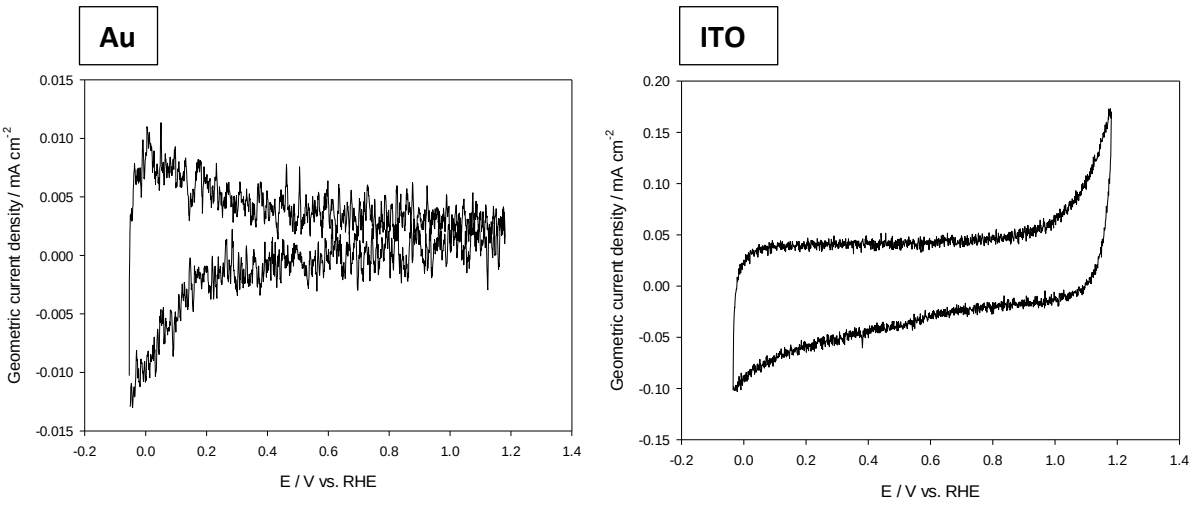

Figure 4.1. CVs of anatase TiO_2 (Film thickness ~250 nm) in Ar purged 0.5 M NaOH. A scan rate of 50 mV s^{-1} was used and the 4th cycles are shown (in order to minimise substrate background on the ITO). Measurements are shown for films deposited on both Au (left) and ITO (right) substrates.

In general the voltammetry was relatively featureless. A small reduction and oxidation current can however be observed below approximately 0.2 V. This is consistent with previous studies and relates the formation and oxidation of Ti^{3+}.[212] The current densities are extremely small on samples prepared on Au substrates, and hence the data appears relatively noisy. The current densities on the ITO substrate are much larger, which was found to be the case when comparing all samples deposited on Au and ITO substrates. Additionally, an anodic peak positive of c.a. 1 V is

present on the ITO sample. This was found to arise from an oxidation process at the ITO substrate (Section 4.3.). Samples on both substrates showed some activity towards oxygen reduction, which was similar between the different substrates. The onset potential was however significantly negative of all Pt particle sizes, with an onset potential of approximately 0.1 V vs. RHE.

4.2. Electrochemical Response of α-Fe_2O_3

CVs of approximately 150 nm thick α-Fe_2O_3 films are shown in Figure 4.2. The measurements were carried out in Ar purged 0.5 M NaOH at a scan rate of 50 mV s^{-1}.

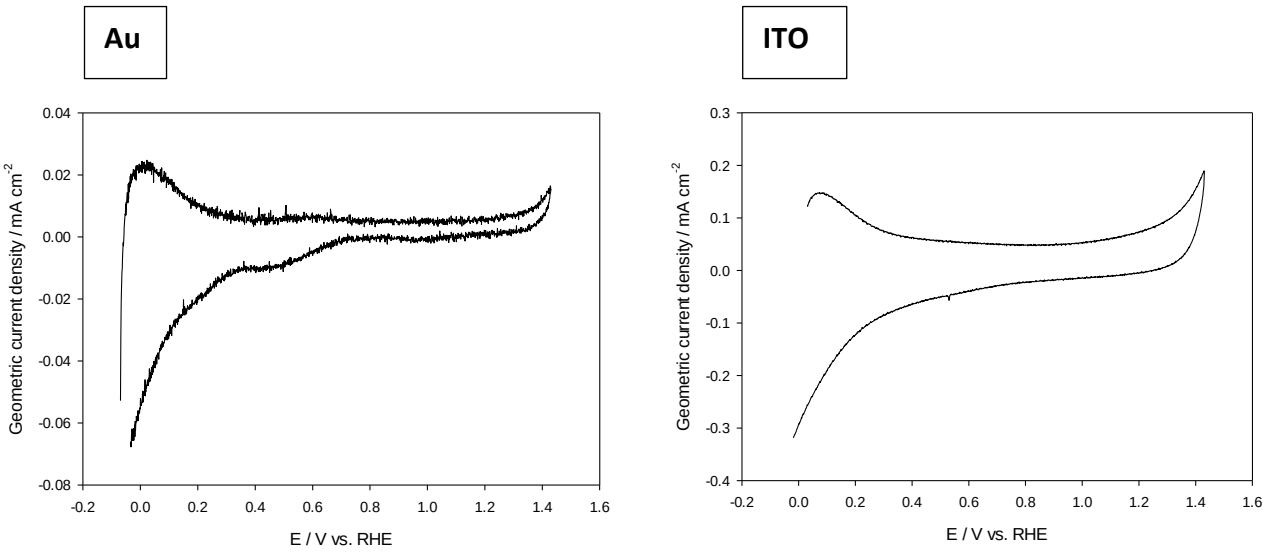

Figure 4.2. CVs of α-Fe_2O_3 (Film thickness ~150 nm) in Ar purged 0.5 M NaOH. A scan rate of 50 mV s^{-1} was used and the 4th cycles are shown (in order to minimise substrate background on the ITO). Measurements are shown for films deposited on both Au (left) and ITO (right) substrates.

A similar reduction and oxidation current appears on both substrate types below approximately 0.2 V. This may be attributed to the interconversion of Fe^{2+} and Fe^{3+}. The slight cathodic peak on the Au sample is unknown. However it has been shown on TiO_2 that features can emerge in the voltammetry due to the filling and emptying of surface states caused by grain boundaries.[213]. Once again, the current densities on the ITO film are much larger. Oxygen reduction also occurred on both samples , although the onset was more positive on the ITO samples. In both cases however, the onset potential was not significantly negative of the smallest Pt particles supported

on Fe_2O_3. The onset potential was shifted negative by only approximately 0.05 V (onset potential of ~ 0.5 V on an Au substrate) relative to the smallest Pt particle diameter.

4.3. Electrochemical Response of ITO

The ITO substrate showed a prominent oxidation peak in the voltammetry, which is shown in the CVs below. The peak begins at approximately 0.8 V on the first cycle and decreases in size with increasing cycle number. The process is most likely to arise from the oxidation of the film, presumably through Sn dissolution. The large charge associated with the process (~ 0.02 mC) would suggest that it is unlikely that the oxidation stems from oxygen vacancies or is solely limited to the surface of the electrode.

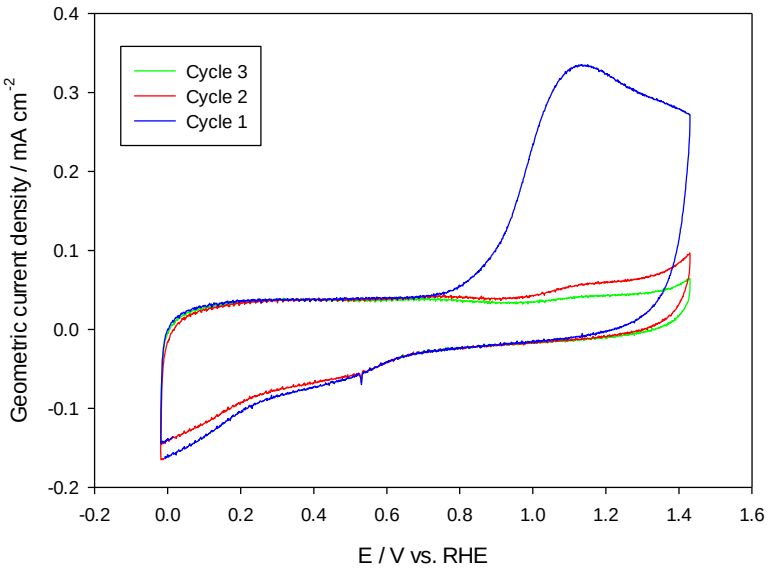

Figure 4.3. Cyclic voltammograms of a blank ITO substrate in Ar purged 0.5 M NaOH. A scan rate of 50 mV s^{-1} was used and the first three cycles are shown.

In addition to the oxidation peak, the ITO substrate showed some level of oxygen reduction at potentials negative of approximately 0.6 V (Figure 4.3)

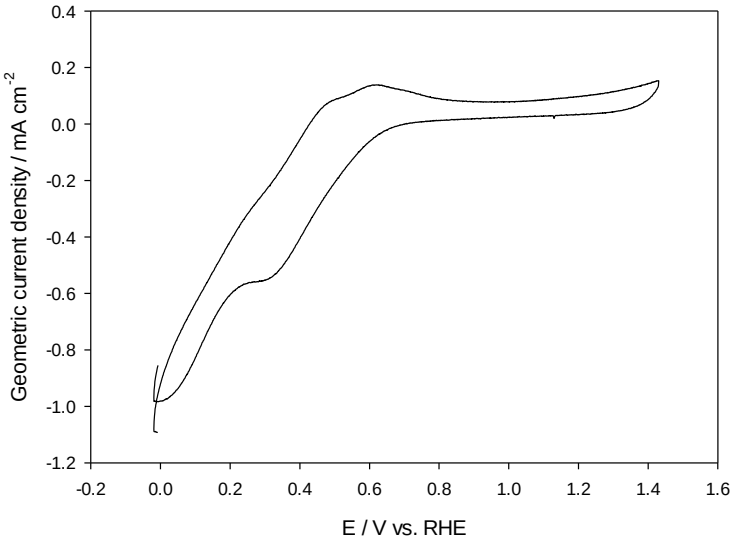

Figure 4.4. Cyclic voltammograms of a blank ITO substrate in O_2 saturated 0.5 M NaOH. A scan rate of 50 mV s^{-1} was used and the first cycle is shown.

4.4. Electrochemical Response of Polycrystalline Au

The polycrystalline Au substrate material showed the characteristic features expected of this material in alkaline media.[214] Positive of approximately 1.3 V, the formation of Au oxide begins to occur, which is subsequently stripped from the surface from approximately 1.2 V on the reverse scan.

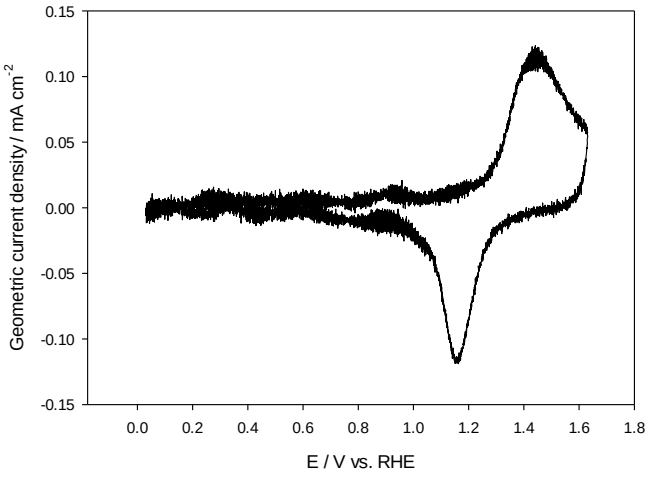

Figure 4.5. Cyclic voltammogram of a bulk polycrystalline Au electrode in Ar purged 0.5 M NaOH. A scan rate of 50 mV s^{-1} was used and data is shown for the first cycle.

The reduction of oxygen occurred at potentials negative of approximately 0.9 V, with the reaction becoming diffusion limited at approximately 0.85 V.

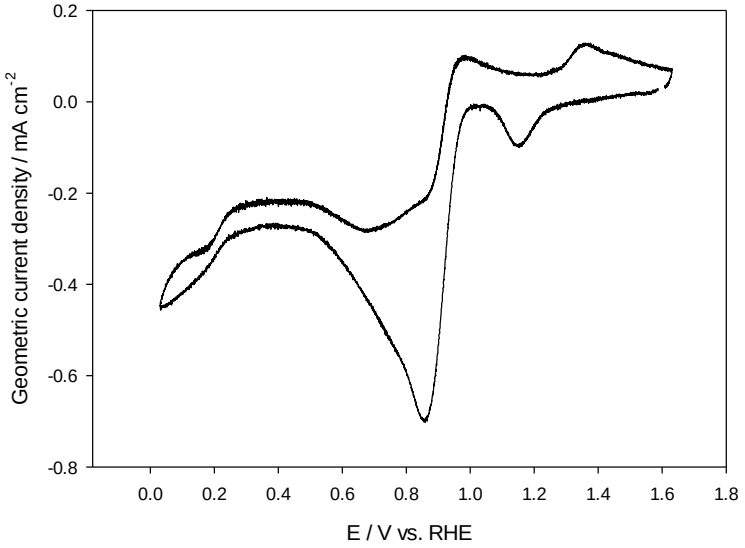

Figure 4.6. Cyclic voltammograms of a blank polycrystalline Au substrate in O_2 saturated 0.5 M NaOH. A scan rate of 50 mV s^{-1} was used and the first cycle is shown.

5. TiO_2 Thickness Effects

5.1. Introduction

The thickness of a photoelectrode material is of significant importance in determining its overall photoelectrochemical characteristics. In particular, the thickness and associated morphology of a material strongly impacts on its ability to generate and transport charge carriers. Furthermore, it is apparent from previous results in the literature that any observed thickness dependence is heavily influenced by the processing conditions and synthesis method employed.[215]

In theory, in the absence of thickness dependant structural/morphological changes, an optimum thickness exists in planar electrodes. This can be rationalised in terms of the hole diffusion length (L_p) and the width of the depletion layer (W) (Figure 5.1).[7]

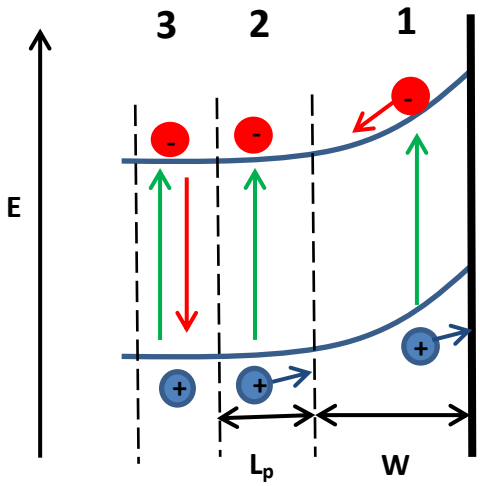

Figure 5.1. Schematic representation of the key regions inside a semiconductor electrode. Region 1 shows the space charge layer where band bending occurs. The electric field in this region separates electrons and holes by driving them towards the bulk and surface respectively. Band bending is absent in region 2, although holes within a short distance (diffusion length, L_p) from the edge of the depletion layer may travel to be separated by the electric field. Charge carriers generated in the region outside of the diffusion length and depletion layer (region 3) will recombine, since there is an absence of driving force for separation and there is a high probability of recombination when charge carriers must travel over a large distance.

Figure 5.1 shows the likely fate of photogenerated charge carriers when generated at different depths in the material. Generally, the space charge region is extremely efficient at separating charge carriers on account of the relatively high strength of electric field, which can typically reach values of 10^5 V cm^{-1}.[82] The depletion layer also typically extends into the semiconductor surface on the order of hundreds of nanometers (although this depends on the nature of the contacting phase, as well as the doping level and surface defect density of the semiconductor)[7] and as such it is generally desirable that the thickness of the photoelectrode should equal or exceed this distance to ensure maximal band bending and charge separation performance . The thickness of the depletion layer is heavily dependent on the doping level of the semiconductor, which is embodied within Equation 5.1:[44]

$$W = \sqrt{\frac{2\,\varepsilon_S V_{sc}}{q\,N_d}} \tag{5.1}$$

Where ε_s is the static dielectric constant of the semiconductor, V_{SC} is the 'built in voltage' (space charge voltage) over the depletion layer, q is the charge on an electron and N_d is the doping density.

It can be deduced from Equation 5.1 that the depletion layer width increases as the dopant density decreases. This is due to the fact that the numbers of free charge carriers will decrease, thus requiring removal of charge from deeper within the semiconductor during the equilibration process. In the case of metal oxide semiconductors, the hole diffusion length is generally small in comparison with the depletion layer width. Typical values for TiO_2 are on the order of tens of nanometers,[216] although this too has been found to vary significantly in response to different synthesis methods and surface treatments.[217] As a result, the maximum profitable film thickness is likely to vary depending on the processing conditions employed during synthesis, since both W and L_p may be altered considerably.

In addition to doping density, the film thickness itself may also alter the magnitude of both V_{SC} and W. In the case of nanocrystalline or very thin films, the dimensions of the film or crystallites may be significantly less than that of the depletion layer expected for a given doping density. Since donor or acceptor impurities are present in only relatively small amounts, the materials are therefore unable to sustain an appreciable internal electric field.[218] The electric field distribution in nanostructured materials has attracted great interest and the maximum potential difference attainable in a spherical semiconductor particle has been previously derived as: [219]

(5.2) $$\Delta\Phi = \frac{kT}{6q}\left(\frac{r_0}{L_D}\right)^2$$

Where q is the electronic charge, r_0 is the radius of the particle and L_D is the Debye length.

As well as influencing charge transport behaviour, the thickness of a material has obvious implications on optical absorption behaviour. As previously noted, the absorption depth (given by 1/α) in indirect band gap semiconductors is significantly higher than that of direct band gaps,[74] with values extending up to hundreds of microns in the former case.[13] With the requirements for charge generation and collection in mind, it is apparent that the optimal film thickness will depend on the magnitudes of W, L_P and 1/α.

Novel approaches to electrode morphology involving nanocrystalline films, nanotubes, and porous electrodes have been applied more recently to achieve a balance between these criteria.[135, 215b, 220] In these instances, the optical absorption and charge transport pathways may be decoupled (Figure 5.2), allowing a long optical path length and a decreased distance over which charge carriers must traverse to the surface.[19] Although band bending is reduced in small nanostructures, holes may easily travel to the surface when the nanostructured features are smaller in size than L_p. Morphological changes may therefore substantially alter any apparent relationship between photoelectrochemical activity and film thickness.

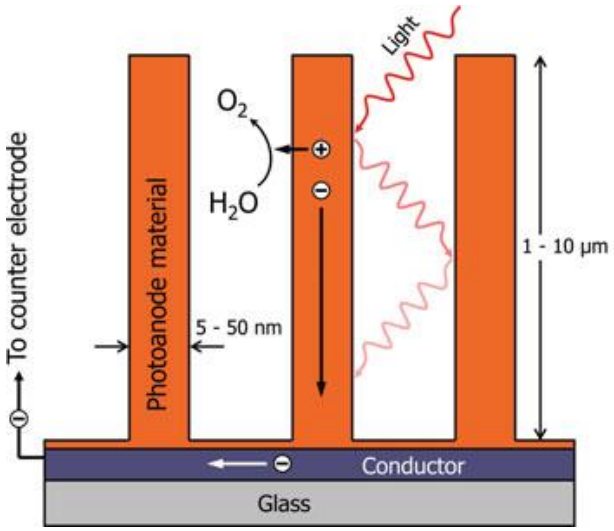

Figure 5.2. Schematic representation of a nanowire array photoanode. The large wire length allows for a significant degree of optical absorption, whereas the thin diameter means photogenerated holes must only travel a maximum of half the wire diameter to reach the surface. Figure taken from ref [19]

5.2. Synthesis of TiO_2 Films with Varying Thickness.

The data presented in this Chapter is derived from a total of 4 samples synthesised on electrochemical screening arrays. The conditions employed in the various experiments and the order in which they were carried out is listed in Tables 5.1 – 5.4. All voltages are expressed vs. RHE.

Table 5.1. #8155 (Au screening array)

Experiments performed	Electrolyte / Illumination
CV x 5 at 50 mV s^{-1} : 0 – 1.4 V	Dark: 0.5 M NaOH
CV x 1 at 50 mV s^{-1} : 0 – 1.4 V	Dark: 0.5 M NaOH + 5mM $K_3[Fe(CN)_6]$
CV x 1 at 50 mV s s^{-1} :0 – 1.6 V	Dark: 0.5 M NaOH + 5mM $K_3[Fe(CN)_6]$
CV x 3 at 50 mV s^{-1} (0 – 1.9 V)	Dark: 0.5 M NaOH + 5mM $K_3[Fe(CN)_6]$
CV x 5 at 50 mV s^{-1} (0 – 1.4 V)	Illuminated (8.5 A lamp emission current): 0.5 M NaOH
CV x 2	Illuminated (8.0 A lamp emission current): 0.5 M NaOH
CV x 2	Illuminated (7.5 A lamp emission current): 0.5 M NaOH
CV x 2	Illuminated (7.0 A lamp emission current): 0.5 M NaOH
OCV measurement x 3	Dark 300s – illuminated 300s (0.5 M NaOH)
OCV measurement x 3	As above with O_2 saturated 0.5 M NaOH
CV x 3 at 50 mV s^{-1} (0 – 1.2 V)	Dark: 0.5 M $HClO_4$ + 10 mM $CuSO_4$
As above at 75 mV s^{-1}	As above
As above at 100 mV s^{-1}	As above
As above at 150 mV s^{-1}	As above

Table 5.2. #8155a (Au screening array)

Experiments performed	Electrolyte / Illumination
CV x 5 at 50 mV s^{-1} : 0 – 1.4 V	Dark: 0.5 M NaOH
CV x 5 at 50 mV s^{-1} (0 – 1.4 V)	Illuminated (8.5 A lamp emission current): 0.5 M NaOH
CV x 2 at 50 mV s^{-1} (0 – 1.4 V)	Illuminated (8.0 A lamp emission current): 0.5 M NaOH

CV x 2 at 50 mV s^{-1} (0 – 1.4 V)	Illuminated (8.0 A lamp emission current): 0.5 M NaOH
CV x 2 at 50 mV s^{-1} (0 – 1.4 V)	Illuminated (7.5 A lamp emission current): 0.5 M NaOH
CV x 2 at 50 mV s^{-1} (0 – 1.4 V)	Illuminated (7.0 A lamp emission current): 0.5 M NaOH
OCV measurement x 3	Dark 300s – illuminated 300s (0.5 M NaOH)
OCV measurement x 3	As above with O_2 saturated 0.5 M NaOH
CV x 3 at 50 mV s^{-1} : 0 – 1.4 V	Dark: 0.5 M NaOH + 5mM $K_3[Fe(CN)_6]$
CV x 3 at 50 mV s^{-1} (0 – 1.2 V)	Dark: 0.5 M $HClO_4$ + 10 mM $CuSO_4$

Table 5.3. #8156 (ITO screening array)

Experiments performed	Electrolyte / Illumination
CV x 5 at 50 mV s^{-1} : 0 – 1.4 V	Dark: 0.5 M NaOH
CV x 5 at 50 mV s^{-1} (0 – 1.4 V)	Illuminated (8.5 A lamp emission current): 0.5 M NaOH
CV x 2 at 50 mV s^{-1} (0 – 1.4 V)	Illuminated (8.0 A lamp emission current): 0.5 M NaOH
CV x 2 at 50 mV s^{-1} (0 – 1.4 V)	Illuminated (7.5 A lamp emission current): 0.5 M NaOH
CV x 2 at 50 mV s^{-1} (0 – 1.4 V)	Illuminated (7.0 A lamp emission current): 0.5 M NaOH
OCV measurement x 3	Dark 300s – illuminated 300s (0.5 M NaOH)
OCV measurement x 3	As above with O_2 saturated 0.5 M NaOH
CV x 3 at 50 mV s^{-1} : 0 – 1.4 V	Dark: 0.5 M NaOH + 5mM $K_3[Fe(CN)_6]$
CV x 3 at 75 mV s^{-1}	Dark: 0.5 M NaOH + 5mM $K_3[Fe(CN)_6]$
CV x 3 at 100 mV s^{-1}	Dark: 0.5 M NaOH + 5mM $K_3[Fe(CN)_6]$
CV x 3 at 125 mV s^{-1}	Dark: 0.5 M NaOH + 5mM $K_3[Fe(CN)_6]$
CV x 3 at 150 mV s^{-1}	Dark: 0.5 M NaOH + 5mM $K_3[Fe(CN)_6]$

Table 5.4. #8156a (ITO screening array)

Experiments performed	Electrolyte / Illumination
CV x 5 at 50 mV s^{-1} : 0 – 1.4 V	Dark: 0.5 M NaOH
CV x 3 at 50 mV s^{-1} : 0 – 1.4 V	Dark: 0.5 M NaOH + 5mM $K_3[Fe(CN)_6]$
CV x 3 at 75 mV s^{-1}	Dark: 0.5 M NaOH + 5mM $K_3[Fe(CN)_6]$

CV x 3 at 100 mV s^{-1}	Dark: 0.5 M NaOH + 5mM $K_3[Fe(CN)_6]$
CV x 3 at 125 mV s^{-1}	Dark: 0.5 M NaOH + 5mM $K_3[Fe(CN)_6]$
CV x 3 at 150 mV s^{-1}	Dark: 0.5 M NaOH + 5mM $K_3[Fe(CN)_6]$
CV x 5 at 50 mV s^{-1} (0 – 1.4 V)	Illuminated (8.5 A lamp emission current): 0.5 M NaOH
CV x 2 at 50 mV s^{-1} (0 – 1.4 V)	Illuminated (8.0 A lamp emission current): 0.5 M NaOH
CV x 2 at 50 mV s^{-1} (0 – 1.4 V)	Illuminated (7.5 A lamp emission current): 0.5 M NaOH
CV x 2 at 50 mV s^{-1} (0 – 1.4 V)	Illuminated (7.0 A lamp emission current): 0.5 M NaOH
OCV measurement x 3	Dark 300s – illuminated 300s (0.5 M NaOH)
OCV measurement x 3	As above with O_2 saturated 0.5 M NaOH

A number of different thicknesses of anatase TiO_2 film were prepared on the screening arrays by use of a moving shutter located close to the sample face. In a similar manner to Pt particle deposition, the shutter position was altered stepwise during deposition to selectively uncover the electrode rows at different times during the synthesis. The resulting varied deposition times imposed at each electrode row allowed for creation of films with 10 different thicknesses ranging from approximately 24 – 260 nm.

The same approach to thickness calibration was used as that described in Chapter 2. Prior to deposition on the electrochemical arrays, a sample of varying TiO_2 thickness was prepared identically on a SiO_2 glass substrate. The films were also prepared under identical conditions to those used for the support layer depositions for the TiO_2 supported Pt particle samples (See Chapter 6 for more detailed TiO_2 characterisation). The thicknesses as measured by AFM at each row are presented in Figure 5.3. The total deposition time was 1 hour, with the thickest film being exposed for the entire duration. The deposition time at subsequent electrode rows was decreased in decrements of 360 s, with the thinnest sample having a deposition time of 360 s.

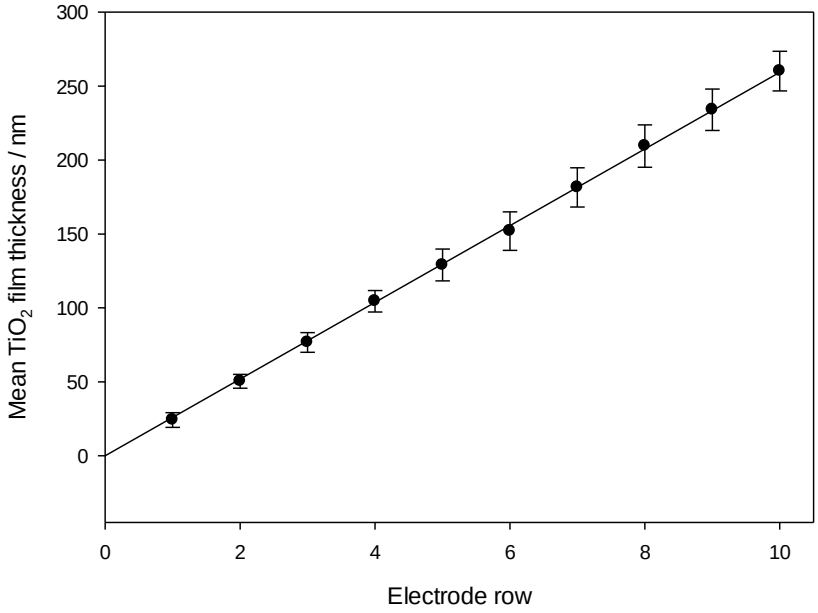

Figure 5.3. Mean TiO_2 film thickness as a function of array position (electrode row number). The deposition time was 60 mins in total with a plasma source RF power of 300 W and O_2 flow rate of 1 sccm. The Ti deposition rate was 4 Å s^{-1} (as measured by QCM) whilst the substrate temperature was maintained at 200 ^{o}C. Thicknesses were measured at 3 electrodes per row and from two sides at each electrode. Error bars represent 1 standard deviation.

AFM images were also obtained at several different thicknesses and on different substrate materials to characterise the surface morphologies (Figure 5.4). The surface of all the substrate materials (Au, ITO and SiO_2), were relatively flat, and all TiO_2 films showed a slight increase in roughness when compared to the substrate materials. As is generally expected, the roughness also increased very slightly from 3.40 to 5.38 nm (RMS) as the film thickness increased.[221] Such a subtle variation in roughness is unlikely to affect the electrochemical data to a significant extent.

Contrary to previous results,[222] anatase TiO_2 films of the same thickness did not show any appreciable change in surface morphology when deposited on the different substrate materials.

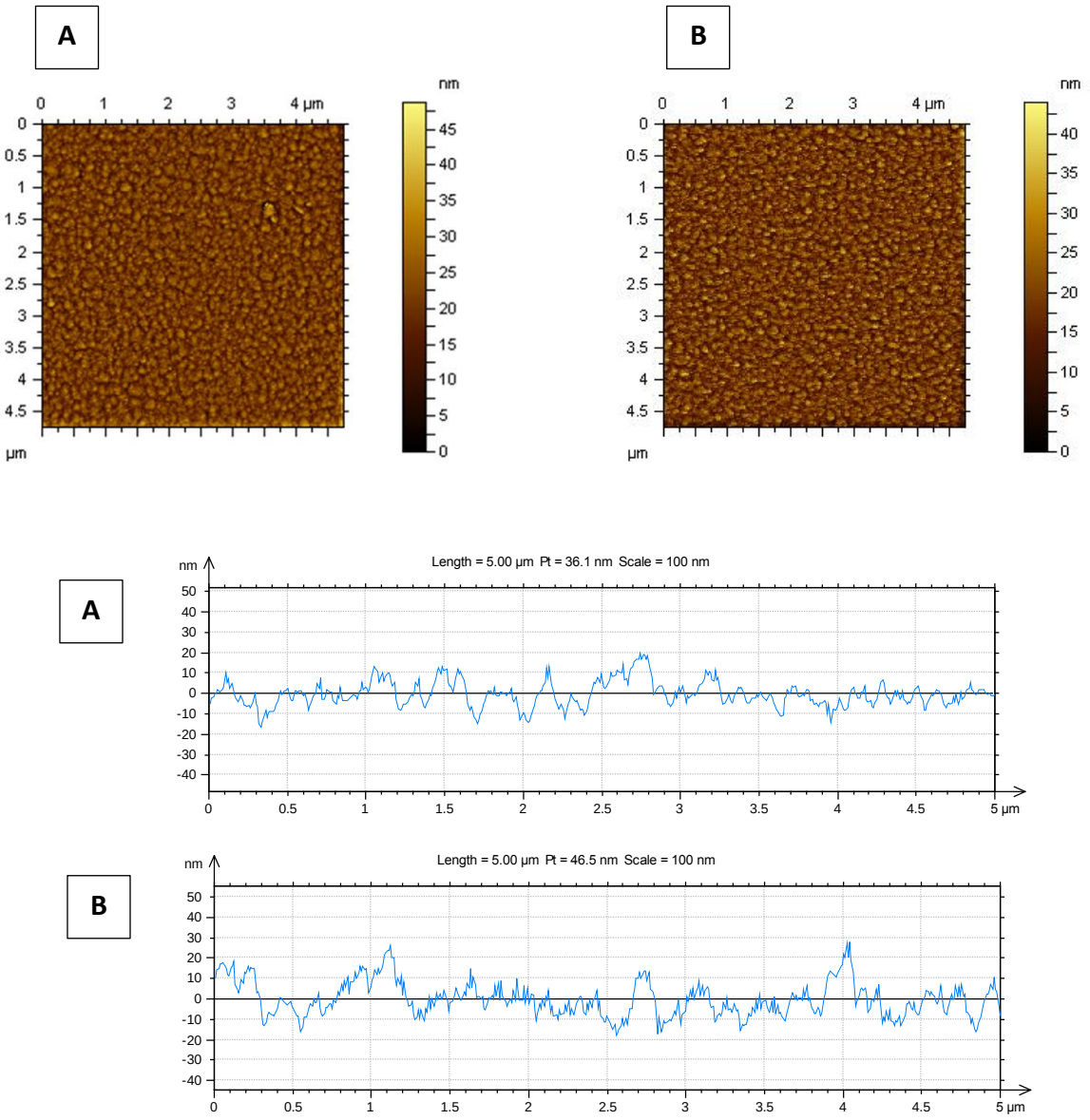

Figure 5.4. AFM images of anatase TiO_2 films with an average thickness of 24.2 (left) and 260.2 nm (right). Samples were deposited on Au electrochemical screening arrays and the imaging area was 5 µm in each case. Extracted cross sections are also shown for each case. Non-contact mode was used for the data acquisition.

5.3. Dark Voltammetric Behaviour of TiO_2

Initially, the voltammetric behaviour of the anatase TiO_2 samples were characterised in the absence of illumination. Cyclic voltammograms were carried out in 0.5 M NaOH at room

temperature using a potential scan rate of 50 mVs^{-1}. The resulting voltammograms of several different thicknesses of TiO_2 ranging from 24 – 260 nm are shown in Figure 5.5. The electrode substrate material used in this case was ITO.

The voltammograms all show similar features to the ~ 250 nm thick TiO_2 film on an ITO substrate presented in Chapter 4. In spite of the overall similarity with the voltammetry presented earlier, it is clear that the anodic feature beginning at around 0.9 V varies significantly with film thickness.

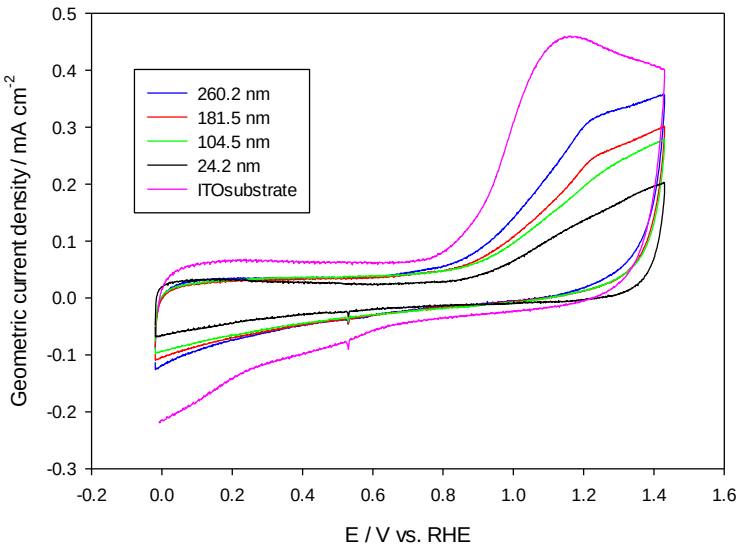

Figure 5.5. Cyclic voltammograms of anatase TiO_2 on ITO with varied film thickness (given in the inset) in 0.5 M NaOH. Measurements were conducted at room temperature with a potential scan rate of 50 mV s^{-1}. The first cycles are shown. Data is shown for array #8156.

Given that the anodic peak at all TiO_2 thicknesses bears a strong resemblance to that seen on the blank substrate, the underlying process is likely to arise from the substrate material. The dependence upon TiO_2 thickness may derive from a change in the ability of the anodic process of ITO to communicate through the TiO_2 layer. Alternatively a change in the area of direct exposure of the substrate through grain boundaries/pin holes was considered.

Similarly to the case with all other samples deposited on ITO substrates, the observed anodic current decreased upon cycling. Figure 5.6 shows the average current density at 1.2 V for the different TiO_2 thicknesses over the first 3 cycles.

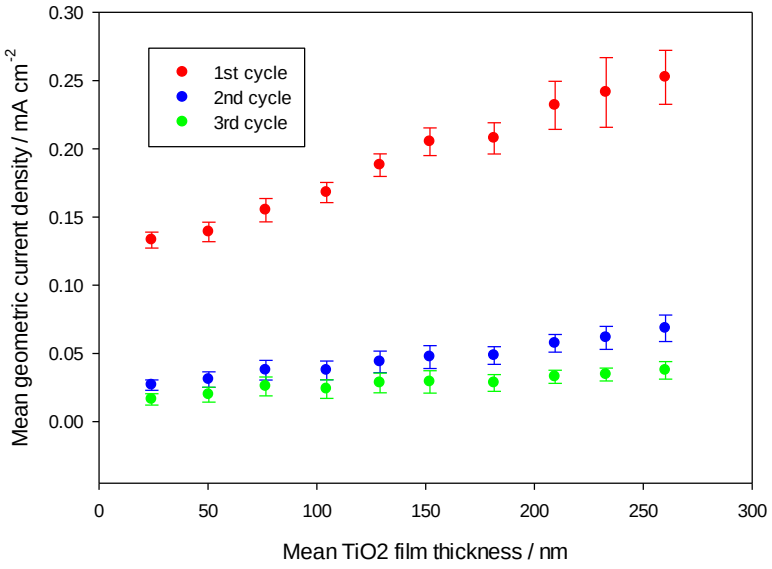

Figure 5.6. Mean current density at 1.2 V vs. RHE as a function of TiO_2 film thickness. Data from the first three cycles are shown, which were carried out in Ar purged 0.5 M NaOH at a potential scan rate of 50 mV s^{-1}. Data is shown for array #8156

It can be seen from the Figure that the current at 1.2 V diminishes with increasing cycle number, although the largest level of decrease occurs after the first cycle. This is consistent with the results on blank ITO substrates, and is likely to arise from an oxidation of the substrate through Sn dissolution as proposed in Chapter 4. Additionally the level of decrease in current is comparatively larger at the higher thicknesses, with the currents of all thicknesses tending to approximately the same value within error after 3 cycles. Initially, the possibility of the substrate being exposed to the electrolyte in varying amounts was considered. Although the surface roughness was relatively low even at higher thicknesses, there remains a possibilty that very small holes exist in the film that are not accurately tracked by the AFM probe. In this case one may expect an increased porosity at the higher thicknesses where the measured roughness was slightly higher. However, identically prepared TiO_2 films on Au substrates showed no clear peaks that could be attributed to the underlying gold substrate, despite evidence for cracks from Cu UPD experiments (see Figure 5.15). Additionally, the Cu UPD results suggest that a higher level of substrate exposure exists for the thinner TiO_2 layers, in which case one would expect a greater substrate contribution at lower thicknesses. Furthermore, the level of substrate exposure required to generate currents of the

magnitude seen in Figure 5.6 would make up a significant fraction of the overall electrode area. For example, the integration of the anodic peak charge at the thickest TiO_2 layers was approximately 0.01 mC, compared with approximately 0.02 mC on the blank ITO electrodes. Therefore direct substrate exposure would be required for approximately half of the overall electrode area in order to generate the response observed at the thickest layers. This is extremely unlikely and therefore direct substrate exposure cannot be the only cause of the anodic current above c.a. 1.20 V. It is possible that through the heating during deposition, some Sn is incorporated into the TiO_2 film. Therefore in addition to substrate exposure, there may be a dissolution of Sn from the TiO_2 film itself. In this case, the thicker TiO_2 films may incorporate a greater amount of Sn during deposition and give rise to larger anodic currents during the initial 3 cycles.

In the absence of such severe electrolyte contact with the substrate, it is therefore likely that the TiO_2 acts as a mediator to the oxidation process occuring at the ITO. In addition to variable incorporation of Sn, the thickness can have an effect on the films interfacial energetics. The variation in TiO_2 thickness is known to alter the strength of its internal electric field as well as the magnitude of the depletion layer width,[223] which may in turn affect the properties of the ITO - TiO_2 interface. Previous results have also confirmed that alterations to the electric field properties of a photoelectrode material strongly influence the nature of the interface with the substrate.[224]Wu et al. found that the ability to transfer electrons through the ITO substrate was strongly dependant on the Schottky barrier height at the TiO_2 – ITO interface.[224] Perhaps therefore a a change in the level of band bending within TiO_2 in response to thickness variation alters the interfacial properties at the substrate.

Any alteration of the electric field at the TiO_2 – electrolyte interface with thickness would typically only occur in materials with low donor densities , whereby formation of a relatively large depletion layer width occurs. At higher donor densities the depletion layer width would be much thinner, thus when the thickness of the TiO_2 is changed the internal potential gradient would not be expected to change appreciably. This however would only be the case where the depletion layer is thinner than the TiO_2 film thickness. Although, direct measurement of the donor densities was not possible in this work, one would expect relatively low values for these materials. This is on account of the relatively high partial pressure of atomic oxygen used during synthesis, in addition to the very low conductivities of the films.

In addition to the current variation of the anodic peak, the onset potential also appeared to shift in response to a change in thickness. Figure 5.7 shows that the onset potential shifts positive as the thickness is decreased, with the lowest thickness displaying a shift of approximately 60 mV with respect to the highest.

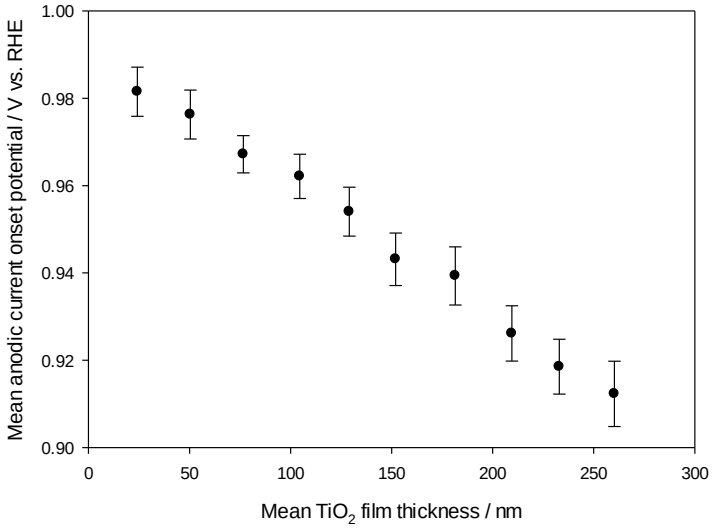

Figure 5.7. Mean anodic peak onset potential of the different thicknesses of TiO_2. The onset was taken as the voltage required to generate 0.035 mA cm^{-2} with respect to the geometric surface are of the electrode. A baseline correction was applied to the currents at all electrodes prior to the calculations being made. Data is shown for array #8156.

The observed trend in Figure 5.7 may arise due to a number of different reasons. If the current of the anodic feature is assumed to result from a process at the ITO – TiO_2 interface, then there is likely to be a change in driving force for electron transfer. Such a situation would arise if the initial equilibration process between the TiO_2 and electrolyte resulted in a variation in the TiO_2 Fermi levl position across the different thicknesses. Likely causes might include a thickness dependant TiO_2 electric field strength, a variation in surface defect concentration or a variation in the proportional area of exposed ITO substrate. Furthermore, an increased incorporation of Sn is likely to affect the characteristics of the internal electric field in the TiO_2 film.

In order to better understand any effects of thickness on the interfacial energetics of TiO_2, voltammetry was carried out using the $Fe(CN)_6^{3-}$ / $Fe(CN)_6^{4-}$ redox couple. Figure 5.8 shows the

cyclic voltammograms obtained with this redox couple at a range of different TiO_2 film thicknesses on an ITO substrate.

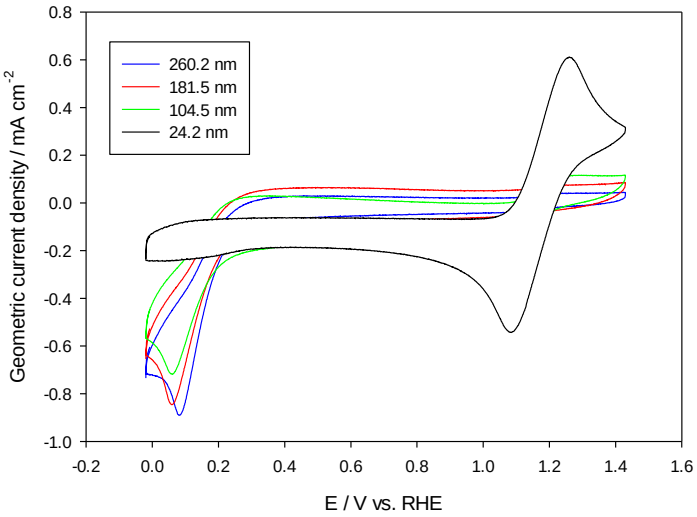

Figure 5.8. Cyclic voltammograms of anatase TiO_2 with varied film thickness (given in the inset) on an ITO substrate. The electrolyte used was 0.5 M NaOH + 5mM $Fe(CN)_6^{3-}$ and measurements were conducted at room temperature with a potential scan rate of 50 mV s^{-1}. The first cycles are shown for array #8156a.

The oxidation of ferrocyanide occured to a limited degree on all thicknesses of TiO_2. Interestingly, the dependence of the oxidative current passed on film thickness is the opposite to that in the initial 3 cycles in NaOH (Figure 5.5). This would support the notion that the increased anodic current at higher TiO_2 thicknesses in NaOH is not solely attributable to higher levels of ITO substrate exposure, and that the change in thickness alters the ability of the film to mediate dissolution of Sn from the substrate. In fact the thickness dependence of the ferrocyanide oxidation above would suggest that the lower thicknesses have a higher level of substrate exposure, which is in agreement with Cu UPD data (see Figure 5.15). The observed trend in Figure 5.8 may occur from a variation in the degree of band bending inside the TiO_2 surface. Since the depletion layer width becomes larger with increasing anodic bias, there may be a point at which this extends all the way to the substrate contact. Any additional bias will therefore be dropped over the Helmholtz layer. Therefore at lower thicknesses, there may be a reduction in the magnitude of the space charge voltage as well as the depletion layer width. Behaviour of this nature has previously been reported in which the depletion layer width of TiO_2 was controlled through alteration of the donor densities.[225] In the case of a smaller depletion layer width, or reduction in space charge voltage, oxidation reactions may take place at the surface via tunneling

of electrons through the potential barrier at the interface.[225] In such cases, the thinner layers lose their rectifying ability and simply function as an added resistance to electron transfer. Both a reduction in the level of band bending an cracks in the TiO_2 film are likley to have an impact in this case.

Conversely to the anodic current in the blank NaOH electrolyte (Figure 5.5) the oxidation of ferrocyanide showed a non linear dependence on TiO_2 thickness (Figure 5.9).

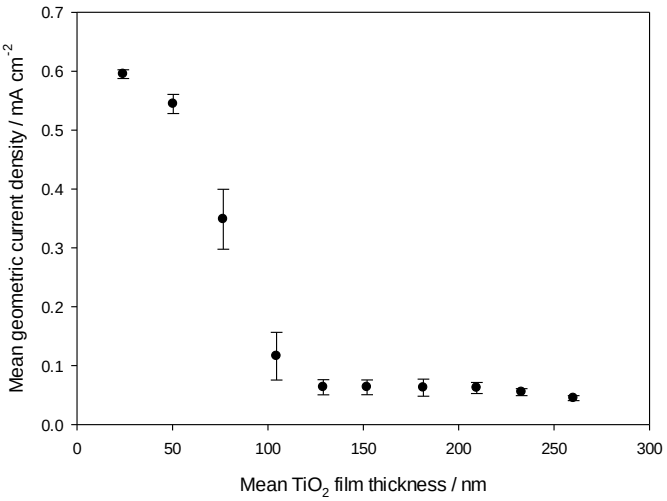

Figure 5.9. Mean geometric current density at 1.24 V vs. RHE in 0.5 M NaOH with 5 mM $Fe(CN)_6^{3-}$. Measurements were conducted at room temperature with a potential scan rate of 50 mV s^{-1}. Data from the first cycles are shown and the error bars represent 1 standard deviation. The data is shown for array #8156a

Relatively little change is seen in the Ferrocyanide oxidation current at thicknesses above 125 nm. Below this value however, a sharp increase in oxidation current can be seen. The same overall trend was also apparent in the reduction of Ferricyanide. The higher thicknesses however show behaviour more inline with that expected of a rectifying semiconductor – liquid junction. Although a small reduction current occurs at all potentials below the formal potential (~1.2 vs. RHE in alkaline media)[212] of the $Fe(CN)_6^{3-}$ / $Fe(CN)_6^{4-}$ redox couple, the reduction current remains relatively small until the applied potential approaches the flat band potential of TiO_2 (approximately -0.05 V vs. RHE).[226] Also the level of oxidation is significantly smaller than reduction at the higher TiO_2 thicknesses.

On the samples prepared on Au substrates, the voltammetry in 0.5 M NaOH was relatively featureless. Only a slight cathodic current was observed below approximately 0.2 V which is shown in the substrate voltammetry in Chapter 4. The cathodic current feature appeared to show no dependence on film thickness.

A similar overall trend towards Ferricyanide reduction (Figure 5.10) could be seen on the samples prepared on Au substrates, although the level of both oxidation and reduction above approximately 0.3 V was significantly less when compared with the ITO substrates in all cases. At all TiO_2 thicknesses the behaviour is more like that expected for a Shottky type diode formed between TiO_2 and the electrolyte.

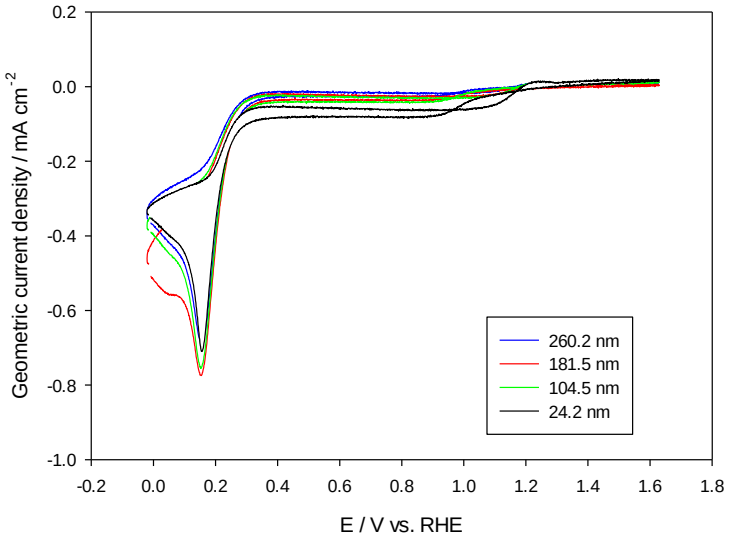

Figure 5.10. Cyclic voltammograms of anatase TiO_2 with varied film thickness (given in the inset) on an Au substrate. The electrolyte used was 0.5 M NaOH + 5mM $Fe(CN)_6^{3-}$ and measurements were conducted at room temperature with a potential scan rate of 50 mV s^{-1}. The first cycles are shown for array #8155.

Unlike the case on ITO substrates, no signifcant oxidation of ferrocyanide occurs at any TiO_2 thickness. Additionally, any small oxidation current present remains relatively unaffected by changes in the film thickness. As in the case of larger TiO_2 thicknesses on ITO, only a small reduction current is present until the applied potential reaches approximately 0.3 V. At this point and below, the driving force to transport electrons to the semiconductor bulk is less, thus significantly increasing the concentration of electrons at the surface. Although the reduction current between the limits of 0.3 and 1 V is much smaller than on ITO, the same relative trend

exists. Relatively little variation occurs as the thickness changes until a value of approximately 125 nm. Below this a sharp increase in reduction current was observed. In light of the increased rectification of films deposited on Au, the small reduction current between 0.3 and 1 V probably involves mediation by surface states or exposed Au through small cracks in the film. The larger currents at lower thicknesses may suggest that the band bending (which drives electrons *away* from the surface positive of the FBP) inside the film decreases as the film thickness decreases. This further supports the notion that thinner films have increasing behaviour like a simple resistor as opposed to a rectifying junction. Additionally, the greater level of substrate exposure may increase the current through offering a larger surface area on which the reaction can take place.

Upon increasing the upper potential limit of the cyclic voltammograms, an anodic peak possibly relating to the oxidation of ferrocyanide emerged (Figure 5.11). The peak still remained signifcantly smaller than that for ferrocyanide oxidation on the ITO substrate and also was only present on the first cycle. All subsequent cycles showed comparable oxidation currents to those under the conditions employed in Figure 5.10 up to the maximum potential limit of 1.9 V.

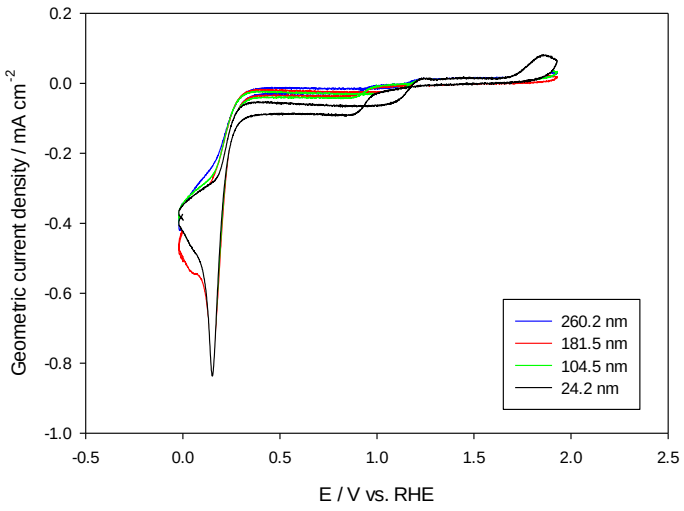

Figure 5.11. Cyclic voltammograms of anatase TiO_2 with varied film thickness (given in the inset) on an Au substrate. The electrolyte used was 0.5 M NaOH + 5mM $Fe(CN)_6^{3-}$ and measurements were conducted at room temperature with a potential scan rate of 50 mV s^{-1}. The first cycles are shown for array #8155.

The anodic peak for the reoxidation is clearly significantly smaller than that observed for the samples prepared on ITO substrates. This together with the much lesser extent of ferricyanide reduction would suggest an increased degree of rectification on the Au substrates. Possible explanations could be, a decreased donor density, a decreased level of surface states or a

variation in the nature of the interfacial energetics on the Au supported TiO_2 at either the substrate or electrolyte interface. Further studies with AC impedance spectroscopy and UPS measurements would be required in order to investigate this further. In spite of the difference in the absolute current values between the two support materials, the relative trend in terms of oxidation current against film thickness remained the same. Also, whilst the magnitudes of the oxidation and reduction currents on ITO/TiO_2 remained relatively unchanged with cycling, the oxidation activity ceased almost entirely on the Au/TiO_2 after just one cycle to the higher potential limit. It is clear therefore that the properties of the films change when cycled to the higher limit. This may result from the oxidation of donors in the film and a subsequent loss in conductivity.

Another key difference of the Au/TiO_2 samples is the greater level of hysteresis between the forward and reverse cycles. This is illustrated in Figure 5.12, where the potential region between 0.8 – 1.2V is enlarged.

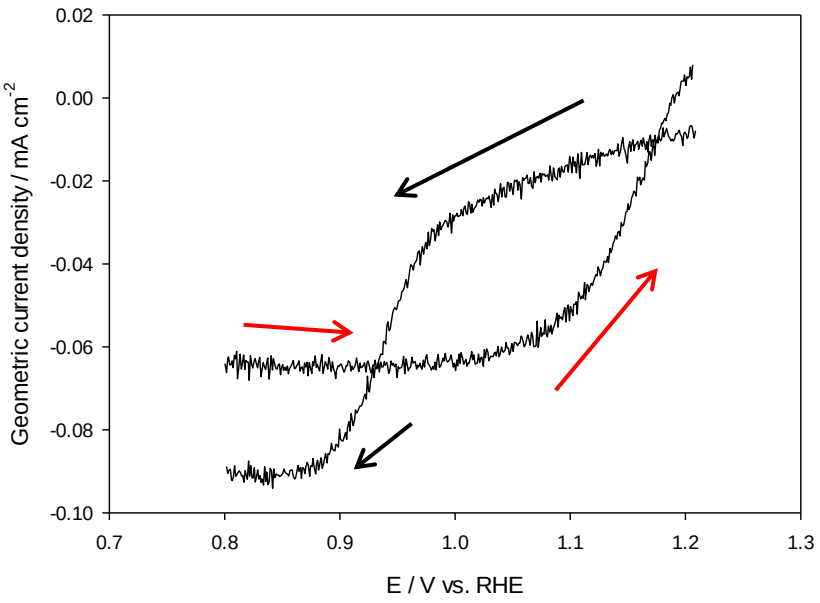

Figure 5.12. Enlarged cyclic voltammogram of an approximately 24 nm thick TiO_2 film deposited on Au. The voltammogram was recorded between the limits of 0 – 1.9 V vs. RHE at room temperature and with a scan rate of 50 mV s^{-1} in 0.5 M NaOH + 5 mM $Fe(CN)_6^{3-}$. Data from the first cycle is shown for array #8155. The red and black arrows denote the direction of the scans.

The behaviour shown in Figure 5.12 was apparent on all thicknesses of TiO_2 and there is a clear variation in the point at which the reduction reaction 'switches off' between the forward and reverse scans. No clear change in the behaviour over the potential region highlighted could be seen with cycling, even at the higher potential limits where there was a clear change in oxidation activity between the various cycles. The variation in maximum positive potential limit did however show some effects. In all cases the positive going cycle did not appreciably change (over the range 0.8 – 1.2 V), however the subsequent reverse scan varied to some degree depending on the upper potential limit. Figure 5.13 shows the difference in geometric current density (i_{pos}-i_{neg}) between the positve and negative going scans at 1.03 V vs RHE.

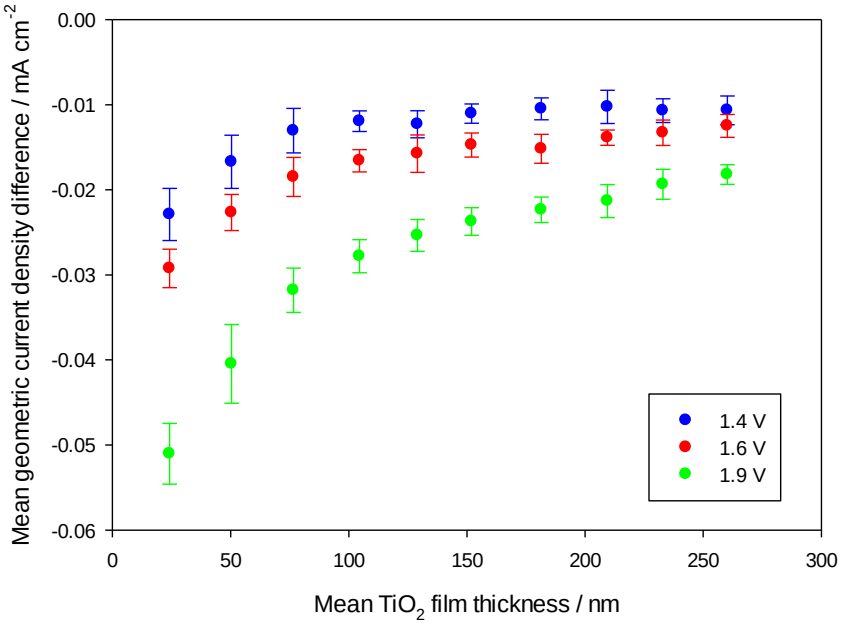

Figure 5.13. The variation in current density (with double layer correction) between the positive and negative going scans (I_{pos}-I_{neg}) at 1.03 V vs. RHE for different TiO_2 thicknesses on Au. Data is shown for the first cycle of array #8155 with different upper potential limits and was recorded at room temperature at a potential scan rate of 50 mV s^{-1}. The electrolyte employed was 0.5 M NaOH + 5mM $Fe(CN)_6^{3-}$.

In all cases there is a relatively consistent variation in the forward and reverse current densities until a thickness of 100 – 125 nm is reached. The level of variation then increases at the lower thicknesses, which becomes more obvious as the upper potential limit also increases. Although no change to this behaviour appears with cycling, the level of oxidation of ferrocycanide does,

making it therefore unlikely that localised concentration differences or surface stabilised species have an effect on the behaviour observed.

Typically for electron transfer to occur significantly positive of the flat band potential, defects must be present in the film. The energies of such defects usually reside within the band gap region, and may mediate charge transfer processes at potentials where a relatively low surface electron concentration would be ordinarily predicted. Typically Ti^{3+} ions in the form of oxygen vacancies contribute this behaviour in TiO_2.[212] Previously it has been shown that Ti^{3+} may be formed by both electrochemical reduction and exposure to UV radiation.[227] The Ti^{3+} ions could also be subsequently reoxidised at higher potentials. It is possible therefore in principle that there may be a cycling between the different oxidation states of titanium on the forward and reverse scans which affects the ability to sustain current positive of the flat band potential of TiO_2. A more likely explanation, is that the discrepancy between the forward and the reverse scans arises from the behaviour of the underlying Au substrate. Cracks in the film may allow Au oxide to form on the forward scan, which subsequently affects its ability to take part in the reduction of ferricyanide on the reverse scan. The higher potential limits may therefore allow a greater level of oxide formation to take place and thus delay the onset of ferricyanide reduction. The very presence of any reactivity in the region highlighted points to mediation by the Au substrate, since the films are expected to be essentially insulating in the dark over this potential region.

In view of the relatively small degree of ferrocyanide oxidation on the samples with Au substrates, voltammetry was also carried out with the addition of 10 mM $CuSO_4$ in 0.5 M $HClO_4$. This was chosen since the oxidation/ reduction behaviour could be investigated in a potential region of low band bending, thus allowing more facile passage of anodic current from the semiconductor. Secondly, the underpotential deposition of Cu on both TiO_2 and Au is of fundamental interest. Potentially, the UPD of copper on gold may also allow assessment of whether the Au substrate is exposed to the electrolyte. In the case of TiO_2 it has previously been shown that adsorption or intercalation of hydrogen and several different metal cations may occur at low potentials.[228] Such effects are of key interest in modification of TiO_2 films for a variety of applications.

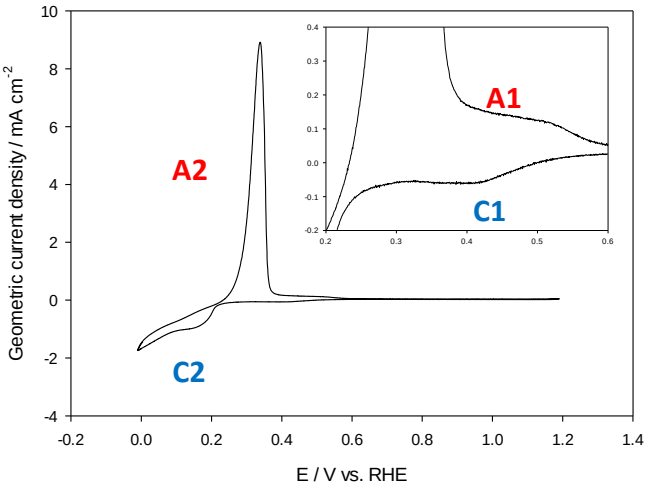

Figure 5.14. Cylic voltammogram of a polycrystalline Au electrode in 0.5 M $HClO_4$ + 10 mM $CuSO_4$. Measurements were conducted at room temperature with a potential scan rate of 50 mV s^{-1}. The first cycle is shown. The region from 0 – 0.4 V is also enlarged to clarify the anodic and cathodic peaks A1 and C1 respectively.

The behaviour of the gold substrate material can be seen in Figure 5.14 and shows two sets of anodic and cathodic peaks. The presence of two anodic and cathodic peaks would suggest a two step deposition process which has previously been shown to be the case on Au electrodes.[229] The first cathodic peak (C1) represents the first stage, in which up to a monolayer of Cu is deposited on the Au surface. This process has also been found to be strongly dependedant on the nature of the anions present in the electrolyte.[229] At more negative potentials another cathodic peak is observed (C2) which results from bulk deposition of Cu. On the positive going scan, the bulk metal is subsequently stripped from the surface (A2) followed by the underpotentially deposited layer (A1). A solution based redox process may also occur. Figure 5.15 shows the voltammetric response of the TiO_2 electrodes.

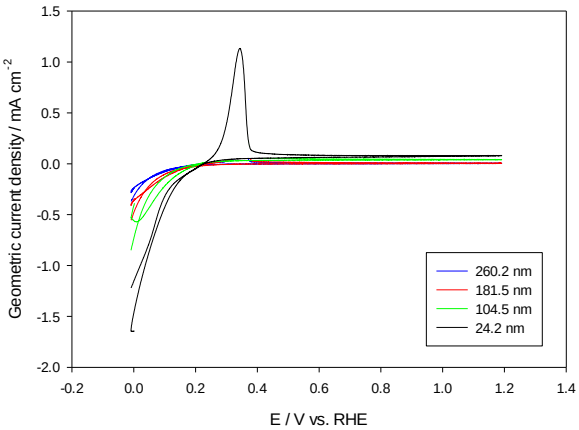

Figure 5.15. Cyclic voltammograms of TiO_2 on Au in 0.5 M $HClO_4$ + 10mM $CuSO_4$. Measurements were conducted at room temperature with a potential scan rate of 50 mV s^{-1}. The first cycles are shown for array #8155a.

It can be seen from Figure 5.15 that the clearly resolved bulk Cu deposition (C2 in figure 5.14) is no longer apparent. A relatively large reduction current beginning at approximately 0.25 V can however be seen, which decreases upon increasing the film thickness. The onset of the cathodic current also shifts progressively negative as the film thickness increases. The same trend in terms of the level of current passed can also be seen in the subsequent anodic peak at around 0.3 V. The position of this peak also appeared to vary slightly in response to changes in film thickness. The change was however relatively minor (Figure 5.16), whereby a slight negative shift in the peak potential was observed as the film thickness decreased.

In all cases no clear peaks in the vicinity of C1 (figure 5.14) could be clearly identified.

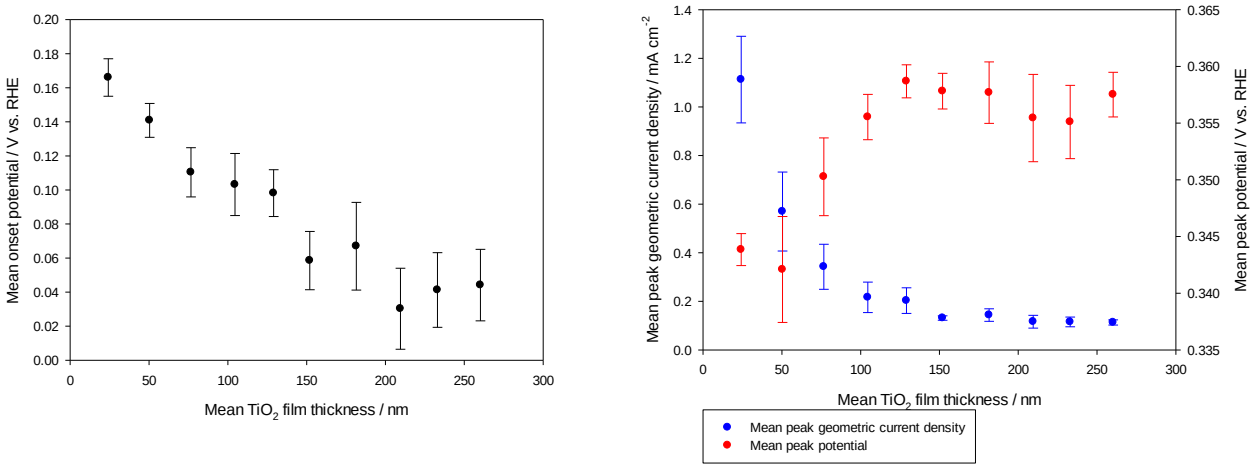

Figure 5.16. Left: Mean Cu reduction onset potential defined by the voltage required to generate -0.23 mA cm^{-2} (geometric). Right: Mean peak potential (red) and and peak current density (blue) for the copper oxidation peak at approximately 0.1 V. Data is derived from array #8155a

The dependance of anodic current on film thickness appeared to exhibit the same overall trend seen on both substrate materials in the oxidation on ferrocyanide. It would therefore appear that the trend in terms of ability to generate anodic current is a property related to the thickness of the TiO_2 film. The substrate material however clearly influences the absolute values of any anodic current, since a relatively significant difference was seen between the two substrates in the oxidation of ferrocyanide. In this case it is likely that a greater level of substrate exposure is present at lower film thicknesses. This together with an intrinsic decrease in ability to sustain an internal electric field at lower thicknesses is likely to reduce the level of rectification in thinner films below ~ 125 nm thickness.

At all TiO_2 electrodes, the cathodic current onset was more negative than on the gold (c.a. 0.21 V for the 24 nm film compared with 0.17 V on Au). Also the maximum anodic current around the vicinity of A2 on Au was significantly less compared with gold, with a maximum of approximately 1.11 mA cm^{-2} (24 nm) compared to 8.44 mA cm^{-2} on Au. The position of the Cu oxidation peak also changed to a much lesser degree than the reduction onset and was positive of that on Au in all cases. The dependence of the scan rate on the voltammetry also varied to that on Au, which is shown in Figure 5.17.

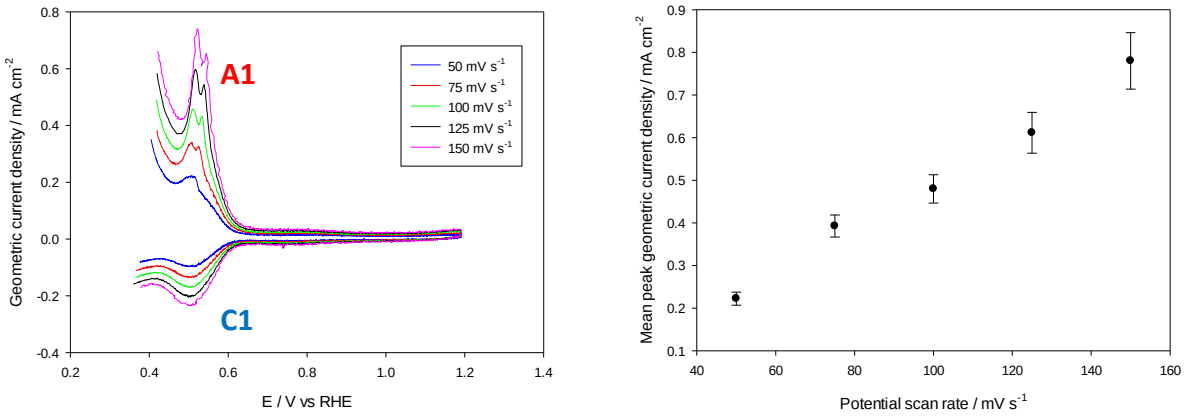

Figure 5.17. Left: Voltammetry of a polycrystalline Au electrode at room temperature in 0.5 M $HClO_4$ + $CuSO_4$ with various scan rates (given in the inset). The CVs are the first cycle in each case and are shown between the limits of 0.35 – 1.20 V vs. RHE. Right: Mean peak current density of the anodic peak A1.

It can be seen from Figure 5.17. that the Au electrode showed the characteristic behaviour expected for the UPD of copper.[229] The UPD stripping peak (A1) as well as the adsorption peak C1 increased linearly in size as the scan rate increased, whereas the bulk stripping peak remained relatively constant (not shown). This indicates a decreased charge passed at higher scan rates in the bulk deposition on acount of the decreased amount of time spent over the region in which this occurs. The lack of change in the current in this region may alteratively suggest that the peak instead relates to a solution based process. The behaviour of selected TiO_2 electrodes in response to scan rate are shown in Figure 5.18.

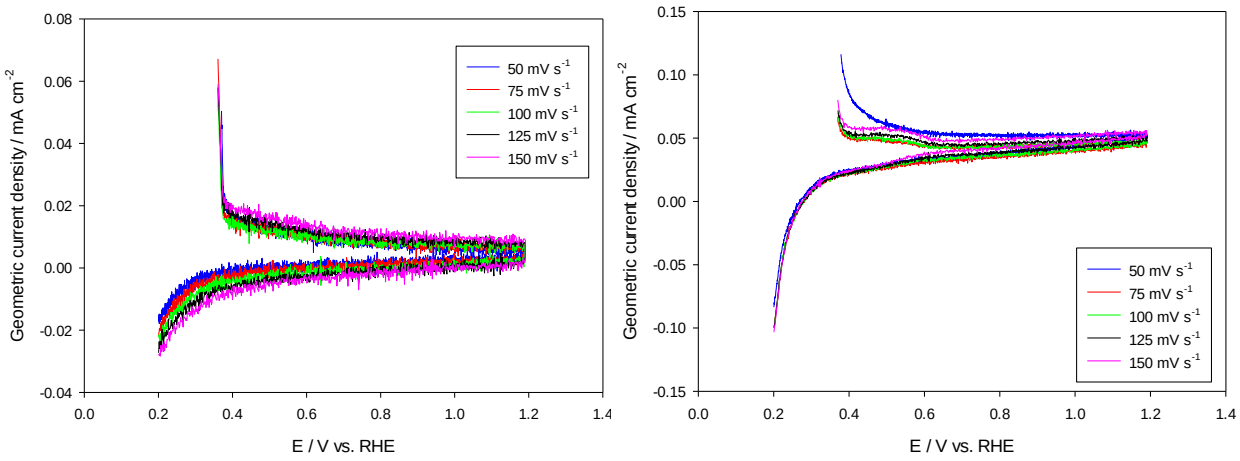

Figure 5.18. Cyclic voltammograms of typical 24.2 nm (Right) and 260.2 nm (left) thick TiO_2 layers on gold. Measurements were conducted in 0.5 M $HClO_4$ + 10 mM $CuSO_4$ at various potential scan rates (given in the inset). For clarity, only the voltammetry between the limits of 0.2 – 1 V vs. RHE are shown. The data is from array #8155.

The potential scan rate can be seen to affect the response of both thicknesses presented to some extent. In the case of the thinner film, a small anodic peak can be seen at approximately 0.4 – 0.6 V, which generally increases in size as the scan rate increases. The obvious exception to the rule is the voltammetry recorded at 50 mVs^{-1}, which in fact shows the largest current recorded in this region. This was determined to be a result of the order in which the data was collected, since the voltammetry was found to change upon cycling (Figure 5.19). Such a variation with the cycle number was not evident on the blank Au substrate. With this in mind, a precise determination of the scan rate dependence was not possible. This is due to the difficulty in deconvoluting the effects relating to cycling and the scan rate employed. Interestingly however, no clear variation in the cathodic current was observed at around 0.2 – 0.35 V in response to scan rate variation at the thinner film. Possibly this may indicate that any diffusion of Cu^{2+} to the Au through cracks is a relatively slow process. At the electrode with the higher thickness, the cathodic current does appear to change with scan rate in the way one would ordinarily expect. In this case no clear UPD peaks can be identified in the region at which they occur on Au and it may be that the behaviour is dominated by a variation in capacitative current.

Figure 5.19 shows the effects that cycling had on the electrodes. In all cases, a reduction in the charge passed for the anodic and cathodic processes occurred. The effects were most significant between the first and second cycles and a greater proportional decrease in charge occurred for the lower thicknesses of TiO_2. Such effects may arise from the gradual degradation of the films, with the effect being more severe on the lower thicknesses.

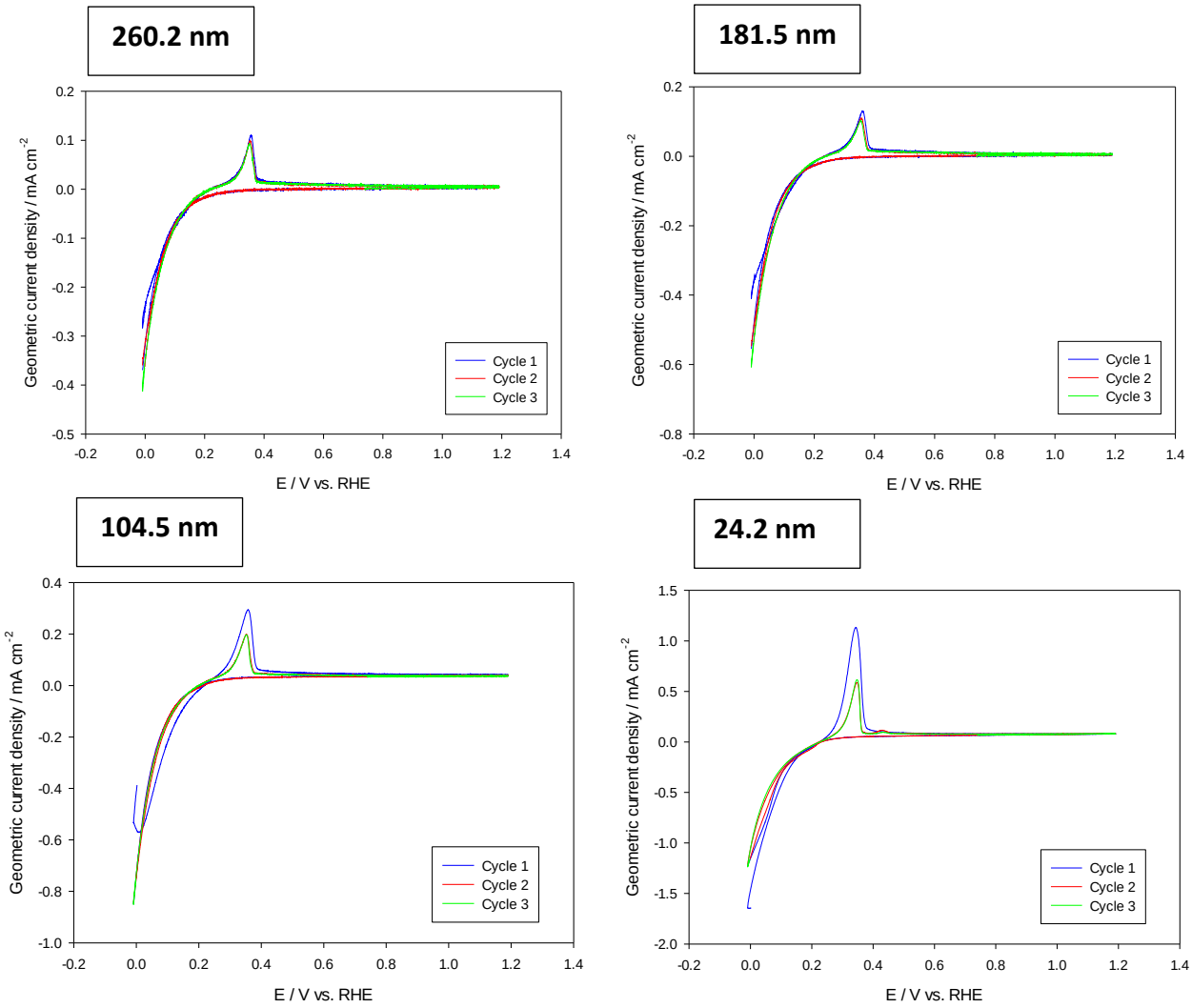

Figure 5.19. Cyclic voltammograms of varying thicknesses of TiO_2 on Au in 0.5 M $HClO_4$ + 10 mM $CuSO_4$. Measurements were carried out at room temperature at a potential scan rate of 50 mV s^{-1}. The first three cycles are shown in each case.

5.4. Photoelectrochemical Behaviour of TiO_2

The photoelectrochemical behaviour of the TiO_2 films was studied by a combination of illuminated CV measurements and illuminated open circuit potential measurements. All measurements were performed at room temperature in 0.5 M NaOH. Correction for variation in illumination intensity was carried out using the same method as that described in Chapter 3. In view of the variation in thickness of the TiO_2 films and the large optical penetration depth of films of this type, it is likely that a significant variation in the degree of optical absorption occurs with film thickness. As such, it is necessary to first determine the sensitivity of each thickness in response to changes in light intensity. This was carried out by performing illuminated CV measurements over a range of different light intensities. Typical voltammograms for both the highest and lowest TiO_2 thickness on an ITO substrate are shown in Figure 5.20.

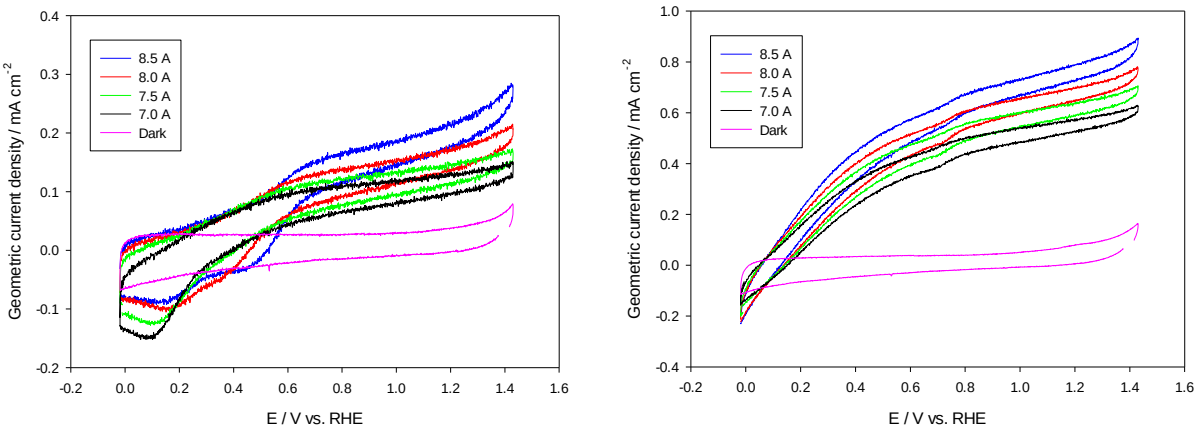

Figure 5.20. Cyclic voltammograms of TiO_2 (left: 24nm, Right:260 nm) on ITO under different illumination conditions. All measurements were conducted at room temperature and at a scan rate of 50 mV s^{-1}. The first cycles are shown except in the dark measurements, where the third cycle is shown. Data is shown for array #8156

The adjustment of the lamp emission current, was found to reproducably alter the intensity in a controlled manner without significant changes to the spectrum in the wavelength range of interest (see Chapter 3). As such, the CVs at different lamp emission currents were utilised to investigate the photocurrent dependence of each film thickness on intensity.

Figure 5.20 shows that the photocurrent increases in both cases as the lamp emission current is increased. It can also be observed that a greater overall increase can be seen at the higher thickness. Although the two electrodes shown have different absolute values in terms of irradiance, the emission current still changes the intensity by the same amount at each electrode location. As such it appears that the thicker sample has a greater sensitivity to intensity variation. This can be seen also when plotting the relative intensity (calculated from the calibration sample) against the photocurrent. Once again it is clear that the intensity has a much smaller effect at the lower TiO_2 thicknesses. Only the thinnest layers however showed behaviour markedly different to the rest, with all thicknesses above c.a. 50 nm showing approximately the same intensity dependance.

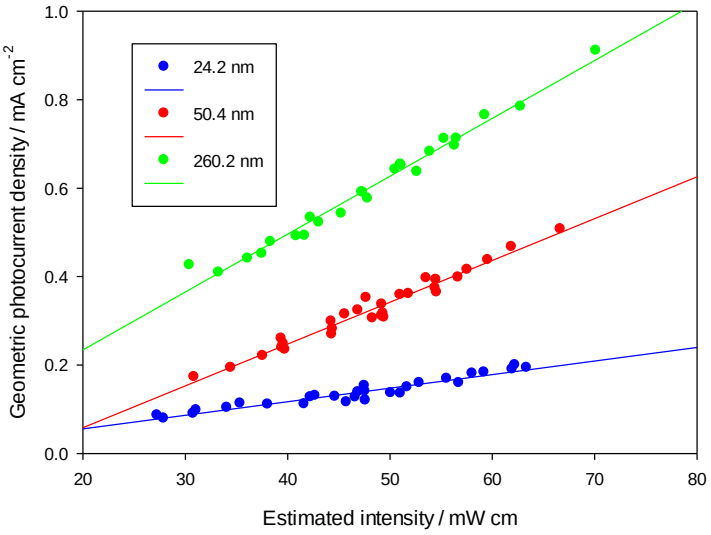

Figure 5.21. The dependence of photocurrent at 0 V vs. MMO on illumination intensity for the three TiO_2 thicknesses on Au. Measurements were conducted at a range of lamp emission currents and intensities were calculated from the photocurrent response of a uniform TiO_2 calibration sample. (described in Chapter 3). Data is derived from array #8156.

In order to correct for variation in illumination intensity the photocurrent values were therefore mulitplied by the calculated relative intensity values before being multiplied by the intensity sensitivity factor. The sensitivity factor was defined as the mean gradient of the intensity vs. photocurrent trend at each film thickness (relative to that on the uniform TiO_2 calibration array). It was clear in this case that trends could be identified even prior to the normalisation step. Despite the level of irradiance non-uniformity, activity trends could be seen over a small section of the array, where the intensity was most uniform. The intensity corrected photocurrents at both the Au and ITO supported samples are shown below at a range of bias voltages. In all cases the

photocurrent thickness dependance displays the opposite trends of those seen in the dark voltammetry. Both reduction and oxidation activities in the dark favoured the lower thicknesses, whereas a decrease in activity is seen at the lower thicknesses in terms of photocurrent generation.

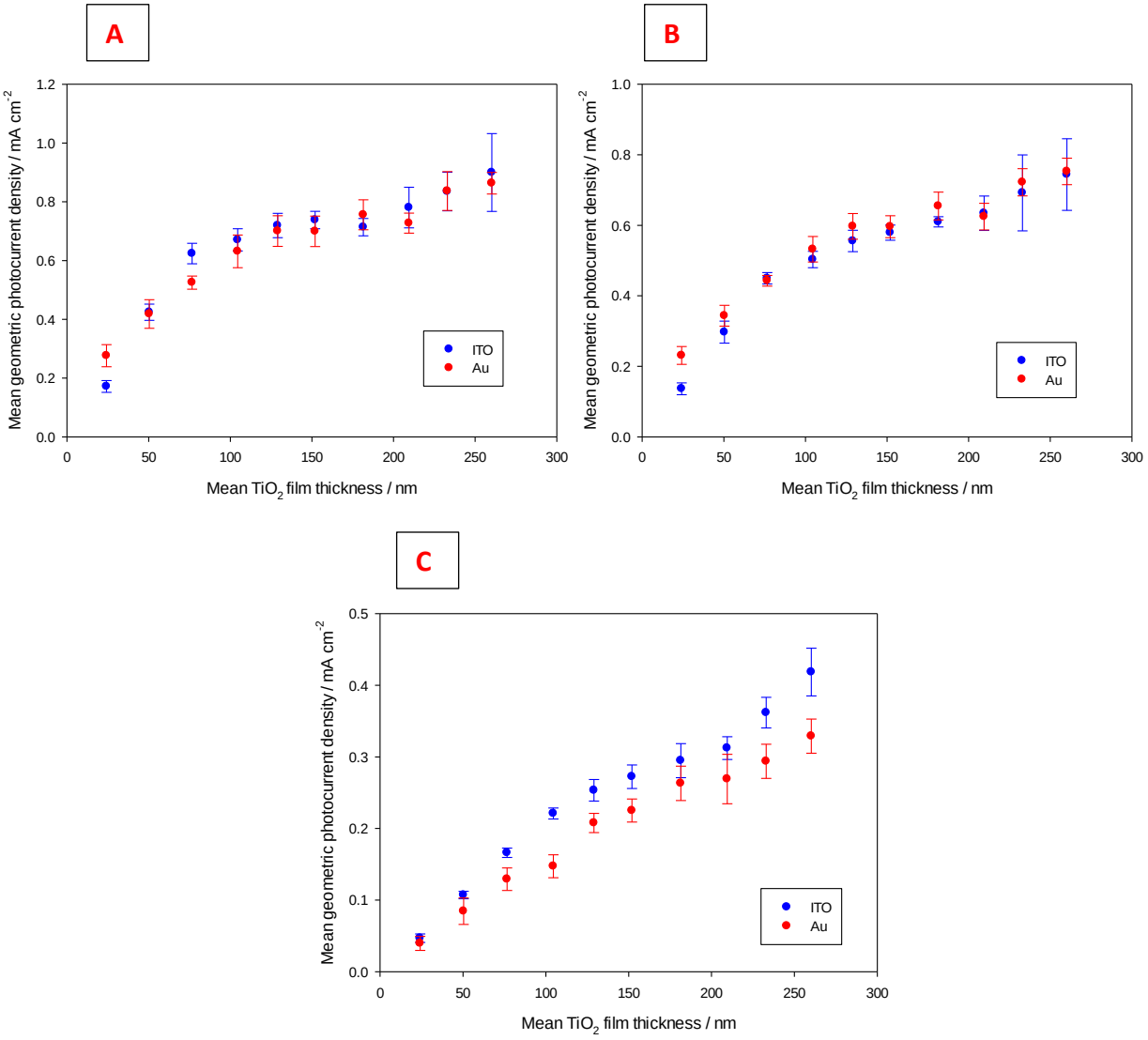

Figure 5.22. Mean geometric photocurrent of ITO and Au supported TiO_2 films at (A) 1.03 V, (B) 0.63 V and (C) 0.27 V vs RHE. Data is derived from the first cycles in each case. Correction for intensity variation has been applied and error bars represent 1 standard deviation. Data is shown for arrays #8156 and #8155a

The data obtained from films deposited on both Au and ITO substrates showed good agreement overall in spite of the relatively significant variation in terms of dark behaviour. The variation in activity at differing film thicknesses was also particularly evident in the lower voltage range. At 0.27 V the thickest film displayed a photocurrent approximately ten times that of the thinnest.

The improvement of the thicker films then reduced to approximately a factor of five at the higher voltages. The clearer variation in the lower voltage range may be suggestive of a variation in the ability to effectively transport holes to the interface.

In addition to the behaviour shown above, a slight decrease in photocurrent was observed after the first cycle. This effect could be seen at all thicknesses of TiO_2 and on both of the substrate materials. The photocurrent at 1.03 V is presented for the first 2 cycles on the ITO substrate in Figure 5.23.

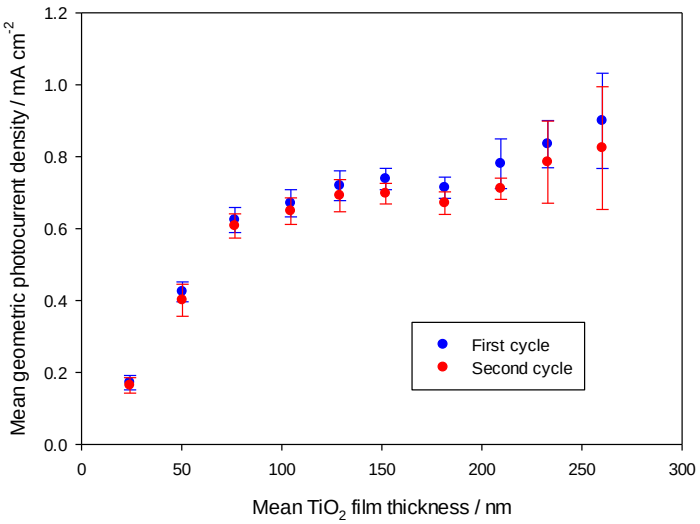

Figure 5.23. Photocurrent density at 1.03 V vs. MMO during the first and second cycle of a TiO_2 film of varying thickness on ITO. Data is shown for array #8156

In spite of the relatively large error bars, particularly at higher thicknesses, the same systematic trend was evident at each repeat of the thickness gradient on the array. The level of photocurrent decay between the first and second cycles obeyed a linear relationship in response to film thickness, with an increasingly large reduction in photocurrent as the film thickness increased. It has previously been noted that the photovoltages generated at TiO_2 - liquid junctions decrease significantly when there is a localised saturation of oxygen at the interface.[230] Since the level of oxygen evolution varies significantly at each thickness, this may explain the varying reduction in photocurrent at the different film thicknesses. In order to assess the degree of photovoltage production at the different TiO_2 thicknesses as well as the effect of O_2 in solution, illuminated open circuit potentials were recorded in both Ar and O_2 saturated media on both substrate types.

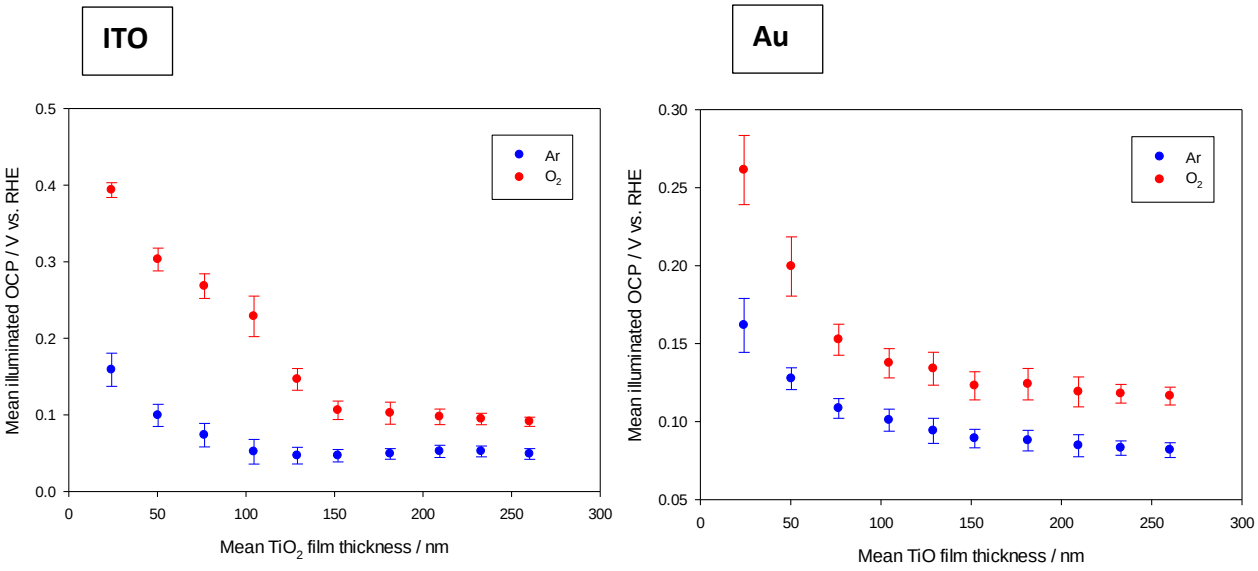

Figure 5.24. Mean illuminated open circuit potential as a function of TiO_2 film thickness in both O_2 and Ar saturated media. Data is shown for both substrate types (Left: ITO and Right: Au). The results are derived from arrays #8156 and #8155a.

On both substrate types (in Ar purged media), the open circuit potentials under illumination stay relatively constant until a thickness of approximately 100 nm is reached. The voltage then becomes increasingly positive below this value. This behaviour may suggest that the lower thicknesses have either a reduction in band bending at equilibrium, or an increased rate of recombination. The open circuit potentials also appear to become more positive in O_2 saturated media. This is a relatively common observation, particularly in nanostructured systems, where the lack of internal electric field may allow scavenging of conduction band electrons by O_2 in solution.[230] Such effects are once again indicative of a reduction in the level of rectification for films with thicknesses lower than approximately 125 nm.

Additionally, the positive shift in open circuit voltage is slightly larger at the lower thicknesses, particularly in the case of the ITO substrate. In all cases, photovoltage generation was prompt, however a clear variation in voltage decay could be observed upon removal of illumination. The voltage at the lower thicknesses, decayed back to a stable value almost instantaneously, however the voltage at the higher thicknesses decayed at a significantly slower rate. The voltage at the thickest electrodes in fact failed to reach a steady value even after the ~300 seconds recorded after ceasing illumination.

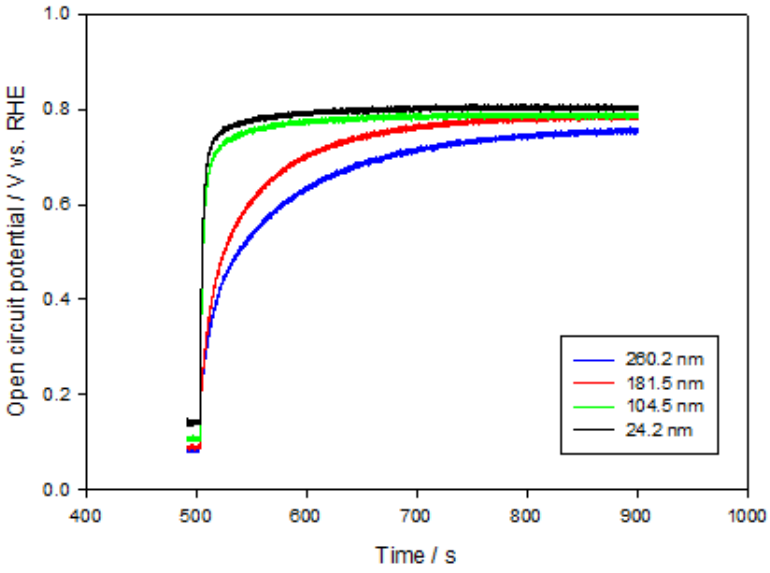

Figure 5.25. The decay of the open circuit potentials upon ceasing illumination at various thicknesses of TiO_2. The illumination was removed at 500 seconds. Data is shown for array #8155a.

5.5. Conclusions

In the case of both substrate types, the passage of anodic and cathodic current in simple electron transfer reactions increased as the TiO_2 film thickness decreased. Attempts to determine the level of substrate exposure across the different film thicknesses could not unambiguously determine whether significant portions of the substrate were exposed, or indeed how much at each thickness. However the lack of any characteristic Au oxide formation/stripping features or ferrocyanide oxidation even up to a maximum potential of 0.9 V (on samples with Au substrates) would suggest that any exposure is relatively small. The ITO substrates on the other hand showed significant levels of anodic current arising from a feature similar to that seen on the blank ITO substrate. The behaviour was consistent with an oxidation process at the substrate, although the exact role of TiO_2 thickness in mediating this is unclear. If it is to be assumed that the behaviour results from substrate exposure, then it is apparent that the level of exposure on the ITO substrate is significantly greater than that on the Au substrate. This would seem unlikely given the proportional area of exposed substrate required to generate currents of the magnitude observed.

The photoelectrochemical results were however in extremely good agreement, in spite of the drastically differing dark behaviours on the two substrates. If hugely different areas of the substrates were exposed this would be unlikely, given the significant effect of substrate exposure

seen in Chapter 3. The open circuit potentials suggested that the photovoltage decreased at lower film thicknesses, which may in part explain the reduced photocurrent. It is possible that the interfacial barrier height changes in response to thickness variation, which would also support some of the trends observed in the dark measurements. A detailed Mott-Shottky analysis would however be required in order to determine whether any variation in band bending and therefore flat band potential occurs in response to thickness variation.

Although some data would suggest a variation in the flat band potential, all the results are not consistent with this. Furthermore if this is the case, it is not clear whether a variation in substrate exposure or intrinsic effects relating to thickness is the cause. The decrease in open circuit potential, in addition to the more rapid voltage decay at lower thicknesses would be consistent with substrate exposure, although the similarities between the results on both substrate materials would suggest a similar level of exposure on each. In spite of this, measurements on the supported Pt particle arrays, showed a reduction in illuminated open circuit potential of approximately 0.2 V between the directly deposited TiO_2 films and the post annealed ones (on electrodes of the same particle size – see Chapter 3). In the case of the post annealed arrays, large clear features relating to Au surface redox behaviour were observed. As such, the reduction in OCP of approximately 0.1 V across the thickness range would be expected to show a significant increase in substrate exposure, and visible Au voltammetric features if this were the primary cause of the behaviour. Since this was not the case, a variation in substrate exposure is unlikely to be the sole cause of the behaviour observed in response to variation of film thickness. The results of the Cu UPD however show substrate exposure to have some influence on the trends. In addition to this factor, the reduced capacity to form an internal electric field at lower thicknesses has an impact. Above approximately 125 nm, the electrodes behave as rectifying n-type semiconductors, and hence exhibit reduced activity towards the reactions in the dark and a greater ability to separate photogenerated charge carriers under illumination. Below this thickness, the electrodes are able to participate in the dark reactions more easily on account of the reduced level of rectification. This in turn decreases their effectiveness in separating photogenerated electron-hole pairs in the illuminated voltammetry.

6. Synthesis and Screening of Anatase TiO_2 Supported Pt Nanoparticles

6.1. TiO_2 Deposition

All of the samples prepared in this work were synthesised by PVD, whereby Ti was evaporated from an e-gun source. Atomic or molecular oxygen was supplied at a constant rate during deposition through a plasma atom source. Initially the conditions to yield the desired thickness were obtained from the calibration of the Ti deposition rate as described in Chapter 2. The films were determined to be an average thickness of 257 nm +/- 26 nm by AFM. Subsequently, a range of synthesis conditions were trialled in order to produce the anatase phase. The final parameters used for the deposition of all TiO_2 support layers on the screening arrays are summarised in Table 6.1.

Table 6.1.

Synthesis parameter	Ti	O
Source	E-gun	Atom source
Deposition rate	4 Å s^{-1}	1 sccm flow rate
Deposition time	60 mins	60 mins
Substrate temperature	200 ^oC	200 ^oC
RF power	N/A	300 W

The O_2 partial pressure during synthesis is particularly important in TiO_2, and has been found to markedly alter its electronic conductivity.[231] A great deal of research has been carried out in order to understand this behaviour and generally (Figure 6.1) a trend of increasing conductivity in response to decreasing oxygen partial pressure during synthesis is observed. The consistent increase in conductivity at lower oxygen partial pressures has led to the widely accepted belief that oxygen vacancies represent the primary defect type that imposes n-type semiconductivity in TiO_2.[232] In the case of this work, all TiO_2 films showed resistances higher than that measureable by the 4 point probe available (> 50 MΩ). In addition to the oxygen partial pressure, the method of synthesis also has an effect on the conductivity of a material. In Figure 6.1 it can be observed that the properties of TiO_2 differ considerably under nominally identical oxygen partial pressures, which is largely related to the different methods used to synthesise the materials. This

observation also creates difficulty in obtaining a reasonable estimation of the expected conductivity at a given oxygen partial pressure from literature reported values.

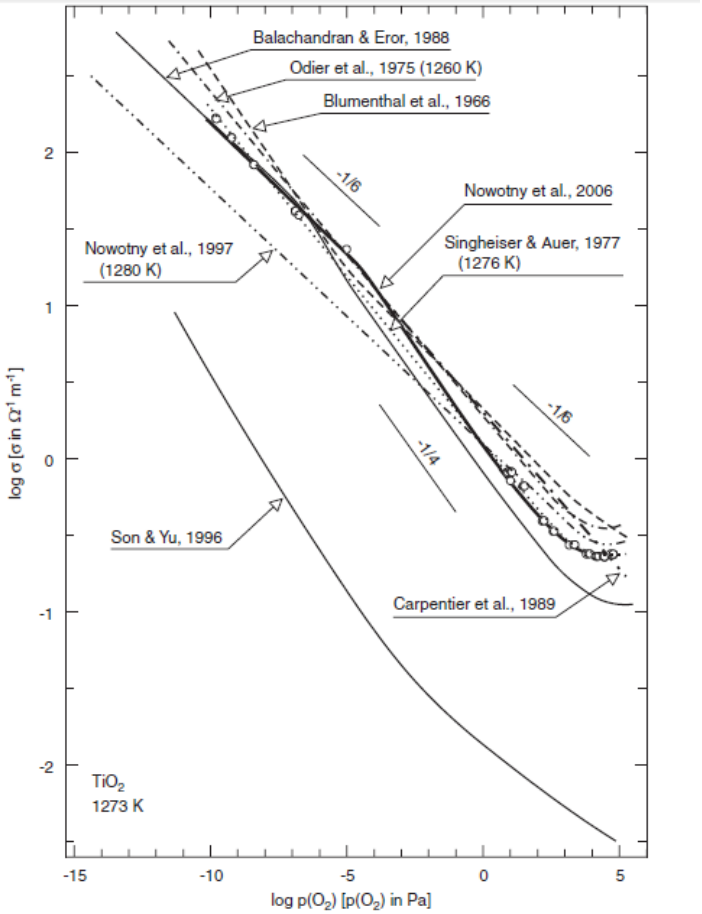

Figure 6.1. Literature reported conductivity values at 1273 K in TiO_2 synthesised with various oxygen partial pressures. Figure taken from ref [20].

The lack of meaningful conductivity data in this case also makes for difficulty in assessing the approximate stoichiometry of the TiO_x layers. Based on previous reported conductivity values in the literature for samples with well-defined and known stoichiometries,[233] it is likely that the materials in this case are close to stoichiometric TiO_2. This is supported by the XPS characterisation carried out, which showed the Ti in the support layer to be predominantly in the Ti^{4+} oxidation state.

XPS characterisation was carried out on the Ti (2p) core level, which indicated a binding energy between 459.91 and 460.10 eV for the Ti ($2p_{3/2}$) level. This is consistent with the Ti^{4+} oxidation state occurring in TiO_2, which typically falls between the ranges of 457.5 and 464.9 eV.[234] In this case the spectra change very little with variation in the size of the supported Pt nanoparticles. The only notable variation relates to the spectrum of electrodes with the largest Pt particle size. The

spectra for the Ti(2p) core level are presented for locations corresponding to both the largest and smallest Pt particle sizes in Figure 6.2.

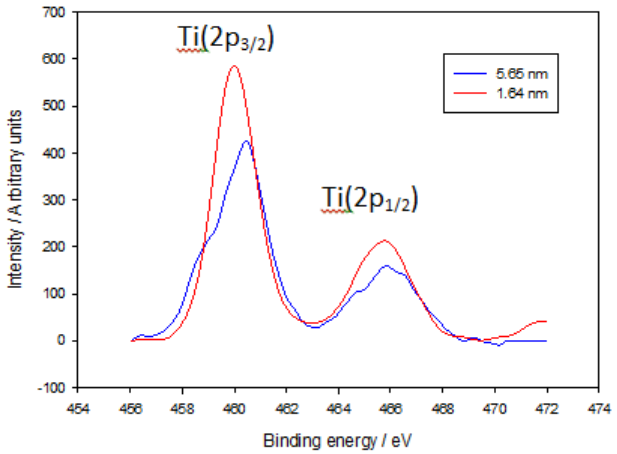

Figure 6.2. XPS spectra of the Ti(2p) core level in TiO_2 supported Pt nanoparticles. Data is shown for locations corresponding to the smallest and largest Pt particle sizes.

The figure above shows the existence of some lower energy shoulders in the spectrum relating to the largest Pt particle size. The position of the Ti($2p_{3/2}$) shoulder at 458.6 eV is in agreement with that expected for Ti^{3+}.[11] This may indicate that the Pt coverage has an effect on the stoichiometry at the surface. It is known that Pt lowers the activation energy for the creation of Ti^{3+}.[147]This, in combination with heating the substrate to 200 ^{o}C during particle deposition, may stimulate creation of oxygen vacancies. This temperature is also in the LTR (low temperature reduction) range referred to in the study strong metal support interactions, where encapsulation is unlikely but strong interaction between the support and particles may exist.[235] The slight shift in the Ti(2p) peaks is likely to arise from a change in the contributions from Ti^{3+} and Ti^{4+} as the particle size changes.

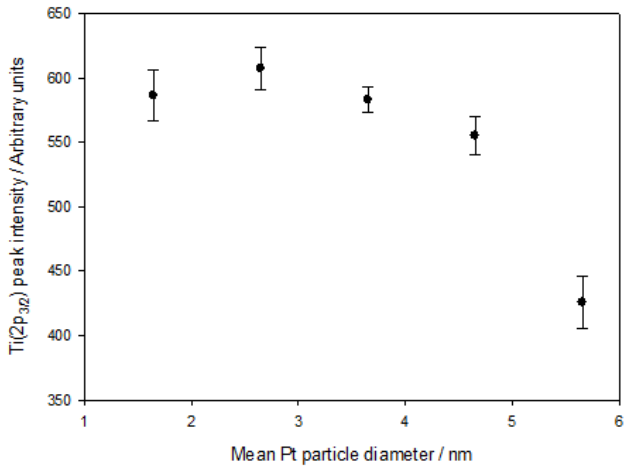

Figure 6.3. Peak intensity of the Ti ($2p_{3/2}$) core level in TiO_2 supported Pt nanoparticles.

The peak intensity also changes slightly as the Pt particle size increases, relating to the increasing coverage of the TiO_2 support at longer Pt deposition times. The initial lack of intensity variation would suggest that 3D type growth occurs primarily from the beginning of the deposition.

XRD characterisation was also carried out on samples with a range of synthesis conditions, which revealed all samples deposited at room temperature to be amorphous. (Figure 6.4).

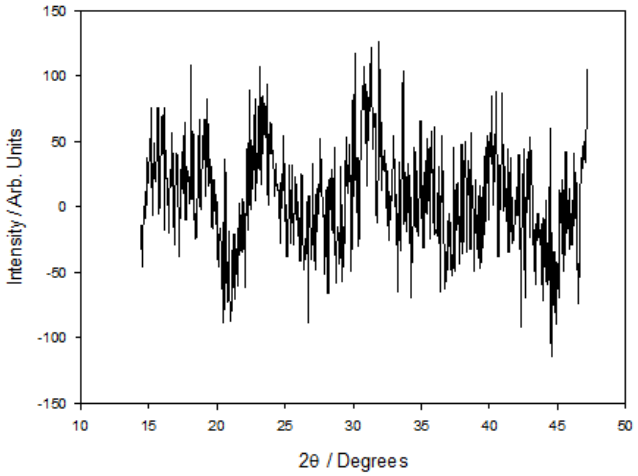

Figure 6.4. X-ray diffraction data for a ~250 nm thick TiO_2 film deposited at room temperature on SiN. A Ti Deposition rate of 4 Å s^{-1} was used with an oxygen flow rate of 1 sccm. The RF power supplied to the atom source was 300 W.

The synthesis of amorphous materials upon deposition at room temperature is in agreement with previous results reported in the literature. Lottiaux reported that substrate temperatures of at

least 623 K were required to produce crystalline films of thicknesses in the range of 35 – 70 nm.[101] Synthesis of anatase TiO_2 films of has however been reported on unheated substrates by sputtering. It was suggested that the relatively high RF power imposed during synthesis gave the impinging gas molecules sufficient energy to induce crystallisation.[236] The film thicknesses in this study were approximately 330 nm.

Initially a post annealing approach was employed, which used the same conditions as the amorphous material presented above. The flow rate was however allowed to vary between 1 and 5 sccm during deposition and the samples were subsequently annealed. This was carried out at a temperature of 450 ^{o}C under an oxygen atmosphere in a tube furnace. The annealing time was 6 hours in each case. The resulting XRD data for the two extremes of oxygen flow rate are presented in figure 6.5.

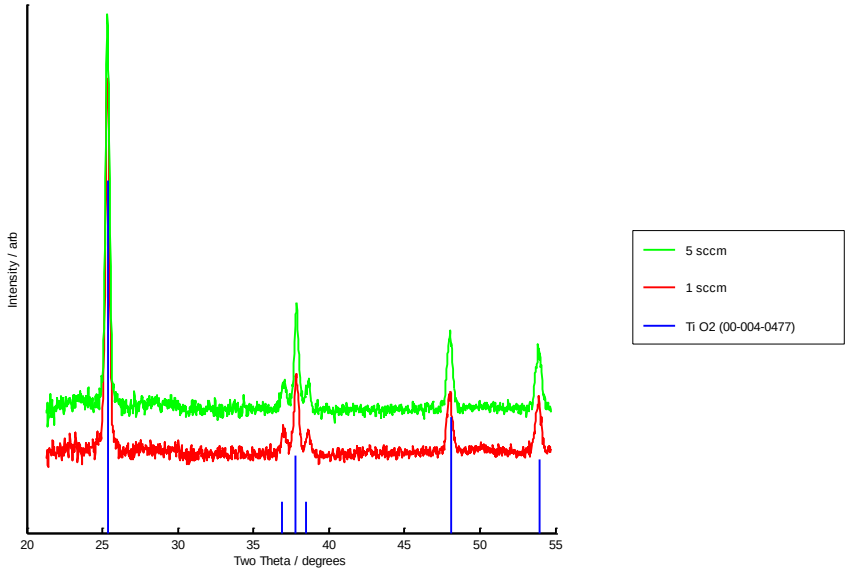

Figure 6.5. X-ray diffraction results for ~250 nm thick TiO_2 films deposited at a rate of 4 Å s^{-1} with varied oxygen flow rates (given in the inset) and an applied RF power of 300 W to the atom source. The films were both annealed at 450 ^{o}C under an oxygen atmosphere for 6 hours. Films were prepared on SiN substrates.

The diffractograms of both materials are in good agreement with that expected for synthetic anatase TiO_2. On visual inspection the films appeared largely identical in appearance, and there is no significant change to the crystallinity or structure in response to varying O_2 flow rates. Where molecular O_2 was used, a slight change in colour was observed as the flow rate changed (Figure 6.6).

Figure 6.6. TiO_2 films (approximately 250 nm thick) deposited on SiO_2 substrates with varied molecular oxygen flow rates (1, 3 and 5 sccm left to right). A Ti deposition rate of 4 Å s^{-1} was used.

The films can be observed to become progressively darker as the O_2 flow rate was reduced. This is likely to represent a change in the stoichiometry of the material. This observation is often reported, whereby increasing concentrations of Ti^{3+} are observed to produce a darker colour in TiO_2 films.[237] In the case of this work, use of atomic oxygen was preferred, since lower stoichiometries introduce a larger number of defect sites that are generally unfavourable for the application of photoelectrochemistry.[237].

In spite of the relatively high level of crystallinity obtained using the post annealing method, it was apparent that this process lead to the formation of cracks in the film which caused shunting at the substrate during photoelectrochemical screening (see Chapter 3). As a result, efforts were undertaken to find a direct route to anatase synthesis without the need for a post annealing step. Instead, the sample was heated to varying temperatures during deposition. When the experiments were carried out, the maximum deposition temperature permissible was approximately 350 ^{o}C, a limit imposed by the temperature stability of the Au screening arrays. Whilst a number of arrays could withstand temperatures in excess of this value, the variation in behaviour between different batches dictated that approximately 350 ^{o}C was the maximum temperature that could the arrays could consistently withstand.

Initially, deposition was carried out at 400 ^{o} C. This produced a relatively weakly crystalline form of rutile. Typical literature reported substrate temperatures for the Anatase to Rutile transformation are approximately 550 – 650 ^{o}C.[238] In each case some level of preferential orientation is apparent with the Rutile films, since several peaks such as the (101) at 36 degrees are not visible. Since rutile is the higher temperature phase, deposition was subsequently carried out at lower

substrate temperatures. Deposition at 300 °C was once again found to form the rutile phase, with anatase formation occurring upon deposition at 200 °C.

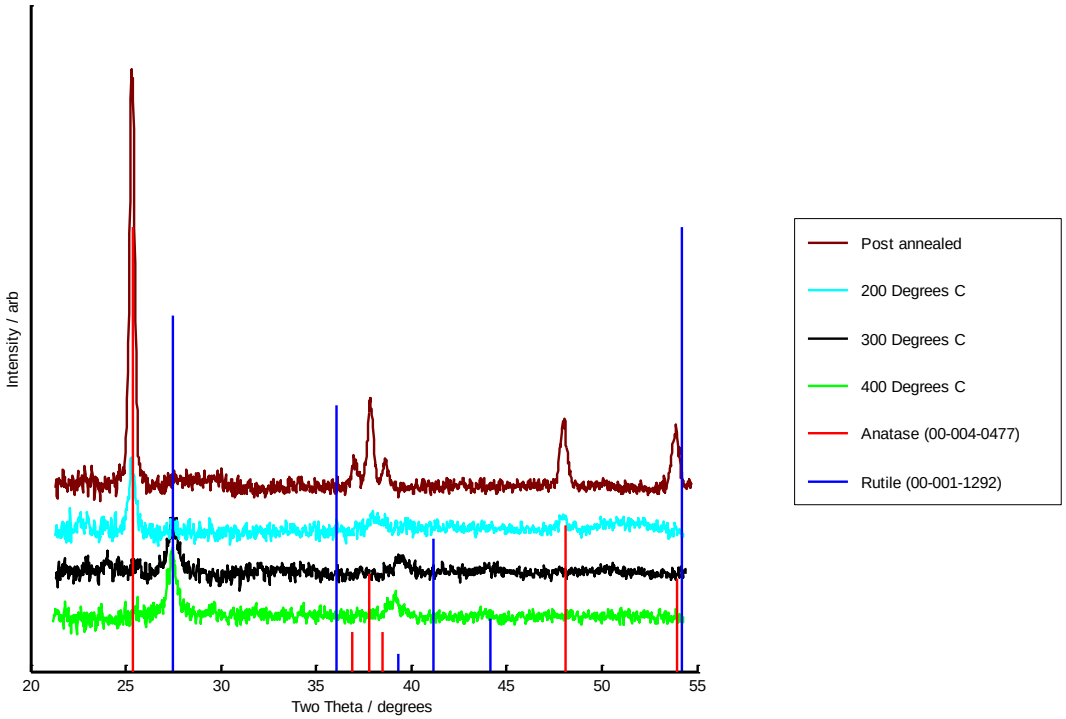

Figure 6.7. X-ray diffraction data for TiO_2 films deposited at different substrate temperatures (given in the inset). In all cases an oxygen flow rate of 1sccm was used with atomic oxygen. An RF power of 300 W was supplied to the atom source in each case. The post annealed sample was annealed for 6 hrs at 450 °C.

It was apparent that the anatase formed by the direct deposition method was less crystalline than that formed via post annealing (Table 6.2). The direct deposition was however chosen for all subsequent depositions due to the incompatibility of the post annealing method with the electrochemical /photoelectrochemical screening. Additionally, the removal of the post annealing phase limits the handling of the sample before screening and thereby reduces the chances of contamination since particle deposition is possible without removing the TiO_2 films from the synthesis chamber.

The XRD data relating to the samples synthesised under different conditions are summarised in Table 6.2. Crystallite sizes (τ) were estimated from the Scherrer equation (Equation 6.1):[239]

(6.1) $$\tau = \frac{K\lambda}{\beta cos\theta}$$

Where K is a dimensionless shape factor (0.9), ʎ is the x-ray wavelength, β is the full width at half maximum and ϴ is the Bragg angle.

Table 6.2.

Oxygen source	Oxygen flow rate / sccm	Substrate temperature / °C	Annealing conditions	Crystalline phase	Crystallite size
Molecular	1	25	450 °C, 6hrs	Anatase	22.10 nm
Atomic	1	25	450 °C, 6hrs	Anatase	27.41 nm
Atomic	5	25	450 °C, 6hrs	Anatase	26.07 nm
Atomic	1	400	N/A	Rutile	15.28 nm
Atomic	1	300	N/A	Rutile	11.42 nm
Atomic	1	200	N/A	Anatase	19.83 nm

6.2. Pt Nanoparticle Deposition

Low equivalent thicknesses of Pt were deposited on the previously prepared TiO_2 substrates at a rate of 0.15 Å s^{-1} in order to form particles. Nucleation and growth at 200 °C resulted in the formation of 10 different particle sizes corresponding to the 10 different rows on the screening arrays. The resulting particles are shown in the TEM images below for the equivalent locations of rows 1, 4, 7 and 10 on the electrochemical screening arrays. These correspond to deposition times of 300, 210, 120 and 30 seconds respectively.

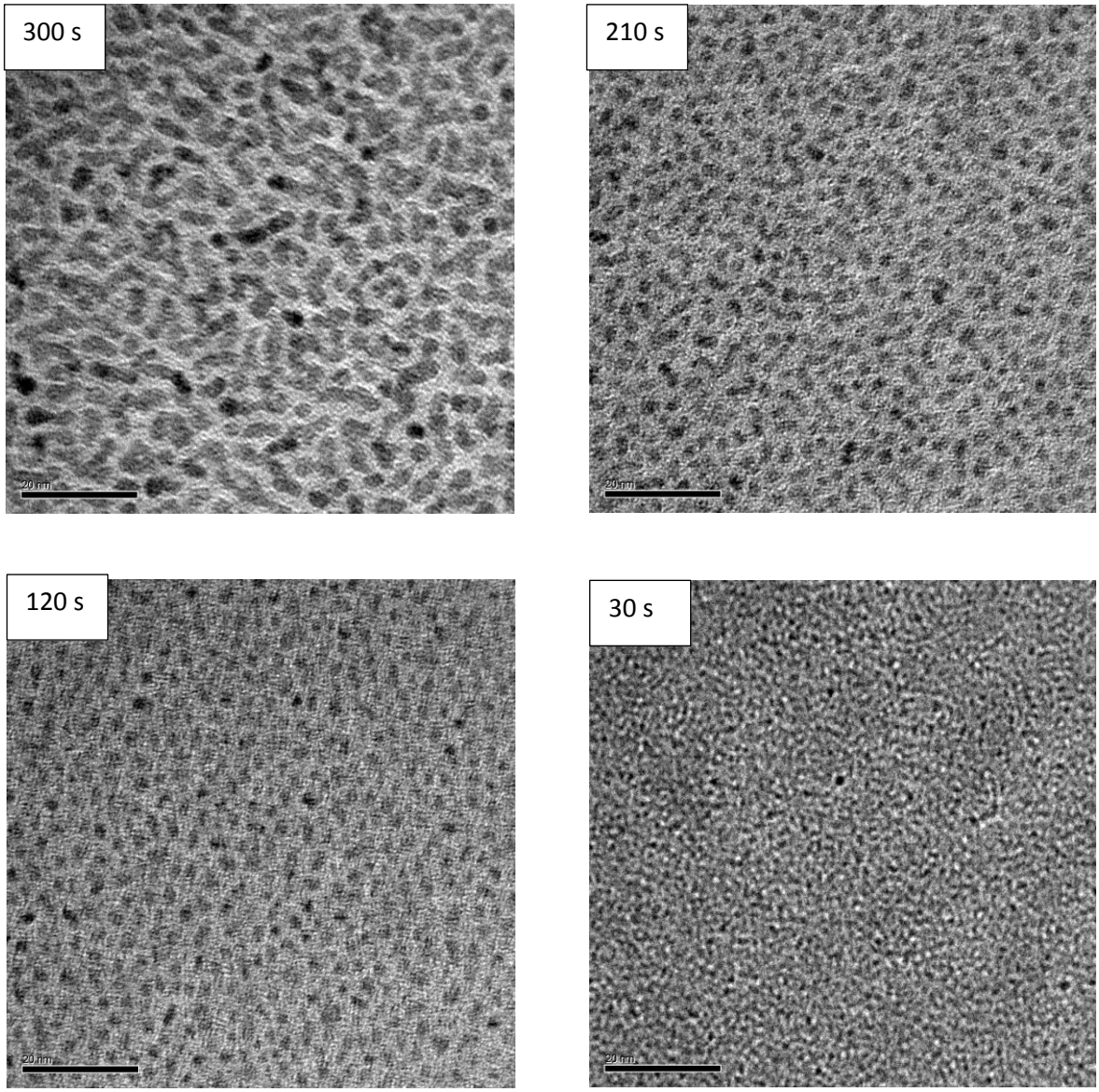

Figure 6.8. TEM images of the Pt particles deposited on anatase TiO_2 at varied deposition times. All images were taken at a magnification of x200K with an accelerating voltage of 300 kV. The scale bars represent 20 nm.

The Pt nanoparticles can be identified from Figure 6.8 as the dark contrasting areas against the lighter TiO_2 support. Initially, small randomly dispersed particles can be seen to form at low Pt deposition times. Subsequently the particles become larger as the deposition time increases, which is consistent with the reported Volmer-Weber type growth expected for Pt on TiO_2.[240] At the longest deposition time the particles begin to coalesce, and produce extended 'worm-like' structures. The average diameters of the deposited nanoparticles were calculated assuming a hemispherical geometry, although clearly a level of error is introduced at the samples with longer

deposition times where coalescence occurs. The analysis was performed with software developed by Ilika technologies.

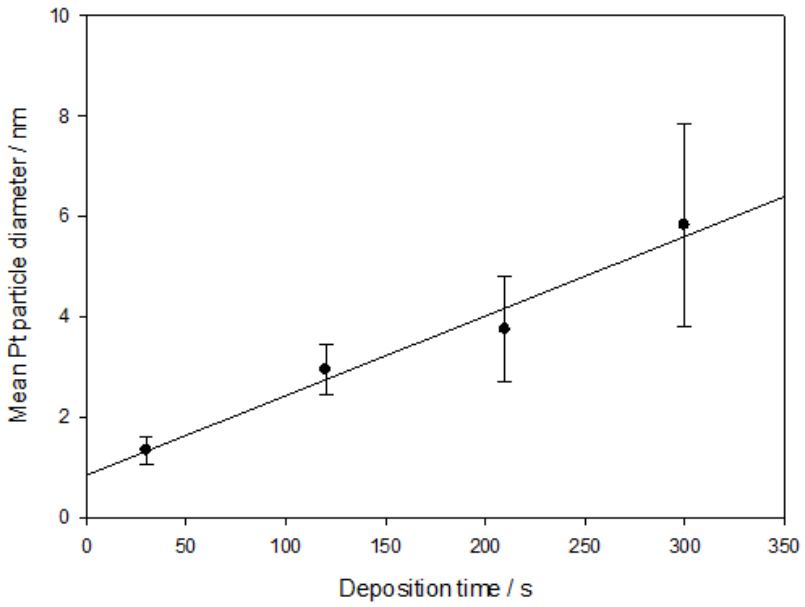

Figure 6.9. Mean particle diameters as a function of deposition time. Values were calculated for the TEM images presented above while assuming a hemispherical particle morphology. Error bars represent 1 standard deviation.

The average diameters of the Pt nanoparticles were found to range from approximately 1.40 to 5.90 nm. The relationship between deposition time and particle diameter also appeared to be approximately linear. The linear regression line between deposition time and particle size was used to estimate the particle diameters for the array positions between the TEM grid locations.

The calculated values as well as those derived from the TEM images are presented in Table 6.3

Table 6.3.

Deposition time / s	Estimated particle diameter / nm	Particle diameter (TEM) / nm
300	5.91	5.82 (+/- 1.82)
270	5.40	
240	4.90	
210	4.40	4.52 (+/- 1.05)
180	3.90	
150	3.40	
120	2.91	2.93 (+/- 0.50)
90	2.39	
60	1.89	
30	1.39	1.33 (+/- 0.27)

Additionally the particle size distributions were characterised for each deposition time on the TEM grids. In each case, the sample data was taken from two different images at each deposition time which produced a sample size of approximately 230 – 250 particles. A Gaussian curve was fitted to each distribution.

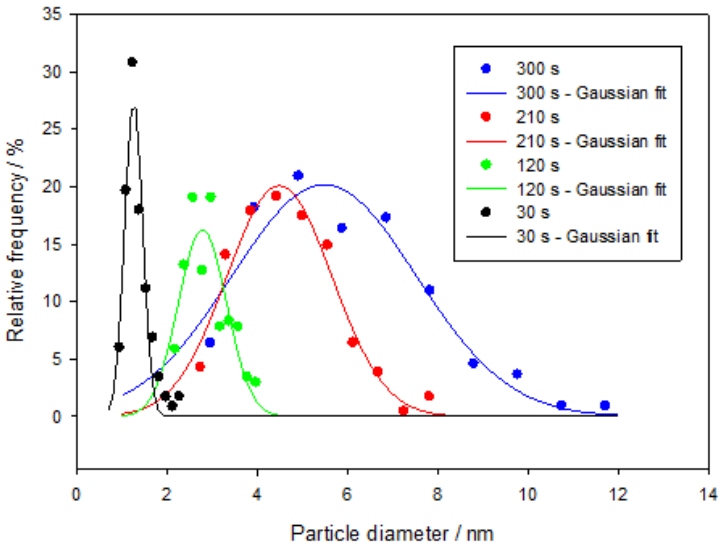

Figure 6.10. Particle size distributions for the different deposition times (given in the inset). The data was calculated from two TEM images for each deposition time, with a sample size of 220 -230 particles in each case.

It can be observed, that the particles formed at lower deposition times are distributed over a relatively narrow size range. As the deposition time increased and the particles grew larger, the size range of the particle distribution became much larger. This is in good agreement with the general trends reported in the literature for the growth of platinum nanoparticles using similar methods.[206]

Additional characterisation of the support and particles was carried out by XPS. Figure 6.11 presents the spectra recorded for the Pt (4f) core level, in which small shift to higher binding energy is observed between the largest and smallest Pt particle sizes.

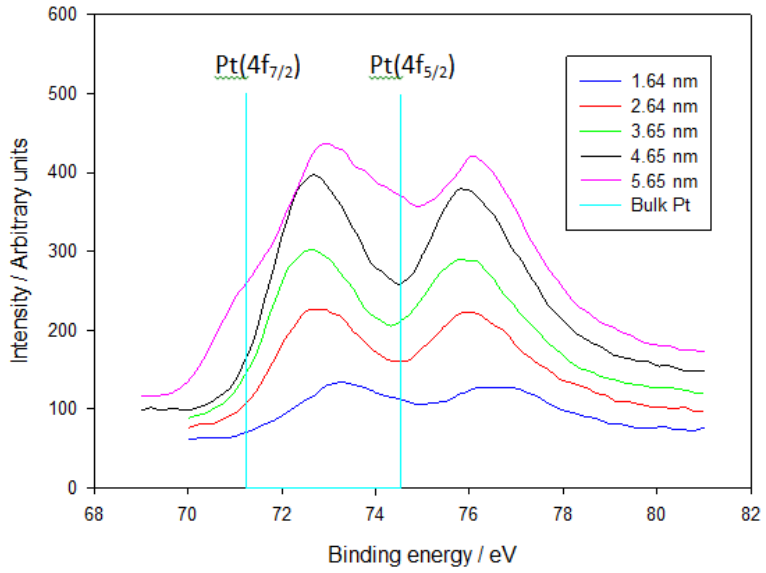

Figure 6.11. XPS spectra of the Pt (4f) core level of TiO_2 supported Pt nanoparticles. Shown also are the peak positions of bulk Pt derived from measurements of a bulk Pt film on TiO_2.

At the largest particle size present on the array, a positive shift in binding energy of 1.46 eV was observed relative to bulk Pt, which further increased to 2.03 eV at the smallest particle size. The general increase in binding energy at smaller particle sizes is consistent with results in the literature,[241] and is typically attributed to final state effects.[242]In this instance the positively charged hole created in the photoemission process is screened over the particle, which leads to a particle size dependant shift in the binding energy. Typically however, these final state effects produce binding energy shifts smaller than those observed here relative to bulk Pt (on the order of 1 eV).[241-242] Additionally, the general appearance of the spectrum relating to the largest

diameter of Pt particle differs slightly to the others. Firstly the binding energy appears to increase again relative to the minimum observed at a particle diameter of approximately 3.65 nm. Secondly two slight shoulder peaks are visible at approximately, 72.1 and 74.6 eV. These peaks are much closer to those of bulk metallic Pt. The binding energies and peak intensities of the Pt($4f_{7/2}$) core level are shown for the various particle sizes in Figure 6.12. Note that in the case of the largest particle size, the largest peaks observed are presented rather than the shoulder peaks.

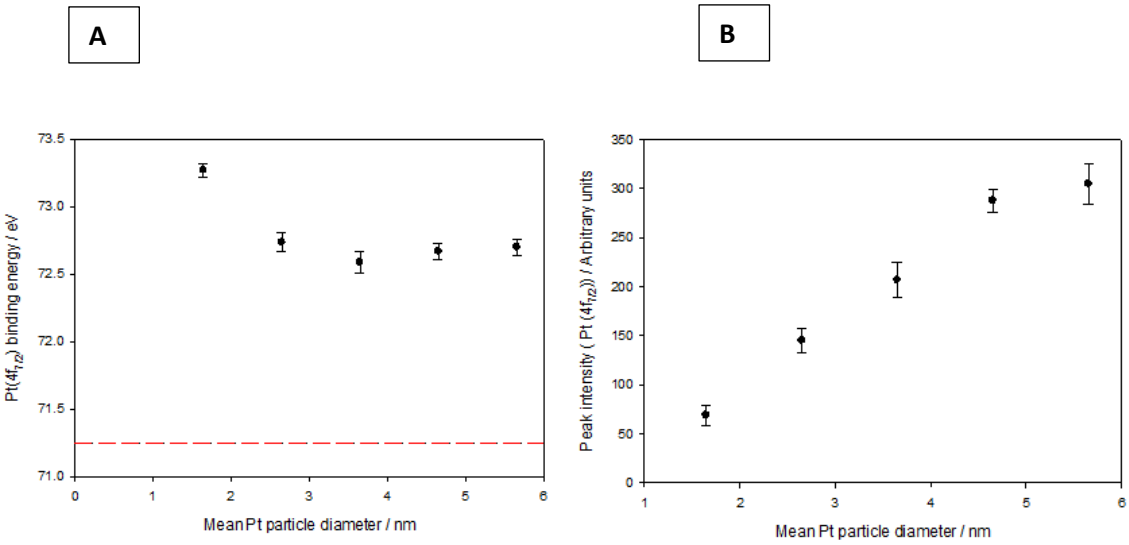

Figure 6.12. Binding energy (A) and peak intensity (B) of the Pt ($4f_{7/2}$) core level in TiO_2 supported Pt nanoparticles.

The observation of the shoulder peak on the largest particle size may suggest that the binding energy shift across the particle size range is not produced entirely by final state effects. The higher binding energy of the main Pt(4f) peaks relative to bulk Pt appear to be more consistent with PtO (72.4 eV- Pt($4f_{7/2}$))[243] rather than metallic Pt. Potentially a differing chemical environment may also contribute to some of the large binding energy shift relative to bulk Pt. Since the arrays were removed from vacuum prior to XPS measurements, it is likely that oxidation of the particles occurred and therefore compromised the results to some extent. It is possible that the apparent increase in binding energy after the minimum at approximately 3.66 nm may indicate that a higher level of PtO species are present at larger particle sizes. Additionally, it can be observed that the intensity of the Pt($4f_{7/2}$) decreases as the particle size is increased. This is to be expected given there is a decrease in the amount of Pt deposited.

6.3. Surface Redox Behaviour

The electrochemical/photoelectrochemical data presented in this chapter is derived from 6 arrays. The experiments carried out and the order in which they were carried out are listed in Tables 6.3 to 6.8. All voltages are expressed vs. RHE.

Table 6.3. #8075 (Au screening array)

Experiments performed	Electrolyte / illumination
CV x 5 at 50 mV s^{-1} (-0.05 – 1.2 V)	Dark: 0.5 M NaOH
CV x 5 at 50 mV s^{-1} (-0.05 – 0.4 V)	Dark 0.5 M NaOH
CV x 3 at 50 mV s^{-1} (-0.05 – 1.2 V)	Dark: O_2 saturated 0.5 M NaOH
CV x 3 at 5 mV s^{-1} (-0.05 – 1.2 V)	Dark: O_2 saturated 0.5 M NaOH
CV x 5 at 50 mV s^{-1} (-0.05 – 1.2 V)	Dark: 0.5 M NaOH
CV x 3 at 50 mV s^{-1} (-0.05 – 1.2 V)	Illuminated with lamp emission current of 8.5 A: 0.5 M NaOH
CV x 3 at 50 mV s^{-1} (-0.05 – 1.2 V)	Illuminated with lamp emission current of 8.0 A: 0.5 M NaOH
CV x 3 at 50 mV s^{-1} (-0.05 – 1.2 V)	Illuminated with lamp emission current of 8.0 A: 0.5 M NaOH
CV x 3 at 50 mV s^{-1} (-0.05 – 1.2 V)	Illuminated with lamp emission current of 7.5 A: 0.5 M NaOH
CV x 3 at 50 mV s^{-1} (-0.05 – 1.2 V)	Illuminated with lamp emission current of 7.0 A: 0.5 M NaOH
CV x 3 at 50 mV s^{-1} (-0.05 – 1.2 V)	Dark: 0.5 M NaOH
CV x 3 at 50 mV s^{-1} (-0.05 – 0.4 V)	Dark 0.5 M NaOH
OCV measurement	3 cycles of 300 s dark followed by 300 s illuminated. 0.5 M NaOH
OCV measurement	As above with O_2 saturated 0.5 M NaOH
CV x 3 at 5 mV s^{-1} (-0.05 – 1.2 V)	Dark: O_2 saturated 0.5 M NaOH

Table 6.4. #8107 (ITO screening array)

Experiments performed	Illumination / electrolyte
CV x 2 at 50 mV s^{-1} (-0.05 – 1.2 V)	Dark: 0.5 M NaOH
CV x 2 at 50 mV s^{-1} (-0.05 – 1.4 V)	Dark: 0.5 M NaOH
CV x 2 at 50 mV s^{-1} (-0.05 – 1.5 V)	Dark: 0.5 M NaOH
CV x 3 at 50 mV s^{-1} (-0.05 – 0.4 V)	Dark: 0.5 M NaOH
CV x 3 at 50 mV s^{-1} (-0.05 – 1.2 V)	Dark: O_2 saturated 0.5 M NaOH
CV x 3 at 5 mV s^{-1} (-0.05 – 1.2 V)	Dark: O_2 saturated 0.5 M NaOH
CV x 5 at 50 mV s^{-1} (-0.05 – 1.2 V)	Dark: 0.5 M NaOH
CV x 3 at 50 mV s^{-1} (-0.05 – 1.2 V)	Illuminated with 8.5 A lamp emission current: 0.5 M NaOH
CV x 3 at 50 mV s^{-1} (-0.05 – 1.2 V)	Illuminated with 8.0 A lamp emission current: 0.5 M NaOH
CV x 3 at 50 mV s^{-1} (-0.05 – 1.2 V)	Illuminated with 7.5 A lamp emission current: 0.5 M NaOH
CV x 3 at 50 mV s^{-1} (-0.05 – 1.2 V)	Illuminated with 7.0 A lamp emission current: 0.5 M NaOH
OCV measurement	3 cycles of 300 s dark followed by 300 s illuminated. 0.5 M NaOH
OCV measurement	As above with O_2 saturated 0.5 M NaOH
CV x 3 at 50 mV s^{-1} (-0.05 – 1.2 V)	Dark: 0.5 M NaOH
CV x 3 at 50 mV s^{-1} (-0.05 – 0.4 V)	Dark: 0.5 M NaOH
CV x 3 at 5 mV s^{-1}	Dark: O_2 saturated 0.5 M NaOH

Table 6.5. #8109 (ITO screening array)

Experiments performed	Illumination / Electrolyte
CV x 5 at 50 mV s^{-1} (-0.05 – 1.2 V)	Dark: 0.5 M NaOH
CV x 3 at 50 mV s^{-1} (-0.05 – 0.3 V)	Dark: 0.5 M NaOH
CV x 3 at 50 mV s^{-1} (-0.05 – 0.4 V)	Dark: 0.5 M NaOH
CV x 3 at 50 mV s^{-1} (-0.05 – 0.5 V)	Dark: 0.5 M NaOH
CV x 3 at 50 mV s^{-1} (-0.05 – 0.6 V)	Dark: 0.5 M NaOH
CV x 3 at 50 mV s^{-1} (-0.05 – 0.3 V)	Dark: 0.5 M NaOH
CV x 3 at 50 mV s^{-1} (-0.05 – 1.2 V)	Dark: 0.5 M NaOH + 5 mM $K_3[Fe(CN)_6]$
CV x 3 at 5 mV s^{-1} (-0.05 – 1.2 V)	Dark: 0.5 M NaOH + 5 mM $K_3[Fe(CN)_6]$
CV x 3 at 50 mV s^{-1} (-0.05 – 1.2 V)	Illuminated with 8.5 A lamp emission current: 0.5 M

	NaOH
CV x 3 at 50 mV s^{-1} (-0.05 – 1.2 V)	Illuminated with 8.0A lamp emission current: 0.5 M NaOH
CV x 3 at 50 mV s^{-1} (-0.05 – 1.2 V)	Illuminated with 7.5 A lamp emission current: 0.5 M NaOH
CV x 3 at 50 mV s^{-1} (-0.05 – 1.2 V)	Illuminated with 7.0 A lamp emission current: 0.5 M NaOH
CV x 3 at 50 mV s^{-1} (-0.05 – 1.2 V)	Dark: 0.5 M NaOH
CV x 3 at 50 mV s^{-1} (-0.05 – 1.2 V)	Dark: 0.5 M NaOH + 5 mM $K_3[Fe(CN)_6]$
CV x 3 at 5 mV s^{-1} (-0.05 – 1.2 V)	Dark: 0.5 M NaOH + 5 mM $K_3[Fe(CN)_6]$

Table 6.6. #8113 (ITO screening array)

Experiments performed	**Illumination / electrolyte**
CV x 5 at 50 mV s^{-1} (-0.05 – 1.4 V)	Dark: 0.5 M NaOH
CV x 3 at 50 mV s^{-1} (-0.05 – 0.4 V)	Dark: 0.5 M NaOH
CV x 5 at 50 mV s^{-1} (-0.05 – 1.4 V)	Dark: 0.5 M NaOH +1 M MeOH
CV x 3 at 50 mV s^{-1} (-0.05 – 1.4 V)	Illuminated with 8.5 A lamp emission current: 0.5 M NaOH + 1M MeOH
CV x 3 at 50 mV s^{-1} (-0.05 – 1.4 V)	Illuminated with 8.0 A lamp emission current: 0.5 M NaOH + 1 M MeOH
CV x 3 at 50 mV s^{-1} (-0.05 – 1.4 V)	Illuminated with 7.5 A lamp emission current: 0.5 M NaOH + 1 M MeOH
OCV measurement	3 cycles of 300 s dark followed by 300 s illuminated. 0.5 M NaOH +1 M MeOH
OCV measurement	3 cycles of 300 s dark followed by 300 s illuminated. 0.5 M NaOH
CV x 3 at 50 mV s^{-1} (-0.05 – 1.4 V)	Dark: 0.5 M NaOH
CV x 3 at 50 mV s^{-1} (-0.05 – 1.4 V)	Illuminated with 8.5 A lamp emission current: 0.5 M NaOH
CV x 3 at 50 mV s^{-1} (-0.05 – 1.4 V)	Illuminated with 7.5 A lamp emission current: 0.5 M NaOH

Table 6.7. #8112 (Au screening array)

Experiments performed	Illumination / electrolyte
CV x 15 at 50 mV s^{-1} (-0.05 – 1.2 V)	Dark: 0.5 M NaOH
CV x 3 at 50 mV s^{-1} (-0.05 – 1.2 V)	Illuminated with 8.5 A lamp emission current: 0.5 M NaOH
CV x 3 at 50 mV s^{-1} (-0.05 – 1.2 V)	Illuminated with 8.0 A lamp emission current: 0.5 M NaOH
CV x 3 at 50 mV s^{-1} (-0.05 – 1.2 V)	Illuminated with 7.5 A lamp emission current: 0.5 M NaOH
CV x 3 at 50 mV s^{-1} (-0.05 – 1.2 V)	Illuminated with 7.0 A lamp emission current: 0.5 M NaOH
OCV measurement	3 cycles of 200 s dark followed by 200 s illuminated. 0.5 M NaOH
OCV measurement	As above with O_2 saturated 0.5 M NaOH
CV x 3 at 50 mV s^{-1} (-0.05 – 1.2 V)	Dark: 0.5 M NaOH

Table 6.8. #8114 (Au screening array)

Experiments performed	Illumination / electrolyte
CV x 5 at 50 mV s^{-1} (-0.05 – 1.4 V)	Dark: 0.5 M NaOH
CV x 5 at 50 mV s^{-1} (-0.05 – 1.4 V)	Dark: 0.5 M NaOH +1 M MeOH
CV x 3 at 50 mV s^{-1} (-0.05 – 1.4 V)	Illuminated with 8.5 A lamp emission current: 0.5 M NaOH + 1M MeOH
CV x 3 at 50 mV s^{-1} (-0.05 – 1.4 V)	Illuminated with 8.0 A lamp emission current: 0.5 M NaOH + 1M MeOH
CV x 3 at 50 mV s^{-1} (-0.05 – 1.4 V)	Illuminated with 7.5 A lamp emission current: 0.5 M NaOH + 1M MeOH
CV x 3 at 50 mV s^{-1} (-0.05 – 1.4 V)	Illuminated with 7.0 A lamp emission current: 0.5 M NaOH + 1M MeOH
OCV measurement	3 cycles of 300 s dark followed by 300 s illuminated. 0.5 M NaOH +1 M MeOH
OCV measurement	3 cycles of 300 s dark followed by 300 s illuminated. 0.5 M NaOH
CV x 3 at 50 mV s^{-1} (-0.05 – 1.4 V)	Dark: 0.5 M NaOH
CV x 3 at 50 mV s^{-1} (-0.05 – 1.4 V)	Illuminated with 8.5 A lamp emission current: 0.5 M NaOH

CV x 3 at 50 mV s^{-1} (-0.05 – 1.4 V)	Illuminated with 8.0 A lamp emission current: 0.5 M NaOH
CV x 3 at 50 mV s^{-1} (-0.05 – 1.4 V)	Illuminated with 7.5 A lamp emission current: 0.5 M NaOH
CV x 3 at 50 mV s^{-1} (-0.05 – 1.4 V)	Illuminated with 7.0 A lamp emission current: 0.5 M NaOH
CV x 3 at 50 mV s^{-1} (-0.05 – 1.4 V)	Dark: 0.5 M NaOH

The surface redox behaviour of an electrode material has a strong effect on its ability to catalyse a number of electrochemical reactions. In particular, the behaviour of platinum towards oxygen reduction, CO oxidation and methanol oxidation has been related to the surface redox properties of platinum.[167, 244] In these cases the ability of Pt to adsorb OH as well as form and reduce Pt oxide is considered to be intimately linked with catalytic activity and is often used to rationalise the observed electrochemical activity trends based on particle size or surface structure. OH adsorption is particularly pertinent in alkaline media due to its adsorption at relatively low potential,[167] and has been speculated to influence the behaviour of Pt towards the aforementioned reactions as well as hydrogen oxidation.[245] The vast majority of studies relating to Pt particle size effects have been carried out in acid electrolytes, although marked changes to the behaviour have been reported in alkali.[165] Cyclic voltammetry was used to assess the surface redox behaviour of anatase TiO2 supported Pt nanoparticles and to elucidate the effects of Pt particle size on such behaviour.

The cyclic voltammetry of a typical sample deposited on an Au electrode array is shown in Figure 6.13. The particles were deposited on anatase TiO_2 in the same manner as that described above.

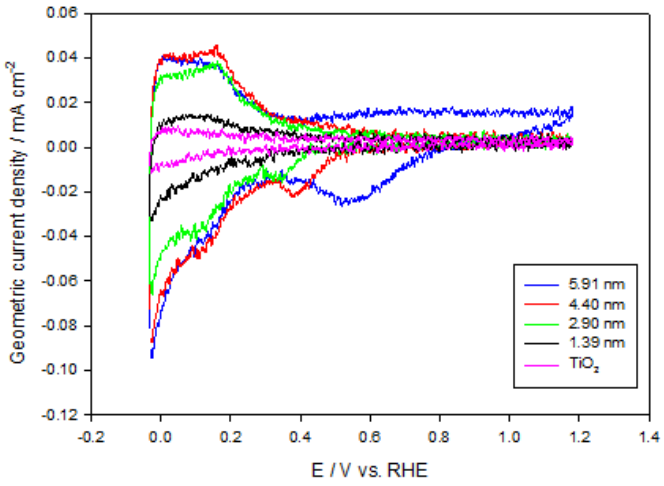

Figure 6.13. Cyclic voltammograms of selected Pt particle sizes on anatase TiO_2 (First cycles shown). Measurements were carried out in 0.5 M NaOH at a potential scan rate of 50 mV s^{-1}. Estimated mean particle diameters are given in the inset. Data is presented for array #8075.

Figure 6.13 shows that the electrochemical response exhibits a number of key features characteristic of Pt in alkaline media.[165] On the cathodic sweep at potentials below approximately 0.3 V an increase in cathodic current appears due to the adsorption of hydrogen onto the Pt surface, similarly to bulk Pt. Typically however, two clear peaks are observable between 0.3 and 0.4 V on bulk Pt due to the occurrence of adsorption at the different crystalline faces of Pt.[245] In this case only one clear peak can be identified at around 0.15 V, which becomes increasingly poorly defined as the particle size decreases. The lack of clear definition in the hydrogen adsorption features or the occurrence of only one peak is often reported in the case of small supported nanoparticles.[246]Changes in pH have also been noted to affect the hydrogen adsorption features on Pt.[247] In alkaline media, the size of the peak relating to the more weakly absorbed hydrogen is often reported to be smaller than in acid. Whilst no conclusive evidence exists to explain this phenomenon, it has been suggested to be a result of competition with adsorbed OH species on the (100) face of Pt.[247]

Negative of the hydrogen adsorption region, the onset of hydrogen evolution can be observed, which is characterised by a sharp increase in cathodic current below 0.05 V. On the subsequent positive going sweep, the adsorbed hydrogen is removed from the surface between the limits of

approximately 0.05 and 0.3 V. Positive of 0.5 V the beginning of oxide formation can be seen at the largest particle size. This is significantly lower than the case of bulk Pt, where oxide formation is generally expected to occur positive of approximately 0.8 V.[244] The formation of a Pt oxide layer is however known to occur at slightly more negative potentials is alkaline media.[248] Additionally a number of adsorbed OH species are known to form on several low index faces of Pt at low potentials.[245] In spite of the oxidative current at low potentials, the degree of oxide formation appears extremely limited when compared with bulk Pt. This is particularly true of the smaller particle sizes. At the smaller particle sizes, almost no anodic current is apparent above approximately 0.5 V. After the hydrogen adsorption region some level of anodic current however persists until about 0.5 V, although no clear peak is visible.

In spite of the extremely low currents recorded in the normal oxide formation region (E > 0.8 V) the reverse scan shows a cathodic peak centred at approximately 0.55 V in the case of the largest particle size. A small peak is observed at all but the smallest particle size which shifts progressively negative as the particle size decreases. In light of the limited degree of oxide formation, the peak may represent reduction of an alternative species to Pt oxide, at least at the smaller particle sizes. It has previously been suggested that a hydrous oxide species may form at low potential in alkaline media, which may even coincide with the hydrogen adsorption/desorption region.[249] The exact nature of the species is unknown, although it has been suggested to take the form of $[Pt(OH)_6]^{2-}$.[249] Potentially the cathodic peak may result from the reduction of these species. Similar behaviour was observed regarding this feature in the samples prepared on ITO substrates (Figure 6.14).

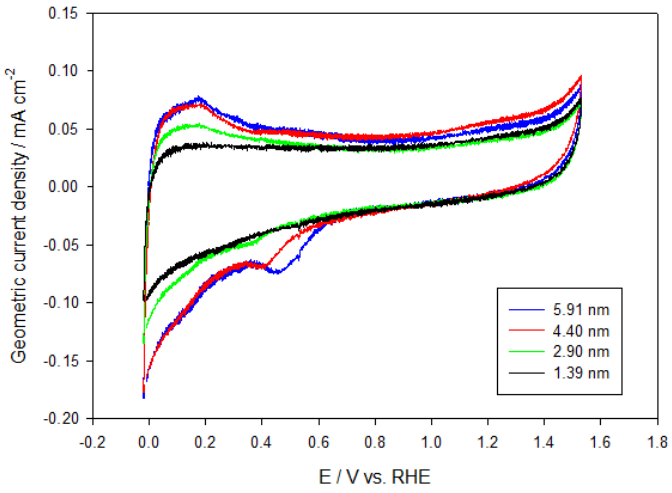

Figure 6.14. Cyclic voltammograms of selected Pt particle sizes on anatase TiO_2 deposited on an ITO substrate. Measurements were carried out in 0.5 M NaOH at 25 ^{o}C with a potential scan rate of 50 mV s^{-1}. Estimated mean particle diameters are given in the inset and the fifth cycles are shown for array #8113.

A significant variation in the absolute values of the current densities can be seen between the samples on ITO and Au substrates. The origin of the larger currents on the ITO substrates were found to be a result of the much larger double layer charging currents observed in the case of the ITO substrate. This was apparent from the blank TiO_2 voltammetry displayed Chapter 4. Once again a large anodic current attributed to the substrate emerged positive of approximately 0.8 V during the first few cycles, which gradually reduced in magnitude with increasing cycle number. This feature was common to all samples prepared on ITO substrates. As a result, the oxide formation features positive of this value are difficult to interpret on the ITO samples.

From Figures 6.13 and 6.14 it is apparent that in general the charges associated with the various voltammetric features decrease as the particle size is reduced. The larger particles pass a larger current due to the increased surface areas created by the larger amounts of platinum deposited. To account for the variation in surface area across the array, the charge under the hydrogen adsorption region was calculated. This was used to estimate the specific Pt surface areas such that the currents could be normalised to this parameter. The area used for the charge integration is shown in Figure 6.18. A complication of this approach however exists in alkaline media, where there is often observed to be a relatively narrow double layer region.[165] This creates difficulty in accurately assigning a baseline value to subtract from the integrated charge. It was found that as the positive potential limit of the cycles increased, the previously mentioned cathodic peak (0.55 V for d = 5.91 nm) grew in size. The position of which was also poorly separated from the onset of hydrogen adsorption. This was particularly true of the smaller particle sizes where a negative shift in the peak position was observed. As the peak current increased, the current in the hydrogen adsorption region also increased slightly.

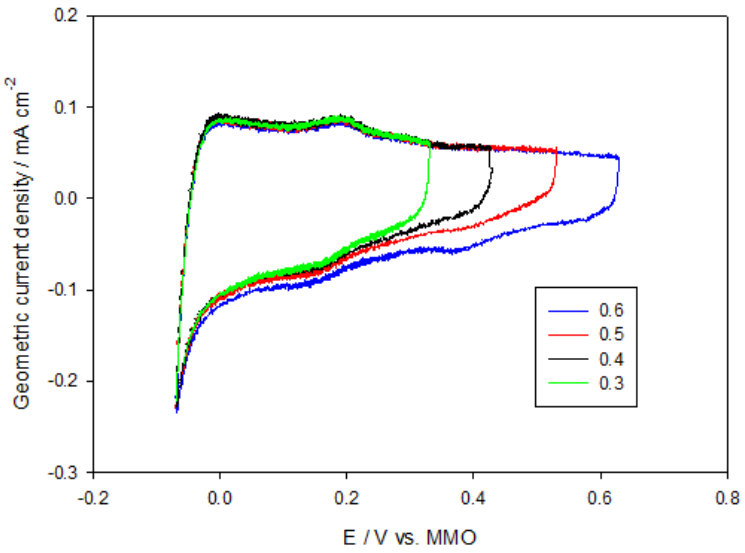

Figure 6.15. Cyclic voltammograms of a typical Pt/TiO_2 electrode on an ITO substrate (estimated mean particle diameter: 5.91 nm) with varied upper potential limits (given in the inset). Measurements were recorded in Ar purged 0.5 M NaOH at a potential scan rate of 50 mV s^{-1}. Data is shown from array #8109

The results obtained when increasing the positive potential limit may suggest that the reduction of the species generated on the positive scan may coincide to some extent with the hydrogen adsorption features. In view of the limited degree of oxide formation, it was considered also that the increased current over the hydrogen adsorption range may have been attributed to the reduction of residual O_2 in the solution. The possibility that the cathodic peak at 0.55 V (for the largest particle size in Figure 6.13) was instead related to this process was also considered. The method of data collection however involved increasing the positive potential limit from the lowest value of 0.3 V up to the highest. Had the experiment been conducted in the opposite manner, the prolonged cycling over a low potential region may have reduced any residual oxygen in the solution and led to the observed behaviour. As a result, this explanation is unlikely to be the cause of the increased cathodic current upon sweeping the potential to a higher positive value. After reaching the highest positive limit, a single cycle employing the lowest potential limit was again recorded. Subsequently, a single cycle was recorded with the maximum potential limit. On both occasions, the behaviour immediately reverted back (Figure 6.16) to that seen in Figure 6.15. It would therefore seem unlikely that the changes observed in the hydrogen adsorption region occur purely as a result of increasing cycle number.

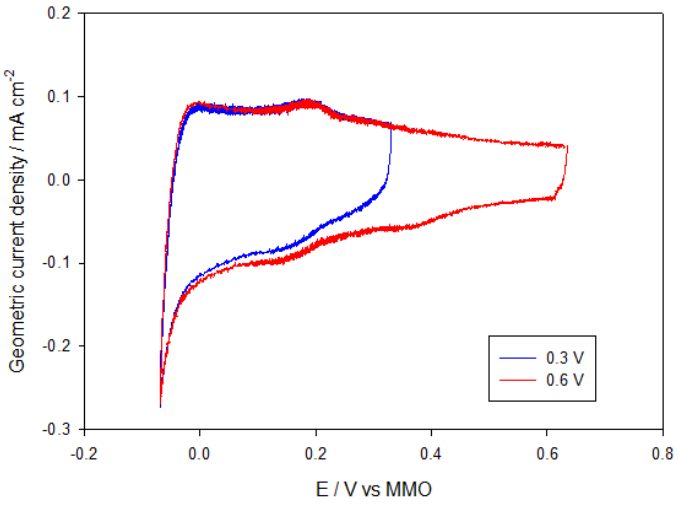

Figure 6.16. Cyclic voltammograms of a typical Pt/TiO_2 electrode on an ITO substrate (estimated mean particle diameter: 5.91 nm) with varied upper potential limits (given in the inset). Measurements were recorded in Ar purged 0.5 M NaOH at a potential scan rate of 50 mV s^{-1}. Data is shown from array #8109

Additionally it was observed that a slight anodic peak was visible beginning at approximately 0.4 V after a number of cycles had been performed (Figure 6.17). The peak was most clearly visible at the larger particle sizes, and also was more pronounced on samples incorporating an ITO substrate. No such feature was observed on either the blank ITO substrate or TiO_2 films without Pt particles. This may result from the adsorption of OH species as previously suggested and may account for the presence of the cathodic peak at smaller particle sizes where no current was observed in the typical region where oxide formation takes place. Furthermore, during methanol oxidation experiments the onset potential approximately coincided with the onset of the peak A1. Generally it is accepted that adsorbed OH species are necessary for the reaction to proceed,[249] and thus it is possible such species begin to form at around the vicinity of A1. However, it cannot be ruled out entirely that some degree of O_2 reduction may contribute to the cathodic peak proposed to relate to OH/oxide stripping. It is likely also that the prolonged cycling has a cleaning effect or induces a restructuring. The emergence of the peak may therefore stem from such effects.

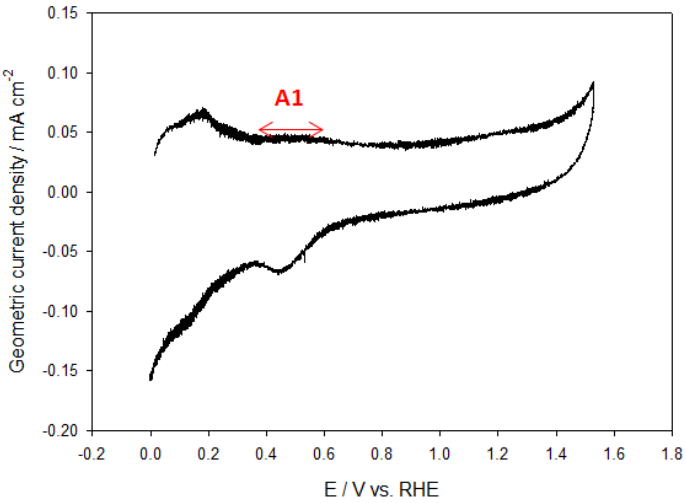

Figure 6.17. Cyclic voltammogram of a Pt/TiO_2 electrode (estimated particle diameter 4.90 nm) on an ITO substrate. Measurements were carried out in Ar purged 0.5 M NaOH with a potential scan rate of 50 mV s^{-1}. The tenth cycle is shown. The suggested region of OH adsorption peak is defined as A1. Data is shown from array #8107

In light of the behaviour shown above, calculations of surface areas were obtained from voltammograms where the upper potential value was limited to 0.4 V. An example of the region over which the charge was integrated is depicted in Figure 6.18. This approach was used in order to prevent any overestimation of the surface areas that might be caused by inclusion of charge relating to processes other than hydrogen adsorption.

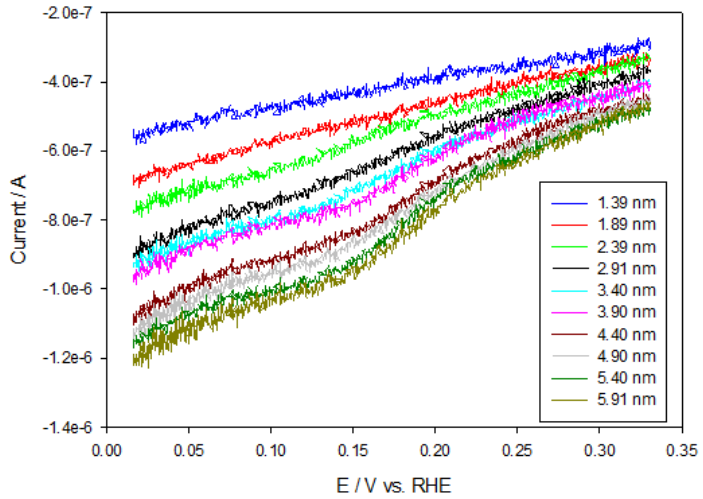

Figure 6.18. Enlarged view of the hydrogen adsorption region used for estimation of Pt surface area (on an ITO substrate). Data is shown for the 10 different particle sizes, which were collected in 0.5 M NaOH at a potential scan rate of 50 mV s^{-1}. Data is shown from array #8075

The charge under the hydrogen adsorption area was subsequently divided by -210 µC, which represents the charge required to form 1 monolayer of hydrogen on 1 cm^2 of platinum.[250] A baseline correction was also applied in all cases. This led to a good general agreement between the values obtained for samples deposited on both ITO and Au substrates.

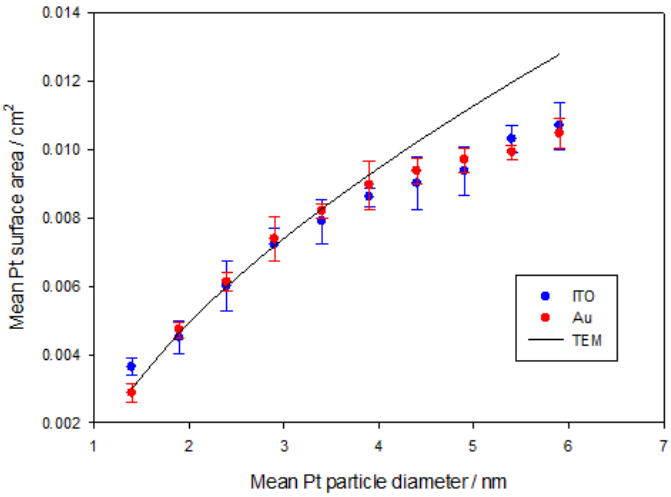

Figure 6.19. Mean Pt surface areas calculated from the charge under the hydrogen adsorption areas on ITO and Au substrates. Also shown is the best fit derived from the surface areas calculated from the TEM images. Data is shown for arrays #8107 and #8075

The estimated Pt surface areas were also in relatively good agreement with those calculated from the TEM images. A greater variation in the calculated surface areas however occurs at the larger particle sizes, where coalescence was observed to take place. As a result, the TEM derived surface areas deviate more from those obtained electrochemically on account of the lesser applicibility of the hemispherial model used in the calculations.

The voltammograms were subsequently normalised to take into account the variation in Pt surface area across the particle size range. The resulting voltammograms for selected Pt particle sizes are shown in Figure 6.20. In this case, Au was used as the substrate material.

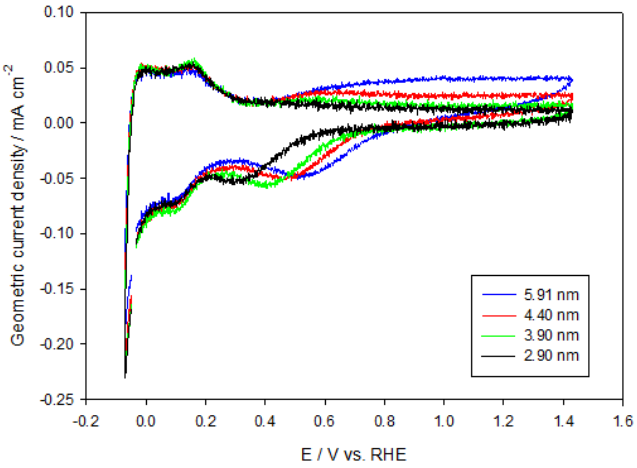

Figure 6.20. CVs of selected Pt particle sizes on anatase TiO_2. Current densities are scaled to the calculated specific Pt surface areas previously calculated. Measurements were conducted in 0.5 M NaOH with a potential scan rate of 50 mV s^{-1}. The first cycles are shown for array #8114.

Generally the voltammetry appears relatively similar, although as noted some differences in the oxide stripping and formation behaviour are apparent between the different particle sizes. Only at the largest 2-3 particle sizes on the array was any clear anodic current generated in the region where oxide formation is expected to occur. The majority of the electrodes show a reduction peak on the reverse scan, which moves negative by approximately 150 - 250 mV between the largest and smallest Pt particle sizes presented in Figure 6.21. Although no clear peak was observed at the smallest particle size, the pronounced negative shift with a decrease in particle size may lead to the peak being obscured by the hydrogen adsorption features.

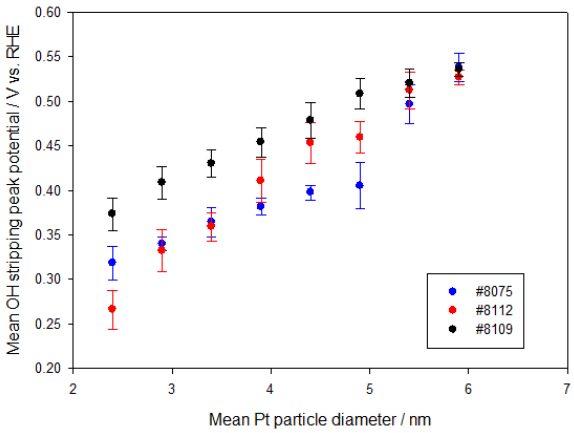

Figure 6.21. Mean peak potential of the oxide stripping peak as a funtion of particle size for three arrays (given in the inset). Measurements were carried out in 0.5 M NaOH at a potential scan rate of 50 mV s^{-1}. Data is not shown for the two smallest particle sizes, as the peak position could not clearly be identified.

The negative shift in the proposed OH reduction peak is consistent with the literature reported trends seen for the oxide stripping peak on carbon and TiO_2 supported Pt nanoparticles in alkaline media, although the level of shift is comparitively larger in this case.[165, 251] The same qualitative effect was also observed on the ITO substrates.

The limited degree of oxide formation may suggest that the kinetics of oxide formation are much slower at the smaller Pt particles. Additionally, the rectifying properties of the support may be altered by the incorporation of Pt on the surface of the TiO_2. It is known that the particle size of a metal has a significant effect on the level of band bending in the semiconductor to which they are attached.[21] It is therefore possible that an increased level of rectification may account for a lack of oxide formation on the smaller particles. Additionally, the Pt particles may create surface states on the TiO_2 support that alters its semiconducting properties to varying degrees.[252]

A variation in the voltammetric behaviour was also evident upon repeated cycling of the electrodes. With increasing cycle number, the proposed OH stripping peak shifted slightly negative, which was particularly apparent at the larger particle sizes (Figure 6.22).

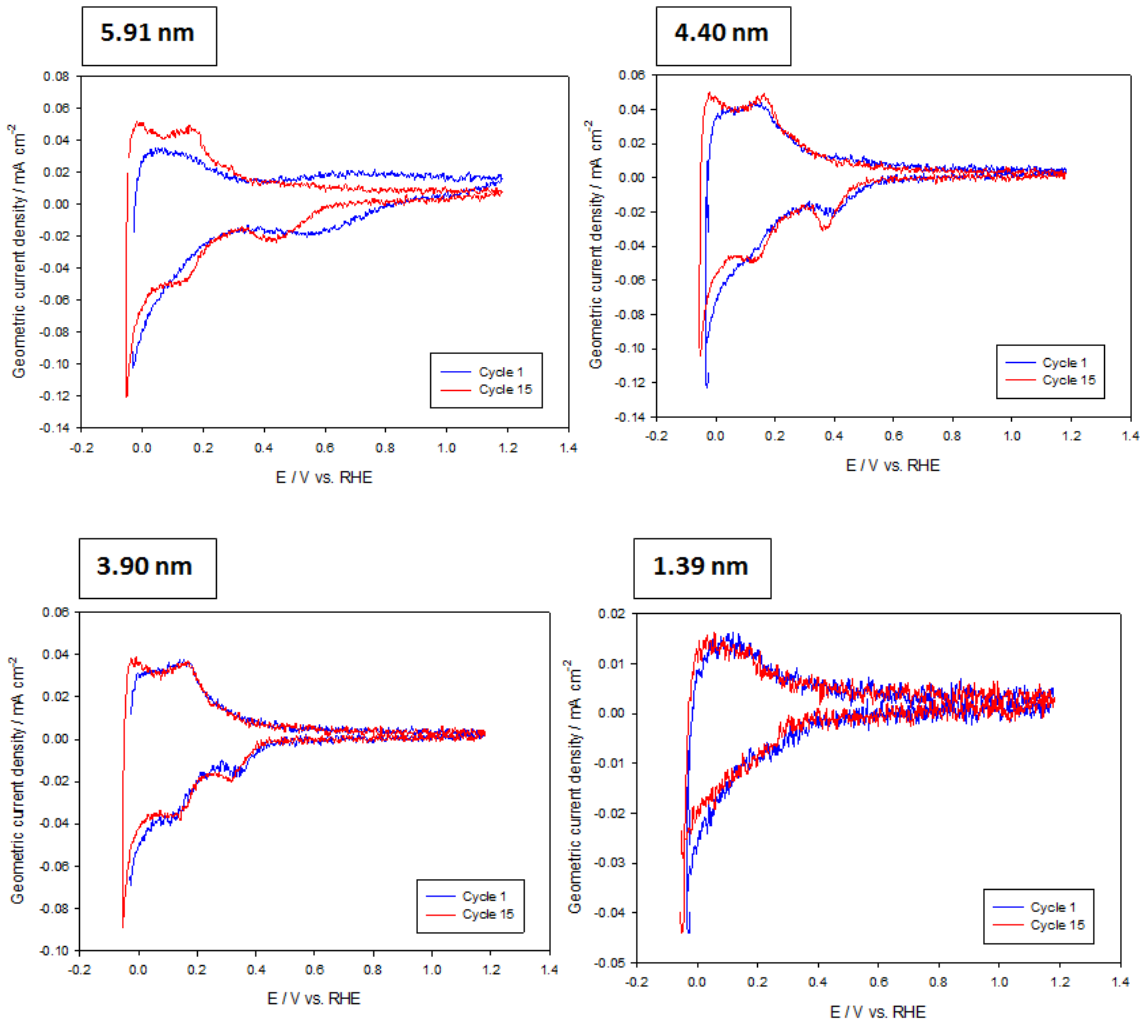

Figure 6.22. Cyclic voltammograms of selected Pt particle sizes on anatase TiO_2 with an Au substrate material. The cycle number is given in the inset. All measurements were conducted in Ar purged 0.5 M NaOH with a potential scan rate of 50 mV s^{-1}. Data is shown for array #8112.

In general, repeated cycling caused the hydrogen adsorption features to become slightly sharper. This is relatively common for Pt, which is often cycled repeatedly as a pretreatment before commencing measurements. After performing multiple cycles, the current attributed to oxide formation diminished at the larger particle sizes, however a reduction peak was still present positive of the hydrogen adsorption region. The small oxidation peak present in Figure 6.17 became visible at this point where the additional oxidation current above 0.6 V had diminished. The peak was generally more pronounced on the ITO substrates, although some level of anodic current remained after the hydrogen adsorption region on the samples with Au substrates also. Furthermore, the same peak was observed on the α-Fe_2O_3 supported samples on both substrate types. The appearance of the peak on all substrates and supports would suggest that the process arises from the Pt rather than any of the support or substrate materials. Additionally, no such

peaks were evident on the blank oxide supports or substrate materials. The changes with cycling are likely to result from a cleaning of the Pt surface. Possibly the cycling to relatively high potential may also lead to some level of dissolution of the smaller particles.

It was observed also that the assigned OH stripping peak was affected to a slightly greater degree at the larger particle sizes. The effect of cycling on the oxide stripping peak is shown for the various particle sizes in Figure 6.23.

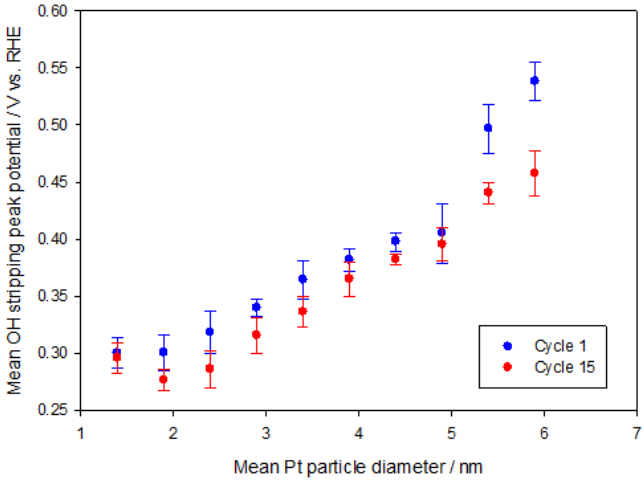

Figure 6.23. Mean peak potential of the oxide stripping peak as a funtion of particle size. The sample in this case was deposited on an Au substrate and measurements were carried out in 0.5 M NaOH at a potential scan rate of 50 mV s^{-1}. The cycle number from which the data was obtained is given in the inset. Data is shown for array #8112

Since the formation of Pt oxide could only be identified at the largest 2 – 3 particle sizes, the more pronounced negative shift of the oxide stripping peak at these particle sizes may result from the ceasation of oxide formation. After cycling the peak may instead be dominated by reduction of a more reversible OH species or an additional background process.

6.4. Ferricyanide Reduction

A number of different factors may contribute to the surface redox behaviour observed in the samples prepared within this work. In addition to intrinsic particle size effects, the semiconducting properties of the TiO_2 support may play a role. In particular the particles may alter the electrical properties of the TiO_2 support to varying degrees depending on their size.

In an attempt to decouple the conventional particle size effects (such as geometric effects and variations in interfacial kinetics) from any alteration of the support behaviour by the particles, a simple redox couple was used. The reduction of $Fe(CN)_6^{3-}$ is a reversible outer sphere electron transfer on metallic electrodes, which represents a kinetically less demanding reaction than the oxide formation/stripping reactions on Pt. As a result, the voltammetry obtained in this media may reflect the intrinsic ability of the electrodes to transfer electrons, in the absence of effects relating to a variation in interfacial kinetics. Cyclic voltammetry was performed in 0.5 M NaOH with the addition of 5 mM $K_3Fe(CN)_6$ at a scan rate of 5 mV s^{-1}. The resulting voltammetry is shown in Figure 6.24.

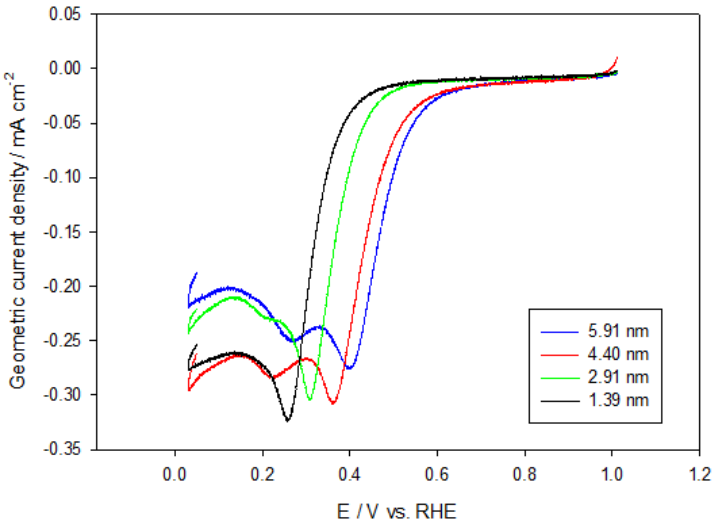

Figure 6.24. First cathodic sweep of selected anatase TiO_2 supported Pt particle sizes (given in the inset) in 0.5M NaOH + 5mM $K_3Fe(CN)_6$. The substrate material was ITO and a potential scan rate of 5 mV s^{-1} was used in all cases. Data is shown from array #8109.

Figure 6.24 shows that a substantial negative shift in the onset of ferricyanide reduction occurred as the Pt particle size reduced. In light of the facile kinetics of the ferricyanide/ferrocyanide redox couple on platinum, the significant negative shift of the reduction relative to bulk Pt may arise from the behaviour of the support. This is to be expected in the case of an n-type semiconductor, since the surface electron concentration is extremely small until the applied voltage is near to the flat band potential of TiO_2 (approximately -0.05 to -0.1 V vs. RHE).[226] Additionally, the onset was more positive than that of the blank TiO_2 support in all cases. In all cases the reoxidation of the reduced species occurred to a negligible degree. The Ferricyanide reduction onset potential and the oxide stripping peak potential are shown in Figure 6.25.

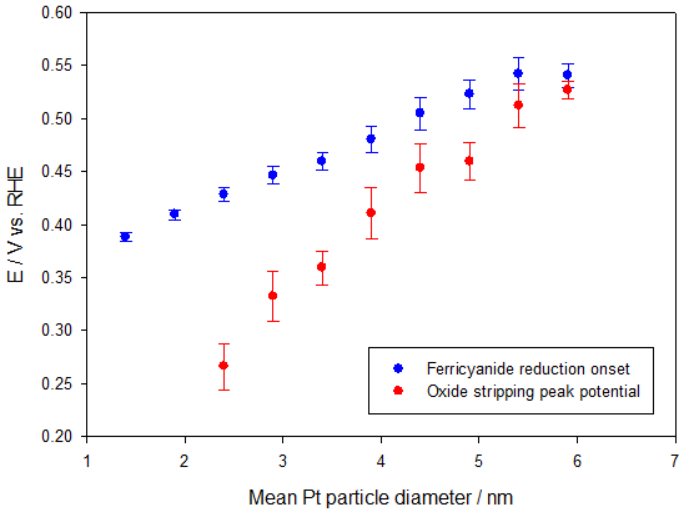

Figure 6.25. Mean peak potential of the oxide stripping peak and the onset of ferricyanide reduction (defined as the potential to reach a geometric current density of -0.038 mA cm^{-2}). Note that the oxide stripping peak potentials were taken from a separate sample prepared on an Au substrate. Data is derived from arrays #8075 and #8109

The overall trend for the ferricyanide reduction onset potential correlates closely with that for the oxide/OH stripping peak Figure 6.25. Since the reduction of ferricyanide is a kinetically undemanding reaction, it may describe the ability of the semiconductor to transfer electrons to the surface of the electrode. The lower onset potential for the larger particles may be indicative of a reduced barrier height, i.e. a lesser degree of band bending inside the semiconductor surface at equilibrium. Additionally, in the event of surface state formation upon addition of Pt, a higher number of surface states may result from increased Pt coverage. Furthermore, if the level of band

bending remained unchanged as the particle size varied, one would simply expect a variation in the reduction peak current density. Since the onset potential also changes, it is clear that the ability of the support to supply electrons is altered. Additionally, it can be observed from Figure 6.24 that two reduction peaks exist in the majority of cases. The second more negative peak also becomes less observable as the particle size decreases. This is likely to arise from the fact that a distribution of particle sizes are present on each electrode, which have varying effects on the level of band bending in the TiO_2. Since the distribution of particle sizes is narrower at smaller average diameters, it is to be expected that any additional reduction peaks will be less easily observed.

The similarity of the trends in Figure 6.25 may suggest that the variation in surface redox behaviour cannot be explained entirely by intrinsic particle size effects which effect interfacial kinetics. Although the ferricyanide reduction onset does not accurately describe the flat band potential, it may serve as an indication of the potential at which the material gains adequate conductivity to drive the simple electron transfer reaction assuming no competing reactions occur. In this case, it may be that the changes in support characteristics dominate the trends in terms of surface redox behaviour.

In addition to the charge transport behaviour of the semiconductor, effects relating to the charge transfer at the Pt particles cannot be ruled out with regard to the variation in surface redox behaviour. If the semiconductor charge transport characteristics are the sole cause of the behaviour, then a constant difference between the ferricyanide reduction onset potential and the oxide stripping peak potential would be expected. Figure 6.25 shows this not to be the case.

Overall it is likely that the semiconducting nature of the support dictates that a large overpotential is required at all particle sizes to reduce adsorbed oxygen containing species as well as Ferricyanide. This rectifying properties were evident from the lack of reoxidation that took place on the subsequent anodic sweep in Ferricyanide containing media. Additionally the particle size may influence the surface redox behaviour by other means, most likely either a reduction in the kinetic ability to reduce adsorbed oxygen containing species or a variation in the adsorption strength of such species. However the notion that the rectification properties of the support have an impact on the surface redox behaviour was brought into question by the results of the Pt/Fe_2O_3 samples (Chapter 7). In this case a similar level of reduction for the oxide/OH stripping peak potential was observed as the particle size decreased. This was in spite of the reoxidation of the reduced ferrocyanide species occuring with relative ease at all Pt particle sizes.

6.5. Oxygen Reduction

A number of previous studies have shown a reduction in ORR specific activity as the size of Pt nanoparticles decrease in both acid and alkaline media. This has been found to be true of platinum supported on both C and TiO_2.[154, 165, 253]

It is generally reported that the kinetics of oxygen reduction are enhanced in alkaline media.[166] This is suggested to result from the lesser degree of specific anion adsorption in alkali. However due to a general lack of alkaline ion exchange membranes, the reaction is most often investigated and optimised in acidic media for the purpose of PEM fuel cells. The oxygen reduction reaction was studied in this work by cyclic voltammetry in oxygen saturated 0.5 M NaOH. CVs were collected at a scan rate of 5 mV s^{-1}, which are shown for selected Pt particle sizes in Figure 6.26

Once again it can be observed that a significant shift in the onset potential occurs in response to a change in particle size. As in the case of ferricyanide reduction, the onset is shifted progressively negative as the particle size decreases. Similarly to the ferricyanide reduction, there is also an extremely large overpotential requirement in the case of all particle sizes. The level of shift in onset potential is in good agreement with previously reported data involving amorphous TiO_2 supported Pt nanoparticles of a similar size range in $HClO_4$.[244]

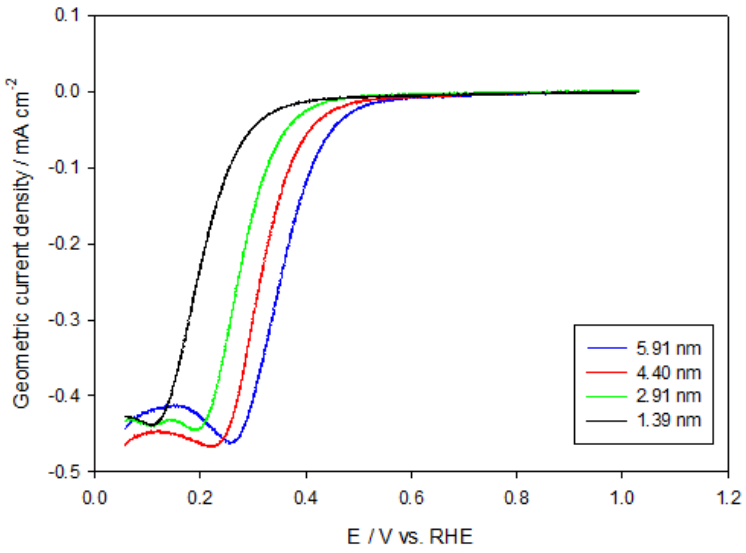

Figure 6.26. First cathodic sweep of selected Pt particle sizes (Given in the inset) on anatase TiO_2 in O_2 saturated 0.5 M NaOH. A potential scan rate of 5 mV s^{-1} was used and the substrate material was ITO. Data is shown for array #8107.

Although the oxygen reduction reaction is a much more kinetically demanding reaction than ferricyanide reduction, the overall onset potential trends of the two processes remain remarkably similar (Figure 6.27). In all cases however, the Oxygen reduction onset potential is comparatively more negative than that for ferrocyanide reduction.

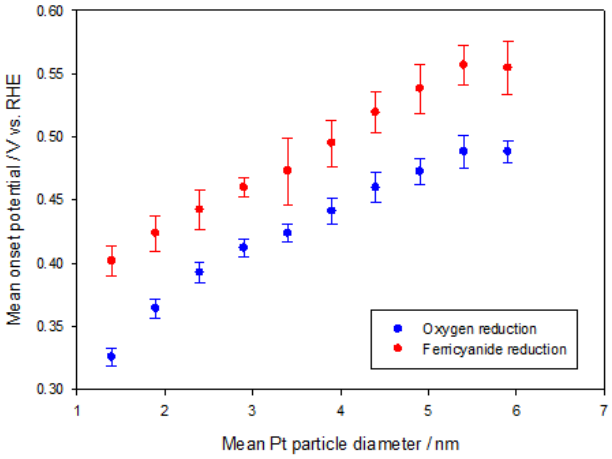

Figure 6.27. Mean onset potential for the oxygen reduction reaction and ferrocyanide reduction. The onset was defined as the voltage to generate -0.028 mA cm^{-2} with respect to the geometric surface area of the electrode. Data was derived from the first cycles where a scan rate of 5 mV s^{-1} was used. Data is shown from arrays #8107 and #8109.

The onset potentials were subsequently calculated where the current densities were scaled to the electrochemically active Pt surface areas. Due to the significant negative shift in onset potential at lower Pt particle sizes, the overall trend remains similar, with an almost linear reduction in ORR specific activity (Figure 6.28).

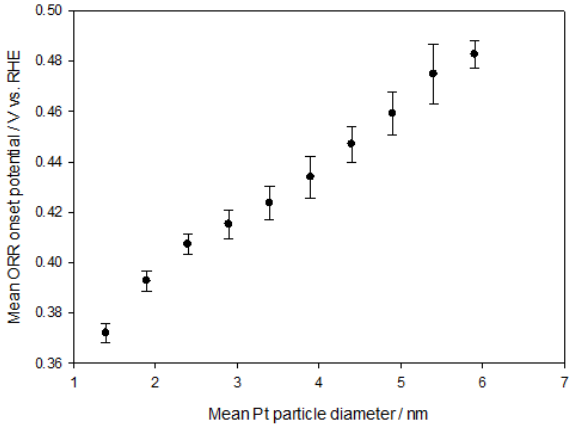

Figure 6.28. Mean ORR onset potential as a function of Pt particle size. The onset potential was defined as the point where a specific current density (with respect to the estimated Pt surface area) of -0.028 mA cm^{-2} was reached. Data is shown from array #8107

It has previously been proposed that the reduction in activity results from the decreasing ability to reduce adsorbed OH or platinum oxide at smaller particles.[167] This is typically rationalised in terms of the observed negative shift in the potential at which platinum oxide is stripped from the surface. In this case, oxide formation was severely limited at all Pt particle sizes, but was particularly evident on smaller particles. It has previously been shown that the oxide formation and stripping features are significantly supressed on anatase TiO_2 supported Pt when compared with equivalently sized particles on rutile TiO_2.[254] The rectifying properties of the TiO_2 substrate were not thought to impart this behaviour, since a number of simple outer sphere reactions were reported to proceed with relative ease on the materials under investigation. The oxidation of ferrocyanide however occurred to a negligible degree on the samples in this work. It is likely therefore that the rectifying properties do indeed contribute to some extent in the negative shift of the oxygen reduction reaction onset.

In light of the similarities between the two trends in figure 6.28, it is possible that the factor causing the negative shift in the onset of ferricyanide reduction also effects the ORR onset trend. This may be a modulation of the support characteristics by the Pt particles or may also be attributed to the change in the oxide/OH stripping potential at different particle sizes. It is likely that both effects contribute partly to the trends observed. Furthermore it was previously found that on carbon supported Pt the trend in terms of oxide reduction correlated well with that of the ORR onset in acid media (0.5 M $HClO_4$). On the other hand, the correlation between the oxide stripping potential and the onset of oxygen reduction were found to agree to a lesser extent where TiO_2 was used as the support.[244] Possibly therefore the discrepancy was influenced by a change in the ability of the support to transfer electrons. This may operate by a variation in the level of band bending imposed by different particle sizes. This is schematised in Figure 6.29 with regard to the known effects of metal particle size on the level of band bending inside the semiconductor.

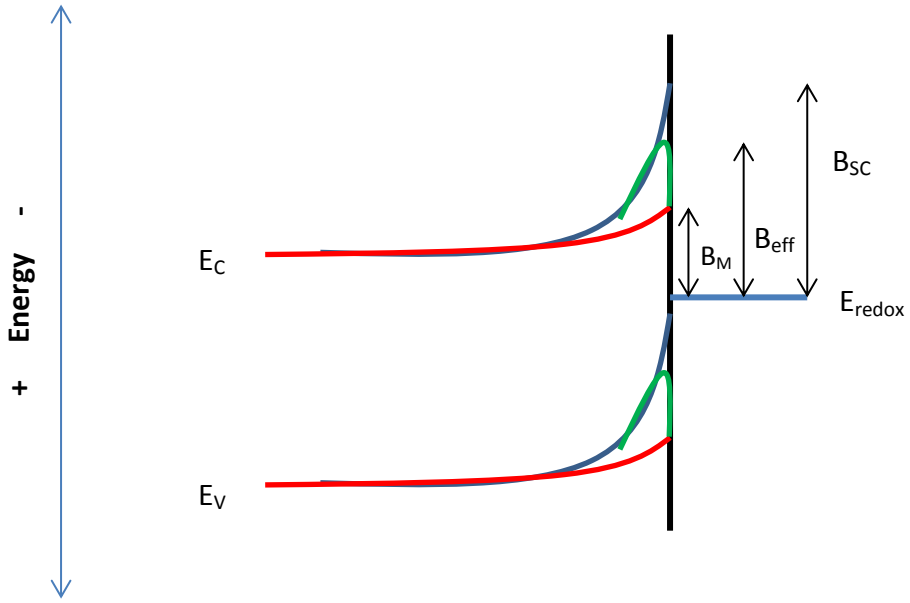

Figure 6.29. The effect of metal particles on the interfacial barrier height (B) of a semiconductor in contact with a solution redox couple of energy E_{redox}. The situation is shown for the semiconductor in contact with the solution (B_{SC}), in contact with a metal contact with a large spatial area (B_M) and a metal contact with a small area (B_{eff}). Figure adapted from ref [21]

It can be seen that the effective level of band bending is larger at small metal contacts, despite the actual barrier height remaining unchanged.[21] The spatial dependance of barrier height may therefore dictate that a less negative bias is required to drive electrodes with large metal contacts into depletion (i.e. where band bending drives electrons to the surface).

6.6. Methanol Oxidation

The oxidation of methanol has gained significant attention due to its application in direct methanol fuel cells (DMFCs). This reaction also accounts for much of the energy losses encountered in fuel cells of this type due to the large overpotential requirements.[255] The activities of the materials prepared in this work were investigated with the use of cyclic voltammetry. It was found that methanol oxidation was severely limited on all particle sizes, and the behaviour deviated significantly from that of bulk Pt. A typical bulk Pt response from the literature is shown in Figure 6.30:[249]

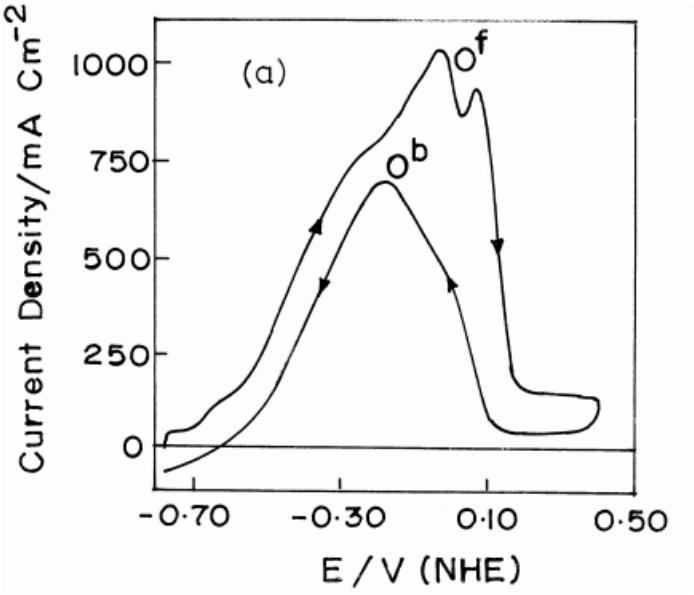

Figure 6.30. CVs of a polycrystalline Pt electrode in 6M KOH + 1M MeOH at a scan rate of 25 mV s^{-1}. Figure taken from ref 160

The mechanism of methanol oxidation on Pt is relatively complex, and has attracted significant attention. Generally it is assumed that methanol is adsorbed at low potential, and is not oxidised until sufficient levels of adsorbed OH species are present on the Pt surface.[166] Upon adsorption of OH the methanol is then oxidised (O^f – Figure 6.30) in multiple stages to yield an adsorbed CHO species. The strength of bonding to this species is largely considered to dictate the overall rate of reaction, which is generally higher in alkaline media due to its weaker adsorption strength at increased pH.[166] At higher potentials the formation of platinum oxide inhibits the reaction and gives rise to a sharp decline in the rate of oxidation. On the reverse scan oxidation generally occurs again upon removal of the inactive platinum oxide layer (O^b – Figure 6.30). The characteristic behaviour of bulk platinum was not present in any of the particles studied in this work and methanol was only oxidised to a very limited degree. Figure 6.31 presents the voltammetry obtained at a range of particle sizes in both the blank 0.5 M NaOH electrolyte as well as that with the addition of 1 M methanol. Measurements were carried out on samples with ITO substrates at room temperature.

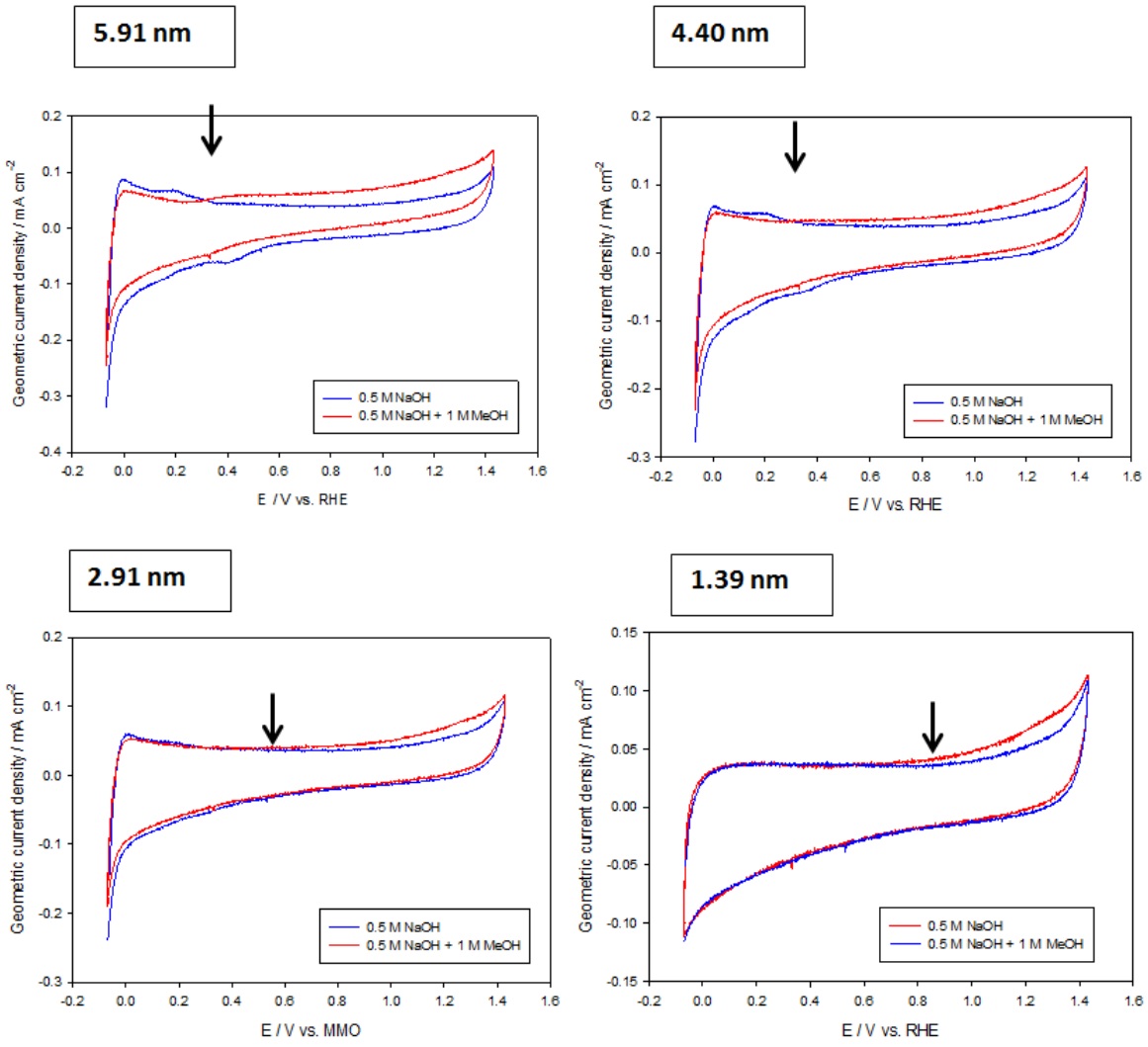

Figure 6.31. CVs of selected Pt particle sizes supported on anatase TiO_2 (array #8113). The measurements were carried out at room temperature in both 0.5 M NaOH and 0.5 M + 1 M NaOH. Data shown in 0.5 M NaOH was collected immediately prior to those with the addition of methanol. The first cycles in methanol containing solution are shown and a scan rate of 50 mV s^{-1} was used in all cases. The apparent MOR onset is marked with an arrow.

An increased oxidation current can be observed positive of c.a. 0.4 V at the largest particle size in methanol containing media. This coincides roughly with the onset of the anodic peak which was previously suggested to involve formation of an adsorbed OH species at low potential. A similar onset potential was observed on the Fe_2O_3 supported particles, although a much larger level of oxidation occurred in general (Chapter 7). Since formation of Pt oxide occurred to a limited degree, the slight oxidation current can be seen to persist in the region where oxide formation would normally be expected to occur. No clear increase in current could be observed on the smaller particle sizes at potentials below approximately 0.8 V. This may be due to the limited

kinetics relating to OH adsorption, which may increase the required overpotential for the reaction to proceed. Alternatively the slight current increase positive of 0.8 V at the smaller particles may simply arise from a random variation in the ITO substrate feature that occurs in this region. In general however the current in this region was found to decrease with increasing cycle number. The methanol oxidation current was calculated at 0.8 V by subtracting the current obtained in NaOH from that recorded with the addition of methanol. The currents recorded in the absence of methanol were taken as the final positive sweeps recorded prior to the measurements in methanol containing media. Currents in the presence of methanol were taken from the first positive going sweep.

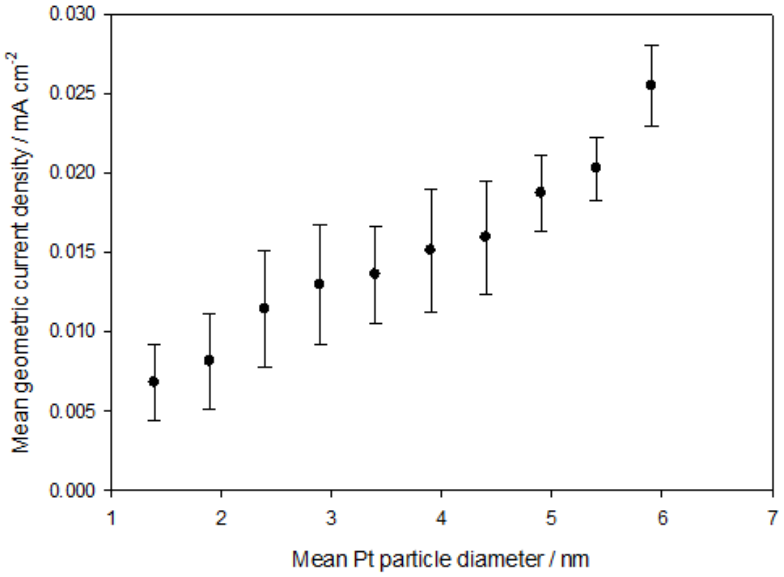

Figure 6.32. Mean methanol oxidation current density as a function of Pt particle size at 0.8 V vs. RHE (array #8113). The methanol oxidation current was calculated by subtracting the value obtained in 0.5 M NaOH from that obtained with the addition of 1 M methanol. All measurements were performed with a potential scan rate of 50 mV s^{-1}.

In Figure 6.32, the increase in current density with methanol in solution was only small fractions of a milliamp per centimeter squared. The very low currents are most likely attributed in part to the rectifying nature of the semiconducting support. In previous studies on amorphous TiO_2 supported Pt in $HClO_4$, equivalently sized particles were however shown to be completely absent of any methanol oxidation activity.[244] The slight level of oxidation current apparent at larger particle sizes in this work may be due to the lesser effects of poisoning intermediates in alkaline media. Additionally, OH species may adsorb onto the Pt surface at much lower potentials in alkali,

therefore providing an increased coverage of the active OH species utilised in the reaction. It is not however certain whether the very small oxidation current produced at the smallest particles in methanol containing media were in fact related to the oxidation of methanol. Only on the largest 4 particle sizes could any voltammetric features related to methanol oxidation be clearly observed.

No clear peak was observed on the reverse scan in this case, due to the limited formation of Pt oxide on the samples prepared. The data also showed a slight decrease in charge over the hydrogen adsorption region, which is likely to arise from residual fragments of methanol blocking adsorption sites. It is evident from figure 6.31 that the reduction in hydrogen adsorption charge is more significant at the larger particle sizes. This may reflect that the adsorption of methanol is hindered at smaller particle sizes. The lack of any clear change to the hydrogen adsorption region at particle diameters below 3- 4 nm may indicate that methanol oxidation does not in fact occur at these particle sizes.

As well as the slight decrease in charge over the hydrogen adsorption region, the level of methanol oxidation current also decreased upon cycling. The reduction in methanol oxidation current however diminished to a greater extent than the charge under the hydrogen adsorption region. The hydrogen adsorption charge appeared to decrease primariliy between the last cycle in the blank NaOH electrolyte and the first cycle in methanol containing media. No clear variation in the hydrogen adsorption charge was observed for the remaining cycles in methanol containing media. The reduction in methanol oxidation current was also particularly evident between the first and second cycles (Figure 6.33), although it continued to decrease very slightly for the remaining cycles. It is therefore unlikely that significant Pt surface area loss occurs. Potentially the film is oxidised which leads to a loss in conductivity and therefore further reduction in MOR activity. Some level of change in the Pt particle size/structure may also take place.

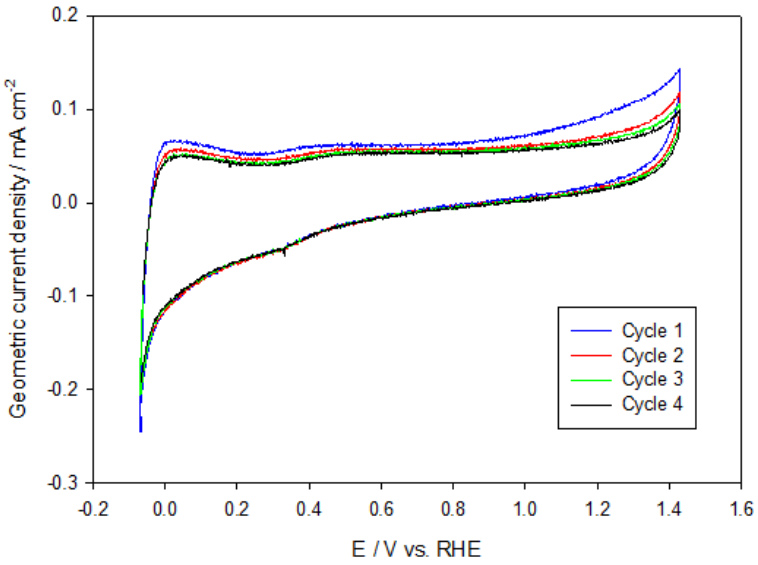

Figure 6.33. The first 4 cycles of a Pt/TiO_2 electrode (estimated particle diameter: 5.91 nm) in 0.5 M NaOH + 1M MeOH (array #8113). The sample was deposited on an ITO substrate and all measurements were conducted at a potential scan rate of 50 mV s^{-1}.

6.7. Photoelectrochemical Behaviour

The photoelectrochemical behaviours of the deposited samples were assessed with the use of illuminated CV measurements as well as illuminated open circuit potential measurements. The open circuit potential measurements were conducted in order to assess the effect of the Pt particles on the level of photovoltage generation. The CV measurements were carried out in 0.5 M NaOH with a scan rate of 50 mV s^{-1} and both dark and illuminated (150 W Xe arc lamp) measurements were recorded. Figure 6.34 shows the voltammetry of selected Pt particle sizes on anatase TiO_2 both in the dark and under illumination.

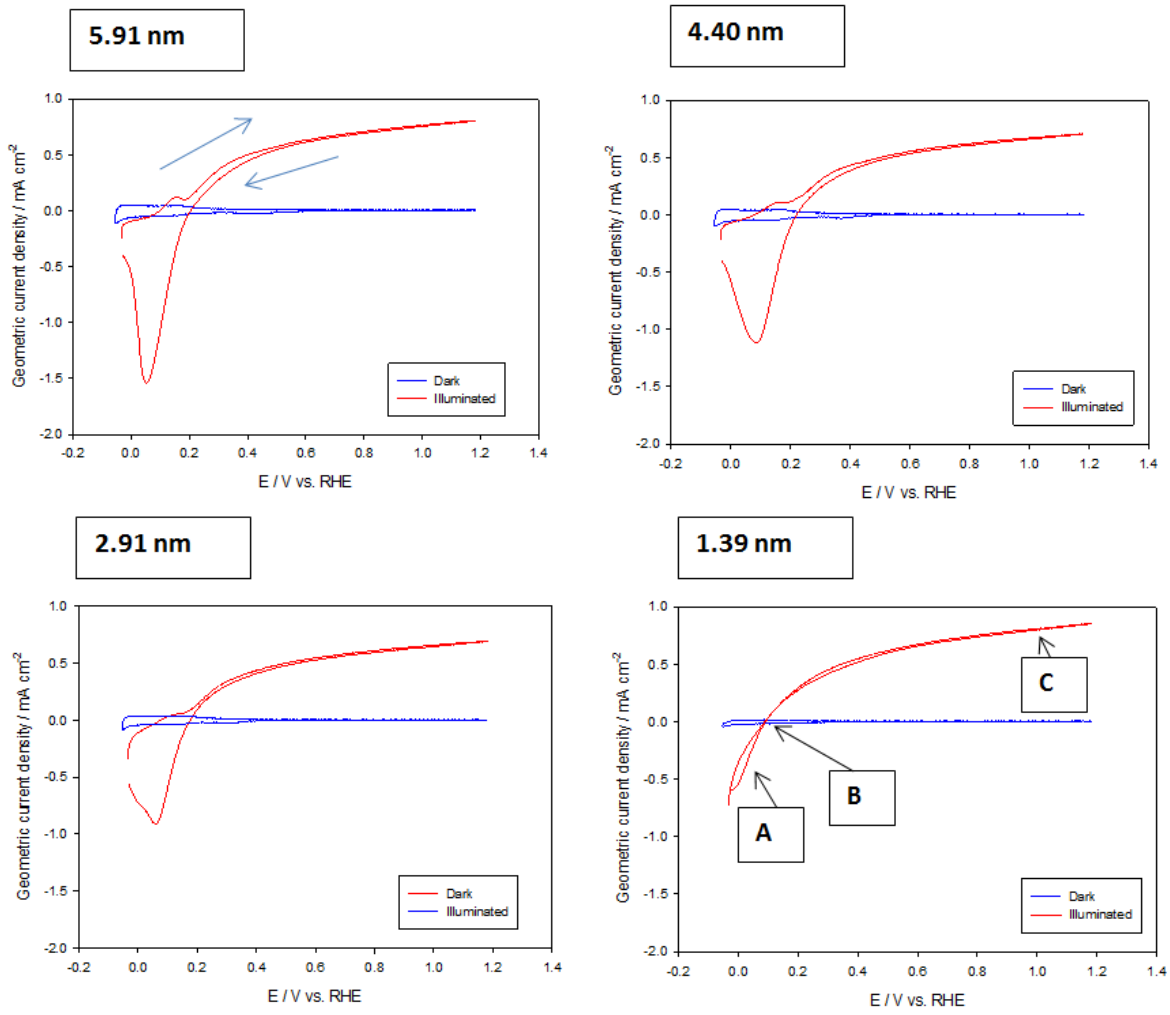

Figure 6.34. Illuminated and dark CVs of selected particle sizes (array #8112). All measurements were conducted in 0.5 M NaOH with a potential scan rate of 50 mV s^{-1}. The first illuminated cycle is shown. The dark measurements were those conducted immediately prior to the illuminated measurements. The measurements are uncorrected with respect to irradiance variation. A B and C in the bottom right figure represent key areas which are referred to in the text.

Upon illumination a greatly increased anodic current occurs positive of 0.1 – 0.2 V relating to the evolution of oxygen. The valence band holes generated under illumination are separated by the electric field in the TiO_2, where the strength increases as the potential is swept positive. In region C the conduction and valence bands are bent in such a way that holes are transported to the surface effectively. On the reverse scan, the level of band bending slowly deceases as the potential is swept negative. The flat band condition occurs approximately at point B where no photocurrent is observed (although the point of zero current is dictated by interfacial kinetics and the rate of recombination also, meaning it may not accurately describe the flat band potential).

Negative of point B, the bands are bent in a way that electrons are directed to the semiconductor surface. A large reduction peak can be seen negative of approximately 0.1 – 0.2 V on the reverse scan. This feature had some dependence on the level of photocurrent generated on the forward scan, although was primarily dependent on particle size. The peak is likely to represent reduction of photogenerated oxygen and hence the variation in behaviour is determined by the ORR activity variation in response to particle size.

Initial trends relating to the Pt particle size were found to be most significant in the lower potential region (Below approximately 0.4 V), where the level of band bending is expected to relatively small. Figure 6.35 shows contour maps of the uncorrected current densities recorded at both the plain TiO_2 calibration sample as well as the Pt/TiO_2 samples under illumination at 0.3 V.

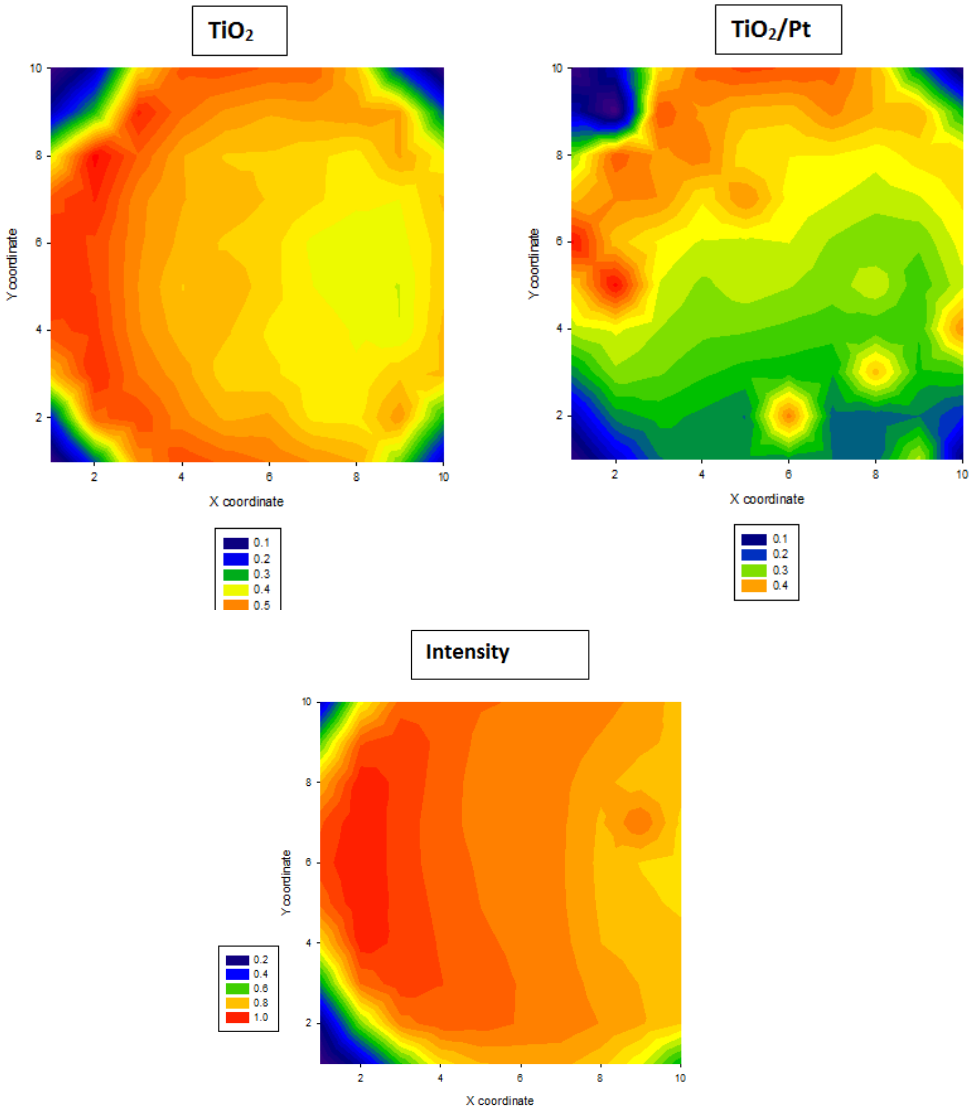

Figure 6.35. Uncorrected geometric current density (mA cm^{-2}) at 0.3 V vs. RHE as a function of array position. Results are shown for the plain TiO_2 calibration array (left) as well as an array of TiO_2 supported Pt particles (right – array #8112). Data from the first anodic sweep under illumination are shown in each case. Note that 10 randomly placed TiO_2 electrodes are present on the right hand sample. Also shown (Bottom) is the relative intensity distribution across the beam area (relative to the most intense region).

The photocurrent of the uniform anatase TiO_2 calibration sample essentially mirrors the intensity distribution across the beam footprint. Even prior to irradiance correction, there is a general trend of increasing photocurrent as the Pt particle size decreases on the array with Pt particles. The photocurrent at the smallest particle size was found to be roughly equal to those of the plain TiO_2

electrodes. A decrease in photocurrent relative to the plain TiO_2 was however observed for all other sizes of Pt nanoparticle. It is known that the level of band bending at the TiO_2/Pt interface is less than that of the TiO_2 – electrolyte interface,[13] which may reduce the driving force for the transportation of holes to the semiconductor surface. Additionally, imposition of catalysts onto a semiconductor surface has been shown to lead to the formation of recombination centres or surface states in some cases.[182]

The photocurrent CVs were subsequently corrected for non-uniform intensity using the method described in Chapter 3. These are presented for selected Pt particle sizes in Figure 6.36.

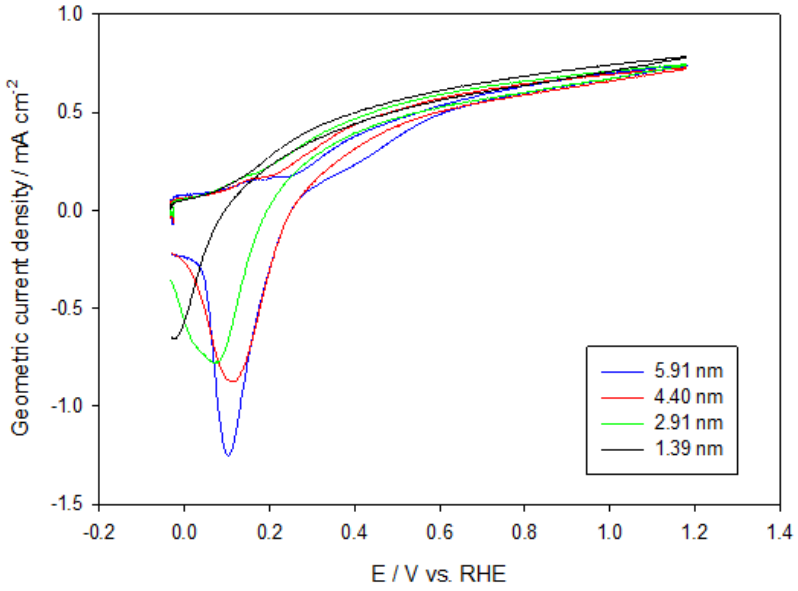

Figure 6.36. Intensity normalised CVs of selected Pt particle sizes on Anatase TiO_2 under illumination. The substrate material was Au and measurements took place in 0.5 M NaOH with a potential scan rate of 50 mV s^{-1}. The first cycles are shown for array #8075 .

Above approximately 0.6 V, the behaviours of the electrodes differ only slightly in response to a change in particle size. Relatively little difference in the recorded current density is also apparent between the positive and negative scans above this potential. The level of variation in current density between the forward and reverse scans also appeared to remain approximately equal across the range of Pt particle sizes. Below 0.6 V, the photocurrent decreases at a more rapid rate on the negative scan than in the positive scan at particle sizes larger than approximately 4.40 nm . Possibly this may result from a buffering of the anodic current by the onset of oxygen reduction.

The behaviour described above was however only apparent in the first cycles under illumination. With repeated cycling, the level of hysteresis between the forward and reverse sweeps decreased significantly. Additionally the relative trends in terms of photocurrent against particle size changed slightly. This was primarily evident at the particles larger in diameter than approximately 4 nm. The photocurrent obtained at 0.25 V during the first three cycles is presented in Figure 6.37. Generally, the Figure shows that the addition of Pt brings about a decrease in the photocurrent relative to TiO_2 without Pt. In this case it is apparent that the addition of Pt is not benificial to the photoevolution of oxygen and may not increase the rate of interfacial electron transfer significantly. A number of possibilties such as formation of surface recombination states and a reduction in interfacial barrier height may explain the trends observed.

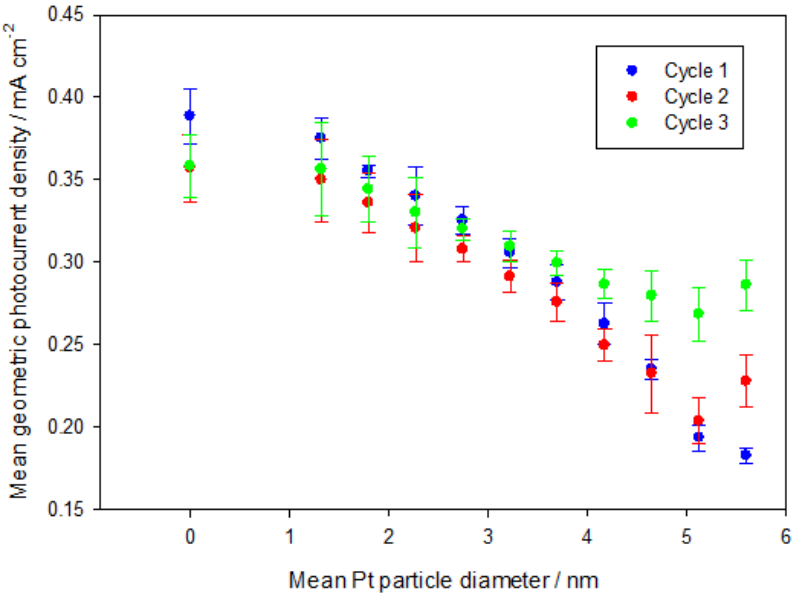

Figure 6.37. Intensity corrected photocurrent density at 0.25 V vs. RHE during the first three illuminated cycles. Measurements were conducted in 0.5 M NaOH with a potential scan rate of 50 mV s^{-1}. Current densities were calculated from the anodic scans (array #8075).

Typically, Pt particles are reported to have a benificial effect on the photoevolution of oxygen at TiO_2 electrodes. The optimal particle size however varies significantly between different publications. An et al. observed that Pt addition only showed an increased activity over plain TiO_2 when the Pt particle size was less than approximately 1.3 nm in diameter.[190b] At larger diameters the photocurrent was less than that of TiO_2 alone. Xu et al. however observed a noticable photocurrent enhancement over TiO_2 when Pt particles of diameters ranging from 20-30 nm were deposited on TiO_2 nanotubes.[192] Few publications show that Pt has a detrimental effect on the photoactivity, although Ivanov observed an approximately 3-fold decrease in photocurrent

relative to plain TiO_2 upon addition of Pt nanoparticles.[254] In this case however the particle sizes were considerably larger, with diameters on the order of µm. Typically the increase in activity with Pt loading in photocatalytic systems is rationalised by improved charge separation, although in this case the depletion layer is likely to fulfil this role. It is also noteworthy that the studies where an improvement is observed upon Pt addition almost always feature some level of nanostructuring at the TiO_2 support (e.g. nanotubes).[190a, 193] As such, the lack of electric field may enhance any effect that the Pt particle size has on charge separation, and act in a similar way to those in photocatalysis.

Although a general reduction in photocurrent occurs in response to increasing particle size in all three cycles, the relative trend changes to some extent. It can be observed in Figure 6.37 that the photocurrent increases at the largest particle sizes upon increasing the number of cycles. The photocurrents at smaller particle sizes change to a much smaller degree. The increase in photocurrent may result from the continued oxidation of the TiO_2 itself, and thus a decrease in donors that decrease the level of band bending. Alternatively, a loss of Pt from the electrode surface was considered. However, the Pt surface area estimated from the hydrogen adsorption region did not change signifcantly. The estimated surface areas for the Pt nanoparticles on anatase TiO_2 are shown in Figure 6.38 before and after photoelectrochemical screening.

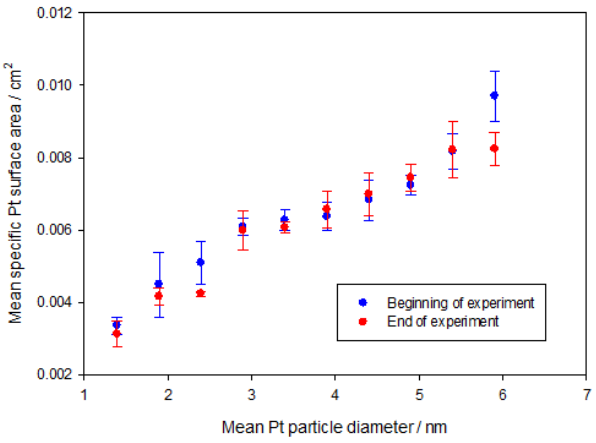

Figure 6.38. Estimated Pt surface areas of Pt nanoparticles supported on anatase TiO_2. Data is shown for the electrodes before and after the photoelectrochemical screening process. Surface areas we estimated from the charge passed in the hydrogen adsorption region. (array #8112)

As noted previously, the decrease in photocurrent at larger Pt particle sizes was most pronounced in the region below approximately 0.4 V. For example an increase in photocurrent density of approximately 0.13 mA cm^{-2} was observed at 0.25 V between the largest and smallest particle sizes. This decreased to approximately 0.05 mA cm^{-2} at a voltage of 0.8 V (Figure 6.39).

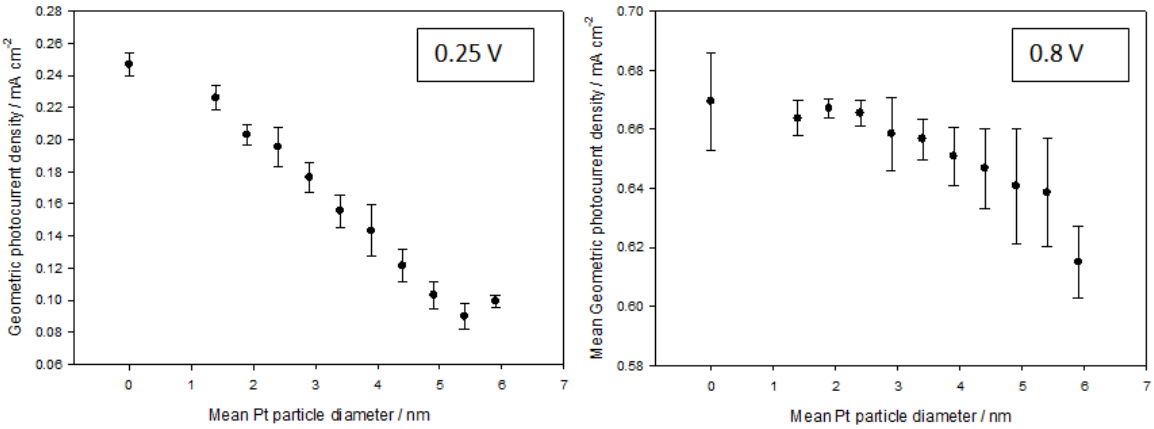

Figure 6.39. Intensity normalised geometric photocurrent density at 0.25 (left) and 0.8 V (right). Data is derived from the first positive going sweep under illumination. The response from the blank TiO_2 electrodes are also shown at the position of 0 nm on the x axis (array #8075).

The greater effect of the Pt particle size at lower applied bias may indicate that the activity variation stems from effects relating to charge separation. At 0.25 V, the depletion region is not well defined, and thus the effects of particle size are more pronounced. At 0.8 V, the depletion layer width is expected to be considerabley larger (which is proprtional to the square root of the space charge voltage),[6] and thus the depletion layer more effectively separates photogenerated charge carriers. As a result, any variation in band bending or recombination rates imparted by the different particle sizes will have a smaller effect. Similarly to the effects of cycling, the application of a larger positive bias brings about an increasingly large photocurrent enhancement as the particle size increases relative to the values at 0.25 V. An additional possibility is that the larger particles influence optical absorption by a shadowing effect on the TiO_2 and therefore attenuate the incoming light. However the wavelength of the incoming light is so large with respect to the Pt particle size it is likely that they are effectively optically transparent. Furthermore, the approximate coverage of the support at the largest particle size is approximately 52 % (calculated from TEM images using proprietry Ilika software) compared to approximately 11 % at the smallest particle size. One would therefore expect an aproximately 5 fold increase in photocurrent at the

smallest size relative to the largest if shadowing had a signifcant influence. In particular, any such effect would be more apparent as the applied voltage increased. This is since the space charge region becomes more defined and shifts the dependence of photocurrent from charge separation ability (related to the level of band bending) to optical absorption. In this case the photocurrent dependence on particle size instead reduces significantly at higher voltages, suggesting attenuation by the particles has a negligible effect.

Some variation in the behaviour also appeared with cycling. The apparent photocurrent onset shifted slightly negative as the number of cycles performed under illumination increased. The photocurrent onset potential is shown for the first three illuminated cycles in Figure 6.40.

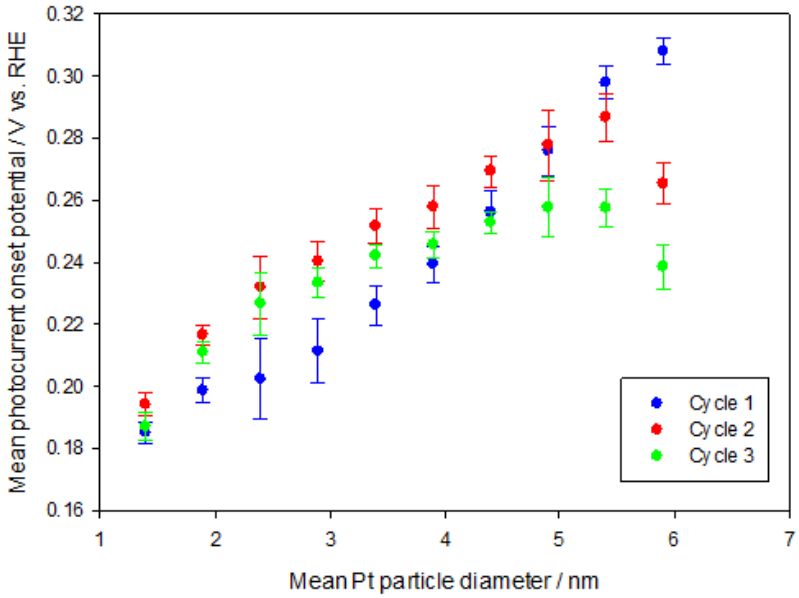

Figure 6.40. Mean photocurrent onset potential from the illuminated CV measurements. The onset was defined as the voltage to generate geometric current density of 0.24 mA cm^{-2}. Measurements were conducted in 0.5 M NaOH with a potential scan rate of 50 mV s^{-1}. (Array #8075)

The trend depicted above is most likely to result from the oxidation of the TiO_2 film. The effects is more marked at larger particle diameters due to the ability of Pt to catalyse the reduction of TiO_2, which would create a larger initial concentration of donor species at higher Pt coverage. Alternatively, there may be a loss of Pt from the electrode surface, however the integrated charge over the hydrogen adsorption region does not change significantly when compared before and after illumination.

As the number of cycles increases, the concentration of oxygen in the electroyte will also increase,

which potentially may affect the photoresponse. On the first cycle, relatively little oxygen is expected to be in the solution due to the bubbling with inert gas prior to the experiments. Upon photocurrent generation however, oxygen is evolved at the electrode. In such cases the relative activities toward the oxygen reduction reaction may be important in the low potential region of the voltammetry. The deleterious effect of oxygen reduction on the net current would however be expected to cause a positive shift in the photocurrent onset. The effect of cycling was found to be the opposite.

Oxygen in solution may also impact upon the level of photovoltage generation. A number of researchers advocate performing photocurrent and photovoltage measurements whilst bubbling Oxygen through the solution such that both the oxidised and reduced form of the redox species (OH^-/O_2) are present in solution.[13, 209] This is required in order to give a well defined solution potential and also more accurately recreates the conditions inside a photoelectrochemical cell. The effect of oxygen in solution has previously been found to markedly alter the level of photovoltage generation at TiO_2 electrodes, particularly in nanstructured electrodes where no appreciable internal electric field is present inside the semiconductor.[230] In such cases oxygen may capture conduction band electrons and lead to a reduction in photovoltage. The illuminated open circuit potential was measured in both Ar and O_2 purged solution to give an indication of the effects of O_2 on the level of photovoltage generation. In both cases, the open circuit potential became increasingly positive as the Pt particle size increased.

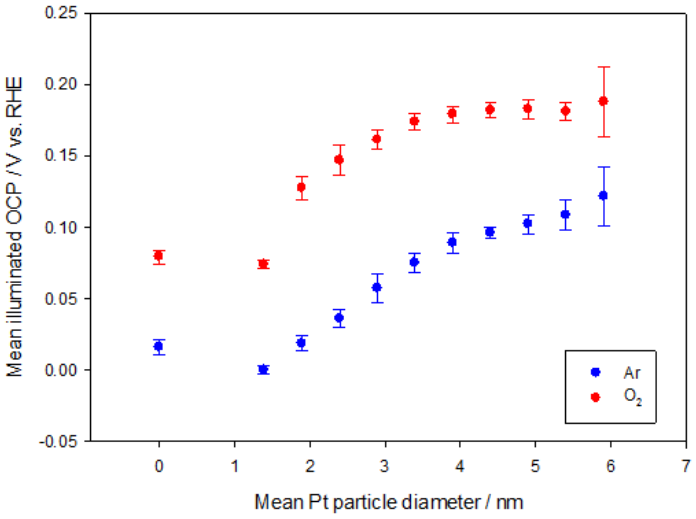

Figure 6.41. Mean illumated OCP values as a function of particle size in both Ar and O_2 purged 0.5 M NaOH. OCP values were caluclated as the average voltage over a 200 s period of illumination. (Array #8112)

At all electrodes on the array, the open circuit potential became more positive when oxygen was present in the solution. The overall trend in response to a change in Pt particle size also remains relatively similar. It would appear therefore that the particle size has little effect on the behaviour in oxygen containing media and that the reduction in photovoltage at larger Pt particles is dominated by the same factor as that in oxygen free media. An important observation is also that the photocurrent onset moved to more negative potentials as the particle size reduced in a similar way to the open circuit potentials presented above. In both measurements there was a variation in voltage of approximately 120 mV across the range of particle sizes. The similarity between the two trends may suggest that the trends in photocurrent response are dominated by a variation in photovoltage production. As such it would seem that any variation in catalytic activity between the various particle sizes is far outweighed by the reduction in photovoltage that occurs when increasing the Pt particle size.

Upon cyling, the cathodic oxygen reduction behaviour also changed significantly. Similarly to the photocurrent onset potential, the ORR onset shifted negative with increasing cycle number. The negative shift was once again more apparent as the particle size increased.

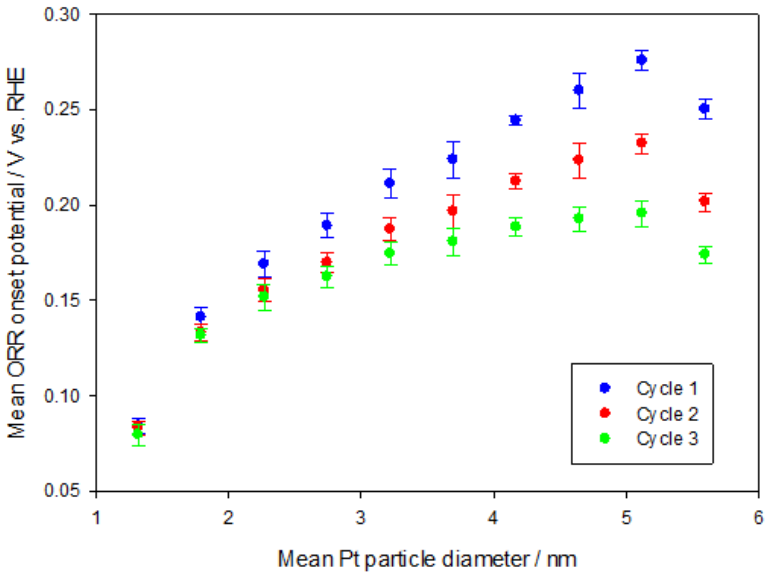

Figure 6.42. Mean ORR onset potential of anatase TiO_2 supported Pt nanoparticles for the first 3 cycles under illumination. Data was collected at 50 mV s^{-1} in 0.5 M NaOH. (Array #8075)

Both the negative shift in photocurrent onset and ORR onset would suggest an increased level of rectification or a change in the characteristics of the Pt particles . The same behaviour could be

observed in the reduction of oxygen in the dark. The onset shifted negative signifcantly after cycling under illumination without any evidence for a loss in Pt surface area (Figure 6.38). The dark ORR onset potential is shown both before and after cycling under illumination in Figure 6.43.

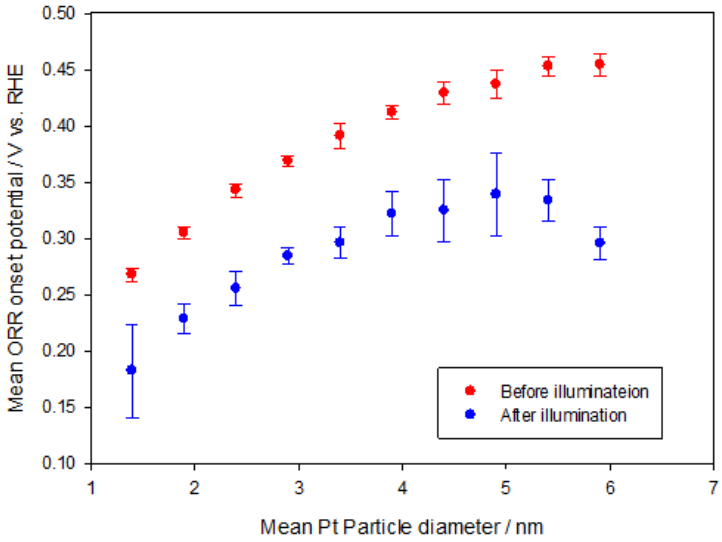

Figure 6.43. Mean ORR onset potential of anatase TiO_2 supported Pt nanoparticles before and after cycling under illumination. Measurements were carried out in O_2 saturated 0.5 M NaOH at a scan rate of 5 mV s^{-1}. Data was taken from the first cathodic sweep in each case, where the onset was defined as the voltage to generate -0.028 mA cm^{-2} (geometric) (Array #8075).

The results would suggest that the TiO_2 loses a greater level of conductivity at larger Pt particle sizes, which may arise from the larger initial concentration of intrinsic TiO_2 defect sites imposed by larger particles. A more likely explanation is that the larger particles are less stable in terms of structure/size. It is to be expected that any interaction between the support and particles is weaker at larger particles due to a lower proportion of surface atoms.

Further studies were conducted in methanol containing electrolyte (0.5 M NaOH + 1 M MeOH). The greater ease at which methanol oxidation takes place may ease the effects of surface recombination to some extent. Additionally, the evolution of oxygen is expected to occur to a smaller extent, and thus remove any contribution that residual O_2 in solution has on the voltammetry. Firstly, the effect of methanol addition on the illuminated OCP was investigated. A significant negative shift of approximately 200 mV was observed at all particle sizes relative to the measurements in Ar purged 0.5 M NaOH.

The illuminated open circuit potential in 0.5 M NaOH both with and without methanol is shown in Figure 6.44.

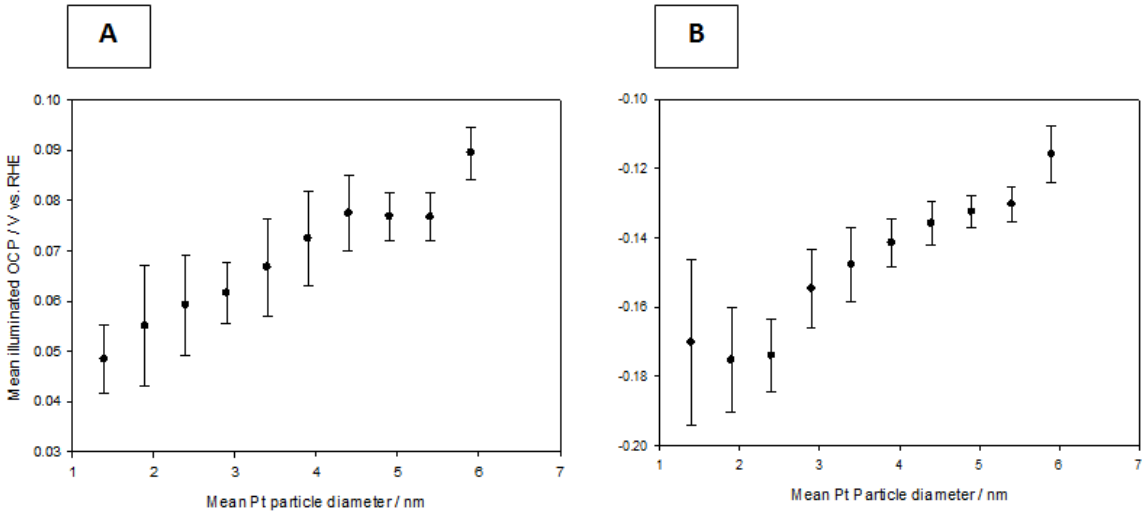

Figure 6.44. Mean illuminated open circuit potential in 0.5 M NaOH (A) and 0.5 M NaOH + 1 M MeOH (B). The data represents the average voltage over a 200 second period of illumination. (Array #8114)

In general the negative voltage shift was relatively systematic, and it appeared that the overall relative trend in response to particle size remained the same. Illuminated voltammetry was also conducted in the presence of methanol. Figure 6.45 shows the behaviour at an electrode with a mean Pt particle diameter of 5.91 nm in both the blank NaOH electrolyte and that with methanol. In general the voltammetry appears almost identical above approximately 0.6 V. Below this, the anodic current generated in methanol containing media is somewhat larger than that in the blank NaOH electrolyte. Once again the greater ease at which methanol is oxidised may contribute to this behaviour, whereby the more rapid removal of holes at the surface may limit recombination in regions where the level of band bending is less pronounced. Additionally, the peak relating to the reduction of oxygen is not evident in the cycle performed in methanol. This would suggest that the anodic photocurrent is primarily attributed to the oxidation of methanol in solution.

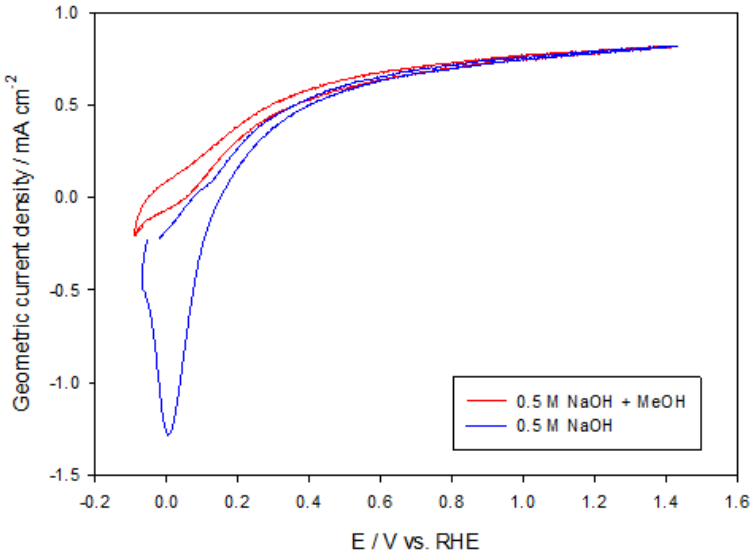

Figure 6.45. Uncorrected illuminated cyclic voltammograms of an electrode of anatase TiO_2 supported Pt nanoparticles (estimated particle diameter : 5.91 nm) in 0.5 M NaOH and 0.5 M NaOH + 1 M MeOH. Data was recorded with a potential scan rate of 50 mV s^{-1} and the first cycles are shown in each case for array #8114.

In spite of the increased photocurrent in methanol containing electrolyte below 0.6 V, the overall particle size trends relating to the photocurrent remained relatively similar between the two measurements (Figure 6.46). This would suggest that the factor which contributes to the particle size trends previously presented continue to dominate the behaviours seen in methanol containing solution. In both cases a general increase in photocurrent occurs as the Pt particle size decreases. A variation in the catalytic activity towards the MOR was observed in the dark, although the absolute difference in current was very small between the range of particle sizes. It is unlikely therefore that the trend relates to this, particularly since particle sizes below approximately 4 – 5 nm showed no clear methanol oxidation activity.

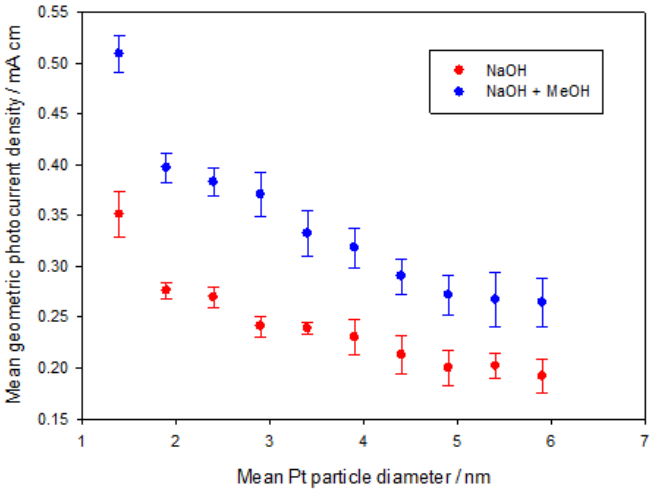

Figure 6.49. Intensity corrected photocurrent density of anatase TiO_2 supported Pt nanoparticles at 0.25 V (Array #8113). Measurements were conducted in either 0.5 M NaOH or 0.5 M NaOH + 1 M MeOH at a scan rate of 50 mV s^{-1}. Data from the first anodic sweep is shown in each case.

In all cases, the photocurrents were still lower than that of the plain TiO_2, and thus the Pt particles do not appear to add any clear benefit.

6.8. General Conclusions

In general the voltammetric behaviour of the TiO_2 supported Pt nanoparticles appeared to deviate significantly from bulk Pt. Most notably the formation of Pt oxide was extremely limited at all particle sizes, and only particle sizes in excess of approximately 4 – 5 nm showed any clear features that could be attributed to this process. Some evidence for the adsorption of OH species at low potentials close to the hydrogen adsorption region was however observed. Potentially however, the reduction of residual oxygen in solution may have contributed to the cathodic peak tentatively proposed to result from the stripping of such species. This is especially possible given the similar potentials at which oxygen reduction and OH/oxide stripping occurred. In the case of rectifying semiconductor contacts however, the position at which a process occurs is dependent to a large degree on the electrical properties of the semiconductor. As such, it is not unexpected

to see various cathodic processes completely different in nature occurring over a similar potential range. Furthermore, the oxide stripping peak on Pt is generally in close proximity to the onset of oxygen reduction. In the event that oxide was not formed then some questions are raised regarding the commonly proposed origin of the Pt particle size effects on the ORR. Typically the reduction in kinetics relating to oxide removal at smaller particle sizes is suggested to account for the negative shift in the ORR onset. If oxide/OH is not present then possibly another cause of this behaviour may exist.

The reduction of Ferricyanide was performed in order to assess whether a variation in the semiconducting properties of TiO_2 was the cause of the characteristics described above. A large shift in the onset potential relative to bulk Pt was observed at all particle sizes, most likely in part to the semiconducting nature of the support, since no subsequent reoxidation was observed.

In the methanol oxidation experiments, only an extremely small methanol oxidation current was observed, which once again was only clearly evident at particle sizes greater than approximately 4 – 5 nm. It seems likely that the limited formation of adsorbed OH species may contribute to this. Although it is possible either that the rectifying nature of the support or an inherent limitation of oxide/OH formation based on particle size contributes to this also.

In the photoelectrochemical measurements, a general reduction in photocurrent was observed at the Pt/TiO_2 samples relative to TiO_2. The same was true of both the OER and the MOR. In both cases the reduction in photocurrent was also increased upon increasing the Pt particle size. It was evident also from the open circuit measurements that a decrease in photovoltage occurred as the particle size increased. Whilst the absolute values of both parameters varied slightly for the different arrays, the overall trend remained the same. Additionally, the general trends observed in the OCP measurements correlated well with those relating to the photocurrent onset in each case.

As a result, it appears that a reduction in photovoltage is the primary mechanism through which the photocurrent is reduced. This may result either from a decrease in the interfacial barrier height (resulting in a more positive flat band potential), an increase in the rate of the deleterious back reaction (ORR), or an increase in the rate of recombination at larger Pt particle sizes. The latter appears more probable given that at voltages in excess of c.a. 0.6 V the level of photocurrent at the different particle sizes were approximately equal to that of TiO_2. This would also explain the more obvious photocurrent reduction at lower voltages where the depletion layer is defined to a lesser degree. Also the addition of methanol brought about an increase in

photocurrent relative to the values recorded in NaOH only at potentials below approximately 0.6 V. Due to the oxidation of methanol occurring at a greater rate than oxygen evolution, it is likely that the current below 0.6 V is enhanced by the more rapid removal of holes at the surface and thus a lesser degree of surface recombination occurs. Furthermore the similar current densities recorded at each particle size (above 0.6 V) in NaOH and NaOH + MeOH would suggest that the current is not limited by the rate of electron transfer, but rather by the level of recombination, which obviously is lesser in both cases above 0.6 V where the semiconductor is driven further into depletion.

7. Synthesis and Screening of Fe_2O_3 Supported Pt Nanoparticles

7.1. Fe_2O_3 Deposition

α-Fe_2O_3 films were deposited as the support for Pt nanoparticles using a PVD method. The α-Fe_2O_3 phase is of particular interest to photoelectrochemical water splitting, due to its low cost, stability in PEC operating environments and favourable band gap (~ 2.1 eV) for visible light absorption.[113] The α-Fe_2O_3 phase however possesses several key deficiencies. The most notable of these are its poor charge separation ability and slow interfacial kinetics for the oxygen evolution reaction.[256] Both of these are key areas which can be affected by the addition of catalyst particles to the semiconductor surface.[257,258]

Iron oxide exists as three main stoichiometric forms at room temperature, consisting of maghemite (γ – Fe_2O_3), hematite (α-Fe_2O_3) and magnetite (Fe_3O_4).[259] The occurrence of the different structures at different temperatures and oxygen stoichiometries is shown in Figure 7.1.[260]

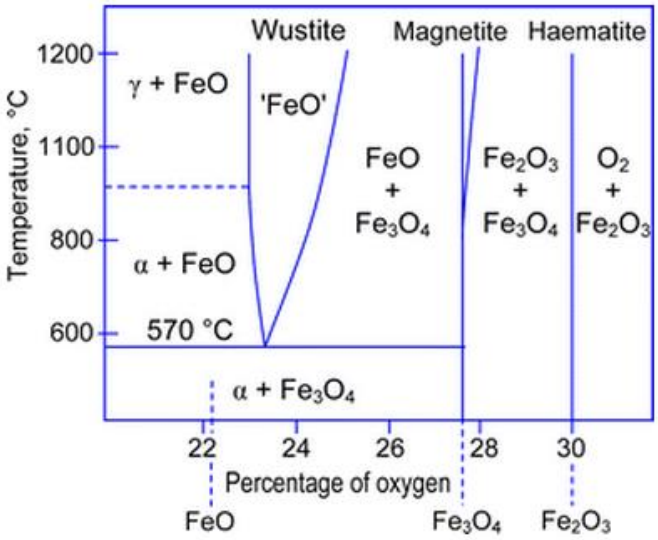

Figure 7.1. Iron oxide phase diagram at different oxygen stoichiometries and temperatures. Figure taken from ref 261.

The α-Fe_2O_3 structure is the most thermodynamically stable of the three phases and crystallises in the rhombohedral system with a space group R-3c.[261] The structure consists of Fe^{3+} ions which are octahedrally coordinated with hexagonally close packed O^{2-} ions. The magnetite and maghemite phases adopt an inverse spinel structure, in which Fe^{2+} or Fe^{3+} coordinates with cubic close packed O^{2-} ions.[262]

Typically substrate temperatures in the literature range from 250 – 500 ^{o}C for forming the α – Fe_2O_3 phase via similar MBE based processes to that used within this work.[263,261] Low temperature formation has however been observed at 200 ^{o}C and below when using an ALD approach.[264], Generally it is observed that α – Fe_2O_3 synthesis requires higher substrate temperatures than the other two phases alluded to.[261] The same is true when a post annealing method is used.[265]

In this work, Fe was deposited from an E-gun source whilst atomic oxygen was also leaked into the chamber at a constant rate. In this instance, the RF power supplied to the plasma atom source was 300 W. The thicknesses of the as deposited films were determined to be an average of 154 +/- 13 nm by AFM. The final deposition parameters used for all α – Fe_2O_3 support layers are summarised in Table 7.1.

Table 7.1.

Synthesis parameter	**Fe**	**O**
Source	E-gun	Atom source
Deposition rate	2.2 Å s^{-1}	1 sccm flow rate
Deposition time	60 mins	60 mins
Substrate temperature	300 ^{o}C	300 ^{o}C
RF power	N/A	300 W

Initially, the intention was to deposit films of the same thickness as the TiO_2 support layers (~ 250 nm). However it was found that due to the magnetic properties of Fe, it was not possible to sweep the electron beam of the e-gun evaporator across a large portion of the source material during deposition. As a result, lower deposition rates than those used for the anatase TiO_2 films were required. Generally however, the optimal thickness of α-Fe_2O_3 is much thinner than that of TiO_2. This is generally considered to be a result of the small hole diffusion length in Fe_2O_3 (< 5 nm).

This dictates that the vast majority of charge carriers generated outside the depletion region will recombine.[256]

In order to mitigate shunting effects resulting from substrate exposure (see Chapter 3), the films were once again deposited directly to avoid the use of post annealing. XPS analysis of the Fe (2p) core level revealed that the Fe was primarily in the Fe^{3+} oxidation state, which is consistent with that expected in Fe_2O_3. The binding energy of the Fe ($2p_{3/2}$) level ranged from approximately 711.80 to 712.15 eV, which is in good agreement with values reported in the literature and is considerably higher than the value of 706 eV for metallic Fe.[261]

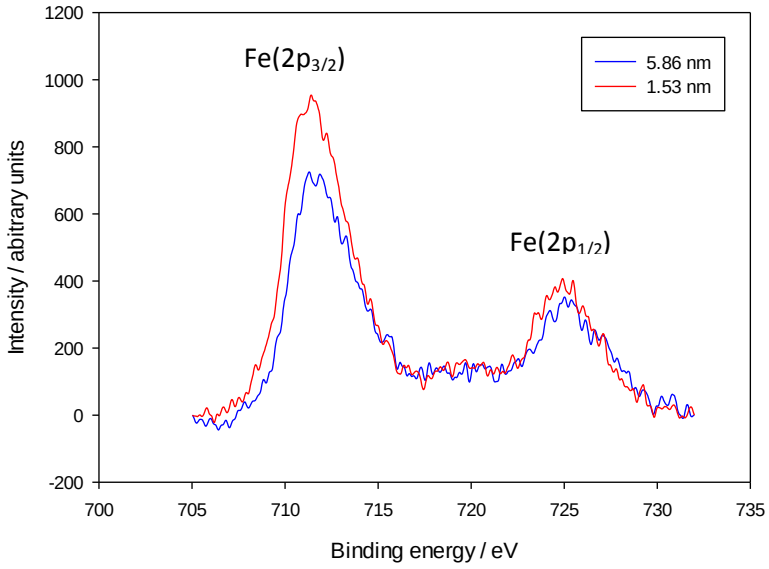

Figure 7.2. XPS spectra of the Fe(2p) core level in Fe_2O_3 supported Pt nanoparticles. The estimated Pt particle diameters are given in the inset.

The appearance of the Fe(2p) core level is often very complex, due to the appearance of multiple secondary peaks and satellite features. In this case, no clear shift in the Fe(2p) binding energy was observed as the Pt particle size changed. However a small satellite feature was observed (which is clearer on electrodes with smaller particles sizes) between the range of approximately 716 – 720 eV. This is a common characteristic of the Fe(2p) level spectrum in Fe_2O_3 relating to Fe^{3+}.[266] The reduced clarity of this feature most likely arises from the decreased overall intensity in the measured spectrum at higher Pt coverage. Furthermore, there were no clear observations of low energy shoulders or satellite features relating to Fe^{2+} or metallic Fe.

A relatively significant drop in the intensity of the Fe($2p_{3/2}$) signal could however be observed as the Pt particle size increased. This is depicted in Figure 7.3. In this instance, the Fe($2p_{3/2}$) intensity did not appreciably change until the Pt particle size increased above approximately 4 nm. This may reflect that 3D growth initially occurs, thus causing little variation to the overall coverage of Pt on the Fe_2O_3. At longer deposition times (Figure 7.5.), the particles were observed to coalesce and become larger. At this point the proportional coverage of the α-Fe_2O_3 becomes much larger, which decreases the intensity of the Fe($2p_{3/2}$) signal observed in the spectrum.

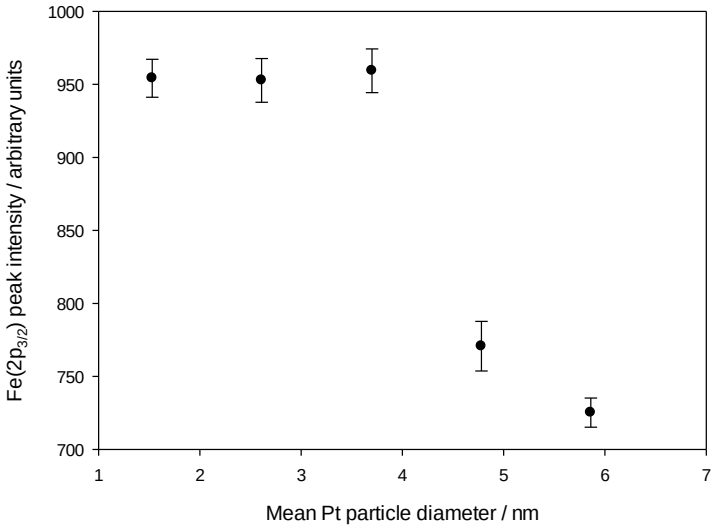

Figure 7.3. Peak intensity of the Fe($2p_{3/2}$) core level in Fe_2O_3 supported Pt nanoparticles.

Films were deposited onto heated substrates at various temperatures in order to optimise the deposition conditions. The x-ray diffraction patterns of several Fe_2O_3 films deposited at different temperatures are shown in Figure 7.4.

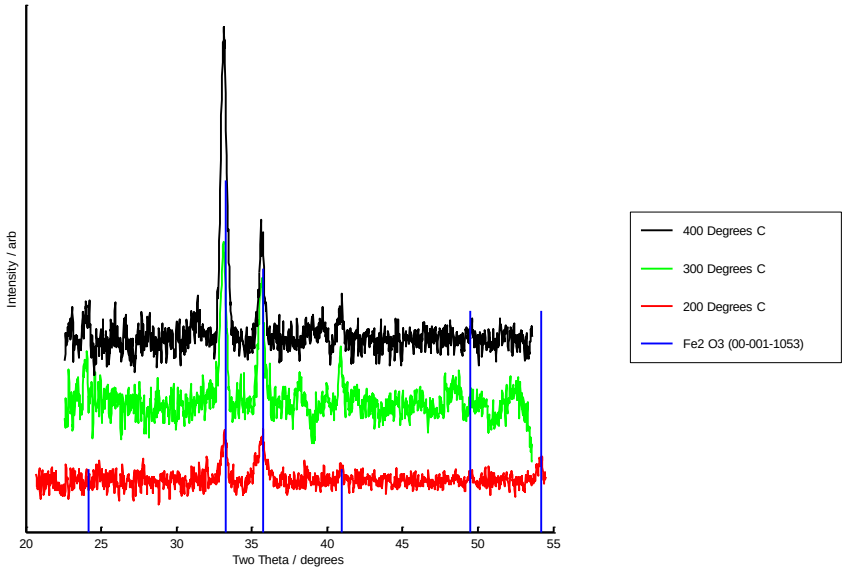

Figure 7.4. X-ray diffraction pattern of Fe_2O_3 films deposited onto heated substrates at various temperatures (Given in the inset). All films were deposited using an Fe deposition rate of 2.2 Å s^{-1}, with an oxygen flow rate of 1 sccm and atom source power of 300 W. The films were deposited on SiN substrates, with a mean film thickness of approximately 154 nm.

Deposition at each temperature from 200 – 400 ^{o}C produced only the α-Fe_2O_3 phase. The level of crystallinity also appeared to increase as the deposition temperature increased. A significant change to the relative ratios of the (104) and (110) peaks at approximately 33.5 and 36^{o} respectively can also be observed (Figure 7.4). Previously it has been noted that the ratios of the (110) and (104) diffraction peaks had a strong influence on the flat band potential of α – Fe_2O_3.[115] This ratio was also found to vary with deposition temperature, whereby the ratio of (110)/(110)+(104) increased with increasing deposition temperature using a CVD method. In this study it was found that the flat band potential moved positive by approximately 0.32 V between the films with the highest levels of orientation in the (110) and (104) directions. The opposite effect of temperature was observed in the work reported herein, whereby the (104) peak became larger relative to the (110) peak as the deposition temperature increased. This suggests that the structure becomes oriented in the (104) direction, which typically results in a surface termination dominated by O^{2-} groups.[262] When oriented in the (110) direction, the surface instead primarily features Fe^{3+} termination.[262] The higher affinity of Fe^{3+} towards OH groups is speculated to

account for the increased photoelectrochemical performance of (110) oriented surfaces relative to those oriented in the (104) direction.[115]

Although in this case the films deposited at 400 ^{o}C were most crystalline, a temperature of 300 ^{o}C was used for all the support depositions carried out in this work. This was to limit the chance of damage to the screening arrays, which often began to occur at temperatures exceeding approximately 350 ^{o}C. It was later found that the ITO screening arrays could withstand much higher temperatures (in excess of 550 ^{o}C), however the fabrication of these arrays had not yet been successfully optimised at the time this work was carried out. Additionally, as noted it is generally found that the photoelectrochemical performance of $\alpha - Fe_2O_3$ is reduced when oriented in the (104) direction,[115] which appeared to occur here when deposited at 400 ^{o}C.

7.2. Pt Particle Deposition

An identical calibration process to that described in the Pt/TiO_2 system was used for the deposition of Pt nanoparticles on α-Fe_2O_3. The previously prepared α-Fe_2O_3 (which shall henceforth be denoted as Fe_2O_3) substrates were also heated to 200 ^{o}C during the deposition of Pt particles. TEM imaging was subsequently used to characterise the particle size distributions as a function of deposition time. Four TEM images representing deposition times of 300, 210, 120 and 30 seconds are shown in the Figure below. These correspond respectively to the equivalent locations of rows 1, 4, 7 and 10 on the electrochemical screening arrays.

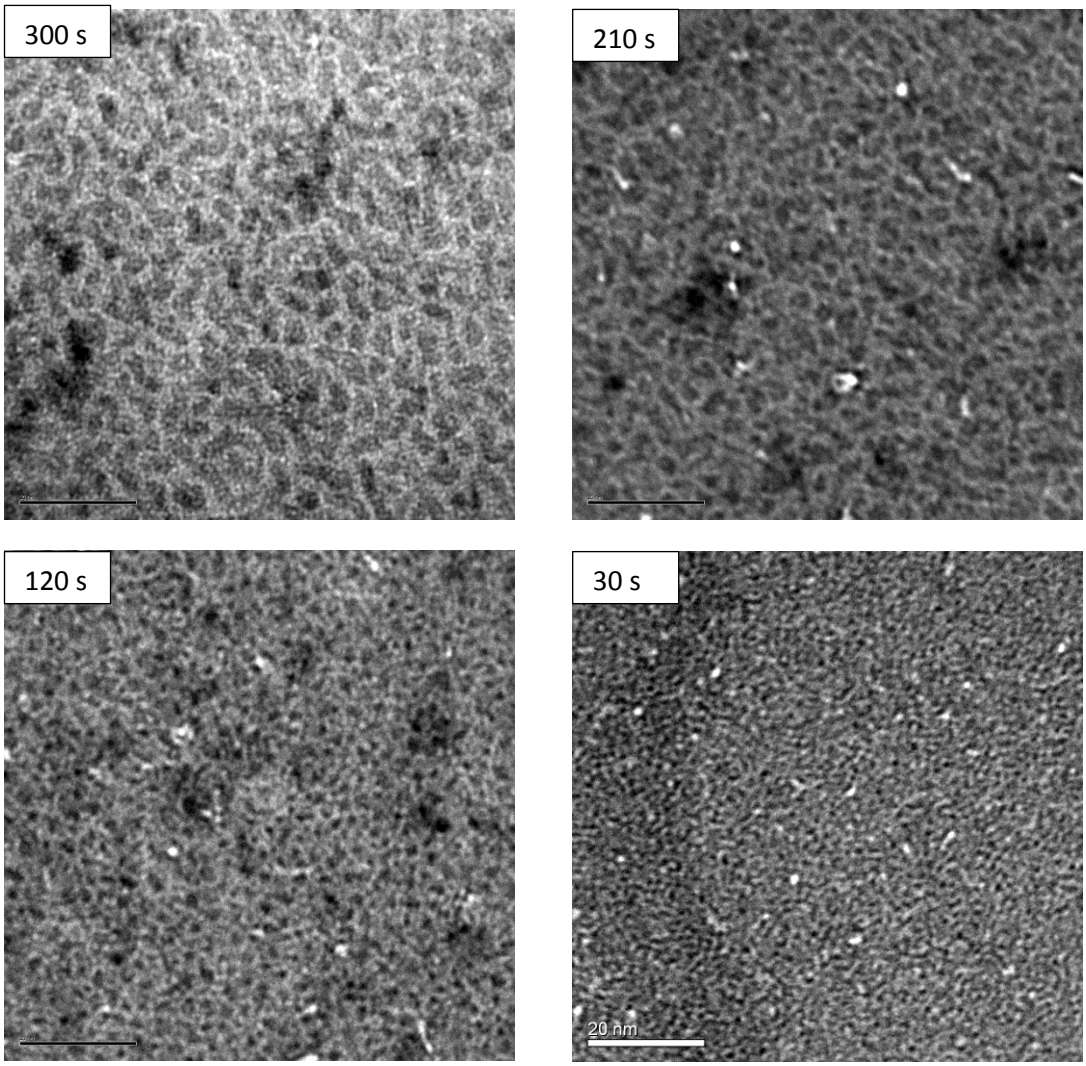

Figure 7.5. TEM images of Pt nanoparticles supported on Fe_2O_3. Images were captured with an accelerating voltage of 300 kV at a magnification of x200k. The scales bars represent 20 nm in each case and the deposition times (s) are given in the insets.

At the initial stages of growth (t_{dep} = 30 s), small randomly dispersed Pt particles formed on the Fe_2O_3 support. At longer deposition times the particles grew linearly in size, which is consistent with a primarily 3D type growth. Whilst the particles appear approximately circular in shape at the lower deposition times, some variation in the particle morphology occurs at deposition times of 210 s and above. The particles at a deposition time of 300 s are clearly observed to coalesce and produce randomly shaped structures with a broad size range.

It is known that the interaction of Pt with reduced metal oxide surfaces is much stronger than that between Pt and stoichiometric oxides.[267] It is likely that the prior heating in vacuum to 200 ^{o}C produces some level of nonstoichiometry in the support material. As a result, the interaction between the α-Fe_2O_3 support and the Pt support may be much stronger than that between the

individual Pt atoms. This may explain why a significant level of coalescence occurs at the higher deposition times.

The overall size range of the Pt nanoparticles were broadly similar to those supported on anatase TiO_2.The mean particle diameters calculated from the TEM images (with an assumption of hemispherical geometry) are shown in Figure 7.6 as function of array position. A linear regression analysis was performed in order to estimate the mean particle diameters at array positions inbetween the TEM grid locations. The estimated values are also shown in Table 7.2.

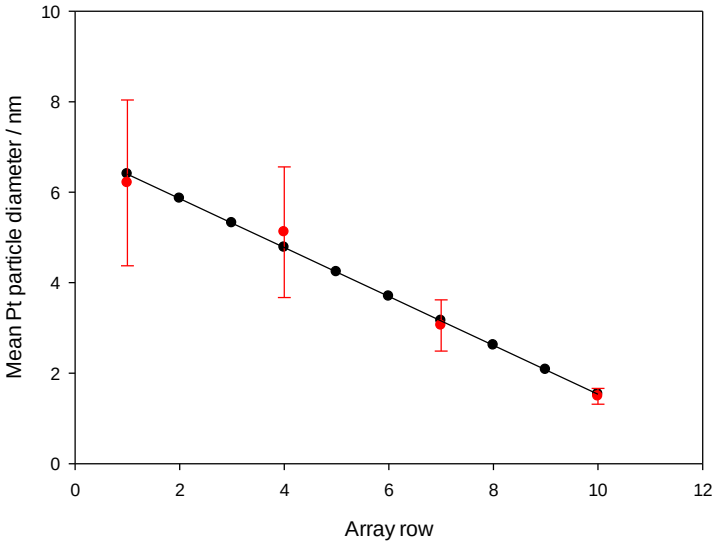

Figure 7.6. Mean Pt particle diameter as a function of position on the electrochemical screening array. The red data points show the mean values derived from the four TEM images shown in Figure 7.3. Error bars are presented with 1 standard deviation. The black data points represent the estimated values obtained from the linear regression which is shown also. A hemispherical particle geometry was assumed for the calculations.

Table 7.2.

Deposition time / s	Estimated particle diameter / nm	Particle diameter (TEM) / nm
300	6.40	6.21 +/- 1.83
270	5.86	
240	5.32	
210	4.78	5.11 +/- 1.44
180	4.23	

150	3.70	
120	3.15	3.05 +/- 0.56
90	2.61	
60	2.07	
30	1.53	1.48 +/- 0.17

The size distributions of the particles were calculated from two TEM images at each of the deposition times corresponding to the images in Figure 7.5. In each case a samples size of approximately 200 - 220 particles was used. In general, the distributions approximated a Gaussian function, which is fitted to each of the data sets shown in Figure 7.7.

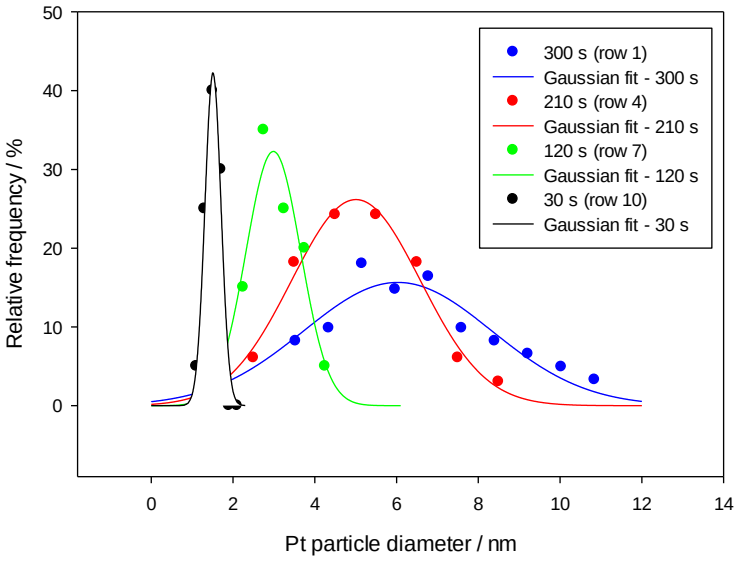

Figure 7.7. Pt particle size distributions for deposition times of 300, 210, 120 and 30 s. A sample size of approximately 200- 220 particles were used in each case, where a hemispherical geometry was assumed for the calculation of particle diameters. A Gaussian function is fitted to the data.

At the shortest deposition time, the particles were confined to a relatively narrow size range, with an average diameter of approximately 1.5 nm. As the deposition time increased, the size range became much broader, which is in qualitative agreement with similar results reported in the literature.[268] The range of particle diameters is particularly large at the longest deposition time of 300 s, which most likely reflects the variable level of particle coalescence across the sample area.

Additional characterisation of the Pt nanoparticles was carried out using XPS. In order to gain an insight into the electronic structure and chemical state of the supported Pt nanoparticles, the

Pt(4f) core level was analysed. Figure 7.8 shows the Pt(4f) core level spectra for a range of Pt particle sizes supported on α-Fe_2O_3.

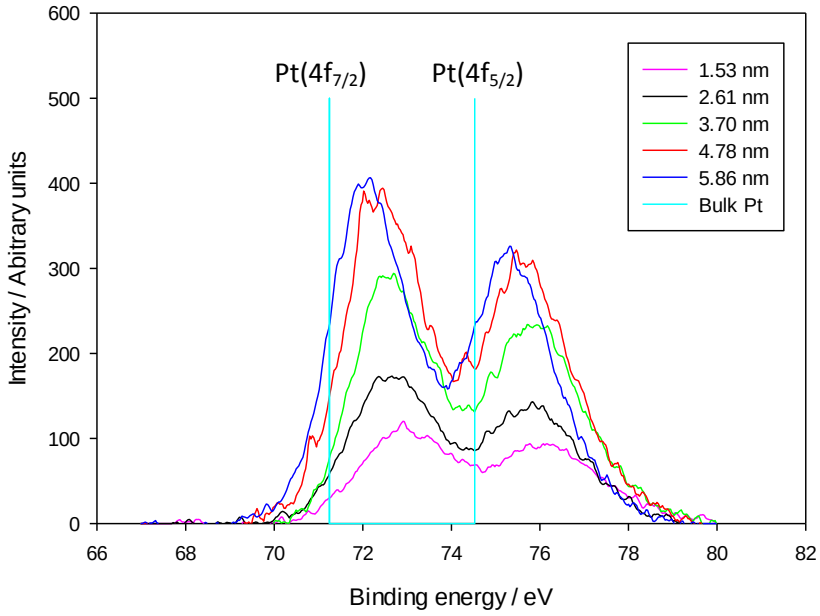

Figure 7.8. XPS spectra of the Pt (4f) core level in Fe_2O_3 supported Pt nanoparticles. The estimated mean Pt particle diameters are given in the inset. The peak positions for bulk Pt were derived from measurements carried out on a continuous Pt film on SiN. The measurements were carried out under identical conditions and with the same spectrometer used for the supported Pt nanoparticles, where Al-Kα excitation was used.

The binding energy of the Pt ($4f_{7/2}$) core level was found to shift positive by approximately 0.85 eV relative to bulk Pt at the largest particle size. This shift relative to bulk Pt further increased to approximately 1.65 eV at the smallest particle size. The overall binding energy shift is relatively similar to that seen across the particle size range with the TiO_2 support. Once again the significant increase in binding energy relative to bulk Pt, may suggest that some initial state effects relating to the chemical state of the Pt may be in operation. The binding energy of the Pt(4f) level in this case is more consistent with that relating to PtO (72.2 eV- Pt($4f_{7/2}$)).[243] Potentially the surface of the particles may therefore be oxidised to some degree. Alternatively, the large increase in binding energy may relate to both final state effects and a strong interaction with the support material. The intensities of the peaks were also found to increase as the Pt particle size increased, which relates to the increased amount of Pt deposited as the deposition time increased. The peak intensities and binding energies of the Pt($4f_{7/2}$) level are shown in Figure 7.9.

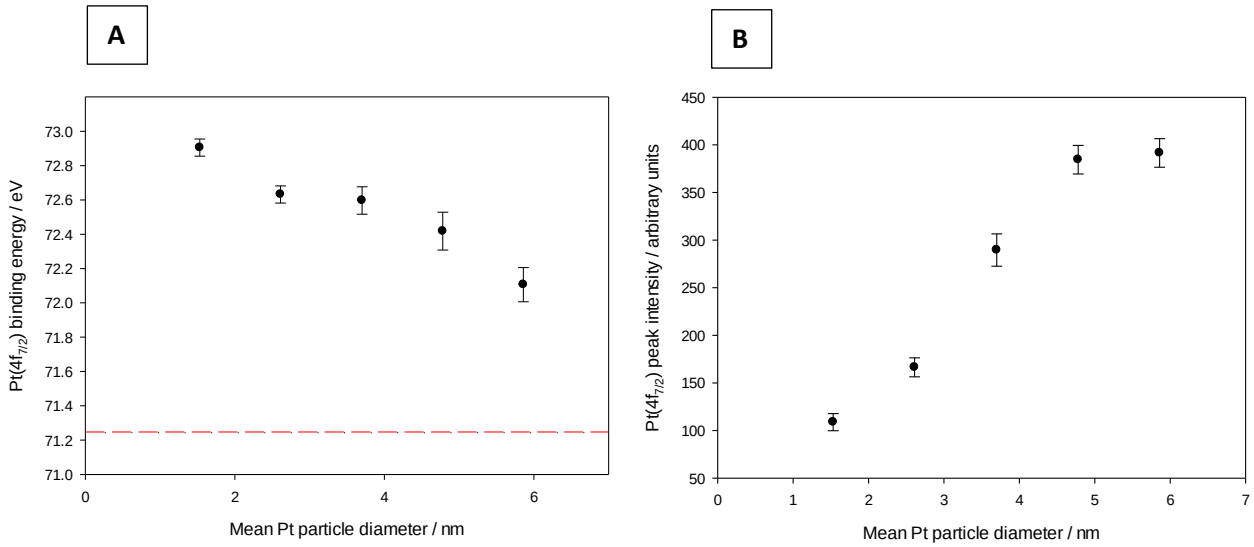

Figure 7.9. Peak position (A) and peak intensity (B) of the Pt ($4f_{7/2}$) core level in Fe_2O_3 supported Pt nanoparticles. The red dotted line in A represents the Pt($4f_{7/2}$) binding energy of bulk Pt. All error bars represent 1 standard deviation.

7.3 Surface Redox Behaviour

The electrochemical / photoelectrochemical data presented in this Chapter is derived from a total of 5 electrochemical screening arrays. The experiments performed and the order in which they were carried out is described for each array in Tables 7.3 – 7.7.

Table 7.3. #8135 (Au screening array)

Experiments performed	Illumination / electrolyte
CV x 5 at 50 mV s^{-1} (-0.05 – 1.4 V)	Dark: 0.5 M NaOH
CV x 3 at 50 mV s^{-1} (-0.05 – 1.4 V)	Dark: O_2 saturated 0.5 M NaOH
CV x 3 at 5 mV s^{-1} (-0.05 – 1.4 V)	Dark: O_2 saturated 0.5 M NaOH
CV x 3 at 50 mV s^{-1} (-0.05 – 1.4 V)	Illuminated at a lamp emission current of 8.5 A: 0.5 M NaOH
CV x 3 at 50 mV s^{-1} (-0.05 – 1.4 V)	Illuminated at a lamp emission current of 8.0 A: 0.5 M NaOH
CV x 3 at 50 mV s^{-1} (-0.05 – 1.4 V)	Illuminated at a lamp emission current of 7.5 A: 0.5 M NaOH
CV x 3 at 50 mV s^{-1} (-0.05 – 1.4 V)	Illuminated at a lamp emission current of 7.0 A: 0.5

	M NaOH
OCV measurement	3 cycles of 200 s illumination followed by 300 s dark: 0.5 M NaOH
OCV measurement	3 cycles of 200 s illumination followed by 300 s dark: O_2 saturated 0.5 M NaOH
CV x 3 at 50 mV s^{-1} (-0.05 – 1.4 V)	Dark: 0.5 M NaOH
CV x 3 at 5 mV s^{-1} (-0.05 – 1.4 V)	Dark: O_2 saturated 0.5 M NaOH
CV x 3 at 50 mV s^{-1} (-0.05 – 1.4 V)	Dark: 0.5 M NaOH + 1 M MeOH

Table 7.4. #8141 (Au screening array)

Experiments performed	**Illumination / electrolyte**
CV x 15 at 50 mV s^{-1} (-0.05 – 1.4 V)	Dark: 0.5 M NaOH
CV x 3 at 50 mV s^{-1} (-0.05 – 1.4 V)	Dark: O_2 saturated 0.5 M NaOH
CV x 3 at 5 mV s^{-1} (-0.05 – 1.4 V)	Dark: O_2 saturated 0.5 M NaOH
CV x 30 at 50 mV s^{-1} (-0.05 – 1.4 V)	Illuminated at a lamp emission current of 8.5 A: 0.5 M NaOH
CV x 3 at 50 mV s^{-1} (-0.05 -1.4 V)	Dark: 0.5 M NaOH
CV x 3 at 50 mV s^{-1} (-0.05 -1.4 V)	Dark: O_2 saturated 0.5 M NaOH
CV x 3 at 5 mV s^{-1} (-0.05 -1.4 V)	Dark: O_2 saturated 0.5 M NaOH
CV x 3 at 50 mV s^{-1} (-0.05 – 1.4 V)	Dark: 0.5 M NaOH + 1 M MeOH

Table 7.5. #8145 (Au screening array)

Experiments performed	**Illumination / Electrolyte**
CV x 3 at 5 mV s^{-1} (-0.05 – 1.4 V)	Dark: O_2 saturated 0.5 M NaOH
CV x 5 at 50 mV s^{-1} (-0.05 – 1.4 V)	Dark: 0.5 M NaOH
CV x 5 at 50 mV s^{-1} (-0.05 – 1.4 V)	Dark: 0.5 M NaOH + 1 M MeOH
CV x 8 at 50 mV s^{-1} (-0.05 – 1.4 V)	Illuminated at a lamp emission current of 8.5 A: 0.5 M NaOH + 1 M MeOH
CV x 3 at 50 mV s^{-1} (-0.05 – 1.4 V)	Dark: 0.5 M NaOH +1 M MeOH
CV x 3 at 50 mV s^{-1} (-0.05 – 1.4 V)	Dark: 0.5 M NaOH
CV x 3 at 50 mV s^{-1} (-0.05 – 1.4 V)	Illuminated at a lamp emission current of 8.5 A: 0.5 M NaOH
OCV measurement	3 cycles of 200 s illuminated followed by 200 s dark: 0.5 M NaOH
OCV measurement	As above in O_2 saturated 0.5 M NaOH
CV x 3 at 50 mV s^{-1} (-0.05 – 1.4 V)	Illuminated at a lamp emission current of 8.5 A: 0.5 M NaOH
CV x 3 at 50 mV s^{-1} (-0.05 – 1.4 V)	Dark : 0.5 M NaOH
CV x 3 at 50 mV s^{-1} (-0.05 – 1.4 V)	Dark: 0.5 M NaOH + 1 M MeOH

Table 7.6. #8147 (ITO screening array)

Experiments performed	Illumination / electrolyte
CV x 5 at 50 mV s^{-1} (-0.05 – 1.4 V)	Dark: 0.5 M NaOH
CV x 3 at 50 mV s^{-1} (-0.05 – 1.4 V)	Dark: 0.5 M NaOH + 5 mM $K_3Fe(CN)_6$
CV x 3 at 5 mV s^{-1} (-0.05 – 1.4 V)	Dark: 0.5 M NaOH + 5 mM $K_3Fe(CN)_6$
CV x 3 at 50 mV s^{-1} (-0.05 – 1.4 V)	Dark: O_2 saturated 0.5 M NaOH
CV x 3 at 5 mV s^{-1} (-0.05 – 1.4 V)	Dark: O_2 saturated 0.5 M NaOH
CV x 3 at 50 mV s^{-1} (-0.05 – 1.4 V)	Illuminated at a lamp emission current of 8.5 A: 0.5 M NaOH
OCV measurement	30 s illuminated followed by 30 s dark
CV x 3 at 50 mV s^{-1} (-0.05 – 1.4 V)	Dark: 0.5 M NaOH
CV x 3 at 50 mV s^{-1} (-0.05 – 1.4 V)	Dark: 0.5 M NaOH + 1 M MeOH
CV x 3 at 50 mV s^{-1} (-0.05 – 1.4 V)	Dark: 0.5 M NaOH

Table 7.7. #8150 (ITO screening array)

Experiments performed	Illumination / electrolyte
CV x 5 at 50 mV s^{-1} (-0.05 – 1.4 V)	Dark: 0.5 M NaOH
CV x 3 at 50 mV s^{-1}	Dark: O_2 saturated 0.5 M NaOH
CV x 3 at 5 mV s^{-1}	Dark: O_2 saturated 0.5 M NaOH
CV x 3 at 50 mV s^{-1}	Dark: 0.5 M NaOH
CV x 3 at 50 mV s^{-1}	Dark: 0.5 M NaOH + 1 M MeOH
CV x 3 at 50 mV s^{-1}	Illuminated at a lamp emission current of 8.5 A: 0.5 M NaOH + 1M MeOH
CV x 3 at 50 mV s^{-1}	Dark: 0.5 M MeOH + 1 M MeOH
CV x 3 at 50 mV s^{-1}	Dark: 0.5 M NaOH
CV x 3 at 50 mV s^{-1}	Illuminated at a lamp emission current of 8.5 A: 0.5 M NaOH

The surface redox behaviours of the various sizes of Pt nanoparticles were evaluated with cyclic voltammetry. It is known that the surface redox behaviour of Pt nanoparticles can change significantly as the particle size is altered, which is often linked to particle size activity trends in several of the reactions investigated herein.[168] By studying the surface redox chemistry of such materials, information may be inferred regarding the underlying causes of particle size activity trends. Furthermore, the study of Pt particle size effects are not commonly reported in alkaline media, which may be of significant interest to technologies such as alkaline fuel cells. The differing reaction mechanisms that may occur at different pHs may also aid in understanding the exact causes of particle size effects in a number of commercially relevant electron transfer reactions.

Screening was carried out on films deposited on both Au and ITO substrates. All measurements were conducted at room temperature in 0.5 M NaOH with a potential scan rate of 50 mV s^{-1}. Figure 7.10 shows selected voltammograms derived from a typical sample prepared on an Au array.

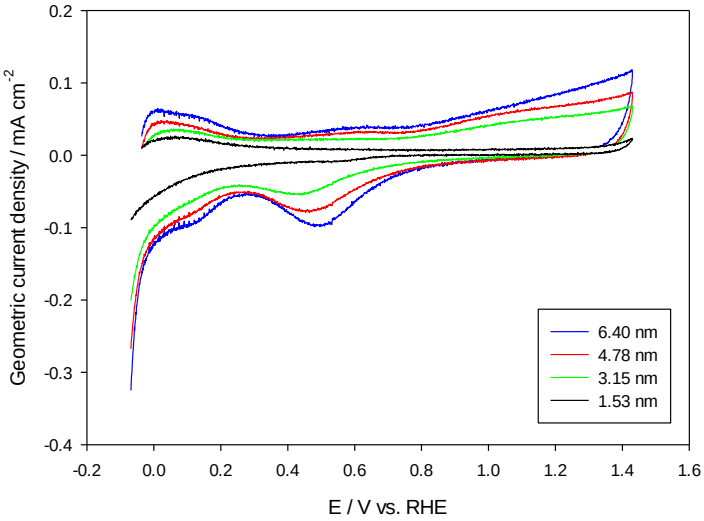

Figure 7.10. Cyclic voltammograms of selected Pt particle sizes supported on Fe_2O_3. Measurements were conducted in Ar purged 0.5 M NaOH with a potential scan rate of 50 mV s^{-1}. The sample was prepared on an Au substrate and the first cycles are shown in each case. (Array #8135)

Similarly to the anatase TiO_2 supported nanoparticles, a number of characteristic features of Pt can be seen in the voltammetry. Between approximately 0.26 and 0.02 V the adsorption of hydrogen occurs on the negative going sweep. Also similar to the results with the anatase TiO_2 support, is the observation of only one clear peak in this region. On the anodic sweep hydrogen desorption occurs between approximately 0 and 0.3 V, which is subsequently followed by a small anodic peak beginning at around 0.4 V. This feature was also observed on the anatase TiO_2 supported particles in a similar potential range, although was more poorly defined. As with the anatase TiO_2 support, this peak is tentatively assigned to the adsorption of OH species at the Pt surface. Upon sweeping the potential more positive, the formation of Pt oxide occurs above approximately 0.8 V, which is subsequently stripped from the Pt surface on the reverse scan. The potential at which the oxide layer is stripped from the Pt surface can be seen to vary in response to changes in Pt particle size.

The same general features can be seen on the samples prepared using ITO substrates (Figure 7.11), although the hydrogen adsorption features are more ill-defined. Additionally the current densities are considerably larger than those with samples on Au substrates on account of the much larger double layer charging current observed on the ITO substrate. A large increase in anodic current is also apparent at potentials positive of approximately 0.8 V on the first few cycles. It is assumed that this process relates to the oxidation of the ITO substrate through Sn dissolution.

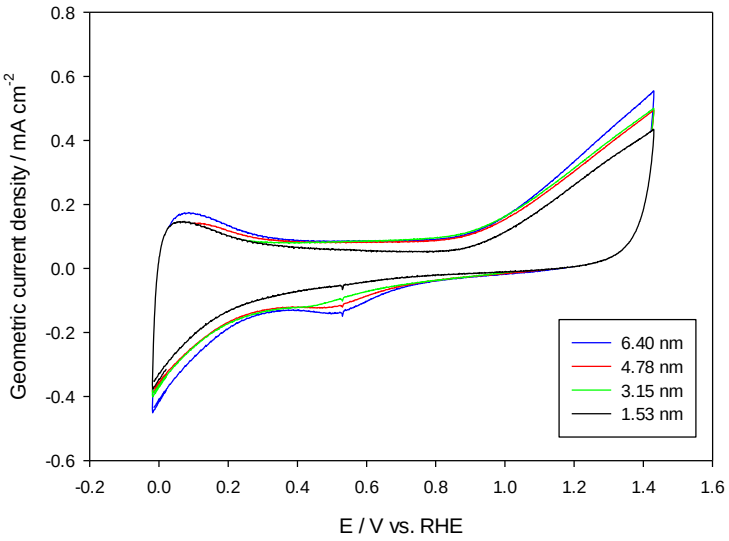

Figure 7.11. Cyclic voltammograms of selected Pt particle sizes supported on Fe_2O_3. Measurements were conducted in Ar purged 0.5 M NaOH with a potential scan rate of 50 mV s^{-1}. The sample was prepared on an ITO substrate and the first cycles are shown in each case. (Array #8147)

Several key observations can be made from Figures 7.10 and 7.11 as the particle size is reduced. Firstly, the current densities associated with all the voltammetric features decrease in magnitude upon decreasing the Pt particle size. This is to be expected given that the overall Pt surface area decreases in magnitude as a result of the reduction in the absolute amount of Pt deposited. In Figure 7.10 it also appears that the reduction in current over the hydrogen adsorption region is slightly more gradual than that relating to oxide formation above approximately 0.8 V. It is difficult to interpret the oxide formation features on the samples prepared with the ITO substrates, since the current densities appear to be dominated by the oxidation of the substrate in this region. A reduction in current can however be observed above 0.8 V as the particle size decreases. This may reflect that the same trend in terms of oxide formation behaviour occurs on the samples with ITO substrates, albeit superimposed upon the background current from substrate oxidation. It was however found that the characteristics of the substrate oxidation feature changed depending on the nature of the electrode-electrolyte interface in the case of anatase TiO_2 (Chapter 5). As a result it cannot be stated with certainty whether or not the current variation occurs solely due to the differing characteristics of the Pt particles.

In order to take into account the variation in the amount of Pt deposited, the voltamogramms were normalised to the specific Pt surface area determined from the charge under the hydrogen adsorption region. The charges obtained were subsequently divided by the charge required to

adsorb hydrogen on 1 cm^2 of polycrystalline Pt (210 µC).[250,269,164b] The calculated Pt surface areas for several arrays using both ITO and Au substrates are presented in Figure 7.12. In general the surface areas obtained are in good agreement. Additionally, the values for the specific Pt surface areas are relatively similar to those obtained on anatase TiO_2, where identical Pt deposition times and rates were used at each row on the array. This may suggest that the nucleation and growth behaviour of Pt does not change significantly between the two support materials.

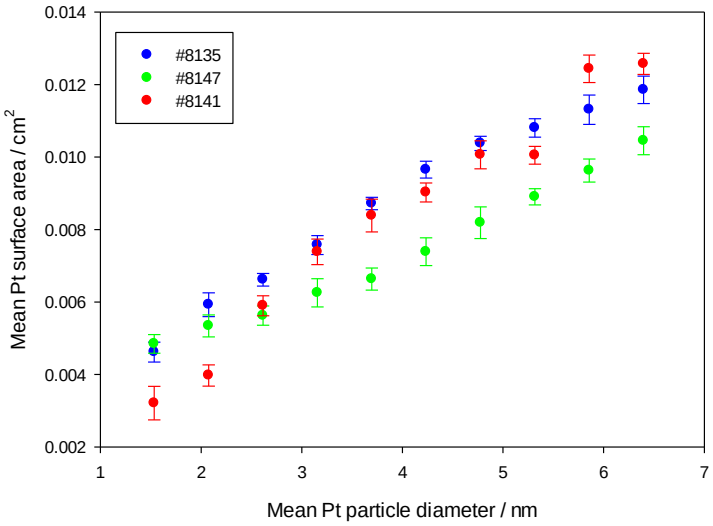

Figure 7.12. Mean Pt surface areas estimated from the Hydrogen adsorption charge. Data was derived from the 5th cycles conducted at room temperature in 0.5 M NaOH. A scan rate of 50 mV s^{-1} was used in each case. The error bars represent 1 standard deviation

Figure 7.13 shows the resulting voltammograms of Fe_2O_3 supported Pt nanoparticles upon normalisation to the specific Pt surface area. The data presented is from an array synthesised on an Au substrate. In general the current densities over the hydrogen adsorption region are approximately equal, with only the smallest particle size presented showing any clear variation. The same is true of the oxide formation region, where all particle sizes presented other than the smallest show almost identical behaviour. This may arise from the slightly smaller currents in the hydrogen adsorption region at a diameter of 1.50 nm, which would suggest the surface area has been slightly overestimated. Nevertheless, the variation in current density over the hydrogen adsorption region is still much smaller than that relating to oxide formation, suggesting that oxide formation is limited at particles of approximately 1.5nm in diameter.

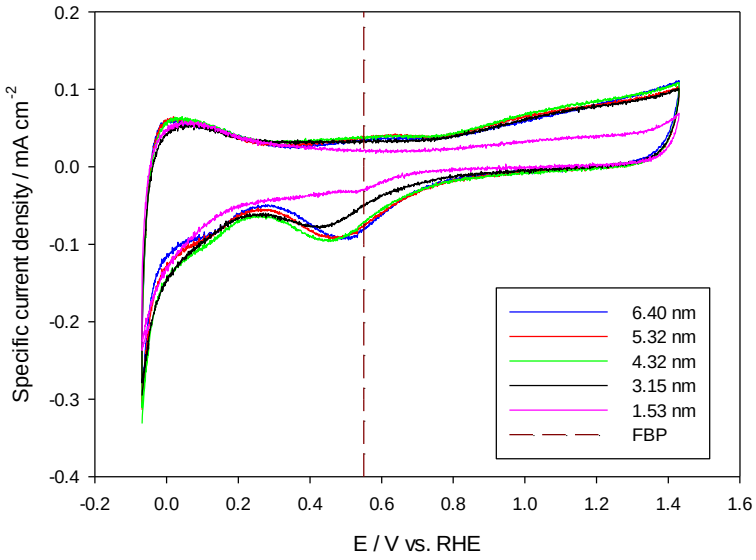

Figure 7.13. CVs of selected Pt particle sizes normalised to the specific Pt surface area estimated from the hydrogen adsorption charge. The first cycles in 0.5 M NaOH are shown, where a scan rate of 50 mV s^{-1} was used. The approximate location of the flat band potential (+/- 0.15 V) in α-Fe_2O_3 is shown as the brown dotted line. (Array #8135)

The most apparent effect of particle size on the voltammetry lies within the oxide formation and stripping behaviour. Firstly it is clear that a general negative shift in the oxide stripping peak potential occurs as the particle size decreases. The same was true of samples prepared on both substrate types, although quantitative analysis was not possible with the samples on ITO. This is due to the coincidence of the oxide stripping feature with the background signal of this substrate type.

The same negative shift in the oxide stripping feature has been observed on a number of occasions using both carbon and amorphous TiO_2 supports in acid and alkaline media.[251,165] In semiconducting supports, the flat band potential (indicated in Figure 7.13) as well as the overall band structure of the material is of significant importance in determining the charge transfer characteristics. In the case of a conducting support, the continuum of energy levels may permit charge transfer reactions to occur across a wide potential range. Thus the voltammetry on conducting supports may purely reflect the variation in catalytic activity between the different particle sizes. Conversely, an ideal semiconductor may only exchange charge via its conduction and valence bands[270]. As a result, only very low dark anodic currents are predicted above the flat

band potential, owing to the lack of appreciable hole concentration in the valence band of the semiconductor. A number of studies have verified this expected behaviour by studying the voltammetry of simple electron transfer reactions with a wide range of standard potentials.[271,118] In these studies, reversible redox couples were chosen with standard potentials spanning the entire range of energies relating to the band structure of the semiconductor being studied. The typical expected response of a semiconductor towards these reactions is depicted as a function of the formal potential of the redox couple in Figure 7.14.

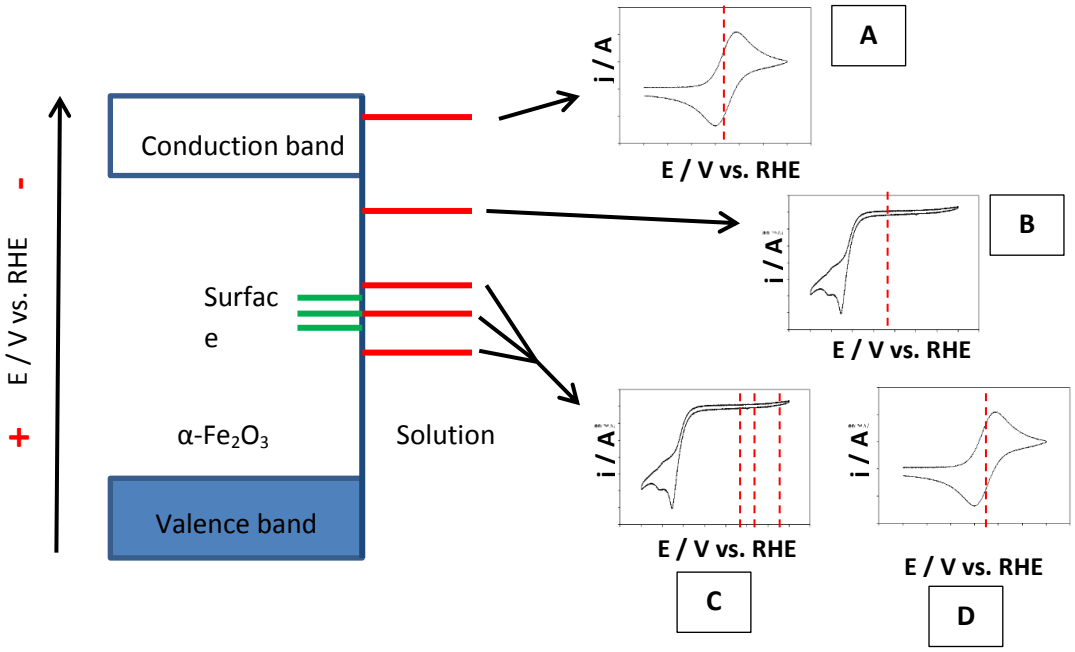

Figure 7.14. Simplified band diagram of an n-type α-Fe_2O_3 electrode relative to the formal potential (E_{redox}) of several hypothetical reversible redox couples (Shown as solid red lines). The expected voltammetry is shown for situations where E_{redox} (dotted red line in voltammograms) is negative of the conduction band edge (A), slightly positive of the conduction band edge (B) and in the centre of the band gap (C). The situation is also shown for surface state (Green solid lines) mediated electron transfer where E_{redox} is in the centre of the band gap (D).

The situation depicted above shows that at potentials negative of the semiconductor conduction band edge (A), reversible behaviour is observed. This stems from the accumulation of electrons at the surface in this potential range, meaning that as the potential is changed, the potential distribution over the Helmholtz region will also change. In this potential range, the behaviour therefore becomes essentially like that of a metal. When the formal potential of the redox potential is higher (as in B), the energy levels in the redox species do not overlap as effectively

with the levels in the conduction band. Some level of rectification is also introduced which leads to more irreversible behaviour in the electron transfer reactions. When the formal potential is even more positive (C and D), the semiconductor electrolyte interface exhibits strong rectifying behaviour. With redox couples of significantly positive formal potentials, a variation in E_{redox} of up to 0.5 V has been shown to have little influence on the onset of the reduction of this species. In this instance the onset is primarily defined by the rectifying nature of the semiconductor as opposed to the formal potential of the redox couple. In the cases of B and C (Figure 7.13) little or no anodic current is to be expected, unless surface states of appropriate energy are able to mediate the process as in situation D.

In light of the behaviour of semiconductor junctions, it is entirely possible that the band structure of a semiconducting support such as TiO_2 or Fe_2O_3 may strongly influence the electrocatalytic function of Pt. Where a significant degree of rectification occurs, the activity towards anodic processes is expected to be particularly effected. In the ideal case, no current flow is expected to occur at potentials positive of the flat band potential. Figure 7.15 shows the specific current density of α-Fe_2O_3 supported Pt nanoparticles at 1.20 V vs. RHE. In this case, it is apparent that some level of oxide formation is apparent at all sizes of Pt nanoparticles. As such it is likely that intraband gap states may aid in mediating the charge transfer reaction at the Pt surface. Additionally, given the evidence of substrate exposure presented in Chapter 5, it is possible that anodic processes are mediated by some extent by the substrate and/or Pt particles directly on the substrate.

In contrast to the behaviour of anatase TiO_2 supported Pt, the specific current density relating to oxide formation changes very little for particle sizes greater than approximately 3 nm. Below approximately 3 nm, the specific current density decreases significantly. Given the similar sizes and surface areas of the Pt particles on the α-Fe_2O_3 and TiO_2 supports, the differing trends may reflect a variation in the support characteristics. This may be in terms of the rectifying ability, band structure, surface state density etc. or the strength of interaction between the support materials and Pt. As a result, the trends observed in the data is likely to be a consequence of both a variation in the intrinsic catalytic function of Pt, as well as a change to the semiconducting characteristics of the support. Additionally, the fact that the α-Fe_2O_3 layers were significantly thinner than the anatase TiO_2 support presented in Chapter 5 cannot be ignored. This is especially true given that a strong dependence of thickness was observed in terms of the ability to sustain anodic current flow at anatase TiO_2.

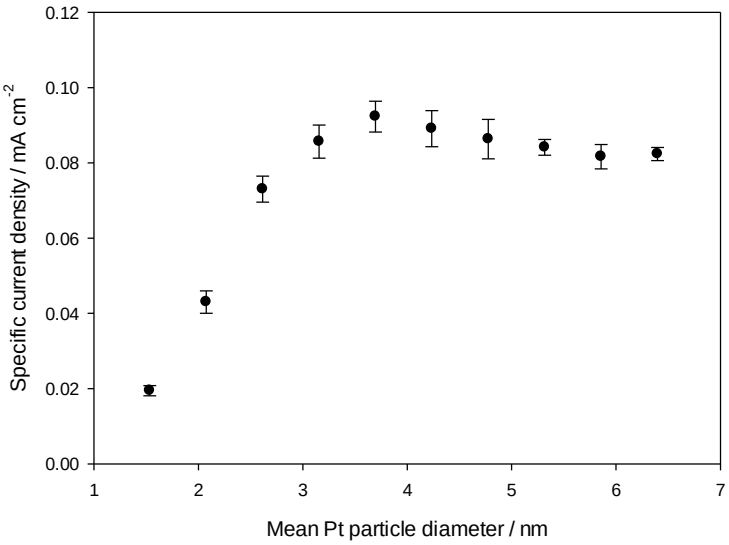

Figure 7.15. Specific current density with respect to the estimated Pt surface area (calculated from the hydrogen adsorption charge) at 1.2 V vs. RHE. The data represent the first anodic cycle in 0.5 M NaOH where a scan rate of 50 mV s^{-1} was used. (Array #8141)

The behaviour described in Figure 7.15 clearly shows that anodic current flow is permitted positive of the flat band potential of α-Fe_2O_3 at all particle sizes. With regard to the cathodic oxide reduction process some additional particle size trends were apparent. Figure 7.16 presents the peak potential for the reduction of Pt oxide at the largest 8 particle sizes on the array. Although some level of oxide formation was apparent on the two smallest particle sizes, no clearly resolved peak relating to the reduction of Pt oxide could be observed. However, a slight increase in cathodic current began at approximately 0.65 V on the smallest particle sizes (see Figure 7.13 – 1.5 nm), which is close to the expected flat band potential of α-Fe_2O_3. Possibly the potential drop over the Helmholtz layer begins to change more over this region due to the accumulation of electrons at the electrode surface. As a result, the increase in capacitive current may partially mask the oxide stripping features in this case.

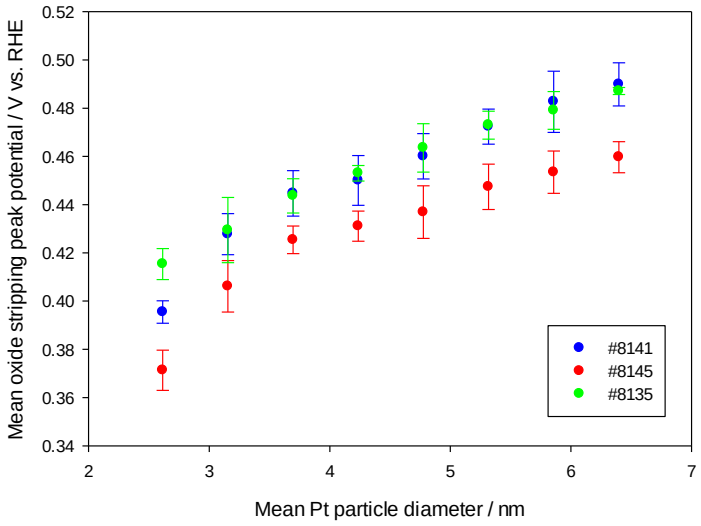

Figure 7.16. Mean peak potential of the oxide stripping peak on several different arrays. Data from the first cycles are shown. Measurements were conducted in 0.5 M NaOH at a scan rate of 50 mV s^{-1}.

The absolute values for the oxide stripping peak potential varied slightly between the different arrays, although the same overall trend was present in each case. On all three arrays the peak potential shifted negative by approximately 80 – 90 mV between the largest and smallest particle sizes presented. No clear negative shift could be observed regarding the oxide formation onset however. Possibly the trend depicted above results from the process being kinetically limited at smaller particle sizes. The same would appear to be true of the oxide formation process, given that the specific current density relating to oxide formation sharply decreased below a particle size of approximately 3 nm. As noted there are a number of explanations for this in addition to intrinsic effects relating to the size of the Pt nanoparticles. Clearly in the initial cycles presented in Figures 7.10 and 7.11 the electrodes do not appear to exhibit strong rectifying behaviour.

The role of surface states is likely to be significant in determining the overall charge transfer characteristics in the data presented above. The exact natures of these states on α-Fe_2O_3, as well as their mechanism of action have been the subject of considerable interest, particularly in the field of photoelectrochemistry.[272,273,274] These states may arise from the termination of the bulk α-Fe_2O_3 structure,[275] or from the resulting hybridization of orbitals contributed by surface bound species such as Pt.[252].

It has also been noted that a change to the electronic structure occurs at the surface of α-Fe_2O_3 with Pt addition. Most notably, density of state calculations from first principles showed the

imposition of a continuous band of states in the band gap region when a continuous film of Pt was attached to α-Fe_2O_3.[252] The same effect has been observed albeit to a lesser extent in bulk doped α-Fe_2O_3.[276]Potentially the change in absolute area of the platinum contacts may also affect the density of surface states and the related electrochemical response. It also remains a possibility that differing levels of substrate exposure contribute to the aforementioned effects.

Similarly to the results on anatase TiO_2 supported Pt, the observed electrochemical response appeared to change after being subjected to a number of cycles. On the α-Fe_2O_3 support, the changes with cycling however occurred more gradually (Figure 7.17). In the case of the anatase TiO_2 supported particles, virtually no anodic or cathodic current was observed positive of approximately 0.5 V after 15 cycles. This was true of all particle sizes on the array, and would suggest that oxide formation becomes hindered upon electrochemical cycling. Qualitatively, the same general observations can however be made for the particles supported on α-Fe_2O_3. In this case, the current relating to oxide formation (E > ~0.8 V) decreases between the first and 15th cycles in all cases. Clearly however the absolute level of current decay varies between the different particle sizes.

Additionally, some slight changes to the hydrogen adsorption features can be seen. In general the single hydrogen adsorption peak becomes slightly sharper, with may reflect some level of restructuring or cleaning of the Pt surface. This observation is often reported on Pt nanoparticles irrespective of the support material as well as on bulk Pt.

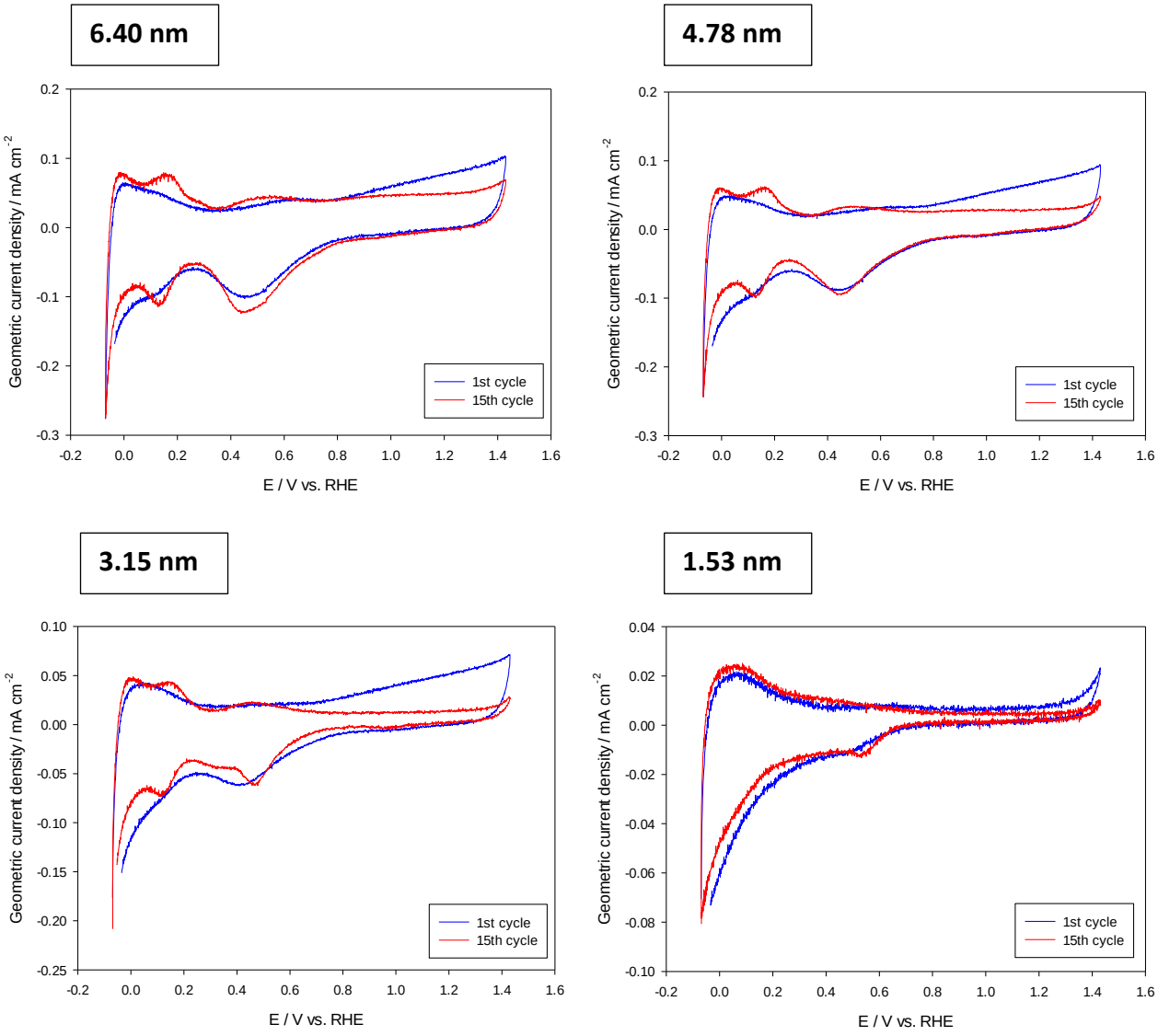

Figure 7.17. The first (Blue) and 15th (Red) cycles recorded for α-Fe_2O_3 supported Pt nanoparticles. Measurements were conducted at room temperature in 0.5 M NaOH with a potential scan rate of 50 mV s^{-1}. (Array #8141)

In addition to the observations pointed out above, the peak relating to OH adsorption (~0.3 – 0.6 V) became slightly more pronounced. The variation in the current density above 0.8 V with cycling also appeared to exhibit a clear particle size dependence. Figure 7.18 shows the geometric current density at 1.2 V vs. RHE on both the first and fifteenth anodic sweep. Presented also is the mean difference in this parameter between the first and fifteenth cycle.

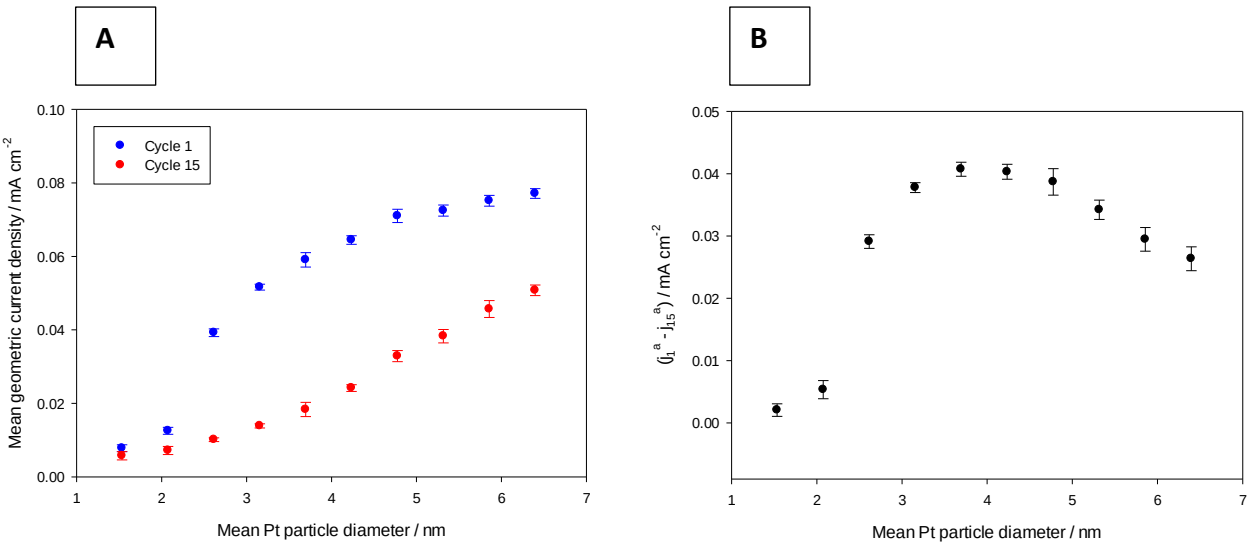

Figure 7.18. A: Mean geometric current density recorded during the first (j_1^a) and fifteenth (j_{15}^a) anodic sweep at 1.2 V vs. RHE. B: Mean difference in geometric current density between the first and fifteenth anodic sweeps at 1.20 V vs. RHE (i.e. $j_1^a - j_{15}^a$). All measurements were performed at room temperature in 0.5 M NaOH with a scan rate of 50 mV s^{-1}. (Array #8141)

Although a slight reduction in current density occurred at all particle sizes between the first and fifteenth cycles, the level of variation was more pronounced at the intermediate particle sizes on the array. The general trend of a reduced oxide formation current may arise from a number of different possibilities. Firstly it is possible that cycling strengthens any interaction between the particles and the support, or that a significant change to the surface area/ structure of the particles occurs. Given the relatively high positive potential limit employed, some dissolution of small particles may be expected. However, any changes which occur are much more apparent in the oxide formation/stripping region compared to the hydrogen adsorption region. If a significant change to the Pt surface area occurred through Pt loss/restructuring, one may expect this to be reflected to a greater degree in the hydrogen adsorption region. Secondly, there may be a reduction in the conductivity of the support, either through oxidation of the intrinsic n-type donor species (Fe^{2+}) or passivation of surface states. Both of these processes have been found to significantly affect the photoelectrochemical/electrochemical characteristics of α-Fe_2O_3.[277,278] The implication of surface states on the band energetics of an n-type semiconductor are schematised in Figure 7.19.

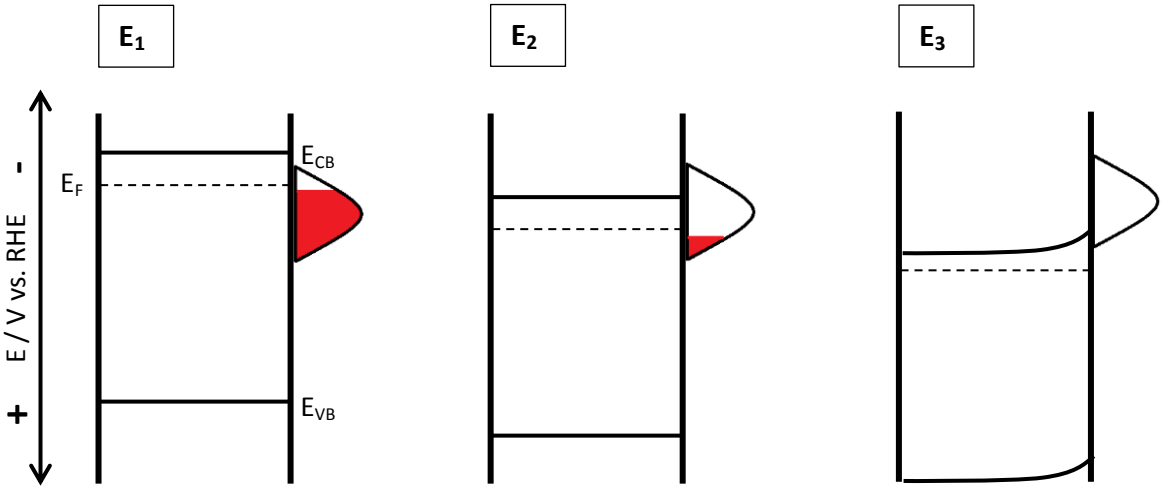

Figure 7.19. Simplified band diagram of an n-type semiconductor in the presence of surface states. The situation is shown are shown for: E_1 - at the flat band potential (V_{FB}). E_2 – With a slight anodic bias, where occupied surface states are emptied and the band edge positions move positive. E_3 – With a large anodic bias which empties the surface states completely and begins to induce band bending in the semiconductor. Occupied and unoccupied surface states are denoted as the red and white filled ares at the surface respectively.

In the event of surface state passivation or oxidation of donors in the film, the level of rectification is likely to increase. As a result, the increased band bending will have a stronger 'blocking' effect on the flow of anodic current. Potentially this may explain the reduction in anodic current after cycling. It can also be inferred that the Pt becomes cleaner with cycling, as evidenced by the sharper appearance of the hydrogen adsorption features. In this case the oxidation of contaminants may occur in the oxide formation region and thus decrease the current in this region as the surface becomes cleaner. The different behaviour between particle sizes may reflect a variation in the level of band bending and therefore a change in the rate of contaminant removal. The change to the electrochemical properties of the sample could also be inferred from the drastic colour change apparent after cycling (Figure 7.20).

A typical array on an ITO substrates is shown in Figure 7.20. In this instance a large number of the electrodes did not make electrical contact with the connections to the potentiostat. As a result, these electrodes were held at open circuit during the screening process. A clear difference in

colour can be observed between the electrodes held at open circuit with those that were repeatedly cycled throughout the experiments.

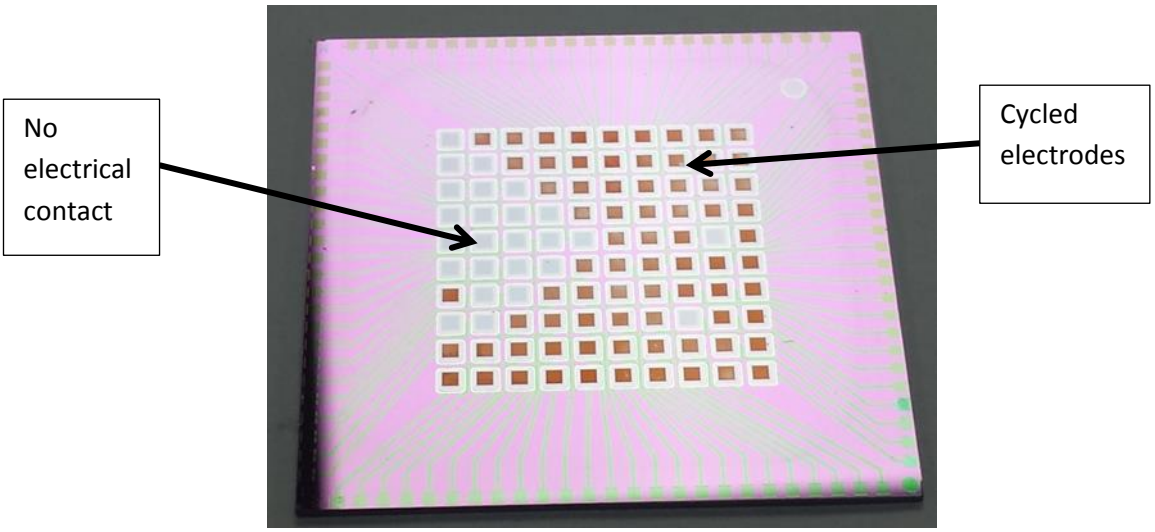

Figure 7.20. An image of an ITO screening array with a film of Fe_2O_3 supported Pt nanoparticles. The image was captured after the electrochemical/photoelectrochemical screening was carried out. The areas of grey electrodes represent the locations at which electrical contact was not made during screening.

It was apparent that after cycling the electrodes changed in appearance to the more familiar rusty red colour characteristic of α-Fe_2O_3. This is a common observation where the stoichiometry changes in iron oxide films.[262] It should be noted that the Fe_2O_3 films appeared largely identical before and after deposition of the Pt particles, and that the silver colour of the uncycled electrodes does not arise solely from the Pt. Additionally, the equivalent thickness of the Pt deposits are sufficiently low (< 1.5 nm) so as to appear optically transparent.

The particle size trends of the voltammetry presented so far will contain contributions from a number of different factors. Specifically, the oxide formation/stripping behaviour is dictated by both intrinsic particle size effects and the nature of the band energetics at the semiconducting support. Furthermore, it is possible that changes in the Pt particle size may modulate these support characteristics to a varying degree.

7.4. Ferrocyanide / Ferricyanide Voltammetry

In order to remove the effects of the intrinsic particle size effects (relating to the interfacial kinetics of oxide formation/stripping), voltammetry was recorded with a simple reversible redox couple. The $Fe(CN)_6^{-4}$ / $Fe(CN)_6^{-3}$ couple was used due to its reversibility on metallic electrodes and it's lack of adsorption on oxide semiconductors. The couple also features a high standard rate constant and should not be sensitive to the electrode surface structure. As a result, voltammetry with this redox couple may allow one to infer details regarding the characteristics of the semiconducting support. Specifically, its voltammetry may describe the ability of the electrodes to transport electrons to and from the surface.

Cyclic voltammetry was recorded in 0.5 M NaOH with the addition of 5 mm $K_3Fe(CN)_6$. All measurements were undertaken at room temperature with a potential scan rate of 50 mV s^{-1}. The data presented is from films deposited on ITO substrates and the responses of several electrodes with varying Pt particle diameters are shown below in Figure 7.21.

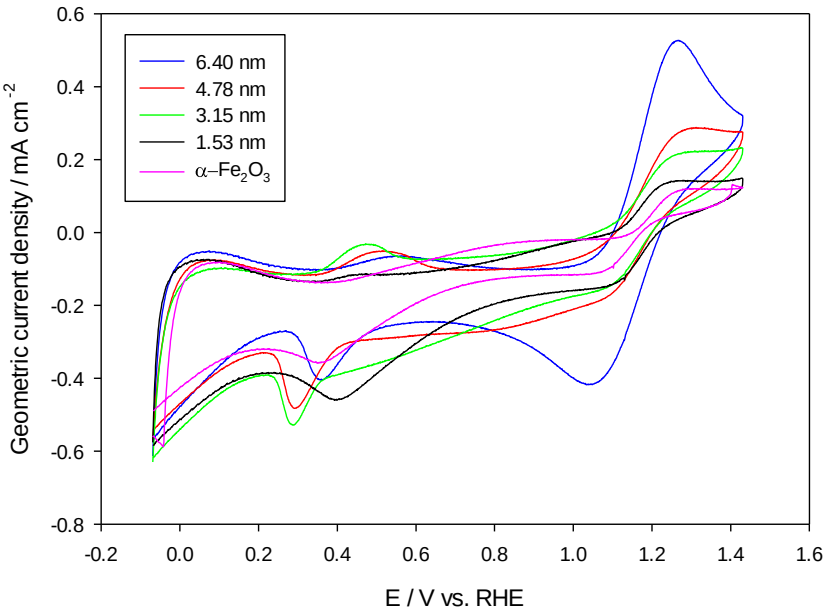

Figure 7.21. Cyclic voltammetry of Fe_2O_3 supported Pt particles (ITO substrate) in 0.5 M NaOH + 5mM $K_3Fe(CN)_6$. Measurements were conducted at a scan rate of 50 mV s^{-1} and the first cycles are shown. (Array #8147)

The behaviour at all particle sizes differs significantly to that seen on the anatase TiO_2 supported nanoparticles. Most notable is the clear occurrence of Ferrocyanide oxidation positive of 1.15 V, which did not occur to any significant degree at any Pt particle size supported on anatase TiO_2.

Additionally the reduction of the oxidised species occurs to some degree at potentials significantly positive of the flat band potential of α-Fe_2O_3 (approximately 0.55 V).

The peak current density of the oxidation process occurred at approximately 1.28 V and the current density increased in response to increasing Pt particle size. There was a particularly large increase in current density at the largest Pt particle size which is evident in Figure 7.22.

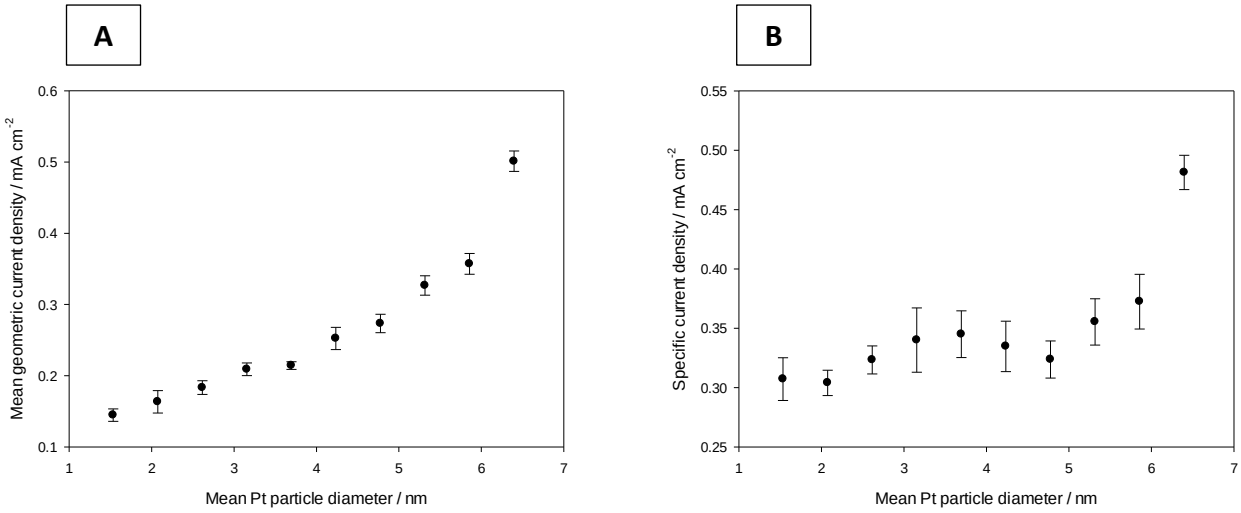

Figure 7.22. Geometric current density at 1.28 V vs. MMO in 0.5 M NaOH + 5 mM $K_3Fe(CN)_6$ (A). Also shown (B) is the current density scaled to the specific Pt surface area. All measurements were conducted at a scan rate of 50 mV s^{-1} and data is shown for the first positive going sweep. (Array #8147)

The specific current density remained approximately equal for the majority of particle sizes, and a clear difference was only observed at the very largest Pt particle size on the array. Possibly this may result from an inaccuracy in determining the real Pt surface area, although it was found that surface based processes such as hydrogen adsorption and oxide formation did not show this same large increase in current at the largest Pt particle size. Alternatively, it may be that the increased Pt coverage caused by particle coalescence causes a significant change to the electronic structure of the support.

The peak separation between the anodic and cathodic processes was substantially larger than that observed for bulk metal electrodes such as Au and Pt. In the case of the largest particle size, the peak separation was found to be approximately 250 mV. On a polycrystalline Au electrode the peak separation reduced to 65 mV, which is in reasonable agreement with the theoretically

predicted separation of 59 mV. The voltammetry in Ferrocyanide containing media was however acquired only on samples with an ITO substrate. It was therefore considered that the conductivity of the ITO substrate may play a role in the increased peak separation relative to Au. It was found however that the peak separation on ITO was close to the theoretically predicted value for a reversible redox couple (65 mV +/- 5 mV). It is therefore likely that the behaviour stems from the properties of the Fe_2O_3 film.

Another deviation from the expected behaviour was the peak currents recorded. Typically in a reversible redox process the peak current (j_p) may be described by the Randles-Sevcik equation:[45]

7.2. $$j_p = 0.45\left(\frac{nF}{RT}\right)^{1/2} nFAC^0 D^{1/2} v^{1/2}$$

Where n is the number of electrons transferred, F is Faraday's constant, R is the ideal gas constant, T is the absolute temperature, A is the electrode area, C^o is the concentration of the electroactive species, D is the diffusion coefficient and *v* is the potential scan rate.

In the case of the Au electrode, substituting in the various parameters (with D = 6.20 x 10^{-6} cm^2 s^{-1})[279] leads to an estimated Ferricyanide concentration of 4.78 mM, in reasonable agreement with the experimentally prepared concentration of 5 mM. In the case of the Fe_2O_3 supported particles, the peak current density of the reduction process was found to be -0.44 mA cm^{-2} at the largest Pt particle size (with respect to the geometric surface area of the electrode). Naturally the real surface rea will deviate from the geometric surface area, since both the Pt particles and the exposed Fe_2O_3 support must be considered. As such the current density with respect to the real surface area is likely to be less than that relating to the geometric surface area. However, even when the Fe_2O_3 surface area is neglected, the calculated concentration of the electroactive species was 2.94 mM at the largest Pt particle size. The Fe_2O_3 support therefore appears to induce an increased level of irreversibility towards the reduction and oxidation reactions in this case.

It could also be observed that only the largest particle size showed the characteristic peak shape expected for a diffusion limited process. The same was also true of the subsequent reduction of Ferricyanide. Although the reduction of Ferricyanide occurred at all potentials below the formal potential of the redox couple, the current appeared to be limited at all but the largest Pt particle size. Also the current gradually increased as the potential was swept negative. The rate of increase in the cathodic current negative of approximately 1.1 V also varied between the different

particle sizes, which may suggest that the current is not just limited by diffusion, but possibly also by the ability of the semiconductor to supply electrons to the electrode surface.

As well as the oxidation and reduction of the ferrocyanide/ferricyanide species, some additional voltammetric features were evident. A reduction peak is observed at approximately 0.35 V in the case of the largest Pt particle diameter. The position of the peak also varied in response to a change of particle size. An enlarged view of this peak is shown for selected Pt particle sizes in Figure 7.23.

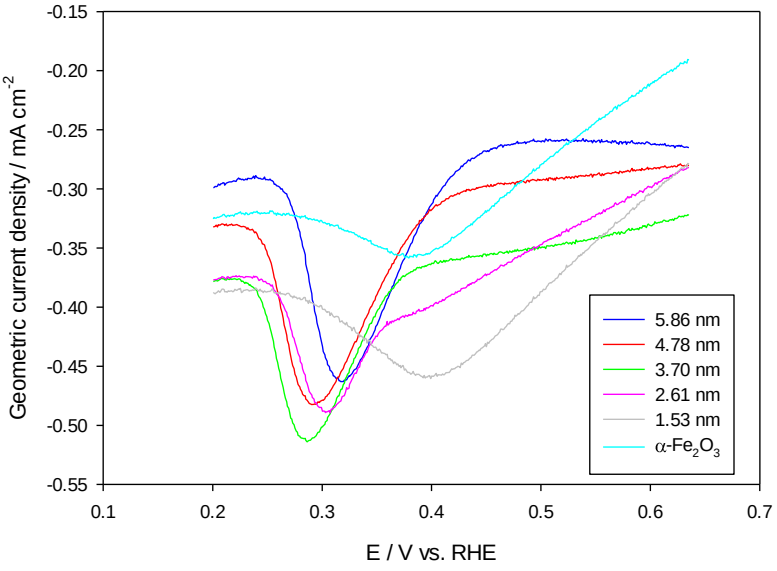

Figure 7.23. Enlarged view of the first negative sweep (0.20 – 0.63 V) in 0.5 M NaOH + 5 mM $K_3Fe(CN)_6$ on α-Fe_2O_3 supported Pt nanoparticles. Measurements were carried out at room temperature with a potential scan rate of 50 mV s^{-1}. (Array #8147)

In general, the cathodic peak shown in Figure 7.23 can be seen to move negative as the Pt particle size decreases. This is similar to the trend observed with the Pt oxide stripping peak described in Section 7.3, although in this case the peak potentials are significantly more negative. At the largest Pt particle size, the oxide stripping peak occurred at 0.45 – 0.50 V, whereas the peak potential of the process above lies at approximately 0.32 V. It was however observed that the oxide stripping peak moved slightly negative after performing multiple cycles, which may explain the negative shift seen here. In the data shown above it is also apparent that the behaviour changes at particle sizes below approximately 3 nm. Below a particle size of approximately 3 nm,

the peak potential began to move positive again. It is possible that the peak shown above may relate to a different process at the smallest 2 – 3 particle sizes present on the array. This is suggested since no clear oxide reduction peak could be observed at the two smallest sizes of Pt particles on the array. Additionally, a peak can be seen on the blank Fe_2O_3 which most likely represents the reduction current becoming diffusion limited. Possibly therefore the peak position may become dominated by the behaviour of the Fe_2O_3 support as opposed to the reduction of Pt oxide at the 3 smallest particle sizes. Alternatively, there may also be a redox process that occurs at the Fe_2O_3 support instead of or in addition to the reduction of Pt oxide.

An additional anodic peak also was evident on the forward scan, which once again shifted negative in peak potential as the Pt particle size decreased. Figure 7.24 shows an enlarged view of this peak, as well as the mean peak potential.

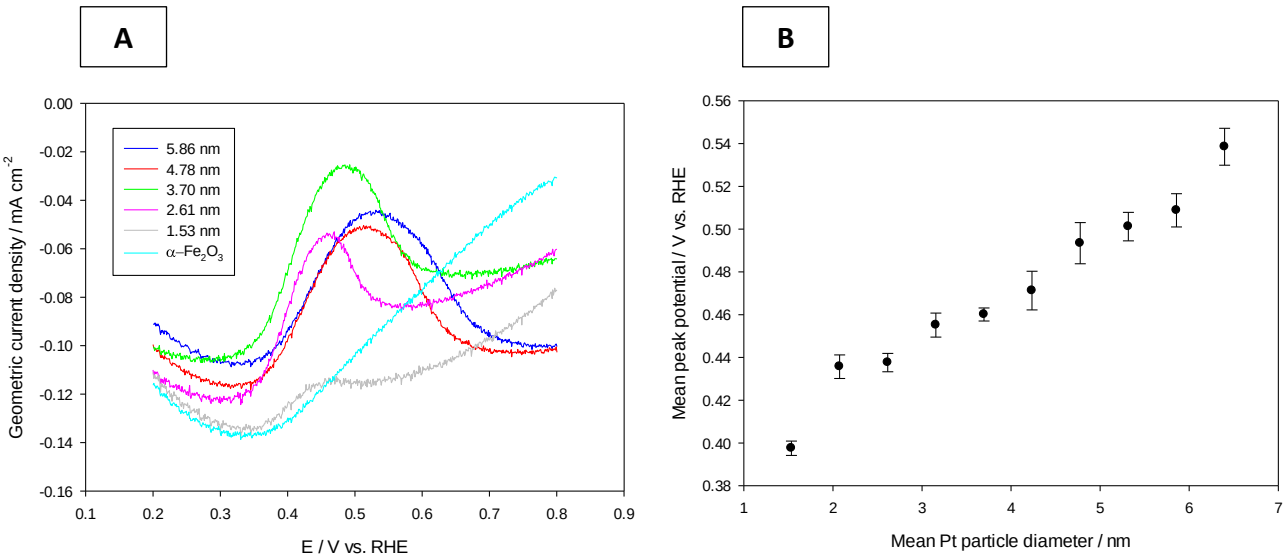

Figure 7.24. Enlarged view of the anodic peak between the limits of 0.2 and 0.8 V (A) in 0.5 M NaOH + 5 mM $K_3Fe(CN)_6$. The data represents the first anodic sweep collected at 50 mV s^{-1}. Also shown (B) is the mean peak potential of the anodic peak. (Array #8147)

The peak depicted above occurs in a similar potential region to that relating to OH adsorption in the blank NaOH (0.5 M) electrolyte; however the proposed OH adsorption peak did not show any clear particle size dependence in terms of the peak position. In this case however, a negative shift in the peak potential of approximately 140 mV is observed between the largest and smallest Pt particle sizes. Also, the OH adsorption peak current was proportional to the Pt surface area, which

is not true of the peak shown in Figure 7.24. No clear peak could be observed on the blank iron oxide support, suggesting that the process either involves a reaction at the Pt surface, or one that is mediated in some way by the Pt particles. Since the feature is not characteristic of Pt alone, it is likely to result from an interaction between Pt and the support. Possibly surface states imposed by Pt are charged and discharged by the reaction with ferricyanide/ferrocyanide. The fact that the peak was only observable in ferricyanide containing media may indicate that the surface states are of appropriate energy only to react with this redox couple and thus do not contribute significantly to the electrochemistry in the blank NaOH electrolyte. Sample contamination remains another possibility, however arrays handled in the same way showed no such peak when the electrolyte did not contain ferricyanide. Additionally, no similar peak was observed on TiO_2 supported particles.

Unlike all other processes however, the absolute peak current density recorded did not continually increase as the Pt particle size increased. Instead, a maximum was observed at a particle size of around 3 - 5 nm. Interestingly, the loss of current in the oxide formation region showed a similar trend to the peak current density of the aforementioned peak in ferricyanide containing media (Figure 7.25). It is possible therefore that the same process governs the loss of current in the oxide formation region and the ability to sustain the anodic current seen in ferricyanide containing media. The exact nature of the peak in Figure 7.24 could not be unambiguously determined; however variable levels of contamination as well as interaction between the support and particles are possibilities.

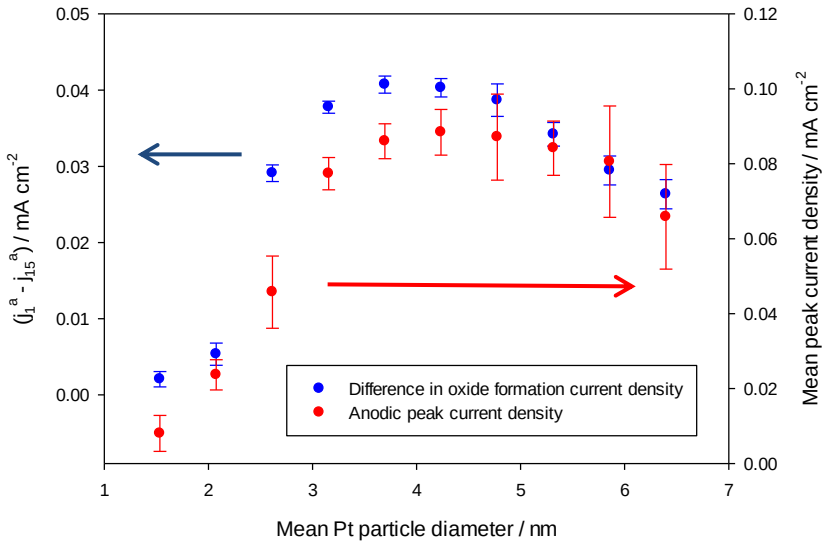

Figure 7.25. The mean difference in current density at 1.20 V during the first and fifteenth anodic sweeps ($j_1^a - j_{15}^a$) in 0.5 M NaOH with a scan rate of 50 mV s^{-1} (Blue). Also shown (Red) is the peak geometric current density of the anodic peak (0.4 – 0.7 V) on the first anodic sweep in 0.5 M NaOH + 5mM $K_3Fe(CN)_6$. The measurements were carried out with a scan rate of 50 mV s^{-1} and a baseline correction was applied to the currents densities. (Arrays #8141 – blue and #8147 – red)

In conclusion the Fe_2O_3 supported particles behave less like ideal rectifying semiconductor- liquid or semiconductor-metal contacts when compared with the anatase TiO_2 supported Pt particles. Both anodic and cathodic current flow occurred significantly positive of the flat band potential in the case of all particle sizes. However, the reduction and oxidation reactions did not appear to reach diffusion control close to the formal potential except at the largest particle size, suggesting that the transfer of electrons to or from the semiconductor surface is limited to some degree on electrodes with smaller Pt particle sizes. In terms of the reduction of Ferricyanide, a slight increase in current continued to occur negative of approximately 1.1 V. However the rate of current increase appeared to exhibit a slight particle size dependence, whereby a more rapid increase was observed at larger particle size between approximately 1.1 and 0.8 V. This may indicate that the size of Pt particle does have an effect on the charge transfer characteristics of the support albeit to a much lesser extent than the effects seen on the TiO_2 supported particles. A possible redox process mediated by the particles and involving the Fe_2O_3 also remains a possibility given the presence of an additional anodic peak in the voltammetry. Some level of sample contamination would however seem likely, although in this case it would appear that the contamination affects the particles on Fe_2O_3 to a greater degree than those on TiO_2.

7.5. Oxygen Reduction

The oxygen reduction reaction (ORR) is an important commercially relevant reaction in the context of hydrogen fuel cells.[280] Additionally it is perhaps the most commonly studied electrochemical reaction with regard to Pt particle size effects. From a number of studies it has been concluded that both Pt particle size and the nature of the support strongly influence the activity towards oxygen reduction.[164a,268] The oxygen reduction reaction therefore represents a well-studied model reaction in which the effects of the Fe_2O_3 support on the reactivity of Pt nanoparticles may be investigated. Additionally, the reduction of oxygen forms one of the deleterious back reactions that may occur in photoelectrochemical and photocatalytic water splitting. This has been shown to be particularly important in alkaline media, whereby the density of chemically adsorbed oxygen molecules at the semiconductor surface increases relative to that in acidic media.[230] Therefore it is important to understand the dependence of the oxygen reduction reaction on Pt particle size in order to correctly interpret trends in the photoelectrochemical water splitting activities.

The oxygen reduction reaction was studied on Fe_2O_3 supported Pt nanoparticles deposited on both ITO and Au arrays. Cyclic voltammetry was used to characterise the behaviour of the different Pt particle sizes, where a potential scan rate of 5 mV s^{-1} was employed. All measurements were carried out at room temperature in 0.5 M NaOH, which had previously been bubbled with high-purity O_2 for 30 minutes prior to data acquisition. The first cathodic sweep is shown for selected Pt particle sizes supported on Fe_2O_3 in Figure 7.26. The data shown is from a sample prepared on an Au substrate.

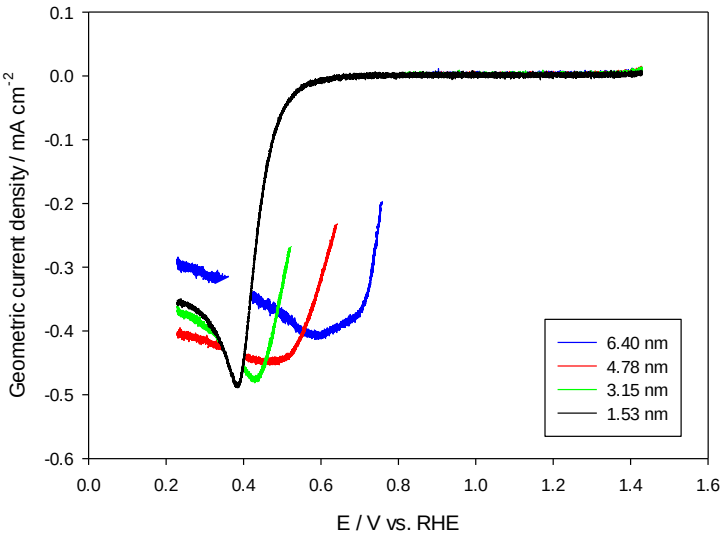

Figure 7.26. The first cathodic sweep of Fe_2O_3 supported Pt nanoparticles in oxygen saturated 0.5 M NaOH. Measurements were performed at a potential scan rate of 5 mV s^{-1} and the data is from a sample deposited on an Au substrate. (Array #8135)

Similarly to the results on the anatase TiO_2 supported particles, a significant negative shift in the ORR onset potential occurs as the Pt particle size decreases. In this instance however, the ORR onset potential does not correlate as strongly with that relating to Ferricyanide reduction (which occurred at all particle sizes negative of the formal potential of the $Fe(CN)_6^{3-}$/ $Fe(CN)_6^{4-}$). This may suggest that the behaviour is dominated by the variation in interfacial charge transfer kinetics as opposed to any electronic effects at the support. Generally speaking, particle sizes of roughly equivalent size show a notable positive shift in the onset potential relative to those on anatase TiO_2. This most likely arises from the increased conductivity of the Fe_2O_3 support as evidenced by the occurrence of ferricyanide reduction and ferrocyanide oxidation at potentials positive of the flat band potential. Moreover, if the activities were controlled by the rectifying properties of the support, then one would still expect a more positive onset potential on Fe_2O_3 relative to TiO_2. This is because the flat band potential of Fe_2O_3 is significantly positive of that on TiO_2,[281] thus requiring a less negative bias to accumulate electrons at the surface of the electrode.

Although the interfacial kinetics may dominate the trends observed above, it was still apparent that some variation in Ferricyanide reduction activity occurred between the different particle sizes. It therefore cannot be ruled out that the electrical properties of the support (or variation thereof) contribute to the activity trends. The ORR onset potentials were calculated for the various particle sizes and are presented for 4 different arrays in Figure 7.27. The Figure shows

results for samples deposited on both ITO and Au substrates, which show a relatively significant variation in behaviour. It is likely that some of this variation arises from the differing experimental histories of the samples prior to collection of the data presented below.

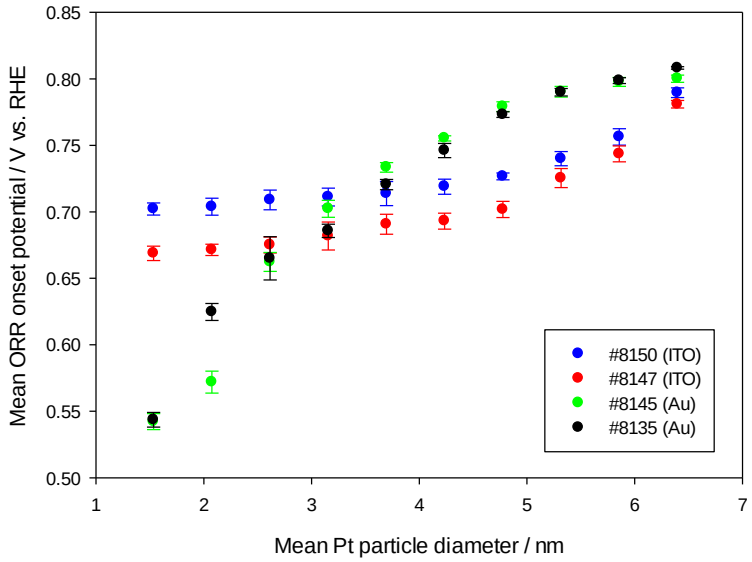

Figure 7.27. Mean ORR onset potential (defined as the voltage to reach a geometric current density of -0.028 mA cm^{-2}). The data was derived from the first cathodic sweep in O_2 saturated 0.5 M NaOH at a scan rate of 5 mV s^{-1}. The responses of four different array numbers are shown, with the substrate materials given in the inset.

Qualitatively, the same overall trend is observed in all the arrays presented above, whereby the ORR onset potential shifts negative as the Pt particle size decreases. Additionally, samples prepared on the same substrate materials are in relatively good agreement with each other. Clearly however, the absolute shift in onset potential between the largest and smallest particle sizes varies significantly between the two substrate materials. On the Au arrays, the onset potential at the smallest particle size was shifted negative by approximately 260 mV relative to the largest particle size. This reduced to approximately 90 – 110 mV on the ITO substrates. The difference in behaviour is unlikely to be solely caused by the varying characteristics of the substrate materials. This is due to the fact that no clear difference in the ORR onset potentials were observed between the samples on Au and ITO substrates in the case of the TiO_2 supported particles.

It has also previously been shown that the level of crystallinity or even the overall crystalline structure of metal oxide films can be sensitive to the substrate type.[282] Furthermore, it has been found that the level of crystallinity of α-Fe_2O_3 films decreased when deposited directly on ITO substrates relative to when deposited on ITO substrates with an additional oxide underlayer.[283] The authors suggested that the increased number of grain boundaries limited the photoelectrochemical performances of Fe_2O_3 films by increasing the rate of recombination. In this work, the photoelectrochemical behaviour also varied between the two substrate types, whereby the films deposited on ITO substrates showed no photo activity at all. Possibly the conductivity of the Fe_2O_3 film is improved on ITO substrates via a similar mechanism to that suggested in the study alluded to above. In this instance the decrease in crystallite size and increase in the number of grain boundaries may create a higher density of defects and surface states. This may mean that the particle size has less of an effect on the electrical properties of the support and therefore the ORR onset.

Whilst the Ferricyanide reduction did not show a large variation in onset potential, it is uncertain as to whether the Pt particle size changes the properties of the support. The occurrence of ferricyanide reduction and ferrocyanide oxidation may simply arise from the presence of surface states with appropriate energies to mediate the reaction. Although it was not possible to do so in this work, it may be of benefit to study the dark behaviour of the electrodes in non-aqueous media. This would allow a large range of redox couples to be employed which span a significant range of the overall energy band structure of the semiconductor. As a result, this may allow one to gain information on whether the reaction is mediated by surface states and to also determine the energy levels of such states relative to the conduction and valence band edges of the semiconductor.

In this work it was not possible to determine whether or not the crystalline structure of the Fe_2O_3 films changed between the different substrate materials. This was due to the Au substrate signal dwarfing any response from the deposited film. Relatively little difference in the diffraction pattern was however observed between the films deposited on ITO and SiN substrates.

The onset potentials were subsequently calculated after the current densities were normalised to the electrochemically determined Pt surface areas. Once again a negative shift in the onset potential could be observed as the Pt particle size decreased. The relative trends remained similar on account of the large initial variation in the onset potential. The voltage required to generate a specific current density of -0.028 mA cm^{-2} is shown for several arrays in Figure 7.28.

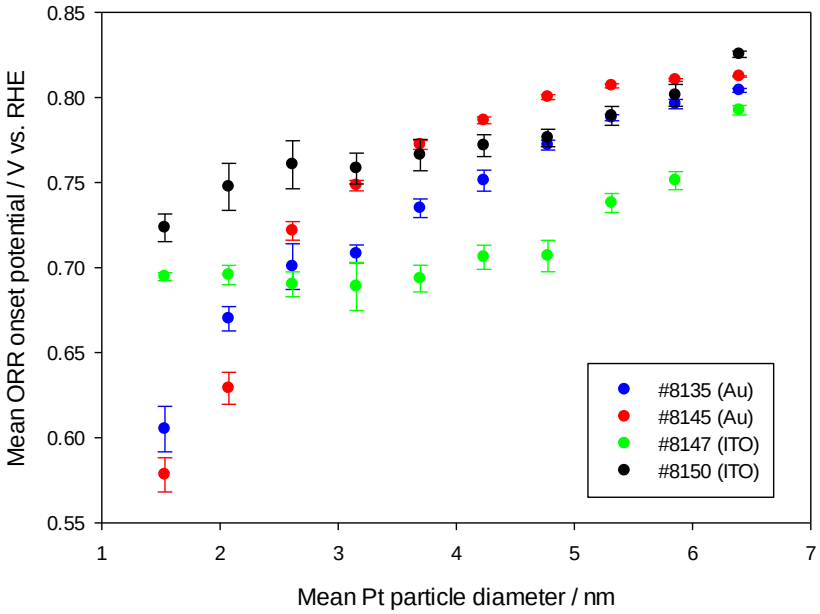

Figure 7.28. Mean ORR onset potential as a function of Pt particle size (defined as the potential to reach a specific current density of -0.028 mA cm^{-2}). The data is derived from the first cathodic sweep in each case where a scan rate of 5 mV s^{-1} was used.

This general decrease in specific activity is consistent with previous results in the literature relating to both carbon and TiO_2 supported Pt nanoparticles in acid media.[154] In the case of alkaline media, systematic studies of ORR particle size effects have been almost exclusively limited to carbon supports. However alternative materials to carbon have been studied, such as Nb- doped TiO_2 and SnO_2, [284,285] albeit without a strong emphasis on particle size effects. Tammevseki et al. however characterised the oxygen reduction activities of thin Pt films deposited on Ti substrates in alkaline media.[251] In this study, quantitative details on the Pt morphology at varying thicknesses was not reported. However, the electrochemically active Pt surface area clearly increased with increasing Pt thickness, which would not be expected to occur to a significant degree if only continuous films of Pt were formed. It was shown, that as the Pt thickness decreased, the peak potential of the Pt oxide reduction peak shifted negative. This also correlated with a reduction in oxygen reduction activity. Similar effects were observed by the same authors on TiO_2 supported Pt in alkaline media.[253]

Although the absolute cause of the particle size effects on Pt are still a topic of heated debate, the overwhelming conclusion appears to be that a change in coverage of oxygenated species results in the decrease in ORR activity at small particle sizes. The increased coverage of OH species is suggested to block sites for the adsorption of O_2 in this case.

The trends in the mean peak potential for the oxide stripping peak and the mean ORR onset potentials are shown for two samples on Au substrates in Figure 7.28. Note that the oxide stripping potentials are not shown for the two smallest Particle sizes, since no clear peak could be observed. Generally, the two trends appear to be in relatively good agreement, which would support the notion that the removal of OH at more negative potentials causes a negative shift in the onset of the ORR. However, the oxide stripping peak showed a slightly smaller overall variation as the particle size changed when compared with the ORR onset. Previously on TiO_2 in acid media, it was proposed that the lack of agreement in the trends came from an increased interaction with the support at smaller particle sizes.[244] It was suggested that the increased strength of interaction decreased the ability of the smaller particles to transfer electrons.

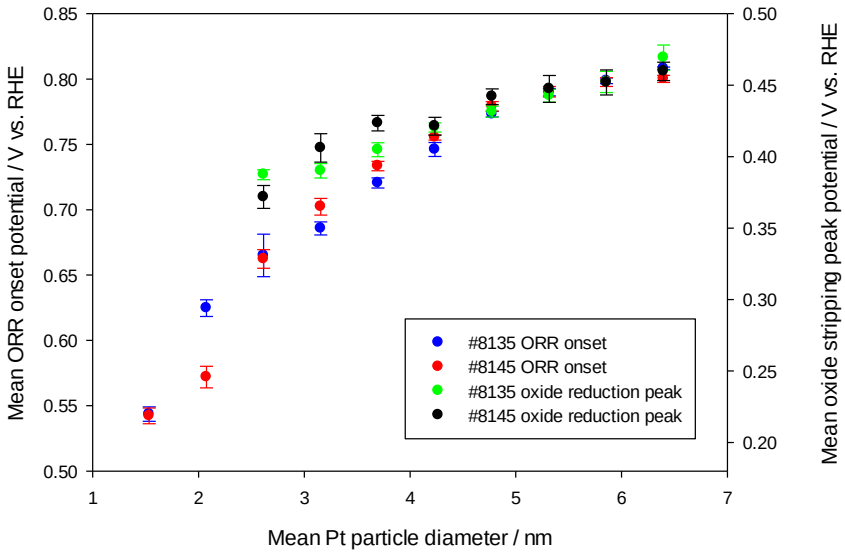

Figure 7.29. Mean peak potentials of the oxide stripping peak and mean ORR onset potentials for two arrays of Fe_2O_3 supported Pt nanoparticles on Au substrates. Measurements were performed in 0.5 M NaOH with and without O_2 in solution for the ORR onset potentials and oxide stripping potentials respectively.

From figure 7.29 it can be seen that the oxide stripping and ORR onset potential trends are in extremely close agreement at Pt particle diameters in excess of approximately 4 nm. Below 4 nm, the trends begin to differ to a slightly greater extent. The effects appeared to be more severe after multiple cycles had been carried out both under illumination and in the dark. After this point, the oxide stripping peak shifted significantly negative and the peak potential appeared to exhibit

little dependence towards particle size. A similar effect was observed at the TiO_2 supported particles, although some particle size dependence still existed in the peak potential. It was interpreted that these effects arose primarily from a loss in conductivity of the support, with possible influence from particle restructuring and Pt loss. A loss in Pt surface area would not appear to be the sole cause however, since the integrated charge under the hydrogen adsorption region remained relatively consistent (See section 7.7).

An enlarged view of the oxide/OH stripping peak is presented in Figure 7.30 immediately prior to the first ORR experiments as well as after multiple cycles in the dark and under illumination. Also shown are the ORR onset potentials recorded directly after the oxide stripping data was acquired.

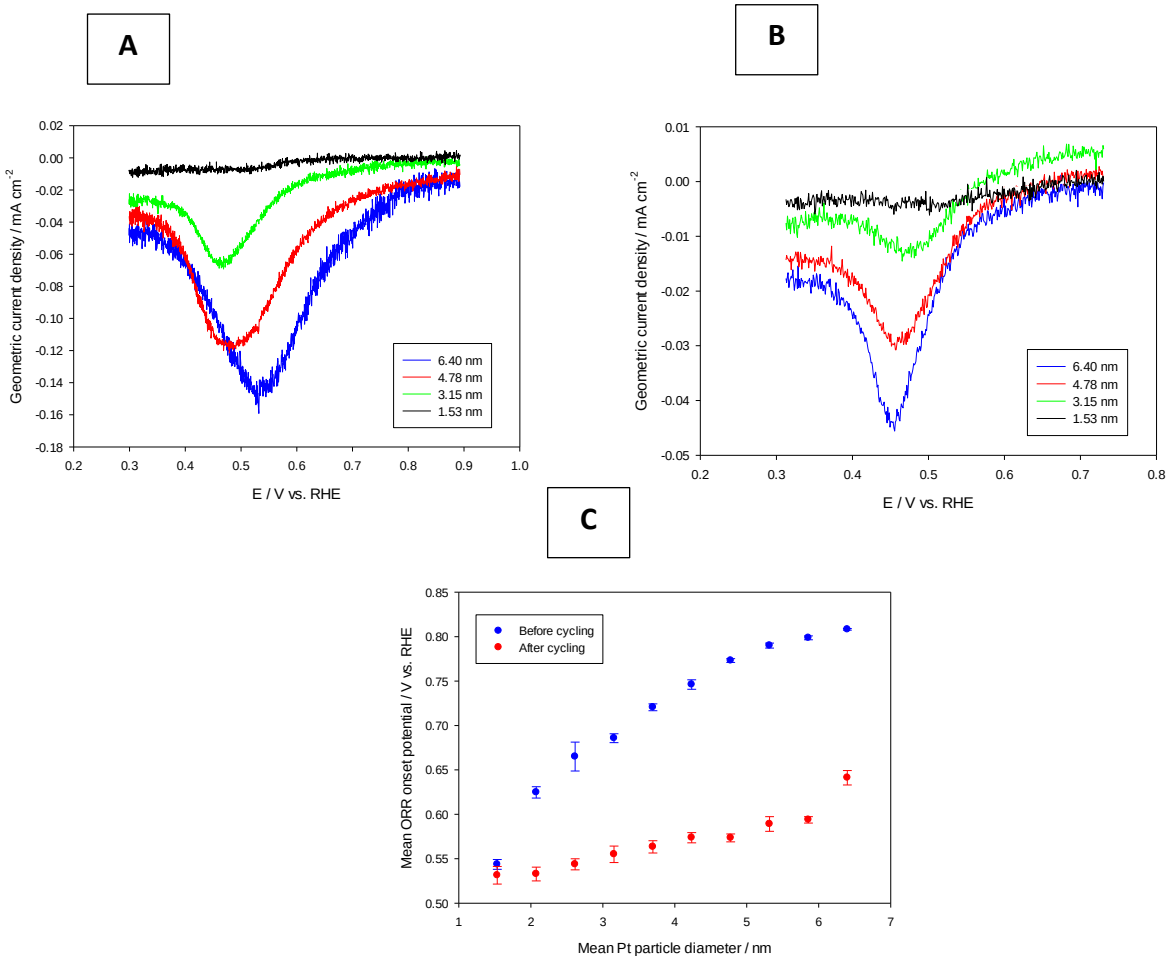

Figure 7.30. Enlarged view of the oxide / OH stripping peak shown both at the beginning (A) and end (B) of the electrochemical / photoelectrochemical screening process. The measurements were performed in Ar purged 0.5 M NaOH with a potential scan rate of 50 mV s^{-1}. Also shown (C), are the mean ORR onset potentials (V at -0.028 mA cm^{-2} geometric current density) recorded at the beginning and end of the screening process. The first cathodic sweeps in O_2 purged 0.5 M NaOH are shown, where a potential scan rate of 5 mV s^{-1} was used. (Array #8135)

The results show that the ORR onset potential trend agrees with the oxide stripping peak potential less after cycling. After cycling, the oxide stripping peak potential is almost independent of particle size, however the ORR onset potential still exhibits a negative shift of approximately 110 mV between the largest and smallest particle sizes. It would appear therefore that the dominant factor controlling the ORR onset changes with cycling. Potentially the oxide stripping peak presented after cycling may not actually relate to oxide stripping, but instead reduction of the Fe_2O_3 film, or reduction of a more reversibly bound OH species. In any case, it is clear that after cycling the oxide/OH stripping peak potential is not the determining factor of the ORR onset. Possibly a similar explanation to that suggested for the TiO_2 supported Pt may determine the ORR characteristics. In this case, it may instead be the rectifying properties of the support and the influence of Pt particle size on this that dominates the behaviour. Although the influence may be stronger after cycling, it is still possible that the variation in the level of band bending affects the ORR before cycling. This is since only when a semiconductor has an extremely high level of doping can its electrochemical characteristics become similar to a conducting support.

Further evidence for this comes from the comparison of the results on the Fe_2O_3 and TiO_2 supports. Both support materials showed the same general trends in terms of the oxide stripping peak potential, albeit with a slight negative shift at roughly equal sized particles on TiO_2. However, the ORR onset potentials were significantly more positive on the Fe_2O_3 support when compared to TiO_2. For example, at a particle size of approximately 6 nm, the oxide stripping peak potential on the Fe_2O_3 and TiO_2 supports were within 5 mV of each other. However the variation in the ORR onset potential extended to approximately 350 mV between the two supports. As a result, it is clear that the potential at which oxide/OH is removed from the surface is not the only determining factor in ORR activity. In addition to intrinsic particle size effects, the nature of the support has a strong influence on the ORR activity of Pt nanoparticles.

7.6. Methanol Oxidation

The methanol oxidation reaction represents another commonly studied reaction with regard to Pt particle size effects. This is largely due to its application in direct methanol fuel cells (DMFCs), in which the methanol oxidation reaction (MOR) contributes significantly to the overall overpotential losses. Additionally, methanol is commonly employed as a hole scavenging species

in the study of photoelectrode materials, and was employed as such in this work. Consequently, the characterisation of methanol photooxidation requires an understanding of the dark methanol oxidation behaviour.

The methanol oxidation activities of the Fe_2O_3 supported nanoparticles were studied with cyclic voltammetry. All measurements were performed at room temperature in 0.5 M NaOH with the addition of 1 M Methanol. The data shown is from samples prepared on Au substrates and a potential scan rate of 50 mV s^{-1} was used. Figure 7.31 presents the voltammetry obtained at several electrodes on an array of Fe_2O_3 supported Pt nanoparticles in methanol containing solution.

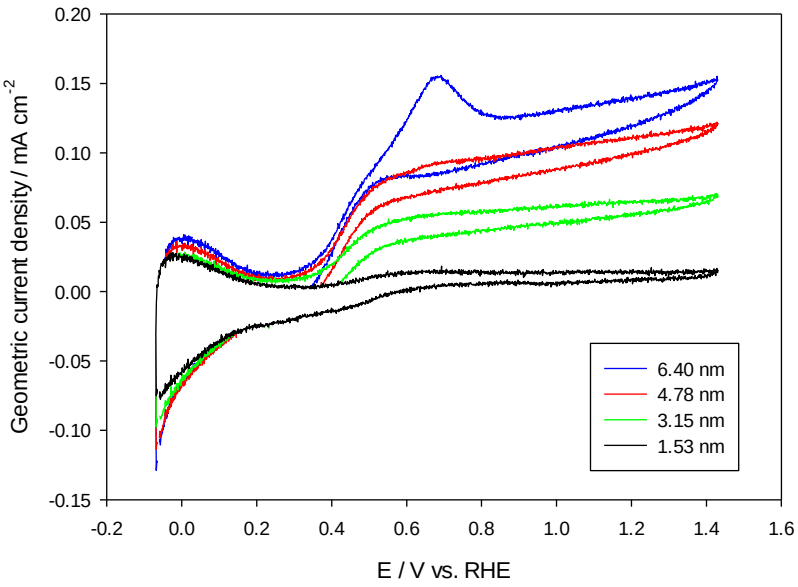

Figure 7.31. Cyclic voltammograms of selected Pt particle diameters supported on Fe_2O_3. Measurements were conducted in 0.5 M NaOH + 1 M MeOH with a potential scan rate of 50 mV s^{-1}. The first cycles are shown in each case. (Array #8145)

Unlike the TiO_2 supported Pt, all Pt particle sizes showed some level of activity towards the oxidation of methanol. The oxidation current can be seen to begin at around 0.3 – 0.4 V, which is in a similar region to the onset of OH adsorption at the Pt surface. In the case of the largest particle diameter presented, the anodic current reaches a peak at around 0.65 V before decaying slightly. Typically an anodic peak is seen at a higher potential range, which results in a sharp decrease in methanol oxidation current. This is due to the formation of Pt oxide which blocks sites

for the adsorption of methanol. In this case, the decay in methanol oxidation current is less severe and occurs at a potential more negative than the onset of oxide formation (approximately 0.8 V). The current also appears to increase at a steady rate throughout the remainder of the positive going sweep.

All other particle sizes presented do not show the same peak, and instead the anodic current generally appears to rise at a constant rate above approximately 0.6 V. The appearance of the positive sweep above 0.6 V however changed in response to particle size variation. The rate of current increase as the potential was swept positive of 0.6 V changed dramatically across the array. This rate of increase became much smaller as the particle size decreased. The current at the smallest particle sizes essentially appeared to be independent of potential above 0.6 V. Additionally, on the reverse scan the current appeared to decrease at a roughly constant rate. In all cases there were no peaks on the reverse scan, which typically occurs due to the oxidation of residual methanol fragments after oxide removal. As a result it would not appear that the level of oxide formation on the forward sweep is enough to significantly inhibit methanol oxidation.

The absolute current densities recorded at the various particle sizes appeared to vary between arrays. The level of variation between the arrays appeared to increase as the particle size increased. It is likely that some of this variation stems from the difference in the number of cycles performed prior to data acquisition. The number of cycles performed prior to the methanol oxidation experiments increases in the order of array numbers #8145 < #8135 < #8141. The current densities recorded at 0.7 V are shown in Figure 7.32 with respect to both the geometric electrode area and the specific Pt surface area. A background correction was applied to the current densities in each case.

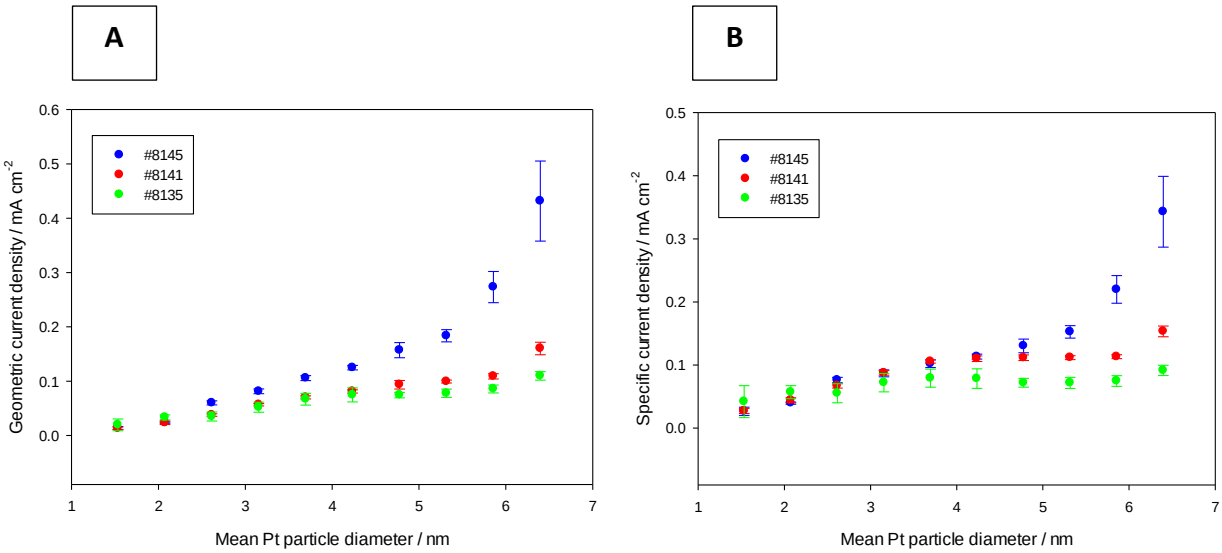

Figure 7.32. Methanol oxidation current density at 0.7 V vs. RHE. Current densities are scaled to the geometric electrode surface area (A) and the specific Pt surface area (B) derived from the hydrogen adsorption charge. Data is shown for the first anodic sweep in 0.5 M NaOH + 1 M MeOH with a scan rate of 50 mV s^{-1}.

A general increase in both geometric and specific current density occurs as the Pt particle size increases. Clearly however, the absolute variation across the range of particle sizes is different between the three arrays presented. Typically the current densities of anodic processes decreased with increasing cycle number, therefore the differences in behaviour may arise from the effects of cycling in this case.

The reduction in specific activity at smaller Pt particle sizes has frequently been reported on carbon supported Pt. Similarly to the study of the ORR, the vast majority of studies have been carried out in acidic media. Some studies of Pt loading effects in alkaline media have however been reported, albeit with an emphasis on morphological and surface area effects as opposed to intrinsic particle size effects (i.e. specific or mass activity).[286,287] Many of the explanations of particle size effects deduced in acid media may however be of importance in alkaline media also. Several differences in MOR behaviour have been noted when comparing the activity of Pt in alkaline and acidic media. Jing et al. found that the rate of methanol oxidation was significantly higher in NaOH when compared with H_2SO_4.[288] They attributed this to the faster adsorption of methanol and the greater ease at which CO oxidation takes place, due to the enhanced availability of oxygen containing species.

With respect to particle size effects, geometric effects are frequently proposed to account for the variation in activity at different particle sizes. Pt single crystal studies have shown that the adsorption of methanol as well as its oxidation is highly sensitive to surface structure.[289],[290] Park et al. suggested that a decrease in particle size decreased the number of favourable sites for the dehydrogenation of methanol to form CO.[291] It was suggested that this arose from a decrease in the proportion of terrace to edge sites. This hypothesis was further supported by studies on Pt with varying roughness factors.[292] In this instance it was suggested that the activity decreased as the surface roughness increased due to the increased number of defects, such as edge sites and kinks. Additionally, Beden et al. found that increasing the surface roughness of Pt led to a decrease in the level of CO poisoning. [293],[294] It has also been suggested that the adsorption strength of methanol at Pt surfaces may also decrease with increasing particle size, and therefore require a higher overpotential for oxidation.[295],[296] Other possible explanations have invoked the behaviour of Pt surfaces towards oxide formation. For example, it has been suggested that both the potential at which oxide formation occurs as well as the coverage of OH may impact on the MOR activity.[296],[297] Cheristiouk et al. also suggested that methanol oxidation may be hindered on smaller particle sizes by a stronger poisoning effect of CO.[169b]

In this case, the reduction in the level of oxide formation at smaller Pt particle sizes may contribute to the trends in Figure 7.31. The decreased capacity to form the OH species may therefore lead to a reduction in activity at smaller particle sizes. Additionally, it remains a possibility that the influence of the particles on the support characteristics may have some effect. Clearly the nature of the support is of importance, since particles of approximately equal size showed almost no activity on the TiO_2 support.

It was also noted that the charge under the hydrogen adsorption region generally decreased in the methanol containing media. However the absolute level of charge decrease appeared to be dependent on the Pt particle size. The charge under the hydrogen adsorption region is shown both with and without the addition of methanol in Figure 7.33.

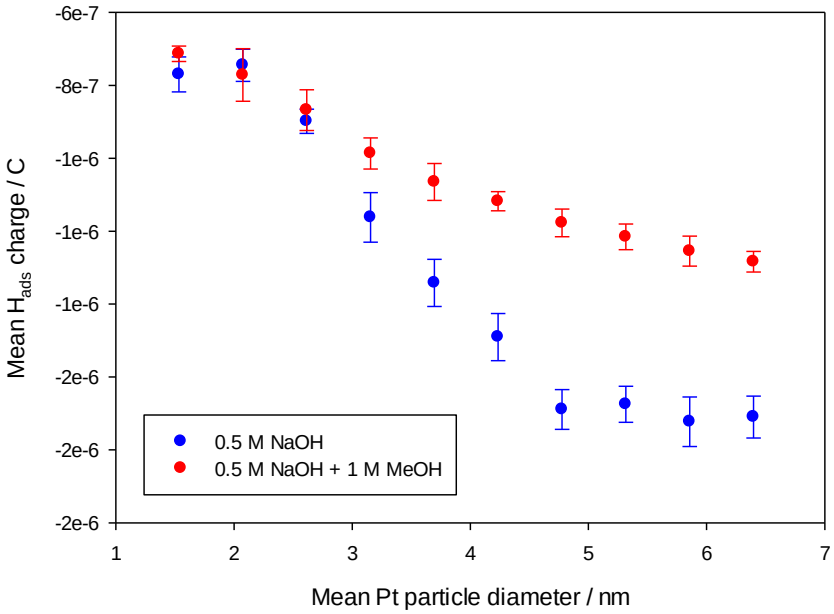

Figure 7.33. Mean charge under the Hydrogen adsorption region as a function of particle size. Data is shown for the last cycle performed in the blank NaOH electrolyte (blue) as well as the first cycle with the addition of methanol. A scan rate of 50 mV s^{-1} was used in each case. (Array #8145)

The reduction in charge under the hydrogen adsorption region appeared to be most significant at the larger Pt particle sizes. There was virtually no change in the values for particle sizes below approximately 3 nm in diameter. It is known that adsorbed fragments of methanol may remain bonded to the electrode surface in the hydrogen adsorption region.[244] Potentially the trend outlined above may indicate that methanol, or intermediates in its oxidation do not bind as strongly to the smaller Pt particles. If the results are believed to be due to a weaker adsorption strength of methanol at smaller particle sizes, then this factor may contribute in part to the reduction in specific activity.

It would appear that the level of oxide formation at the different Pt particle sizes has an influence in determining the activity towards the MOR. When comparing the results of Fe_2O_3 and TiO_2 supported Pt, it is apparent that oxide formation was more limited on the TiO_2 support. TiO_2 supported Pt was also much less active towards the MOR, presumably due to the lack of OH species required to oxidise methanol. Possibly there is a stronger interaction between Pt and TiO_2, or the semiconducting properties of TiO_2 may inhibit the flow of anodic current. However, MOR activity still remained on the Fe_2O_3 supported particles even after extensive cycling (to the point

that no appreciable level of oxide formation occurred). This would suggest that at least on the Fe_2O_3 support, the effect of cycling does not prevent the flow of anodic current, but instead specifically prevents oxide formation (Figure 7.34).

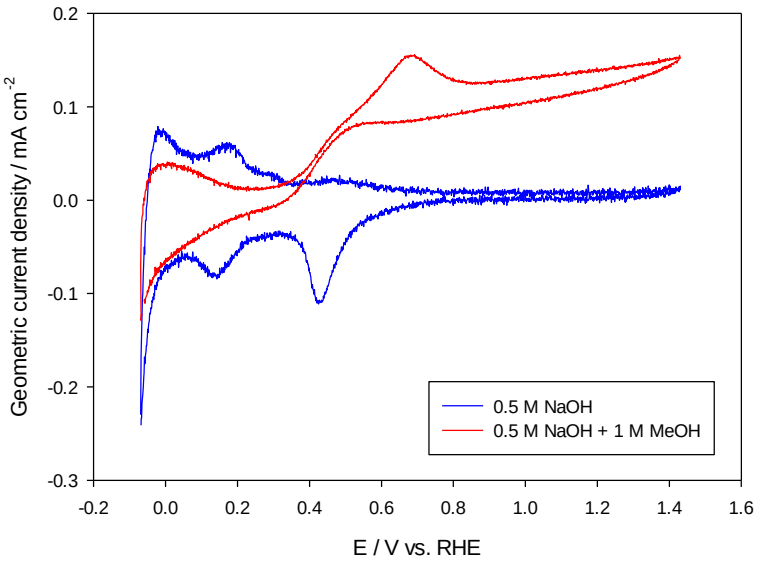

Figure 7.34. Cyclic voltammograms in 0.5 M NaOH and 0.5 M + 1M MeOH after 30 cycles under illumination.(Array #8141)

The results would indicate that the blocking of anodic current by decreased conductivity is not the sole cause of the reduction in the level of oxide formation on Fe_2O_3 supported Pt. However it was observed that the number of cycles performed on the samples had an influence on both oxide formation and the methanol oxidation current, suggesting that the level of oxide formation is still an important factor. The extent that the support conductivity influences this behaviour could not be directly determined, however even in stoichiometric form, anodic current flow should be more facile at the Fe_2O_3 support. The more positive flat band potential of Fe_2O_3 would mean that the expected level of band bending would be less over the potential range at which methanol oxidation takes place. As a result, the energy required for electrons to surmount the potential barrier at the interface would be less on Fe_2O_3. In conclusion it is apparent that a number of different factors may contribute to the observed activity trends, as well as the variation between the TiO_2 and Fe_2O_3 supports. It would appear that intrinsic particle size effects are in operation, which are also strongly influenced by the nature of the support.

7.7. Photoelectrochemical Behaviour

One of the main areas still to be addressed in Fe_2O_3 photoanodes is overcoming the slow oxygen evolution kinetics. The interfacial kinetics in this case are slow not just compared with metals, but also compared with other metal oxide materials. Previous research has discovered that surface states play an important role in reactions at the Fe_2O_3 surface, although it still remains unclear whether these states participate in deleterious side reactions or are themselves intermediates in the oxygen evolution reaction.[275] Due to these inherent deficiencies of Fe_2O_3, the study of surface bound catalysts has received a great deal more attention than on TiO_2. Due to the intrinsic differences in electronic structure between Fe_2O_3 and TiO_2, the electrochemical and photoelectrochemical characteristics differ significantly. As a result of these differing characteristics, the role of Pt on the surface may change entirely. Not only is the type of metal important in defining the photoelectrochemical behaviour, but also the position of its Fermi level relative to the band edges and flat band potential of the semiconductor. The Fermi level of bulk Pt is shown relative to the band edge positions of Fe_2O_3 and anatase TiO_2 in Figure 7.35.[298,192]

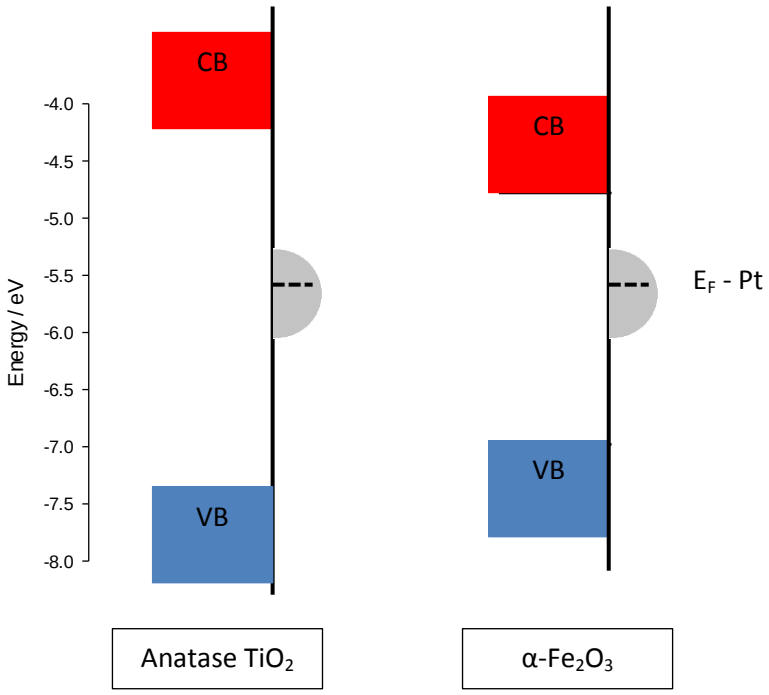

Figure 7.35. Positions of the valence (VB) and conduction (CB) bands of anatase TiO_2 and α-Fe_2O_3 against the absolute vacuum energy scale (0 V vs RHE ~ -4.5 eV). Also shown is the Fermi energy of Pt.

A clear difference can be seen not only in the valence and conduction band positions, but also their positions relative to the Fermi level of Pt. In the case of anatase TiO_2, the Fermi level of Pt lies approximately in the middle of the band gap, thus there is an equal chance of hole and electron transfer to the Pt in this case. The Fermi level of Pt however lies closer to the conduction band in Fe_2O_3, thus electron transfer to the Pt may be more favourable. The position of a metals Fermi level relative to the band edges in semiconductor is known to be of importance in determining their photoresponse. For example Xu et al found that the nature and mechanism of any improvement afforded by metal nanoparticle addition to TiO_2 was strongly dependant on the metal Fermi energy.[192] Nosaka et al. also observed a direct dependence of metal Fermi energy on the efficiency of photocatalytic ammonia production from azide ions at semiconductor particles.[187]

Photoelectrochemical characterisation of Fe_2O_3 supported nanoparticles was carried out using illuminated cyclic voltammetry and illuminated open circuit potential measurements. Screening was carried out on both Au and ITO substrates, although the photoresponse was poor on the ITO substrates. As a result, data is presented primarily for the Au substrate samples.

Due to the aforementioned deficiencies of Fe_2O_3, the photocurrents in all cases were much smaller than those recorded for TiO_2 supported Pt. At the Fe_2O_3 supported particles, the voltammetry was more complex, and showed peaks in addition to those arising from oxygen evolution. The first cycles recorded under illumination are presented in Figure 7.36. The last cycles recorded before illumination are also shown for comparison.

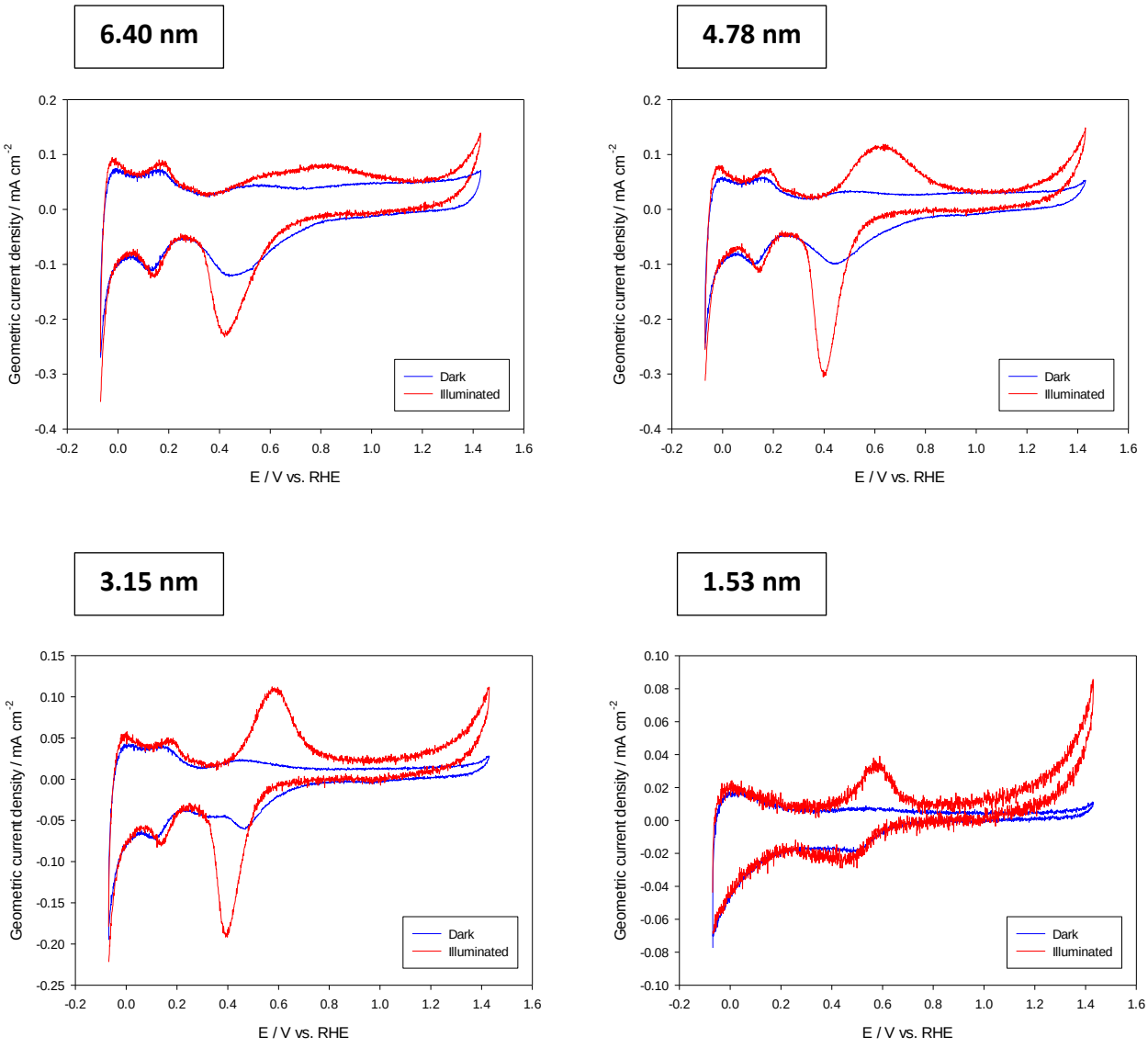

Figure 7.36. Cyclic voltammograms of selected Fe_2O_3 supported Pt nanoparticle electrodes. Measurements are shown for the last cycle in the dark as well as the first cycle under illumination. The voltammetry is not corrected for intensity non-uniformity. All measurements were performed in 0.5 M NaOH with a scan rate of 50 mV s^{-1}.(Array #8135)

In all cases the voltammetry below approximately 0.3 V is relatively similar in the dark and under illumination. This is because this potential range is negative of the flat band potential of Fe_2O_3. As a result, the support is driven into forward bias where the electrode is expected to become more metal –like in behaviour. Additionally, the driving force to transport photogenerated holes to the surface is removed. Thus no photocurrent is expected to occur in this region.

Positive of approximately 0.4 V a clear increase in anodic current is observed. Initially, it appears as though the voltammetry represents a clean Pt surface in the dark, with oxide formation less hindered. It could be confirmed however that, the current increase was due to anodic photocurrent generation. The voltammetry under chopped illumination (Figure 7.37) shows the characteristic spiked transient associated with hole trapping which is manifested in a sharp photocurrent increase, followed by decay to a steady value. Upon interrupting the illumination, an immediate decrease in photocurrent is observed followed by a cathodic overshoot, which is expected upon recombination of surface trapped holes. From the integration of the charge passed in the anodic peak (at the largest particle size), approximately 3.1 x 10^{15} electrons are transferred per centimetre squared. Assuming the 0001 face of Fe_2O_3 is exposed, the density of Fe atoms at the surface is approximately 3.9 x 10^{14} atoms per centimetre squared. As a result, it is unlikely that the process simply results from the trapping of holes at the surface of Fe_2O_3. Clearly, the species formed in the course of this peak is long lived, given the recovery of a cathodic peak on the reverse scan at the relatively low sweep rate of 50 mV s^{-1}. Furthermore, the dissipated charge after removal of illumination does not equal that passed in the anodic current under illumination. This indicates that the species formed is stable and is not affected by the recombination of electron-hole pairs after removal of illumination.

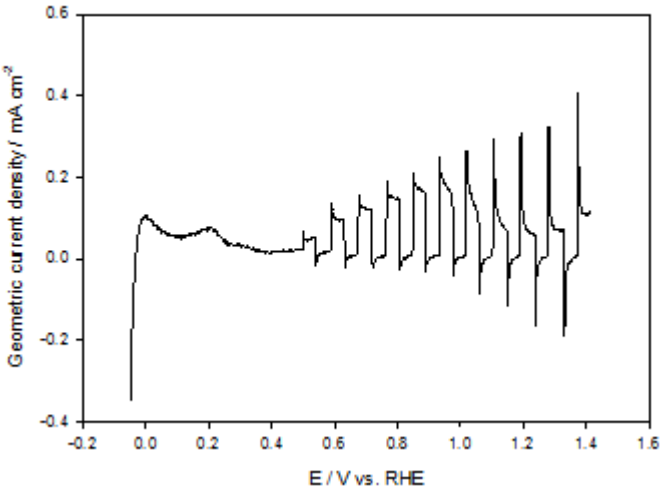

Figure 7.37. Positive going sweep of an electrode of Fe_2O_3 supported Pt nanoparticles (estimated mean Pt diameter: 6.40 nm) under chopped illumination. Data was collected at a scan rate of 50 mV s^{-1} in Ar purged 0.5 M NaOH. (Array #8135)

The anodic photocurrent peak varies in both peak current and peak potential as the Pt particle size changes. Additionally, it can be observed that the peak becomes broader as the Pt particle size increases. Clearly the occurrence of this peak shows that holes are available at the surface at potentials positive of approximately 0.4 V. After the peak however, the current remains at a relatively constant value until approximately 1.20 V. Above this point, the photocurrent begins to increase due to the evolution of oxygen. This represents a large overpotential relative to the flat band potential of Fe_2O_3, which is a common observation relating to the poor interfacial kinetics of the oxygen evolution reaction on Fe_2O_3 surfaces. It is possible that the peak relates to Pt oxide formation which is in some way enhanced by the presence of illumination. Interestingly, the onset potential of the peak changes very little as the particle size increases, and coincides with a peak emerging in the illuminated voltammetry of the bare Fe_2O_3 support.

On the negative sweep, a cathodic peak occurs with a peak potential at around 0.40 V, although this varied slightly as the particle size changed. The charge passed in the anodic and cathodic photocurrent peaks initially appeared to be slightly different. In all cases the charge passed in the cathodic process was comparatively larger than that under the anodic peak. This is likely to arise partly from the reduction of photogenerated oxygen occurring over a similar potential region to the cathodic peak. This is suggested since the charges were in closer agreement when the upper potential limit was confined to below 1.20 V. The calculated charges are shown in Figure 7.36. In light of the similar charges it was assumed that the peaks related to a common redox process occurring at the Pt and/or Fe_2O_3 surface. The scan rate dependence of the voltammetry was also investigated. An electrode of Fe_2O_3 supported Pt nanoparticles is also shown at different scan rates in Figure 7.38.

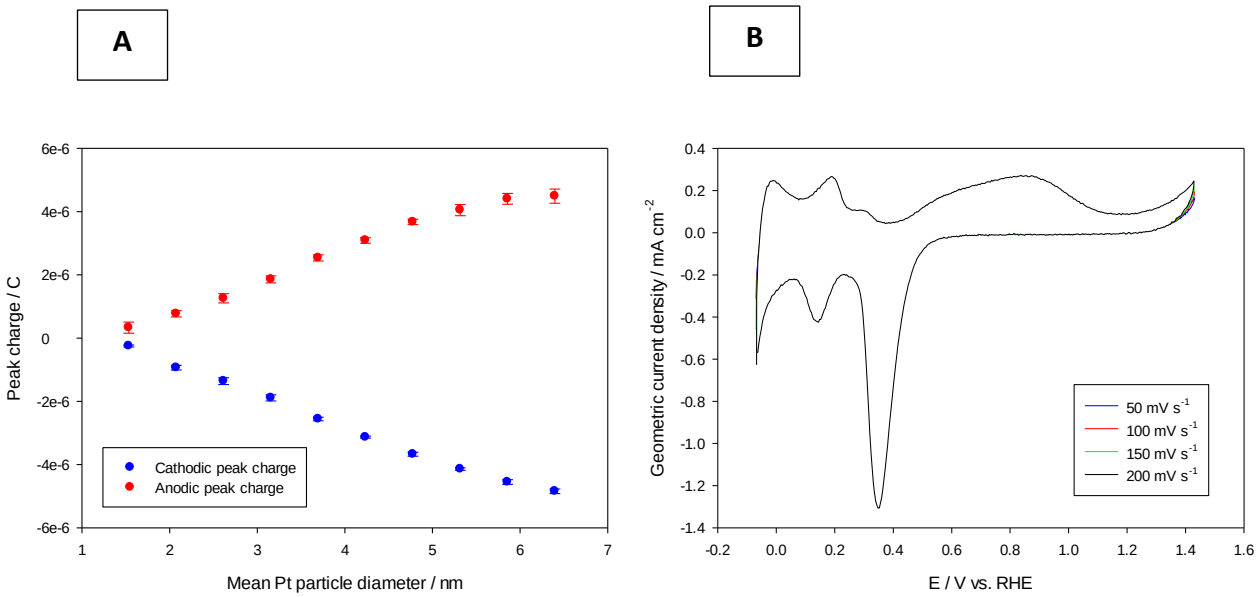

Figure 7.38. Peak charge (A) of the anodic and cathodic peaks from the illuminated voltammetry of Fe_2O_3 supported Pt nanoparticles. Data was collected in 0.5 M NaOH with a potential scan rate of 50 mV s^{-1}. Also shown (B) is the scan rate dependence on the voltammetry at Fe_2O_3 supported Pt nanoparticles (estimated particle diameter = 5.32 nm). Identical conditions were used to the data in A, although the scan rate (given in the inset) was altered. All data is was collected after the 25th cycle under illumination. (Array #8141)

As the Pt particle size increased, the charge under the anodic and cathodic peaks increased. This however was after the 25th cycle under illumination, at which point the voltammetry had stabilised. Some significant changes to the responses occurred in the previous cycles, which are discussed below. At all Pt particle sizes, the increase in scan rate led to a positive shift in the anodic peak potential. The absolute level of positive shift however increased as the Pt particle size increased. The peak potential shifted positive by approximately 240 mV at a particle diameter of 6.40 nm, compared with 60 mV at a particle diameter of 1.50 nm. The cathodic peak also showed a slight negative shift in response to increasing the scan rate, although the effect of scan rate was much smaller in this case. At a particle diameter of 6.40 nm a negative shift of approximately 45 mV was observed, compared with approximately 25 mV at a particle diameter of 1.50 nm. At all scan rates, the total charge passed in the anodic and cathodic peaks were equal, which is suggestive of a surface based process. Clearly however the electron transfer is irreversible to some degree, given the significant change in peak potential as the scan rate changed. This appears to be particularly true of the anodic process.

The exact nature of the species formed in the anodic peak could not directly be determined, and a more detailed spectroscopic investigation would be required towards this aim. However, some information about the nature of the species formed under the anodic peak could be inferred from the illuminated and dark voltammetry as a whole, in addition to its variation with cycling.

The most obvious possibility is that oxide formation occurs at the Pt particles via hole transfer from the Fe_2O_3 valence band. Evidence for this process came from the dark and illuminated voltammetry in methanol containing media (Sections 7.6 and 7.8 respectively). It was observed that in the dark methanol oxidation, no oxidation peak was apparent on the reverse scan. Where a significant level of oxide formation takes place, one would normally expect an increase in methanol oxidation current upon removal of the inactive oxide phase at the Pt surface. Also a decrease in methanol oxidation current would be expected upon oxide formation on the forward sweep, which did not occur in the dark voltammetry. In the illuminated voltammetry, there did appear to be a peak on the reverse scan, which may suggest an increased level of oxide formation under illumination. This may either be through photoassisted oxide formation or through removal of surface contamination.

In the first cycles under illumination (Figure 7.36), a slight shoulder to the anodic peak can be observed beginning at approximately 0.4 V on the largest particle size, which may indicate that in fact two anodic processes are occurring. Additionally, the shoulder at 0.6 V is in close proximity to an anodic peak observed at the blank Fe_2O_3 support when under illumination (Figure 7.39).

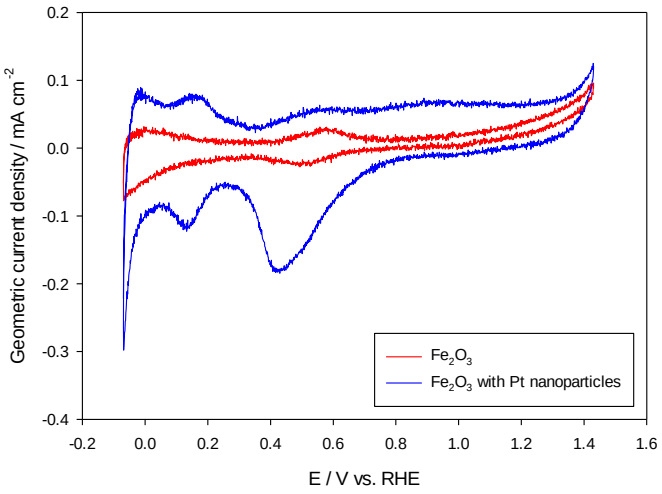

Figure 7.39. The first cycles under illumination of a blank Fe_2O_3 electrode and an electrode of Fe_2O_3 supported Pt nanoparticles (estimated Pt particle diameter = 6.40 nm). Measurements were performed in 0.5 M NaOH with a scan rate of 50 mV s^{-1}. (Array #8135)

The peaks on the Fe_2O_3 are likely to be due to a change in the oxidation state of Fe in Fe_2O_3. Possibly this arises from the charging of surface states or 'trapping' of charge carriers. It would appear that the same process occurs to some extent on the electrodes with Pt particles.

The voltammetry recorded in this work changed dramatically with increasing cycle number, which may reflect that substantial changes occur to the Pt particles and/or Fe_2O_3 support when cycled under illumination. The development of the anodic photocurrent peak (0.4 – 1.20 V) is shown at different cycle numbers in Figure 7.40.

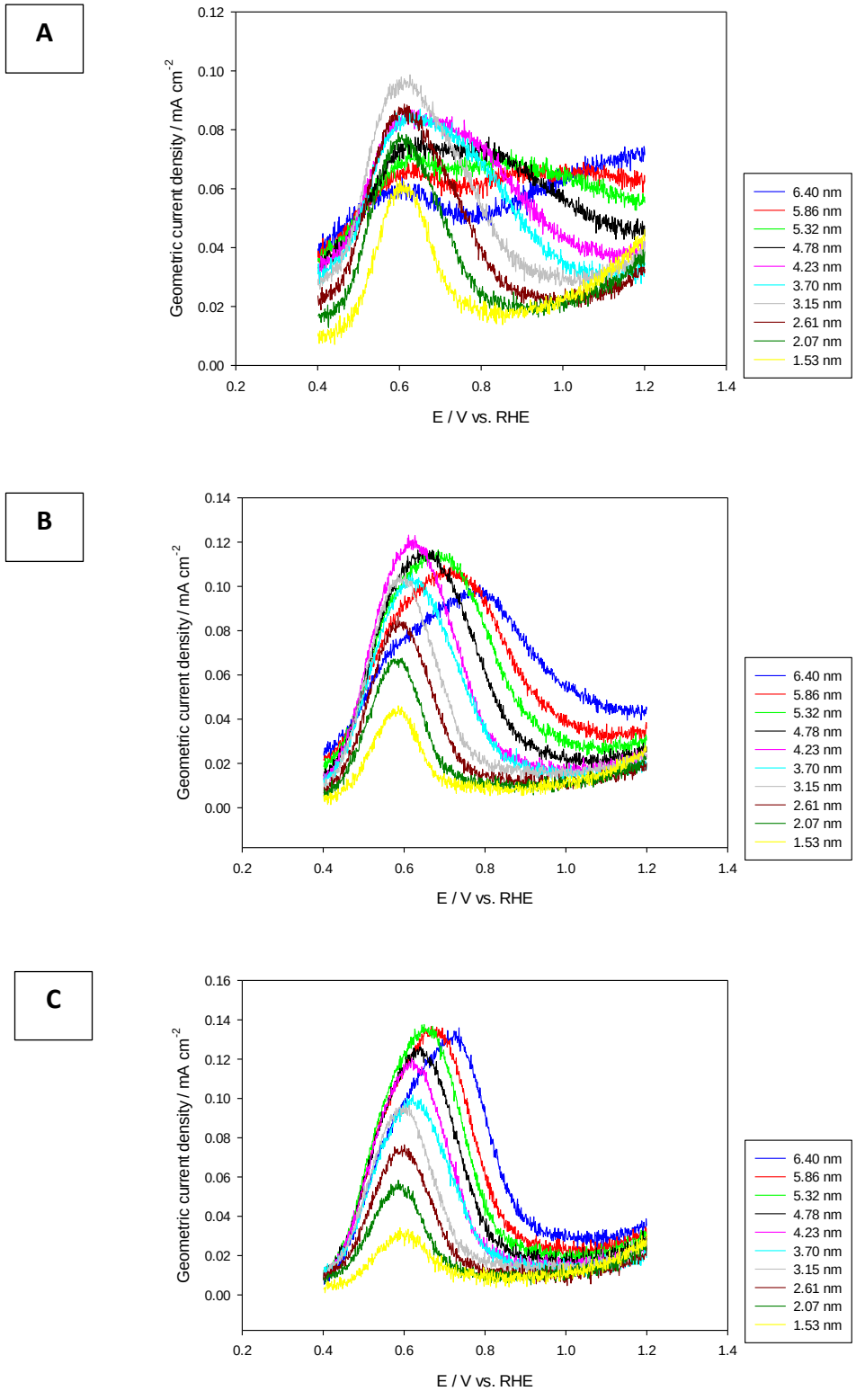

Figure 7.40. The development of the anodic photocurrent peak (0.4 – 1.2 V) with cycling. Data is shown for the 1st (A), 10th (B) and 20th (C) anodic sweep under illumination. All measurements were performed in 0.5 M NaOH with a scan rate of 50 mV s^{-1}. (Array #8141)

Initially it is assumed that the peak may correspond to oxide formation in addition to charging of surface/trap states, at least at the largest particle sizes. During the first cycle (A), the peak current density reaches a maximum at a particle diameter of approximately 3 nm, before decaying as the particle size either increases or decreases from this value. It could be noted that the decay in charge over the oxide formation region was most apparent on larger particle sizes in the dark. It is possible therefore that an additional process occurs in this region. One explanation may be that the surfaces of large and intermediately sized particles have a higher level of contamination, which is gradually removed with cycling. The more pronounced increase in the photocurrent peak current density may therefore arise from removal of such contaminants which facilitates the formation of Pt oxide. Another possibility is that the Pt catalysed reduction of the support during prior heating in vacuum leads to the formation of more Fe^{2+} sites that act as recombination sites. The oxidising power of the photogenerated holes may slowly oxidise these centres leading to a lower rate of recombination. The former would appear more likely in this case given the necessary handling of the arrays outside of vacuum prior to electrochemical screening.

On the 10^{th} cycle, the peak current densities increase at particle sizes above approximately 3 nm relative to the 1^{st} cycle. The peaks also shift slightly negative over this particle size range. This may relate to both a decrease in the rate of recombination, as well as an increased reversibility of Pt oxide formation/stripping. At particle sizes of approximately 3 nm and below, the voltammetry did not change significantly throughout the cycles. Interestingly, this is the range of particle sizes at which oxide formation in the dark became hindered. This may indicate that an increased level of rectification is observed at smaller particle sizes, as was observed in the case of the TiO_2 support. In this case, an increased driving force to generate anodic photocurrent would be present. In turn this would lessen the effects of any surface contamination or defect mediated recombination.

With further cycling (Figure 7.40 C), the peak current densities increased again, although this time the increase was limited primarily to particle sizes above approximately 4.5 nm. Over this particle size range the peak voltage also shifted slightly negative. At this point, the peak current density increased with increasing Pt particle size. Given the smaller level of band bending expected with larger particle sizes, removal of any surface contamination would be hindered to a greater extent. The reduced driving force to transport holes to the surface may therefore cause a slower removal of such contaminants from the surface and a concomitantly slower increase in the level of Pt oxide formation.

In spite of the increased oxidative current under illumination, the level of oxide formation in the dark was subsequently decreased severely. It is likely that conductivity loss may be experienced by oxidation of intrinsic n-type defects in the Fe_2O_3. Given the strongly oxidising potential of the valence band holes, some level of Pt loss and/ or restructuring is also possible. However, calculation of the Pt surface area (from the hydrogen adsorption charge) revealed little variation between the un-illuminated and illuminated samples after correction for double layer charging.

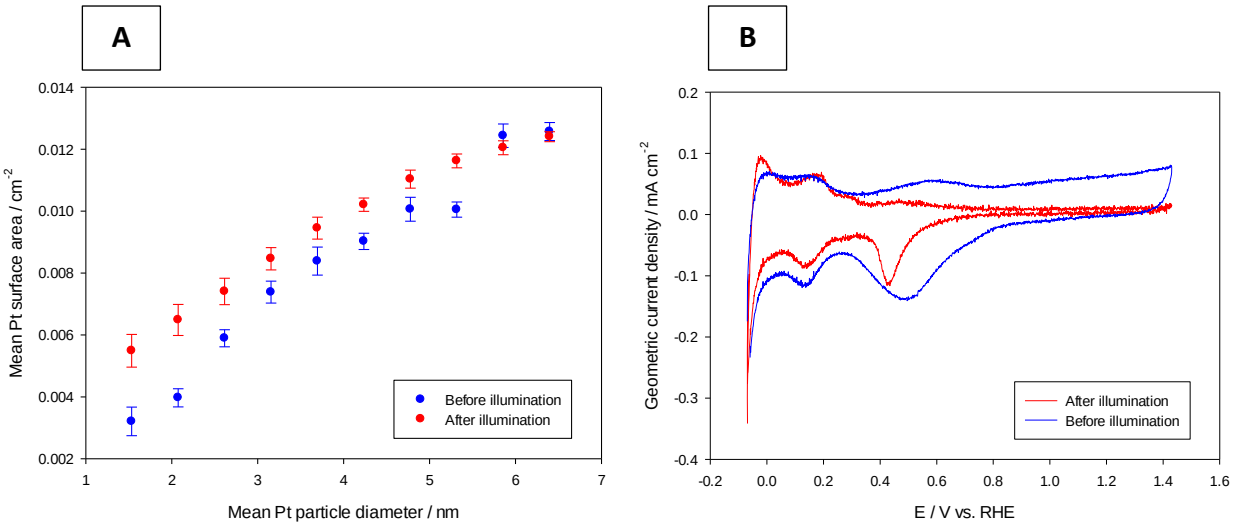

Figure 7.41. The Pt surface areas calculated from the hydrogen adsorption charge before and after cycling under illumination (A). Also shown (B) is an electrode of Fe_2O_3 supported Pt nanoparticles (estimated Pt particle diameter = 6.40 nm) before and after cycling under illumination. All measurements were carried out in 0.5 M NaOH with a scan rate of 50 mV s^{-1}. (Array #81410

In the absence of significant Pt loss, it would appear that the support becomes more rectifying after cycling under illumination. The initial lack of oxide formation at smaller particles in the dark as well as their more stable behaviour under illumination may indicate that an initial higher level of rectification occurs at smaller particle sizes. The increase in illuminated Pt oxide formation and decrease in dark oxide formation therefore supports an increased level of rectification at larger particle sizes after illuminated cycling.

The most important factor to be addressed is how the particle size dependent illuminated voltammetry affects the efficiency of photoelectrochemical reactions. Even after multiple cycles where photocurrent enhancement was observed, a large overpotential was still required for oxygen evolution to occur. The photocurrent at 0.35 V is shown for the 1st cycle under

illumination in Figure 7.42. Also shown is the charge under the anodic photocurrent peak (0.4 – 1.2 V). It would appear that no improvement to the level of photocurrent generated occurs at any Pt particle size. However unlike the Pt particles on TiO_2, the majority of particle sizes do not bring about a significant decrease in photocurrent.

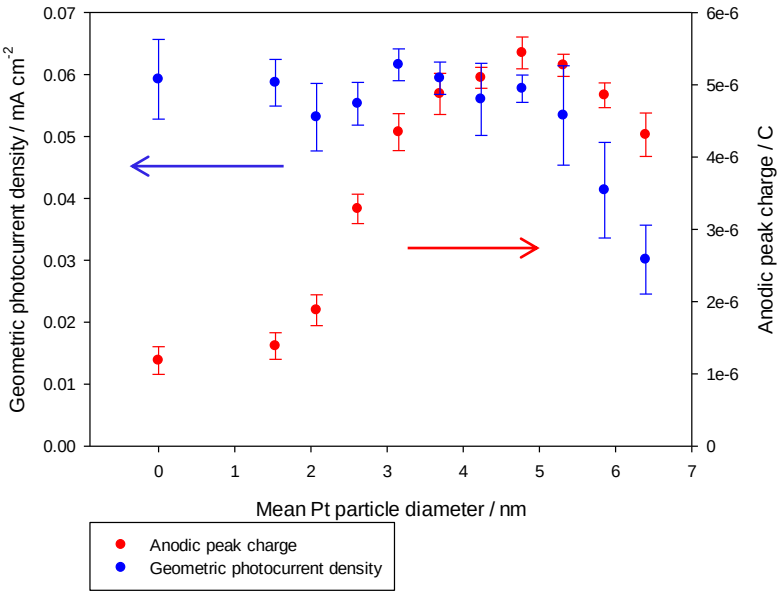

Figure 7.42. Geometric photocurrent density at 1.37 V vs. RHE (Blue) and the charge under the anodic photocurrent peak (0.4 – 1.2 V). Measurements were performed in 0.5 M NaOH with a scan rate of 50 mV s^{-1}. Data is shown for the 1st anodic sweep under illumination. The photocurrent values have been corrected for intensity variation (see Chapter 3). (Array #8141)

It can be seen in Figure 7.42, that only particle diameters greater than approximately 5 nm appear to have any effect on the photocurrent relative to the blank Fe_2O_3. This correlates roughly with the point where the anodic peak charge began to decrease. This is likely to arise from an increased rate of recombination at particles larger than approximately 3-5 nm in diameter or an increased level of sample contamination. The behaviour was also assessed after multiple cycles had been performed on the electrodes, at which point it was observed that the anodic photocurrent peak continually grew in size as the Pt particle size increased. The photocurrent density at 1.37 V is shown in addition to the anodic peak (0.4 – 1.2 V) charge for the 25th cycle in Figure 7.43.

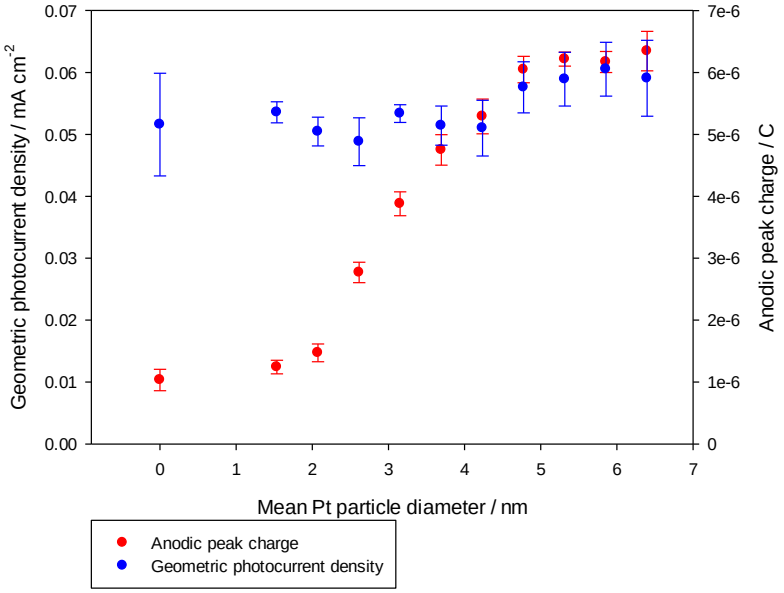

Figure 7.43. Geometric photocurrent density at 1.37 V vs. RHE (Blue) and the charge under the anodic photocurrent peak (0.4 – 1.2 V). Measurements were performed in 0.5 M NaOH with a scan rate of 50 mV s^{-1}. Data is shown for the 25th anodic sweep under illumination. The photocurrent values have been corrected for intensity variation (see Chapter 3). (Array #8141)

These results suggest that the charge passed in the anodic photocurrent peak has no real effect on the rate of oxygen evolution. This is most likely because the rate is still limited primarily by slow charge transfer kinetics where the forming the species in the aforementioned peak is not the rate limiting step.

The effect of Pt particle size on the open circuit voltage was also assessed. The OCP response to illumination differed significantly to that observed on the TiO_2 supported particles. Most notable is the decreased stability of the voltage over the timescale of the experiments. The open circuit potential measurements for several electrodes of Fe_2O_3 supported nanoparticles are shown in Figure 7.44.

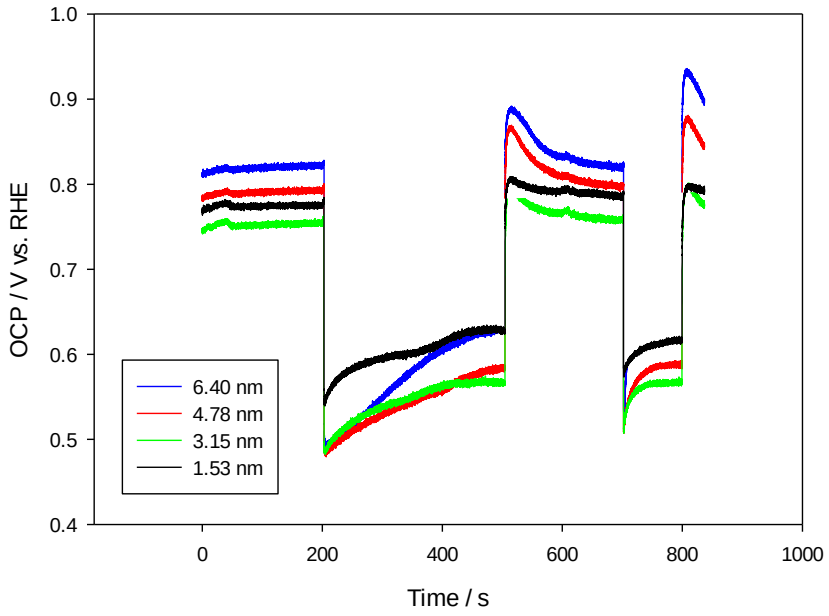

Figure 7.44. Open circuit potential as a function of time for selected Fe_2O_3 supported Pt nanoparticle electrodes. The arrows denote the time at which illumination was started and stopped throughout the experiment. The electrolyte used was 0.5 M NaOH. Measurements were recorded after 30 illuminated cycles had been performed on the electrodes.(Array #8135)

Initially, the OCP values in the dark appeared to be random across the array, and showed no clear particle size dependence. This is commonly reported and is due to the poorly defined solution potential in the dark.[13] Upon illumination the voltage rapidly shifts negative, with the largest Pt particle diameters showing the most negative open circuit potential. The voltage then decays, which occurs most notably at larger Pt particle sizes (Figure 7.45). This is likely to arise from the charging of trap states. This process is known to alter the potential distribution at the interface by the build-up of positively charged holes at the surface. This may therefore change the band edge positions and lead to a partial pinning of the Fermi level.[119]

The larger voltage decay at larger particle sizes is therefore likely to stem from the increased charge carrier trapping ability of larger Pt particles. Further evidence for the charging of trap states comes from the response after the removal of illumination. At this point, the voltage overshoots the initial OCP value in the dark. This results from the slow recombination of surface trapped holes in the dark. Once again the level of overshoot is larger as the Pt particle size increases.

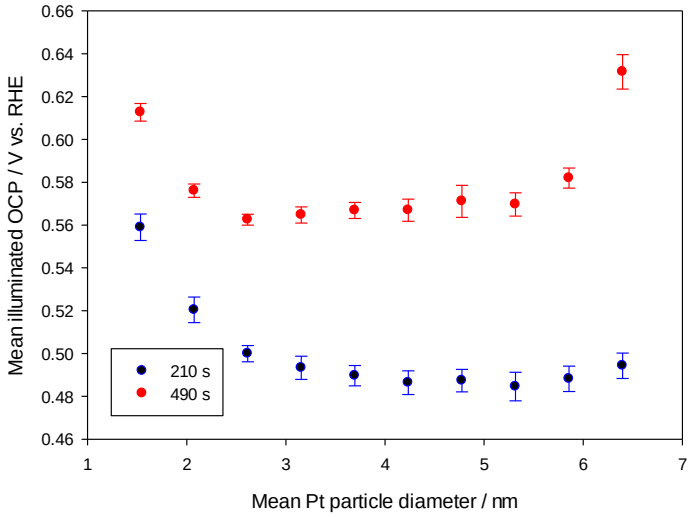

Figure 7.45. Mean illuminated OCP measured at 210 (Blue) and 490 (Red) s. Measurements were conducted in 0.5 M NaOH. (Array #8135)

The results so far show that Pt may potentially be effective in promoting charge separation. However, the slow OER kinetics at Fe_2O_3 means that the behaviour is simply dominated by the charge transfer behaviour of the support. Evidently therefore, the addition of Pt does not increase the rate of interfacial charge transfer. Further investigation was carried out with methanol in solution as a hole scavenger. This allows removal of the poor charge transfer kinetics, such that the effects of the Pt charge separation ability can be systematically investigated in a reaction of potential interest.

7.3. Methanol Photooxidation

Methanol photooxidation experiments were carried out in 0.5 M NaOH with the addition of 1 M methanol. Samples deposited on Au substrates were screened using cyclic voltammetry at a scan rate of 50 mV s^{-1}. The dark and illuminated cycles of selected electrodes of Fe_2O_3 supported nanoparticles are shown in Figure 7.46.

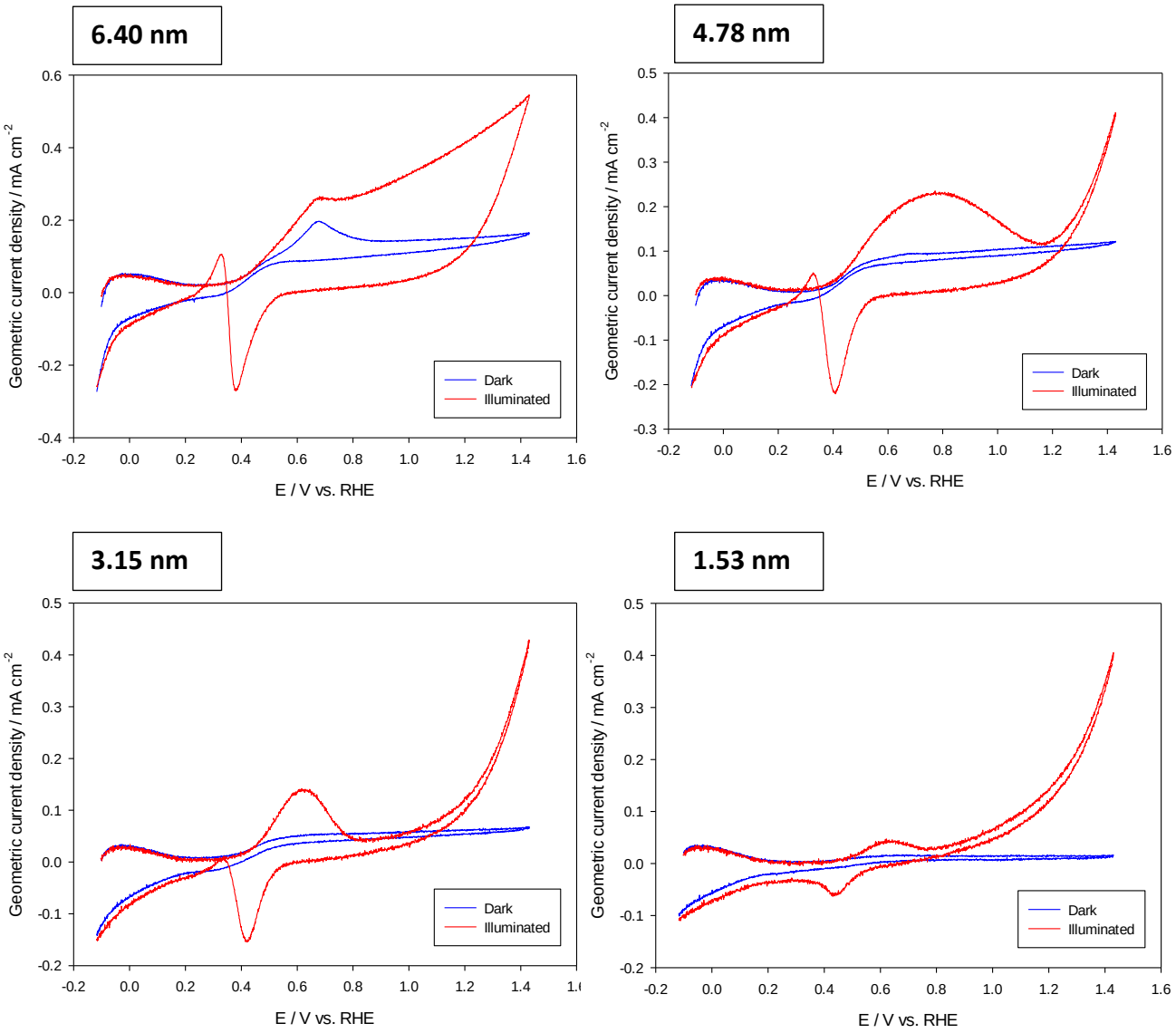

Figure 7.46. Dark and illuminated CVs of Fe_2O_3 supported Pt nanoparticles in 0.5 M NaOH + 1 M MeOH. The last cycles recorded in the dark are shown as well as the first cycles under illumination. A potential scan rate of 50 mV s^{-1} was used and correction for light intensity variation has not been applied. (Array #8145)

Several key differences between the illuminated and dark voltammetry exist, which were alluded to in Section 7.7. Firstly an anodic peak in the illuminated voltammetry is present between 0.4 – 1.2 V on the positive scan. This is similar to the feature observed in NaOH without methanol, and is likely to partly relate to the same anodic process. In most cases the peak is considerably broader than that in NaOH, which presumably relates to the superimposition of this peak onto that relating to the oxidation of methanol. Positive of 1.2 V there is again a rapid increase in current. In all cases the current positive of 1.2 V was much larger than that recorded in the blank NaOH electrolyte. On the reverse scan, there is a cathodic peak centred at around 0.4 V. This is likely to relate to reduction of the same species formed in the anodic sweep in methanol free media. Negative of approximately 0.4 V there is a slight increase in anodic current, which presumably relates to the oxidation of residual fragments of methanol at the electrode surface. As noted in the previous section, this would suggest that an increased level of oxide formation occurs in the illuminated voltammetry relative to that in the dark.

The voltammetry changed significantly with cycling, with the greatest change exhibited by particle sizes above approximately 3 nm. In the first cycles shown in Figure 7.46, the photocurrent decreases significantly on the reverse scan at larger particle sizes. Additionally, a clear peak shape is seen on the anodic scan. With increasing cycle number the photocurrent on the reverse scan increased (Figure 7.45) and the peak on the forward scan became significantly larger. After approximately 6 cycles, the anodic peak on the negative scan (approximately 0.3 V) disappeared entirely for particle sizes above approximately 4 nm. At particle sizes below approximately 3 nm, there was relatively little change to the response with cycling.

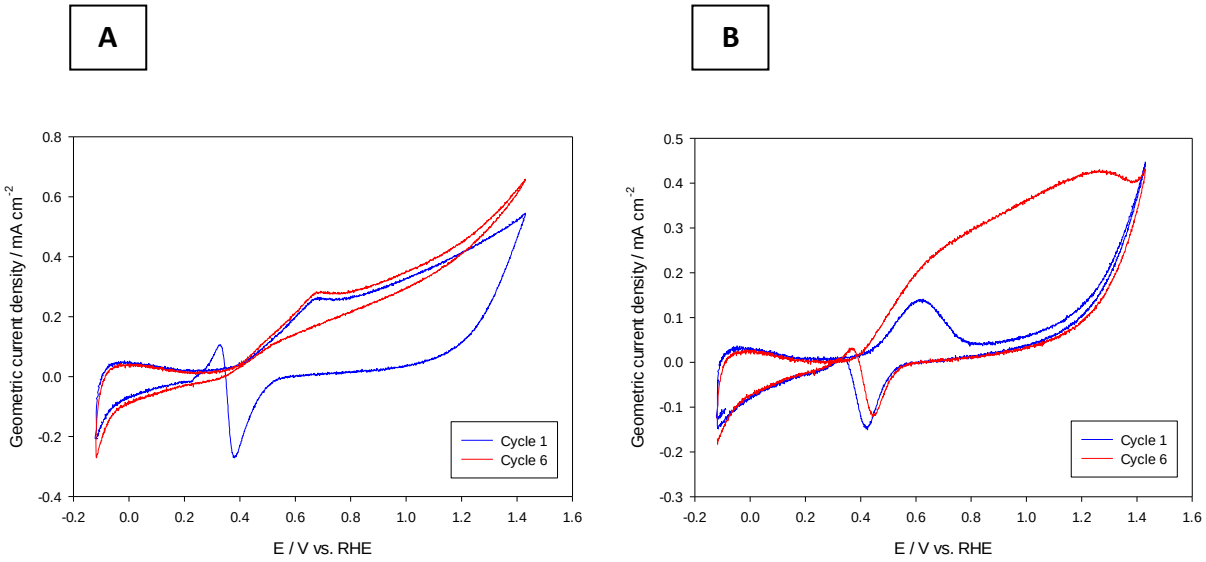

Figure 7.47. The first and sixth illuminated cycles of Fe_2O_3 supported nanoparticles in 0.5 M NaOH + 1 M MeOH. Data is shown for an estimated mean particle size of 6.40 nm (A) and 3.15 nm (B). A scan rate of 50 mV s^{-1} was used in all cases. (Array #8145)

It can be seen from Figure 7.47 that the methanol oxidation current decreases on the reverse scan in the first cycles. With cycling, the methanol oxidation increases on the reverse scan at the largest particle size presented. The same was found to be true of the largest 6 particle sizes on the array (i.e. d > ~ 3 nm). At the smaller particle size presented in Figure 7.45, the methanol oxidation current increased on the positive cycle, although the behaviour remained relatively similar on the reverse scan. It is possible that the effects relate to a decrease in the ability to form Pt oxide with prolonged cycling. Such effects may arise from a change to the particle structure or through poisoning of the electrode surface in a way that inhibits oxide formation. It would appear that any such effects are more prevalent at larger Pt particle sizes.

The exact nature of the changes that occur with cycling however remains unclear. It has been proposed that oxygen in solution can be beneficial to the degradation of organic species. This is caused by the formation of reactive O_2^- species by conduction band electrons. It is likely that with this concentration of methanol (1 M) in the electrolyte, some oxygen is still generated in solution. Possibly this may stimulate the production of O_2^- and relate to the increase in current. The oxidation of organic species, may also lead to the formation of highly reducing intermediates such as hyroxymethyl radicals. It has been shown that such species may inject electrons into

semiconductors and produce an increase in photocurrent via 'current doubling' phenomena. This is seldom observed in Fe_2O_3 however.

The overall response showed that larger particle sizes were more efficient at promoting the photooxidation of methanol. Additionally, all particle sizes brought about a significant increase in photocurrent relative to the bare Fe_2O_3 support. The photocurrent at 1.1 V is shown for the first and sixth anodic scan in Figure 7.49.

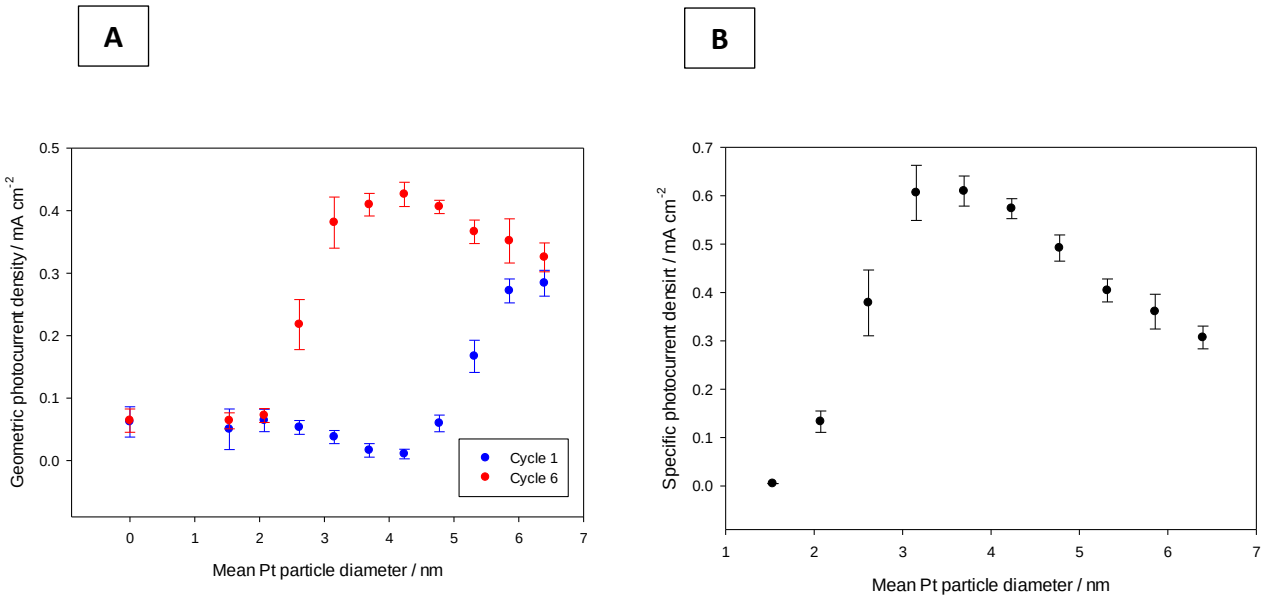

Figure 7.49. Geometric photocurrent density (corrected for intensity variation) at 1.2 V vs. RHE in 0.5 M NaOH + 1 M MeOH (A). Data is shown for the first and sixth cycles of Fe_2O_3 supported Pt nanoparticles under illumination. A scan rate of 50 mV s^{-1} was used in all case. Also shown (B) are the current densities of the sixth cycle scaled to the specific Pt surface area. (Array #8145)

In the first cycle, relatively little photocurrent is generated at particle sizes below approximately 5 nm. On the sixth cycle, the activity becomes approximately equal for particle sizes above 3 nm. In terms of specific activity, this leads to a maximum at approximately 3 nm, before decaying sharply (Figure 7.49 A). It was clear that cycling under illumination promoted anodic current flow in the form of an anodic peak in the methanol free media. It is likely that the increased conductivity of the support under illumination allows the Pt particles to remove any surface contamination. Furthermore the ability to sustain anodic current leads to a much greater ability to form Pt oxide. It is likely therefore that these effects allow the Pt particles to be more effective at catalysing the methanol oxidation reaction, thereby producing trends related primarily to the Pt particle size

dependence on the MOR. The specific activity trend however shows intermediately sized particles to be most effective, which may result from the intrinsic particle size activity trends being superimposed on similar band bending arguments to those presented in Chapter 6. Shadowing effects by the particles are also a possibility, although this appeared to have little effect with similarly sized particles on the TiO_2 support.

7.4. General Conclusions

Of all the dark reactions studied, particles supported on Fe_2O_3 were more active than those on anatase TiO_2. In general, the specific activity of the MOR and ORR both decreased as the Pt particle size decreased. The enhanced activity relative to the TiO_2 support would seem to be partly attributed to the greater level of conductivity in the support, presumably by a higher defect density or lower film thickness.

The initial cycles under illumination showed an anodic peak representing formation of a species that remained stable after removal of illumination. It is likely that the improved film conductivity enhances the generation of oxide on the Pt particles. The process initially was limited at larger particle sizes, which improved with cycling. The cleanliness of the surface is likely to have had an influence on this behaviour. As a result, it appeared that the peak was influenced primarily by the characteristics of the Pt particles as opposed to any change in their level of interaction with the support. The formation of oxide did not appear to significantly enhance the rate of oxygen evolution, suggesting that the process is primarily governed by the slow kinetics of the reaction at the support or an additional rate limiting step other than oxide formation at the Pt.

The Pt particles appeared to significantly enhance the photooxidation of methanol, which may relate to the enhanced ability to form oxidising species on the Pt surface. Some notable changes occurred with cycling, which stabilised relatively quickly. The exact reason for this could not be unambiguously identified, although it is possible that an intrinsic reduction in the ability to form Pt oxide occurs with cycling, as was observed in the dark voltammetry. Additionally, intermediates in the oxidation of methanol may poison the surface to some degree and hinder the build-up of poisoning oxide species at the Pt surface. Upon stabilisation, the activity was relatively similar at particle sizes above approximately 3 nm, which would suggest that the catalytic role of Pt is not

the only cause for the activity variation at different Pt particle sizes. The reduction in the level of band bending with increased particle size remains a possibility, and may account for the large variation in ORR onset potential in addition to the variation in behaviour towards ferricyanide reduction. Furthermore, the oxide stripping peak position was in poor agreement with the ORR onset after cycling, highlighting that the kinetics of oxide removal are not the sole cause of an increased overpotential requirement for the ORR at smaller particles. This is further exemplified by the close agreement of the oxide stripping peak potential on TiO_2 and Fe_2O_3 supported Pt in spite of a large variation in the ORR onset potentials.

8. Conclusions and Further Work

A new high-throughput method was developed towards the screening of photoanode materials for photoelectrochemical water splitting. The effects of Pt particle size on the photoelectrochemical characteristics of anatase TiO_2 and α-Fe_2O_3 was studied in addition to the effects of TiO_2 film thickness.

Strong rectifying behaviour was observed in the case of TiO_2 supported particles, which arises from the effects of the depletion layer formed inside the semiconductor surface at potentials positive of the flat band potential. This behaviour was found to have significant implications on the charge transfer characteristics of the Pt particles. The aforementioned rectifying behaviour could be confirmed by the absence of anodic current relating to simple reversible electron transfer reactions. As a result, oxide formation appeared to be hindered, which became increasingly apparent as the Pt particle size decreased. Any variation in the behaviour of particles on the two supports was also more pronounced at smaller particle sizes.

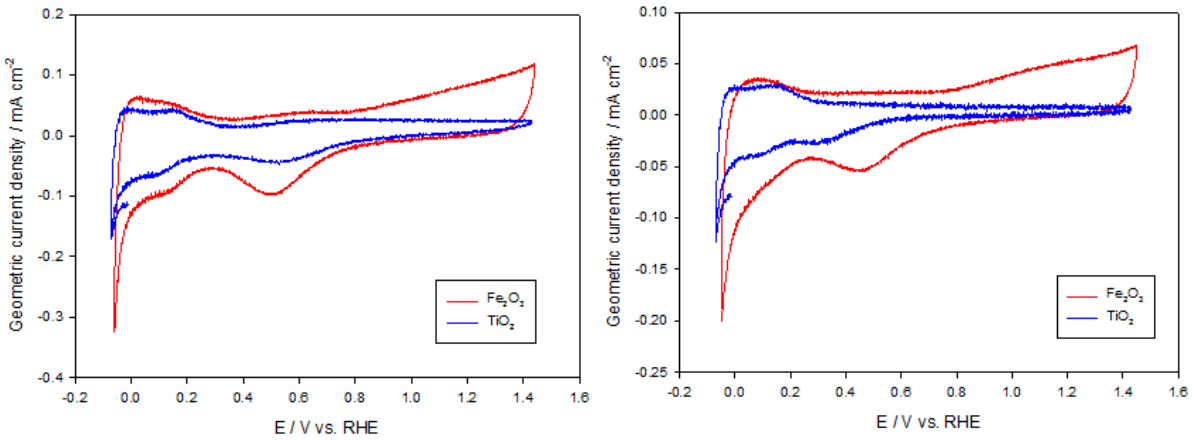

Figure 8.1. Comparison of CVs of Pt nanoparticles on TiO_2 and Fe_2O_3 supports. Data is shown for the largest particle size on the array (left – Estimated particle diameter = TiO_2: 5.90 nm, Fe_2O_3: 6.40 nm) and the fourth smallest particle size on each array (Right – Estimated particle diameter = TiO_2: 2.91 nm, Fe_2O_3: 3.15 nm). The first cycle of CVs recorded in Ar purged 0.5 M NaOH are shown.

Figure 8.1 shows that oxide formation occurs to a much greater extent on particle supported on Fe_2O_3. This together with the ability to oxidise ferrocyanide would suggest a reduction in the level of rectification on the Fe_2O_3 support. This is to be expected given the more positive flat band

potential of Fe_2O_3. It can also be noted that the oxide stripping peak position is in good agreement between larger sized particles, with the level of variation increasing at the smaller particle sizes. In spite of this, the oxygen reduction onset potentials varied to a considerable extent across all particle diameters on the two supports, as can be seen in Figure 8.2.

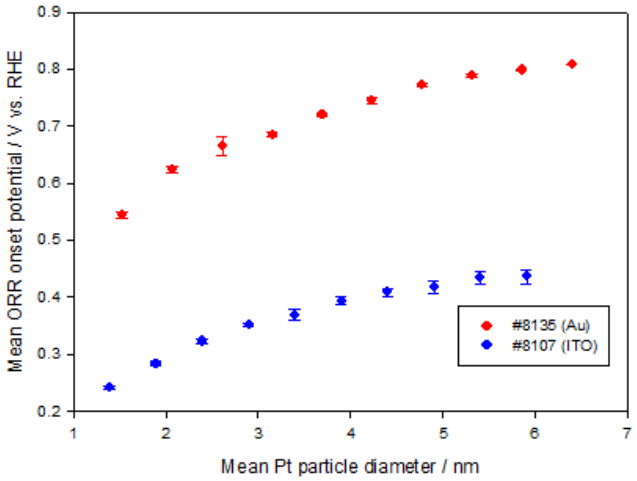

Figure 8.2. Mean ORR onset potential for Pt particles supported on Fe_2O_3 (#8135) and TiO_2 (#8107). The onset was defined as the potential required to generate a geometric current density of -0.028 mA cm^{-2}. Data is shown for the first negative going sweep in O_2 saturated 0.5 M NaOH at a scan rate of 5 mV s^{-1}.

The mean particle diameters of the particles on the two supports were determined to be relatively similar across the arrays. It can also be observed that the relative trends in response to particle size are remarkably similar, albeit systematically shifted negative for the TiO_2 support. Such observations suggest that the particle size dependence of the reaction stems from a similar origin on the two supports. In light of the smaller variation in the oxide stripping peak it is therefore unlikely that the particle size dependence arises purely from a variation in the kinetics relating to oxide removal. Furthermore, the agreement of the ferricyanide reduction and ORR trends on the TiO_2 support suggest that the change in the level of band bending (and in turn the ability to supply electrons to the electrode surface) dominated the activity trends. In light of the systematic shift in the ORR onset potentials on the two supports, it is likely that the response of the particles on Fe_2O_3 is affected at least in part by a similar mechanism.

In the case of the Fe_2O_3 support however, oxidation of ferrocyanide occurred to some degree at all particle sizes. It is possible however that variable band bending in response to particle size still exists. This is since a specific activity trend still existed despite the structural insensitivity of the

ferrocyanide oxidation reaction. Additionally, a further anodic peak was observed in the ferricyanide containing media, which may suggest that surface states play a role in mediating the charge transfer process. It was also shown that samples with a variation in TiO_2 thickness could show characteristics of a variation in the level of band bending (as evidenced by the photoelectrochemical behaviour) whilst still maintaining the ability to take part in anodic charge transfer reactions in the dark.

With repeated cycling the characteristics of the particles on both support types changed dramatically. Specifically, it appeared that the formation of Pt oxide became hindered, with no clear oxide formation at all after 15 cycles on the TiO_2 support.

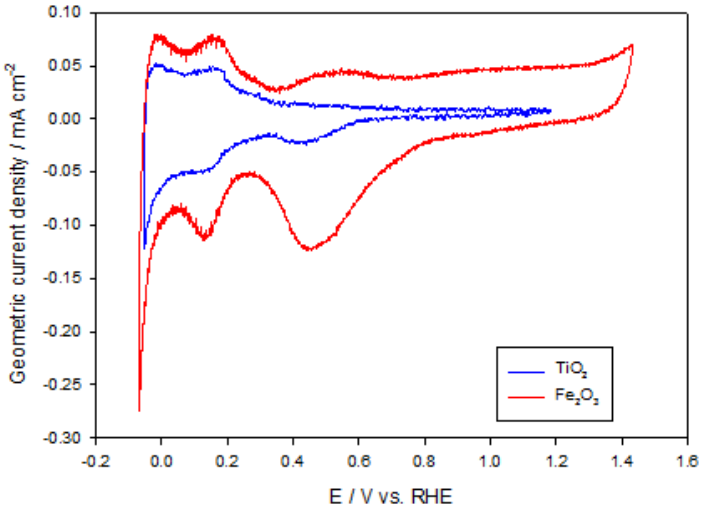

Figure 8.3. The 15th cycles of the largest particle diameters deposited on TiO_2 (Estimated particle diameter = 5.90 nm) and Fe_2O_3 (estimated particle diameter = 6.40 nm) supports. Data is shown for sample prepared on Au substrates and screened in Ar purged 0.5 M NaOH at a scan rate of 50 mV s^{-1}.

Any changes to the Fe_2O_3 supported particles were much less severe, however it appeared in both cases that the Pt surface became cleaner and/or some level of restructuring took place. In both cases the hydrogen adsorption/desorption features became sharper and clearer. A reduction in the double layer charging current also was apparent. In spite of this, the hydrogen adsorption charge did not change appreciably with prolonged cycling on either support. It should be noted that the oxide formation features ceased to appear on the Fe_2O_3 support after cycling also, although a greater number of cycles were required in order to bring about this behaviour.

The effect of cycling also brought about a negative shift in the ORR onset on both supports, which may be due to a loss in the conductivity of the support materials. Any change in this parameter affected larger particles to a greater extent. If a reduction in Pt surface area was the sole cause of this behaviour, it would generally be expected that the less stable smaller particles would be more susceptible to dissolution. It cannot however be ruled out that the nature of the particles change, since it was not possible to carry out any meaningful post-screening characterisation. This would be a key area of interest for future work. In particular, XPS characterisation may provide a greater understanding of any change to the particles after cycling, such that these changes could then be correlated with the characteristics observed in the voltammetry.

The decay in the level of oxide formation also did not fit entirely with an argument based purely on decreased conductivity and a concomitant increase in the level of rectification. This comes from the observation that methanol oxidation activity was still observed on Fe_2O_3 supported nanoparticles under conditions where no discernible level of oxide formation took place. It would appear therefore (at least in the case of the Fe_2O_3 support) that cycling specifically causes a reduction in Pt oxide formation, and not simply a deactivation of the ability to sustain anodic current. The TiO_2 support on the other hand was sufficiently insulating so as to prevent anodic current flow in even simple reversible electron transfer processes. It is therefore not possible to comment as to whether the rate of oxide formation is adversely affected to a greater extent than any other reaction after cycling.

In the photoelectrochemical measurements, it did appear that the size of Pt particles had an influence on the level of band bending in the support and therefore its ability to direct photogenerated holes to the electrode surface. In the case of the TiO_2 support, a negative shift in the photocurrent onset potential occurred as the particle size decreased. The onset was also positive of that observed for bare TiO_2 at all but the smallest particle size. Additionally the absolute level of photocurrent generated below approximately 0.6 V vs. RHE decreased as the particle size increased. Interestingly, any variation between the behaviours of different particle sizes and the blank support narrowed significantly above ~0.6 V. In fact, the level of photocurrent was practically equal in this voltage range, which would suggest any effects of shadowing and optical attenuation by the particles is negligible. Although the illuminated behaviour of the Fe_2O_3 supported particles was drastically different, similar overall observations could be made.

In the case of the Fe_2O_3 support, the anodic photocurrent behaviour under illumination was dominated by a peak which was proposed to represent photoassisted Pt oxide formation. Similarly to the photocurrent onset on the TiO_2 support, the peak potential of this peak shifted

positive as the particle size increased. Also similar to the TiO_2 support, was the similarity of the response at all particle sizes in the higher voltage range (> ~1 V). In the higher voltage region, the behaviour is dominated by the support, where the slow OER kinetics at the Fe_2O_3 means that the behaviour is controlled by this factor rather than charge separation ability or variation in optical absorption. Additionally, the illumination intensity had little effect on the observed behaviour at all particle sizes, meaning that optical absorption is not the limiting factor or the primary source of the variation in behaviour across the particle size range. In the dark measurements, there was no clear change in the onset of oxide formation across the particle size range, although the stripping peak shifted progressively negative as the particle size reduced. This would indicate that the kinetics relating to oxide formation are more limited at smaller particle sizes. The negative shift in the photocurrent peak potential at smaller particle sizes would however suggest the opposite. It is therefore likely that both intrinsic particle size effects as well as a change to the level of band bending affect the illuminated response.

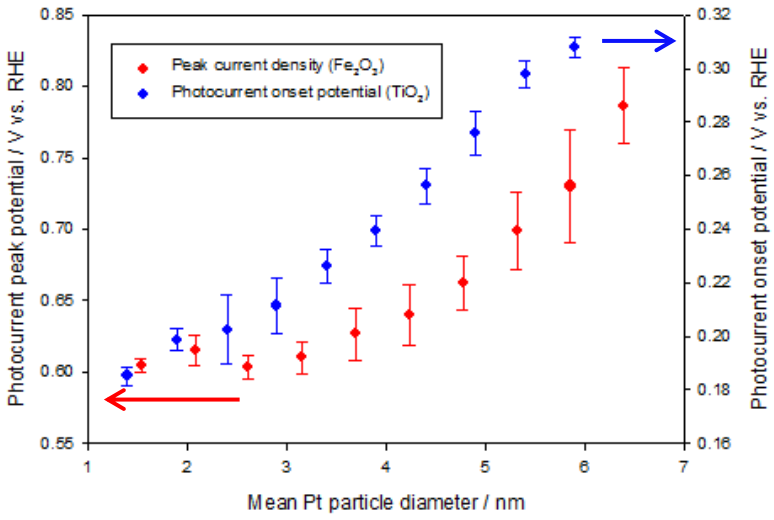

Figure 8.4. Mean photocurrent onset potential of TiO_2 supported nanoparticles and the mean anodic photocurrent peak potential of Fe_2O_3 supported Pt nanoparticles. Measurements were carried out in Ar purged 0.5 M NaOH at a scan rate of 50 mV s^{-1}. Data is shown for the first illuminated cycles of arrays #8075 and #8135.

Although some general similarities between the photocurrent vs. particle size trends were observed, the actual appearance of the voltammetry differed markedly on the two supports. Naturally the onset of any light mediated process on Fe_2O_3 is considerably more positive when compared with TiO_2. As with mentioned in the ORR trends, this is due to the flat band potential of

Fe_2O_3 being considerably more positive that of TiO_2. In Figure 8.4, the photocurrent onset potential of TiO_2 supported particles and peak potential of the anodic photocurrent peak on Fe_2O_3 supported particles are presented. The two parameters are not directly comparable, since no oxide formation or discernible anodic peak was observed in the illuminated voltammetry of TiO_2 supported particles. Additionally, little variation in the photocurrent response to particle size was observed at Fe_2O_3 supported particles in the region where oxygen evolution takes place. Qualitatively however, the two plots show the ability to generate photocurrent in a region where the level of band bending is relatively small. In the case of the onset potential on TiO_2, a variation of approximately 130 mV was observed across the particle size range. A similar level of variation (~180 mV) can be observed for the photocurrent peak potential on the Fe_2O_3. At TiO_2 supported particles, the absence of any anodic voltammetric features of Pt would suggest that the behaviour under illumination is dominated by the support. The lack of any real variation above 0.6 V also supports this conclusion. Any variation seen at lower voltages is therefore linked to the modulation of the supports electrical properties in response to changes in particle size.

The Fe_2O_3 supported particles however show characteristics of Pt in the illuminated voltammetry, suggesting that intrinsic particle size effects may exist in addition to variation in the supports electrical properties. Given the behaviour in the dark, it would seem that the latter effects dominate. Additionally, the dominating slow rate of oxygen evolution on Fe_2O_3 above 0.8 V shows that the incorporation of Pt has no real benefit to the rate of charge transfer. It is not in fact clear whether photo assisted oxygen evolution actually involves transfer at the Pt particles at all.

Interestingly, it was clear that the imposition of Pt particles was in fact beneficial for the photooxidation of methanol on Fe_2O_3. On the other hand, only a slightly larger photocurrent was observed on TiO_2 supported particles below ~0.6 V in the presence of methanol. In spite of this, the activity was still poorer than TiO_2 alone. The lack of variation (across the particle size range as well as when compared with methanol free electrolyte) above 0.6 V would suggest that methanol simply acts as a hole scavenger and that the same mechanism attributed to particle size variation operates in this media. On the other hand, a clear increase in photocurrent was observed at all particle sizes relative to blank Fe_2O_3 on Fe_2O_3 supported particles. The increased formation of oxidant species is likely to account for this factor, since a large increase in Pt oxide formation was observed under illumination. Owing to the larger surface area of Pt at larger particle sizes, the activity increased as the particle size increased. In this case, it therefore seems that the characteristics of the Pt particles as opposed to the support dominate the behaviour. Unlike in the dark however, an apparent specific activity maximum occurred at a particle size of around 3-4 nm.

It is likely therefore that both the increased band bending at smaller particle sizes and the higher intrinsic activity at larger particle sizes oppose each other to create this apparent maximum at an intermediate particle size. It therefore appears that Pt particles actually benefit the photooxidation of methanol on Fe_2O_3.

For future work it would be of interest to study particles on doped supports or with a higher level of intrinsic defects. This may allow visualisation of activity trends in the absence of support conductivity trends and confirm whether the interpretations put forward in this work are valid. Additionally, study of the samples in this work with AC impedance spectroscopy would be of key importance. Through these experiments, one would be able to more accurately determine the flat band potential of the electrodes and therefore comment with more certainty on the change in band bending in the support with particle size variation.

A key deficiency in this study was the inability to determine any changes that occurred to the particles throughout the screening process. Of particular interest would be to study the XPS spectra of the Pt(4f) level to visualise whether any loss of Pt occurs or any agglomeration effects, which could be determined by shifts in the binding energy of this level. More accurate preparation of defined particle sizes with solution based methods may also be of interest, both for rationalising the activity trends observed as well as showing the accuracy or inaccuracy of the high-throughput method employed in this work. Post screening TEM analysis would also be of fundamental importance, however screening of samples on sufficiently thin samples compatible with TEM imaging is challenging.

The high-throughput method employed has shown promise in screening photoanode materials, and therefore future work could also be directed towards the screening of more complex multicomponent oxides. It is clear from existing experimental evidence that this may provide the most promising route to obtaining materials that satisfy the requirements for efficient photoelectrochemical water splitting. In the existing configuration, it is likely that screening of materials with varying optical characteristics would prove to be difficult. This is since corrections for illumination intensity in addition to the sensitivity to varying light intensity would be required. Nevertheless, if samples are confined to a narrower spatial region, sufficiently large variations in behaviour could be observed without the need for any correction at all. To this end the method may be acceptable as a primary screen in more complex systems. Alternatively, more costly illumination sources with a higher level of uniformity would allow the method to be used to its full potential in future studies.

9. References

1. Dunn, S. Hydrogen futures: toward a sustainable energy system. *International journal of hydrogen energy* **2002,** *27* (3), 235-264.
2. Petit, J.; Raynaud, D.; Lorius, C.; Jouzel, J.; Delaygue, G.; Barkov, N.; Kotlyakov, V. Historical isotopic temperature record from the Vostok ice core. *Trends: A Compendium of Data on Global Change* **2000**.
3. Petit, J.-R.; Jouzel, J.; Raynaud, D.; Barkov, N. I.; Barnola, J.-M.; Basile, I.; Bender, M.; Chappellaz, J.; Davis, M.; Delaygue, G. Climate and atmospheric history of the past 420,000 years from the Vostok ice core, Antarctica. *Nature* **1999,** *399* (6735), 429-436.
4. Katz, J. E. Metal oxide-based photoelectrochemical cells for solar energy conversion. California Institute of Technology, 2008.
5. Petroleum, B. BP Statistical Review of World Energy 2015. London: 2015.
6. Rajeshwar, K. Semiconductor electrodes and photoelectrochemistry. Wiley-VCH, ISBN: 2002; pp 978-3.
7. van de Krol, R. Principles of photoelectrochemical cells. In *Photoelectrochemical hydrogen production*, Springer: 2012; pp 13-67.
8. Nowotny, J.; Bak, T.; Nowotny, M.; Sheppard, L. Titanium dioxide for solar-hydrogen I. Functional properties. *International journal of hydrogen energy* **2007,** *32* (14), 2609-2629.
9. Woodhouse, M.; Parkinson, B. Combinatorial approaches for the identification and optimization of oxide semiconductors for efficient solar photoelectrolysis. *Chemical Society Reviews* **2009,** *38* (1), 197-210.
10. Bak, T.; Nowotny, J.; Rekas, M.; Sorrell, C. Photo-electrochemical hydrogen generation from water using solar energy. Materials-related aspects. *International journal of hydrogen energy* **2002,** *27* (10), 991-1022.
11. Diebold, U. The surface science of titanium dioxide. *Surface science reports* **2003,** *48* (5), 53-229.
12. Kudo, A.; Kato, H.; Tsuji, I. Strategies for the development of visible-light-driven photocatalysts for water splitting. *Chemistry Letters* **2004,** *33* (12), 1534-1539.
13. Walter, M. G.; Warren, E. L.; McKone, J. R.; Boettcher, S. W.; Mi, Q.; Santori, E. A.; Lewis, N. S. Solar water splitting cells. *Chemical reviews* **2010,** *110* (11), 6446-6473.
14. Trasatti, S. Electrocatalysis by oxides—attempt at a unifying approach. *Journal of Electroanalytical Chemistry and Interfacial Electrochemistry* **1980,** *111* (1), 125-131.
15. Guerin, S.; Hayden, B. E. Physical vapor deposition method for the high-throughput synthesis of solid-state material libraries. *Journal of combinatorial chemistry* **2006,** *8* (1), 66-73.
16. Hannah, L. The High Throughput Synthesis & Screening of Electrocatalysts for the Reduction of Nitrate in Groundwater and Waste Streams. *PhD Thesis* **2013**.
17. NREL. Reference Solar Spectral Irradiance: Air Mass 1.5. http://rredc.nrel.gov/solar/spectra/am1.5/.
18. LOT-qd. Distribution of Luminance; Beam uniformity. http://lot-qd.com/fileadmin/Mediapool/products/lightsources/eu/LQ_Distribution_of_luminance__beam_uniformity_eu.pdf.
19. Osterloh, F. E. Inorganic nanostructures for photoelectrochemical and photocatalytic water splitting. *Chemical Society Reviews* **2013,** *42* (6), 2294-2320.
20. Nowotny, J.; Bak, T.; Nowotny, M.; Sheppard, L. Titanium dioxide for solar-hydrogen II. Defect chemistry. *International journal of hydrogen energy* **2007,** *32* (14), 2630-2643.
21. Rossi, R. C.; Lewis, N. S. Investigation of the size-scaling behavior of spatially nonuniform barrier height contacts to semiconductor surfaces using ordered nanometer-scale nickel arrays on silicon electrodes. *The Journal of Physical Chemistry B* **2001,** *105* (49), 12303-12318.
22. Lewis, N. S.; Crabtree, G. Basic research needs for solar energy utilization: report of the basic energy sciences workshop on solar energy utilization, April 18-21, 2005**2005**.
23. Goldemberg, J.; Johansson, T. B.; Anderson, D. *World energy assessment: overview: 2004 update*. United Nations Development Programme, Bureau for Development Policy: 2004.

24. Soria, A.; Szabo, L.; Russ, P.; Suwala, W.; Hidalgo, I.; Purwanto, A. World Energy Technology Outlook 2050. *European Commission, Joint Research Centre* **2006,** *21*.
25. Bose, B. Global energy scenario and impact of power electronics in 21st century. *Industrial Electronics, IEEE Transactions on* **2013,** *60* (7), 2638-2651.
26. Neftel, A.; Friedli, H.; Moor, E.; Lötscher, H.; Oeschger, H.; Siegenthaler, U.; Stauffer, B. Historical carbon dioxide record from the Siple Station ice core. *Trends '93: A Compendium of Data on Global Change. ORNL/CDIAC-65. Carbon Dioxide Information Analysis Center, Oak Ridge National Laboratory, Oak Ridge, Tenn* **1994**, 11-14.
27. Lewis, N. S.; Nocera, D. G. Powering the planet: Chemical challenges in solar energy utilization. *Proceedings of the National Academy of Sciences* **2006,** *103* (43), 15729-15735.
28. Winter, C.-J. Hydrogen energy—Abundant, efficient, clean: A debate over the energy-system-of-change. *International Journal of Hydrogen Energy* **2009,** *34* (14), S1-S52.
29. Dunderdale, J. *Energy and the environment: the proceedings of a symposium organized jointly by the Inorganic Chemicals Group and the Environment Group of the Industrial Division of the Royal Society of Chemistry: University of Leeds, 3rd-5th April 1990*. CRC Pr I Llc: 1990.
30. Dincer, I. Renewable energy and sustainable development: a crucial review. *Renewable and Sustainable Energy Reviews* **2000,** *4* (2), 157-175.
31. ISE, F. New world record for solar cell efficiency at 46%

French-German cooperation confirms competitive advantage of European photovoltaic industry. *Fraunhofer ISE Press Release* **2014**, https://www.ise.fraunhofer.de/en/press-and-media/press-releases/press-releases-2014/new-world-record-for-solar-cell-efficiency-at-46-percent.
32. Amouyal, E. Photochemical production of hydrogen and oxygen from water: A review and state of the art. *Solar Energy Materials and Solar Cells* **1995,** *38* (1), 249-276.
33. Holladay, J. D.; Hu, J.; King, D. L.; Wang, Y. An overview of hydrogen production technologies. *Catalysis Today* **2009,** *139* (4), 244-260.
34. Pletcher, D.; Walsh, F. C. *Industrial electrochemistry*. Springer Science & Business Media: 1990.
35. Minggu, L. J.; Daud, W. R. W.; Kassim, M. B. An overview of photocells and photoreactors for photoelectrochemical water splitting. *International Journal of Hydrogen Energy* **2010,** *35* (11), 5233-5244.
36. Heller, A. Conversion of sunlight into electrical power and photoassisted electrolysis of water in photoelectrochemical cells. *Accounts of chemical research* **1981,** *14* (5), 154-162.
37. Ma, G.; Hisatomi, T.; Domen, K. Semiconductors for Photocatalytic and Photoelectrochemical Solar Water Splitting. In *From Molecules to Materials*, Springer: 2015; pp 1-56.
38. Pinaud, B. A.; Benck, J. D.; Seitz, L. C.; Forman, A. J.; Chen, Z.; Deutsch, T. G.; James, B. D.; Baum, K. N.; Baum, G. N.; Ardo, S. Technical and economic feasibility of centralized facilities for solar hydrogen production via photocatalysis and photoelectrochemistry. *Energy & Environmental Science* **2013,** *6* (7), 1983-2002.
39. Bott, A. W. Electrochemistry of semiconductors. *Current Separations* **1998,** *17*, 87-92.
40. Bao, D.; Yao, X.; Wakiya, N.; Shinozaki, K.; Mizutani, N. Band-gap energies of sol-gel-derived SrTiO3 thin films. *Applied Physics Letters* **2001,** *79* (23), 3767-3769.
41. Khan, S. U.; Akikusa, J. Photoelectrochemical splitting of water at nanocrystalline n-Fe2O3 thin-film electrodes. *The Journal of Physical Chemistry B* **1999,** *103* (34), 7184-7189.
42. Lévy‐Clément, C.; Lagoubi, A.; Neumann‐Spallart, M.; Rodot, M.; Tenne, R. Efficiency and Stability Enhancement of n‐Si Photoelectrodes in Aqueous Solution. *Journal of The Electrochemical Society* **1991,** *138* (12), L69-L71.
43. Kittel, C. *Introduction to solid state physics*. Wiley: 2005.
44. Tan, M. X.; Laibinis, P. E.; Nguyen, S. T.; Kesselman, J. M.; Stanton, C. E.; Lewis, N. S. Principles and applications of semiconductor photoelectrochemistry. *Progress in Inorganic Chemistry, Volume 41* **1994**, 21-144.
45. Pletcher, D. *A first course in electrode processes*. Royal Society of Chemistry: 2009.
46. Gerischer, H. Charge transfer processes at semiconductor-electrolyte interfaces in connection with problems of catalysis. *Surface Science* **1969,** *18* (1), 97-122.
47. Nozik, A. J.; Memming, R. Physical chemistry of semiconductor-liquid interfaces. *The Journal of Physical Chemistry* **1996,** *100* (31), 13061-13078.
48. Leng, W.; Zhang, Z.; Zhang, J.; Cao, C. Investigation of the kinetics of a TiO2 photoelectrocatalytic reaction involving charge transfer and recombination through surface states by electrochemical impedance spectroscopy. *The Journal of Physical Chemistry B* **2005,** *109* (31), 15008-15023.

49. Bard, A. J.; Bocarsly, A. B.; Fan, F. R. F.; Walton, E. G.; Wrighton, M. S. The concept of Fermi level pinning at semiconductor/liquid junctions. Consequences for energy conversion efficiency and selection of useful solution redox couples in solar devices. *Journal of the American Chemical Society* **1980,** *102* (11), 3671-3677.
50. Peter, L. M. Energetics and kinetics of light-driven oxygen evolution at semiconductor electrodes: the example of hematite. *Journal of Solid State Electrochemistry* **2013,** *17* (2), 315-326.
51. Lewis, N. S. Progress in understanding electron-transfer reactions at semiconductor/liquid interfaces. *The Journal of Physical Chemistry B* **1998,** *102* (25), 4843-4855.
52. Kumar, A.; Santangelo, P. G.; Lewis, N. S. Electrolysis of water at strontium titanate (SrTiO3) photoelectrodes: distinguishing between the statistical and stochastic formalisms for electron-transfer processes in fuel-forming photoelectrochemical systems. *The Journal of Physical Chemistry* **1992,** *96* (2), 834-842.
53. Noufi, R. N.; Kohl, P. A.; Frank, S. N.; Bard, A. J. Semiconductor Electrodes XIV. Electrochemistry and Electroluminescence at n - Type in Aqueous Solutions. *Journal of The Electrochemical Society* **1978,** *125* (2), 246-252.
54. Salvador, P.; Gutierrez, C. Mechanisms of Charge Transfer at the Semiconductor - Electrolyte Interface I. Kinetics of Electroreduction at Dark of and in Aqueous Solution on a Sintered Nb - doped Electrode: Influence of pH. *Journal of The Electrochemical Society* **1984,** *131* (2), 326-336.
55. Butler, M. Photoelectrolysis and physical properties of the semiconducting electrode WO2. *Journal of Applied Physics* **1977,** *48* (5), 1914-1920.
56. Tyagai, V. A. *Russian Journal of Physical Chemistry* **1965,** *38*, 1335.
57. Gärtner, W. W. Depletion-layer photoeffects in semiconductors. *Physical Review* **1959,** *116* (1), 84.
58. Li, J.; Peat, R.; Peter, L. Surface recombination at semiconductor electrodes: Part II. Photoinduced "near-surface" recombination centres in p-GaP. *Journal of electroanalytical chemistry and interfacial electrochemistry* **1984,** *165* (1), 41-59.
59. Memming, R. Surface recombination at higher injection levels. *Surface Science* **1964,** *1* (1), 88-101.
60. Khan, S. U.; Bockris, J. O. M. A model for electron transfer at the illuminated p-type semiconductor-solution interface. *The Journal of Physical Chemistry* **1984,** *88* (12), 2504-2515.
61. Fujishima, A.; Honda, K. Electrochemical evidence for the mechanism of the primary stage of photosynthesis. *Bulletin of the chemical society of Japan* **1971,** *44* (4), 1148-1150.
62. Paracchino, A.; Laporte, V.; Sivula, K.; Grätzel, M.; Thimsen, E. Highly active oxide photocathode for photoelectrochemical water reduction. *Nature materials* **2011,** *10* (6), 456-461.
63. Nozik, A. p - n photoelectrolysis cells. *Applied Physics Letters* **1976,** *29* (3), 150-153.
64. Kudo, A.; Miseki, Y. Heterogeneous photocatalyst materials for water splitting. *Chemical Society Reviews* **2009,** *38* (1), 253-278.
65. Turchi, C. S.; Ollis, D. F. Photocatalytic degradation of organic water contaminants: mechanisms involving hydroxyl radical attack. *Journal of catalysis* **1990,** *122* (1), 178-192.
66. Grätzel, M. Photoelectrochemical cells. *Nature* **2001,** *414* (6861), 338-344.
67. Grätzel, M. Dye-sensitized solar cells. *Journal of Photochemistry and Photobiology C: Photochemistry Reviews* **2003,** *4* (2), 145-153.
68. Dare-Edwards, M. P.; Goodenough, J. B.; Hamnett, A.; Seddon, K. R.; Wright, R. D. Sensitisation of semiconducting electrodes with ruthenium-based dyes. *Faraday Discussions of the Chemical Society* **1980,** *70*, 285-298.
69. Morisaki, H.; Watanabe, T.; Iwase, M.; Yazawa, K. Photoelectrolysis of water with TiO2 - covered solar - cell electrodes. *Applied Physics Letters* **1976,** *29* (6), 338-340.
70. Miller, E. L.; Paluselli, D.; Marsen, B.; Rocheleau, R. E. Development of reactively sputtered metal oxide films for hydrogen-producing hybrid multijunction photoelectrodes. *Solar energy materials and solar cells* **2005,** *88* (2), 131-144.
71. Licht, S. Multiple band gap semiconductor/electrolyte solar energy conversion. *The Journal of Physical Chemistry B* **2001,** *105* (27), 6281-6294.
72. Khaselev, O.; Turner, J. A. A monolithic photovoltaic-photoelectrochemical device for hydrogen production via water splitting. *Science* **1998,** *280* (5362), 425-427.
73. Graetzel, M. The artificial leaf, bio-mimetic photocatalysis. *Cattech* **1999,** *3* (1), 4-17.
74. Lewerenz, H.-J.; Peter, L. *Photoelectrochemical Water Splitting: Materials, Processes and Architectures*. Royal Society of Chemistry: 2013.

75. Khaselev, O.; Turner, J. A. Photoelectrolysis of HBr and HI Using a Monolithic Combined Photoelectrochemical/Photovoltaic Device. *Electrochemical and solid-state letters* **1999,** *2* (7), 310-312.
76. Bolton, J. R.; Strickler, S. J.; Connolly, J. S. Limiting and realizable efficiencies of solar photolysis of water. *Nature* **1985,** *316*, 495.
77. Bludau, W.; Onton, A.; Heinke, W. Temperature dependence of the band gap of silicon. *Journal of Applied Physics* **1974,** *45* (4), 1846-1848.
78. Blakemore, J. Semiconducting and other major properties of gallium arsenide. *Journal of Applied Physics* **1982,** *53* (10), R123-R181.
79. Mo, S.-D.; Ching, W. Electronic and optical properties of three phases of titanium dioxide: Rutile, anatase, and brookite. *Physical Review B* **1995,** *51* (19), 13023.
80. Fermin, D.; Ponomarev, E.; Peter, L. A kinetic study of CdS photocorrosion by intensity modulated photocurrent and photoelectrochemical impedance spectroscopy. *Journal of Electroanalytical Chemistry* **1999,** *473* (1), 192-203.
81. Murphy, A.; Barnes, P.; Randeniya, L.; Plumb, I.; Grey, I.; Horne, M.; Glasscock, J. Efficiency of solar water splitting using semiconductor electrodes. *International journal of hydrogen energy* **2006,** *31* (14), 1999-2017.
82. Lewis, N. S. Chemical control of charge transfer and recombination at semiconductor photoelectrode surfaces. *Inorganic chemistry* **2005,** *44* (20), 6900-6911.
83. Bube, R. *Fundamentals of solar cells: photovoltaic solar energy conversion*. Elsevier: 2012.
84. Lewis, N. S. Mechanistic studies of light-induced charge separation at semiconductor/liquid interfaces. *Accounts of Chemical Research* **1990,** *23* (6), 176-183.
85. Bak, T.; Nowotny, J.; Rekas, M.; Sorrell, C. Photo-electrochemical properties of the TiO 2-Pt system in aqueous solutions. *International journal of hydrogen energy* **2002,** *27* (1), 19-26.
86. Glasscock, J. A.; Barnes, P. R.; Plumb, I. C.; Savvides, N. Enhancement of photoelectrochemical hydrogen production from hematite thin films by the introduction of Ti and Si. *The Journal of Physical Chemistry C* **2007,** *111* (44), 16477-16488.
87. Zhao, G.; Kozuka, H.; Lin, H.; Takahashi, M.; Yoko, T. Preparation and photoelectrochemical properties of Ti 1− x V x O 2 solid solution thin film photoelectrodes with gradient bandgap. *Thin Solid Films* **1999,** *340* (1), 125-131.
88. Adamczyk, Z.; Nowotny, J. Effect of segregation on near-surface and bulk transport phenomena in ionic crystals. *Journal of Physics and Chemistry of Solids* **1986,** *47* (1), 11-27.
89. Riha, S. C.; Klahr, B. M.; Tyo, E. C.; Seifert, S. n.; Vajda, S.; Pellin, M. J.; Hamann, T. W.; Martinson, A. B. Atomic layer deposition of a submonolayer catalyst for the enhanced photoelectrochemical performance of water oxidation with hematite. *ACS nano* **2013,** *7* (3), 2396-2405.
90. Meekins, B. H.; Kamat, P. V. Role of water oxidation catalyst IrO2 in shuttling photogenerated holes across TiO2 interface. *The Journal of Physical Chemistry Letters* **2011,** *2* (18), 2304-2310.
91. Nowotny, J.; Bak, T.; Nowotny, M.; Sheppard, L. TiO2 surface active sites for water splitting. *The Journal of Physical Chemistry B* **2006,** *110* (37), 18492-18495.
92. Gamelin, D. R. Water splitting: Catalyst or spectator? *Nature chemistry* **2012,** *4* (12), 965-967.
93. Gerischer, H. In *Photoelectrochemical solar cells*, 2nd Photovoltaic Solar Energy Conference, 1979; pp 408-423.
94. Skotheim, T.; Petersson, L. G.; Inganäs, O.; Lundström, I. Photoelectrochemical Behavior of n‐Si Electrodes Protected with Pt‐Polypyrrole. *Journal of The Electrochemical Society* **1982,** *129* (8), 1737-1741.
95. Sclafani, A.; Herrmann, J. Comparison of the photoelectronic and photocatalytic activities of various anatase and rutile forms of titania in pure liquid organic phases and in aqueous solutions. *The Journal of Physical Chemistry* **1996,** *100* (32), 13655-13661.
96. Paz, Y.; Luo, Z.; Rabenberg, L.; Heller, A. Photooxidative self-cleaning transparent titanium dioxide films on glass. *Journal of Materials Research* **1995,** *10* (11), 2842-2848.
97. Cai, R.; Hashimoto, K.; Itoh, K.; Kubota, Y.; Fujishima, A. Photokilling of malignant cells with ultrafine TiO 2 powder. *Bulletin of the Chemical Society of Japan* **1991,** *64* (4), 1268-1273.
98. Sharma, R. K.; Bhatnagar, M.; Sharma, G. Mechanism of highly sensitive and fast response Cr doped TiO 2 oxygen gas sensor. *Sensors and Actuators B: Chemical* **1997,** *45* (3), 209-215.
99. Cerri, I.; Nagami, T.; Davies, J.; Mormiche, C.; Vecoven, A.; Hayden, B. Innovative catalyst supports to address fuel cell stack durability. *International Journal of Hydrogen Energy* **2013,** *38* (1), 640-645.
100. Reidy, D.; Holmes, J.; Morris, M. The critical size mechanism for the anatase to rutile transformation in TiO 2 and doped-TiO 2. *Journal of the European Ceramic Society* **2006,** *26* (9), 1527-1534.

101. Lottiaux, M.; Boulesteix, C.; Nihoul, G.; Varnier, F.; Flory, F.; Galindo, R.; Pelletier, E. Morphology and structure of TiO 2 thin layers vs. thickness and substrate temperature. *Thin solid films* **1989,** *170* (1), 107-126.
102. Czanderna, A.; Rao, C. R.; Honig, J. The anatase-rutile transition. Part 1.—Kinetics of the transformation of pure anatase. *Transactions of the Faraday Society* **1958,** *54*, 1069-1073.
103. Yoganarasimhan, S.; Rao, C. R. Mechanism of crystal structure transformations. Part 3.—factors affecting the anatase-rutile transformation. *Transactions of the Faraday Society* **1962,** *58*, 1579-1589.
104. Kumar, S. R.; Pillai, S. C.; Hareesh, U.; Mukundan, P.; Warrier, K. Synthesis of thermally stable, high surface area anatase–alumina mixed oxides. *Materials Letters* **2000,** *43* (5), 286-290.
105. Pillai, S. C.; Periyat, P.; George, R.; McCormack, D. E.; Seery, M. K.; Hayden, H.; Colreavy, J.; Corr, D.; Hinder, S. J. Synthesis of high-temperature stable anatase TiO2 photocatalyst. *The Journal of Physical Chemistry C* **2007,** *111* (4), 1605-1611.
106. Tang, H.; Prasad, K.; Sanjines, R.; Schmid, P.; Levy, F. Electrical and optical properties of TiO2 anatase thin films. *Journal of Applied Physics* **1994,** *75* (4), 2042-2047.
107. Henderson, M. A. An HREELS and TPD study of water on TiO 2 (110): the extent of molecular versus dissociative adsorption. *Surface Science* **1996,** *355* (1), 151-166.
108. Menetrey, M.; Markovits, A.; Minot, C. Reactivity of a reduced metal oxide surface: hydrogen, water and carbon monoxide adsorption on oxygen defective rutile TiO 2 (110). *Surface science* **2003,** *524* (1), 49-62.
109. Lo, W. J.; Chung, Y. W.; Somorjai, G. Electron spectroscopy studies of the chemisorption of O 2, H 2 and H 2 O on the TiO 2 (100) surfaces with varied stoichiometry: Evidence for the photogeneration of Ti+ 3 and for its importance in chemisorption. *Surface Science* **1978,** *71* (2), 199-219.
110. Nakamura, R.; Nakato, Y. Primary intermediates of oxygen photoevolution reaction on TiO2 (rutile) particles, revealed by in situ FTIR absorption and photoluminescence measurements. *Journal of the American Chemical Society* **2004,** *126* (4), 1290-1298.
111. Kobayakawa, K.; Nakazawa, Y.; Ikeda, M.; Sato, Y.; Fujishima, A. Influence of the density of surface hydroxyl groups on TiO2 photocatalytic activities. *Berichte der Bunsengesellschaft für physikalische Chemie* **1990,** *94* (12), 1439-1443.
112. Bickley, R.; Jayanty, R. Photo-adsorption and photo-catalysis on titanium dioxide surfaces. Photo-adsorption of oxygen and the photocatalyzed oxidation of isopropanol. *Faraday Discussions of the Chemical Society* **1974,** *58*, 194-204.
113. Sivula, K.; Le Formal, F.; Grätzel, M. Solar water splitting: progress using hematite (α - Fe2O3) photoelectrodes. *ChemSusChem* **2011,** *4* (4), 432-449.
114. Ahn, H.-J.; Kwak, M.-J.; Lee, J.-S.; Yoon, K.-Y.; Jang, J.-H. Nanoporous hematite structures to overcome short diffusion lengths in water splitting. *Journal of Materials Chemistry A* **2014,** *2* (47), 19999-20003.
115. Kilner, J. A.; Skinner, S.; Irvine, S.; Edwards, P. *Functional materials for sustainable energy applications*. Elsevier: 2012.
116. Peter, L. M.; Wijayantha, K. U.; Tahir, A. A. Kinetics of light-driven oxygen evolution at α-Fe 2 O 3 electrodes. *Faraday discussions* **2012,** *155*, 309-322.
117. Kay, A.; Cesar, I.; Grätzel, M. New benchmark for water photooxidation by nanostructured α-Fe2O3 films. *Journal of the American Chemical Society* **2006,** *128* (49), 15714-15721.
118. Fredlein, R. A.; Bard, A. J. Semiconductor Electrodes XXI. The Characterization and Behavior of n - Type Electrodes in Acetonitrile Solutions. *Journal of The Electrochemical Society* **1979,** *126* (11), 1892-1898.
119. Cummings, C. Y.; Marken, F.; Peter, L. M.; Upul Wijayantha, K.; Tahir, A. A. New insights into water splitting at mesoporous α-Fe2O3 films: a study by modulated transmittance and impedance spectroscopies. *Journal of the American Chemical Society* **2011,** *134* (2), 1228-1234.
120. Maruthamuthu, P.; Ashokkumar, M. Doping effects of transition metal ions on the photosensitization of WO 3 particles. *Solar Energy Materials* **1988,** *17* (6), 433-438.
121. Koffyberg, F.; Benko, F. p - Type NiO as a Photoelectrolysis Cathode. *Journal of The Electrochemical Society* **1981,** *128* (11), 2476-2479.
122. Nikitine, S.; Zielinger, J.; Coret, A.; Zouaghi, M. Evaluation des parametres des photoporteurs dans la cuprite a 79° K. *Physics Letters* **1965,** *18* (2), 105-106.
123. Salvador, P.; Gutiérrez, C.; Campet, G.; Hagenmüller, P. Influence of mechanical polishing on the photoelectrochemical properties of SrTiO3 polycrystalline anodes. *Journal of The Electrochemical Society* **1984,** *131* (3), 550-555.

124. Yoon, K. H.; Chung, K. S. Photoelectrochemical effects of BaTiO3 thin film electrodes prepared by the sol‐gel method. *Journal of applied physics* **1992,** *72* (12), 5743-5749.
125. Kudo, A.; Kato, H.; Nakagawa, S. Water splitting into H2 and O2 on new Sr2M2O7 (M= Nb and Ta) photocatalysts with layered perovskite structures: factors affecting the photocatalytic activity. *The Journal of Physical Chemistry B* **2000,** *104* (3), 571-575.
126. Ding, J.; Bao, J.; Sun, S.; Luo, Z.; Gao, C. Combinatorial discovery of visible-light driven photocatalysts based on the ABO3-type (A= Y, La, Nd, Sm, Eu, Gd, Dy, Yb, B= Al and In) binary oxides. *Journal of Combinatorial chemistry* **2009,** *11* (4), 523-526.
127. Kurihara, T.; Okutomi, H.; Miseki, Y.; Kato, H.; Kudo, A. Highly efficient water splitting over K3Ta3B2O12 photocatalyst without loading cocatalyst. *Chemistry Letters* **2006,** *35* (3), 274-275.
128. Kato, H.; Kudo, A. New tantalate photocatalysts for water decomposition into H 2 and O 2. *Chemical Physics Letters* **1998,** *295* (5), 487-492.
129. Takata, T.; Shinohara, K.; Tanaka, A.; Hara, M.; Kondo, J.; Domen, K. A highly active photocatalyst for overall water splitting with a hydrated layered perovskite structure. *Journal of photochemistry and photobiology A: Chemistry* **1997,** *106* (1), 45-49.
130. Aroutiounian, V.; Arakelyan, V.; Shahnazaryan, G. Metal oxide photoelectrodes for hydrogen generation using solar radiation-driven water splitting. *Solar Energy* **2005,** *78* (5), 581-592.
131. Wong, W. K. Doped TiO_2 for solar energy applications. *Solar energy* **1986,** *36* (2), 163 - 168.
132. Klosek, S.; Raftery, D. Visible light driven V-doped TiO2 photocatalyst and its photooxidation of ethanol. *The Journal of Physical Chemistry B* **2001,** *105* (14), 2815-2819.
133. Ghosh, A. K.; Maruska, H. P. Photoelectrolysis of water in sunlight with sensitized semiconductor electrodes. *Journal of the electrochemical society* **1977,** *124* (10), 1516-1522.
134. Houlihan, J.; Armitage, D.; Hoovler, T.; Bonaquist, D.; Madacsi, D.; Mulay, L. Doped polycrystalline TiO 2 electrodes for the photo-assisted electrolysis of water. *Materials Research Bulletin* **1978,** *13* (11), 1205-1212.
135. Cesar, I.; Kay, A.; Gonzalez Martinez, J. A.; Grätzel, M. Translucent thin film Fe2O3 photoanodes for efficient water splitting by sunlight: nanostructure-directing effect of Si-doping. *Journal of the American Chemical Society* **2006,** *128* (14), 4582-4583.
136. He, J.; Parkinson, B. Combinatorial Investigation of the Effects of the Incorporation of Ti, Si, and Al on the Performance of α-Fe2O3 Photoanodes. *ACS combinatorial science* **2011,** *13* (4), 399-404.
137. Shaban, Y. A.; Khan, S. U. Visible light active carbon modified n-TiO 2 for efficient hydrogen production by photoelectrochemical splitting of water. *International journal of hydrogen energy* **2008,** *33* (4), 1118-1126.
138. Barnes, P.; Randeniya, L.; Murphy, A.; Gwan, P.; Plumb, I.; Grey, I.; Li, C. In *TiO 2 photo-electrodes for water splitting prepared by flame pyrolysis*, International Conference on Materials for Hydrogen Energy, Sydney, Australia, 2004.
139. Ishikawa, A.; Takata, T.; Kondo, J. N.; Hara, M.; Kobayashi, H.; Domen, K. Oxysulfide Sm2Ti2S2O5 as a stable photocatalyst for water oxidation and reduction under visible light irradiation ($\lambda \leqslant 650$ nm). *Journal of the American Chemical Society* **2002,** *124* (45), 13547-13553.
140. Hitoki, G.; Takata, T.; Kondo, J. N.; Hara, M.; Kobayashi, H.; Domen, K. An oxynitride, TaON, as an efficient water oxidation photocatalyst under visible light irradiation ($\lambda \leqslant 500$ nm). *Chemical Communications* **2002,** (16), 1698-1699.
141. Liu, M.; You, W.; Lei, Z.; Zhou, G.; Yang, J.; Wu, G.; Ma, G.; Luan, G.; Takata, T.; Hara, M. Water reduction and oxidation on Pt–Ru/Y2Ta2O5N2 catalyst under visible light irradiation. *Chem. Commun.* **2004,** (19), 2192-2193.
142. Hitoki, G.; Ishikawa, A.; Takata, T.; Kondo, J. N.; Hara, M.; Domen, K. Ta3N5 as a Novel Visible Light-Driven Photocatalyst (. LAMBDA.< 600 nm). *Chemistry Letters* **2002,** (7), 736-737.
143. Kasahara, A.; Nukumizu, K.; Hitoki, G.; Takata, T.; Kondo, J. N.; Hara, M.; Kobayashi, H.; Domen, K. Photoreactions on LaTiO2N under visible light irradiation. *The Journal of Physical Chemistry A* **2002,** *106* (29), 6750-6753.
144. Murata, Y.; Fukuta, S.; Ishikawa, S.; Yokoyama, S. Photoelectrochemical properties of TiO 2 rutile microalloyed with 4d and 5d transition elements. *Solar energy materials and solar cells* **2000,** *62* (1), 157-165.
145. Ni, M.; Leung, M. K.; Leung, D. Y.; Sumathy, K. A review and recent developments in photocatalytic water-splitting using TiO2 for hydrogen production. *Renewable and Sustainable Energy Reviews* **2007,** *11* (3), 401-425.
146. Shiyanovskaya, I.; Hepel, M. Bicomponent WO 3/TiO2 Films as Photoelectrodes. *Journal of the Electrochemical Society* **1999,** *146* (1), 243-249.

147. Bumajdad, A.; Madkour, M. Understanding the superior photocatalytic activity of noble metals modified titania under UV and visible light irradiation. *Physical Chemistry Chemical Physics* **2014,** *16* (16), 7146-7158.
148. Kowalska, E.; Mahaney, O. O. P.; Abe, R.; Ohtani, B. Visible-light-induced photocatalysis through surface plasmon excitation of gold on titania surfaces. *Physical Chemistry Chemical Physics* **2010,** *12* (10), 2344-2355.
149. Linic, S.; Christopher, P.; Ingram, D. B. Plasmonic-metal nanostructures for efficient conversion of solar to chemical energy. *Nature materials* **2011,** *10* (12), 911-921.
150. Hsu, Y.-P.; Lee, S.-W.; Chang, J.-K.; Tseng, C.-J.; Lee, K.-R.; Wang, C.-H. Effects of platinum doping on the photoelectrochemical properties of Fe2O3 electrodes. *Int. J. Electrochem. Sci* **2013,** *8*, 11615-11623.
151. Hu, Y.; Song, X.; Jiang, S.; Wei, C. Enhanced photocatalytic activity of Pt-doped TiO 2 for NOx oxidation both under UV and visible light irradiation: A synergistic effect of lattice Pt 4+ and surface PtO. *Chemical Engineering Journal* **2015,** *274*, 102-112.
152. Somorjai, G.; Rioux, R. High technology catalysts towards 100% selectivity: Fabrication, characterization and reaction studies. *Catalysis Today* **2005,** *100* (3), 201-215.
153. Henry, C.; Chapon, C.; Giorgio, S.; Goyhenex, C. Size effects in heterogeneous catalysis. In *Chemisorption and ReactiVity on Supported Clusters and Thin Films*, Springer: 1997; pp 117-152.
154. Hayden, B. E.; Pletcher, D.; Suchsland, J.-P.; Williams, L. J. The influence of support and particle size on the platinum catalysed oxygen reduction reaction. *Physical Chemistry Chemical Physics* **2009,** *11* (40), 9141-9148.
155. Mukerjee, S. Particle size and structural effects in platinum electrocatalysis. *Journal of Applied Electrochemistry* **1990,** *20* (4), 537-548.
156. Kinoshita, K. Particle size effects for oxygen reduction on highly dispersed platinum in acid electrolytes. *Journal of The Electrochemical Society* **1990,** *137* (3), 845-848.
157. Van Hardeveld, R.; Van Montfoort, A. The influence of crystallite size on the adsorption of molecular nitrogen on nickel, palladium and platinum: An infrared and electron-microscopic study. *Surface Science* **1966,** *4* (4), 396-430.
158. Yoo, S. J.; Jeon, T.-Y.; Lee, K.-S.; Park, K.-W.; Sung, Y.-E. Effects of particle size on surface electronic and electrocatalytic properties of Pt/TiO 2 nanocatalysts. *Chemical communications* **2010,** *46* (5), 794-796.
159. Tauster, S. Strong metal-support interactions. *Accounts of Chemical Research* **1987,** *20* (11), 389-394.
160. Haruta, M.; Daté, M. Advances in the catalysis of Au nanoparticles. *Applied Catalysis A: General* **2001,** *222* (1), 427-437.
161. Tauster, S.; Fung, S.; Garten, R. Strong metal-support interactions. Group 8 noble metals supported on titanium dioxide. *Journal of the American Chemical Society* **1978,** *100* (1), 170-175.
162. Pesty, F.; Steinrück, H.-P.; Madey, T. E. Thermal stability of Pt films on TiO 2 (110): evidence for encapsulation. *Surface science* **1995,** *339* (1), 83-95.
163. Belton, D.; Sun, Y.; White, J. Metal-support interactions on rhodium and platinum/titanium dioxide model catalysts. *The Journal of Physical Chemistry* **1984,** *88* (22), 5172-5176.
164. (a) Shao, M.; Peles, A.; Shoemaker, K. Electrocatalysis on platinum nanoparticles: particle size effect on oxygen reduction reaction activity. *Nano letters* **2011,** *11* (9), 3714-3719; (b) Tamizhmani, G.; Dodelet, J.; Guay, D. Crystallite Size Effects of Carbon - Supported Platinum on Oxygen Reduction in Liquid Acids. *Journal of The Electrochemical Society* **1996,** *143* (1), 18-23.
165. Genies, L.; Faure, R.; Durand, R. Electrochemical reduction of oxygen on platinum nanoparticles in alkaline media. *Electrochimica Acta* **1998,** *44* (8), 1317-1327.
166. Spendelow, J. S.; Wieckowski, A. Electrocatalysis of oxygen reduction and small alcohol oxidation in alkaline media. *Physical Chemistry Chemical Physics* **2007,** *9* (21), 2654-2675.
167. Markovic, N.; Gasteiger, H.; Ross, P. N. Kinetics of oxygen reduction on Pt (hkl) electrodes: implications for the crystallite size effect with supported Pt electrocatalysts. *Journal of the Electrochemical Society* **1997,** *144* (5), 1591-1597.
168. Hayden, B. E.; Pletcher, D.; Suchsland, J.-P.; Williams, L. J. The influence of Pt particle size on the surface oxidation of titania supported platinum. *Physical Chemistry Chemical Physics* **2009,** *11* (10), 1564-1570.
169. (a) Maillard, F.; Schreier, S.; Hanzlik, M.; Savinova, E.; Weinkauf, S.; Stimming, U. Influence of particle agglomeration on the catalytic activity of carbon-supported Pt nanoparticles in CO monolayer oxidation. *Physical Chemistry Chemical Physics* **2005,** *7* (2), 385-393; (b) Cherstiouk, O.; Simonov, P.; Savinova, E. Model approach to evaluate particle size effects in electrocatalysis: preparation and

properties of Pt nanoparticles supported on GC and HOPG. *Electrochimica Acta* **2003,** *48* (25), 3851-3860.
170. (a) Cherstiouk, O.; Simonov, P.; Zaikovskii, V.; Savinova, E. CO monolayer oxidation at Pt nanoparticles supported on glassy carbon electrodes. *Journal of Electroanalytical Chemistry* **2003,** *554*, 241-251; (b) Gasteiger, H. A.; Kocha, S. S.; Sompalli, B.; Wagner, F. T. Activity benchmarks and requirements for Pt, Pt-alloy, and non-Pt oxygen reduction catalysts for PEMFCs. *Applied Catalysis B: Environmental* **2005,** *56* (1), 9-35.
171. Mukerjee, S.; McBreen, J. Effect of particle size on the electrocatalysis by carbon-supported Pt electrocatalysts: an in situ XAS investigation. *Journal of Electroanalytical Chemistry* **1998,** *448* (2), 163-171.
172. Watanabe, M.; Sei, H.; Stonehart, P. The influence of platinum crystallite size on the electroreduction of oxygen. *Journal of electroanalytical chemistry and interfacial electrochemistry* **1989,** *261* (2), 375-387.
173. Zeng, K.; Zhang, D. Recent progress in alkaline water electrolysis for hydrogen production and applications. *Progress in Energy and Combustion Science* **2010,** *36* (3), 307-326.
174. Trasatti, S. *Electrodes of conductive metallic oxides*. Elsevier Scientific Software: 1980; Vol. 2.
175. Birss, V. I.; Damjanovic, A. Oxygen Evolution at Platinum Electrodes in Alkaline Solutions I. Dependence on Solution pH and Oxide Film Thickness. *Journal of The Electrochemical Society* **1987,** *134* (1), 113-117.
176. Conway, B.; Barnett, B.; Angerstein‐Kozlowska, H.; Tilak, B. A surface‐electrochemical basis for the direct logarithmic growth law for initial stages of extension of anodic oxide films formed at noble metals. *The Journal of chemical physics* **1990,** *93* (11), 8361-8373.
177. (a) Bockris, J. M. Kinetics of activation controlled consecutive electrochemical reactions: anodic evolution of oxygen. *The Journal of Chemical Physics* **1956,** *24* (4), 817-827; (b) Damjanovic, A.; Dey, A.; Bockris, J. M. Kinetics of oxygen evolution and dissolution on platinum electrodes. *Electrochimica Acta* **1966,** *11* (7), 791-814.
178. Scarr, R. F. The Mechanism of Oxygen Evolution on Nickel, Platinum, and Other Metals and Alloys. *Journal of The Electrochemical Society* **1969,** *116* (11), 1526-1532.
179. Beer, H. B. Dimensionally Stable Anodes. In *Electrochemistry in Industry*, Springer: 1982; pp 19-28.
180. Trasatti, S. Electrocatalysis: understanding the success of DSA®. *Electrochimica Acta* **2000,** *45* (15), 2377-2385.
181. Rasiyah, P.; Tseung, A. The role of the lower metal oxide/higher metal oxide couple in oxygen evolution reactions. *Journal of the Electrochemical Society* **1984,** *131* (4), 803-808.
182. Yang, X.; Du, C.; Liu, R.; Xie, J.; Wang, D. Balancing photovoltage generation and charge-transfer enhancement for catalyst-decorated photoelectrochemical water splitting: A case study of the hematite/MnOx combination. *Journal of Catalysis* **2013,** *304*, 86-91.
183. Ye, H.; Park, H. S.; Bard, A. J. Screening of electrocatalysts for photoelectrochemical water oxidation on W-doped BiVO4 photocatalysts by scanning electrochemical microscopy. *The Journal of Physical Chemistry C* **2011,** *115* (25), 12464-12470.
184. Heller, A.; Aspnes, D.; Porter, J.; Sheng, T.; Vadimsky, R. Transparent metals preparation and characterization of light-transmitting platinum films. *The Journal of Physical Chemistry* **1985,** *89* (21), 4444-4452.
185. Hill, J. C.; Landers, A. T.; Switzer, J. A. An electrodeposited inhomogeneous metal-insulator-semiconductor junction for efficient photoelectrochemical water oxidation. *Nature Materials* **2015**.
186. Subramanian, V.; Wolf, E.; Kamat, P. V. Semiconductor-metal composite nanostructures. To what extent do metal nanoparticles improve the photocatalytic activity of TiO2 films? *The Journal of Physical Chemistry B* **2001,** *105* (46), 11439-11446.
187. Nosaka, Y.; Norimatsu, K.; Miyama, H. The function of metals in metal-compounded semiconductor photocatalysts. *Chemical physics letters* **1984,** *106* (1), 128-131.
188. Anpo, M.; Takeuchi, M. The design and development of highly reactive titanium oxide photocatalysts operating under visible light irradiation. *Journal of catalysis* **2003,** *216* (1), 505-516.
189. Subramanian, V.; Wolf, E. E.; Kamat, P. V. Catalysis with TiO2/gold nanocomposites. Effect of metal particle size on the Fermi level equilibration. *Journal of the American Chemical Society* **2004,** *126* (15), 4943-4950.
190. (a) Almeida, L. C.; Zanoni, M. V. Decoration of Ti/TiO2 nanotubes with Pt nanoparticles for enhanced UV-Vis light absorption in photoelectrocatalytic process. *Journal of the Brazilian Chemical Society* **2014,** *25* (3), 579-588; (b) An, W.-J.; Wang, W.-N.; Ramalingam, B.; Mukherjee, S.; Daubayev, B.;

Gangopadhyay, S.; Biswas, P. Enhanced water photolysis with Pt metal nanoparticles on single crystal TiO2 surfaces. *Langmuir* **2012,** *28* (19), 7528-7534.
191. Song, J. T.; Iwasaki, T.; Hatano, M. Pt co-catalyst effect on photoelectrochemical properties of 3C-SiC photo-anode. *Japanese Journal of Applied Physics* **2014,** *53* (5S1), 05FZ04.
192. Xu, G.; Liu, H.; Wang, J.; Lv, J.; Zheng, Z.; Wu, Y. Photoelectrochemical Performances and Potential Applications of TiO 2 Nanotube Arrays Modified with Ag and Pt Nanoparticles. *Electrochimica Acta* **2014,** *121*, 194-202.
193. Aurora, P.; Rhee, P.; Thompson, L. Titania Nanotube Supported Gold Photoanodes for Photoelectrochemical Cells. *Journal of The Electrochemical Society* **2010,** *157* (7), K152-K155.
194. (a) Jiang, R.; Chu, D. A combinatorial approach toward electrochemical analysis. *Journal of Electroanalytical Chemistry* **2002,** *527* (1), 137-142; (b) Yanase, I.; Ohtaki, T.; Watanabe, M. Application of combinatorial process to LiCo 1− X Mn X O 2 (0≦ X≦ 0.2) powder synthesis. *Solid State Ionics* **2002,** *151* (1), 189-196; (c) Aljohani, T. A.; Hayden, B. E.; Anastasopoulos, A. The high throughput electrochemical screening of the corrosion resistance of Ni–Cr thin film alloys. *Electrochimica Acta* **2012,** *76*, 389-393.
195. Reddington, E.; Sapienza, A.; Gurau, B.; Viswanathan, R.; Sarangapani, S.; Smotkin, E. S.; Mallouk, T. E. Combinatorial electrochemistry: a highly parallel, optical screening method for discovery of better electrocatalysts. *Science* **1998,** *280* (5370), 1735-1737.
196. (a) Gerken, J. B.; Chen, J. Y.; Massé, R. C.; Powell, A. B.; Stahl, S. S. Development of an O2‐Sensitive Fluorescence‐Quenching Assay for the Combinatorial Discovery of Electrocatalysts for Water Oxidation. *Angewandte Chemie International Edition* **2012,** *51* (27), 6676-6680; (b) Nakayama, A.; Suzuki, E.; Ohmori, T. Development of high throughput evaluation for photocatalyst thin-film. *Applied surface science* **2002,** *189* (3), 260-264.
197. Xiang, C.; Suram, S. K.; Haber, J. A.; Guevarra, D. W.; Soedarmadji, E.; Jin, J.; Gregoire, J. M. High-Throughput Bubble Screening Method for Combinatorial Discovery of Electrocatalysts for Water Splitting. *ACS combinatorial science* **2014,** *16* (2), 47-52.
198. Gregoire, J. M.; Xiang, C.; Mitrovic, S.; Liu, X.; Marcin, M.; Cornell, E. W.; Fan, J.; Jin, J. Combined catalysis and optical screening for high throughput discovery of solar fuels catalysts. *Journal of the Electrochemical Society* **2013,** *160* (4), F337-F342.
199. Katz, J. E.; Gingrich, T. R.; Santori, E. A.; Lewis, N. S. Combinatorial synthesis and high-throughput photopotential and photocurrent screening of mixed-metal oxides for photoelectrochemical water splitting. *Energy & Environmental Science* **2009,** *2* (1), 103-112.
200. (a) Gregoire, J. M.; Xiang, C.; Liu, X.; Marcin, M.; Jin, J. Scanning droplet cell for high throughput electrochemical and photoelectrochemical measurements. *Review of Scientific Instruments* **2013,** *84* (2), 024102; (b) Woodhouse, M.; Herman, G.; Parkinson, B. Combinatorial approach to identification of catalysts for the photoelectrolysis of water. *Chemistry of materials* **2005,** *17* (17), 4318-4324.
201. Jaramillo, T. F.; Baeck, S. H.; Kleiman‐Shwarsctein, A.; McFarland, E. W. Combinatorial electrochemical synthesis and screening of mesoporous ZnO for photocatalysis. *Macromolecular rapid communications* **2004,** *25* (1), 297-301.
202. Baeck, S.; Jaramillo, T.; Brändli, C.; McFarland, E. Combinatorial electrochemical synthesis and characterization of tungsten-based mixed-metal oxides. *Journal of combinatorial chemistry* **2002,** *4* (6), 563-568.
203. Arai, T.; Konishi, Y.; Iwasaki, Y.; Sugihara, H.; Sayama, K. High-throughput screening using porous photoelectrode for the development of visible-light-responsive semiconductors. *Journal of combinatorial chemistry* **2007,** *9* (4), 574-581.
204. Xiang, C.; Haber, J.; Marcin, M.; Mitrovic, S.; Jin, J.; Gregoire, J. M. Mapping Quantum Yield for (Fe–Zn–Sn–Ti) O x Photoabsorbers Using a High Throughput Photoelectrochemical Screening System. *ACS combinatorial science* **2014,** *16* (3), 120-127.
205. Guerin, S.; Hayden, B. E.; Lee, C. E.; Mormiche, C.; Russell, A. E. High-throughput synthesis and screening of ternary metal alloys for electrocatalysis. *The Journal of Physical Chemistry B* **2006,** *110* (29), 14355-14362.
206. Anastasopoulos, A.; Davies, J.; Hannah, L.; Hayden, B.; Lee, C.; Milhano, C.; Mormiche, C.; Offin, L. The Particle Size Dependence of the Oxygen Reduction Reaction for Carbon‐Supported Platinum and Palladium. *ChemSusChem* **2013,** *6* (10), 1973-1982.
207. Guerin, S.; Hayden, B. E.; Lee, C. E.; Mormiche, C.; Owen, J. R.; Russell, A. E.; Theobald, B.; Thompsett, D. Combinatorial electrochemical screening of fuel cell electrocatalysts. *Journal of combinatorial chemistry* **2004,** *6* (1), 149-158.

208. Salvador, P. Influence of pH on the Potential Dependence of the Efficiency of Water Photo - oxidation at n - TiO2 Electrodes. *Journal of The Electrochemical Society* **1981,** *128* (9), 1895-1900.
209. Chen, Z.; Jaramillo, T. F.; Deutsch, T. G.; Kleiman-Shwarsctein, A.; Forman, A. J.; Gaillard, N.; Garland, R.; Takanabe, K.; Heske, C.; Sunkara, M. Accelerating materials development for photoelectrochemical hydrogen production: Standards for methods, definitions, and reporting protocols. *Journal of Materials Research* **2010,** *25* (01), 3-16.
210. Bell, S.; Will, G.; Bell, J. Light intensity effects on photocatalytic water splitting with a titania catalyst. *International Journal of Hydrogen Energy* **2013,** *38* (17), 6938-6947.
211. Snaith, H. J.; Schmidt-Mende, L.; Grätzel, M.; Chiesa, M. Light intensity, temperature, and thickness dependence of the open-circuit voltage in solid-state dye-sensitized solar cells. *Physical Review B* **2006,** *74* (4), 045306.
212. Hayden, B. E.; Malevich, D. V.; Pletcher, D. Electrode coatings from sprayed titanium dioxide nanoparticles–behaviour in NaOH solutions. *Electrochemistry communications* **2001,** *3* (8), 390-394.
213. Jankulovska, M.; Berger, T.; Wong, S. S.; Gómez, R.; Lana - Villarreal, T. Trap states in tio2 films made of nanowires, nanotubes or nanoparticles: An electrochemical study. *ChemPhysChem* **2012,** *13* (12), 3008-3017.
214. Tong, Y. J. Unconventional promoters of catalytic activity in electrocatalysis. *Chemical Society Reviews* **2012,** *41* (24), 8195-8209.
215. (a) Kundu, S.; Kafizas, A.; Hyett, G.; Mills, A.; Darr, J. A.; Parkin, I. P. An investigation into the effect of thickness of titanium dioxide and gold–silver nanoparticle titanium dioxide composite thin-films on photocatalytic activity and photo-induced oxygen production in a sacrificial system. *Journal of Materials Chemistry* **2011,** *21* (19), 6854-6863; (b) Vidyarthi, V. S.; Hofmann, M.; Savan, A.; Sliozberg, K.; König, D.; Beranek, R.; Schuhmann, W.; Ludwig, A. Enhanced photoelectrochemical properties of WO 3 thin films fabricated by reactive magnetron sputtering. *international journal of hydrogen energy* **2011,** *36* (8), 4724-4731.
216. Grimes, C. A.; Mor, G. K. *TiO2 nanotube arrays: synthesis, properties, and applications*. Springer Science & Business Media: 2009.
217. Salvador, P. Hole diffusion length in n - TiO2 single crystals and sintered electrodes: Photoelectrochemical determination and comparative analysis. *Journal of applied physics* **1984,** *55* (8), 2977-2985.
218. (a) Bisquert, J.; Garcia-Belmonte, G.; Fabregat-Santiago, F. Modelling the electric potential distribution in the dark in nanoporous semiconductor electrodes. *Journal of Solid State Electrochemistry* **1999,** *3* (6), 337-347; (b) Hagfeldt, A.; Graetzel, M. Light-induced redox reactions in nanocrystalline systems. *Chemical Reviews* **1995,** *95* (1), 49-68.
219. Goossens, A. Potential distribution in semiconductor particles. *Journal of The Electrochemical Society* **1996,** *143* (6), L131-L133.
220. (a) Sivula, K.; Formal, F. L.; Grätzel, M. WO3– Fe2O3 photoanodes for water splitting: A host scaffold, guest absorber approach. *Chemistry of Materials* **2009,** *21* (13), 2862-2867; (b) Mor, G. K.; Prakasam, H. E.; Varghese, O. K.; Shankar, K.; Grimes, C. A. Vertically oriented Ti-Fe-O nanotube array films: toward a useful material architecture for solar spectrum water photoelectrolysis. *Nano letters* **2007,** *7* (8), 2356-2364.
221. Chopra, K. L. Thin film phenomena**1969**.
222. Kim, D. Effect of a TiO 2 Buffer Layer on the Properties of ITO Films Prepared by RF Magnetron Sputtering. *Transactions on Electrical and Electronic Materials* **2013,** *14* (5), 242-245.
223. Sánchez-Tovar, R.; Lee, K.; García-Antón, J.; Schmuki, P. Photoelectrochemical Poperties of Anodic TiO2 Nanosponge Layers. *ECS Electrochemistry Letters* **2013,** *2* (3), H9-H11.
224. Wu, K. R.; Hung, C. H.; Yeh, C. W.; Chang, H. C.; Sun, J. C. In *Characteristics of Visible-Light Enabled TiO2/ITO Films*, Advanced Materials Research, Trans Tech Publ: 2011; pp 152-156.
225. Seger, B.; Tilley, S. D.; Pedersen, T.; Vesborg, P. C.; Hansen, O.; Grätzel, M.; Chorkendorff, I. Silicon protected with atomic layer deposited TiO 2: conducting versus tunnelling through TiO 2. *Journal of Materials Chemistry A* **2013,** *1* (47), 15089-15094.
226. Harris, L. A.; Wilson, R. Semiconductors for photoelectrolysis. *Annual review of materials science* **1978,** *8* (1), 99-134.
227. (a) Cao, F.; Oskam, G.; Searson, P. C.; Stipkala, J. M.; Heimer, T. A.; Farzad, F.; Meyer, G. J. Electrical and optical properties of porous nanocrystalline TiO2 films. *The Journal of Physical Chemistry* **1995,** *99* (31), 11974-11980; (b) Bennett, T.; Adnan, R. H.; Alvino, J. F.; Kler, R.; Golovko, V. B.; Metha, G. F.; Andersson, G. G. Effect of Gold Nanoclusters on the Production of Ti3+ Defect Sites in Titanium

Dioxide Nanoparticles under Ultraviolet and Soft X-ray Radiation. *The Journal of Physical Chemistry C* **2015**.
228. Rosário, A.; Santos, M.; Mascaro, L.; Bulhões, L.; Pereira, E. Copper underpotential deposition on TiO 2 electrodes: A voltammetric and electrochemical quartz crystal nanobalance study. *Thin Solid Films* **2010,** *518* (10), 2669-2673.
229. Herzog, G.; Arrigan, D. W. Determination of trace metals by underpotential deposition–stripping voltammetry at solid electrodes. *TrAC Trends in Analytical Chemistry* **2005,** *24* (3), 208-217.
230. Tsujiko, A.; Itoh, H.; Kisumi, T.; Shiga, A.; Murakoshi, K.; Nakato, Y. Observation of cathodic photocurrents at nanocrystalline TiO2 film electrodes, caused by enhanced oxygen reduction in alkaline solutions. *The Journal of Physical Chemistry B* **2002,** *106* (23), 5878-5885.
231. Kim, M.-H.; Baek, S.-B.; Paik, U.; Nam, S.; Byun, J. Electrical Conductivity and Oxygen Diffusion in Nonstoichiometric TiO~ 2~-~ x. *JOURNAL-KOREAN PHYSICAL SOCIETY* **1998,** *32*, S1127-S1130.
232. Nowotny, M.; Bak, T.; Nowotny, J. Electrical properties and defect chemistry of TiO2 single crystal. I. Electrical conductivity. *The Journal of Physical Chemistry B* **2006,** *110* (33), 16270-16282.
233. (a) Weast, R. C. *Handbook of chemistry and physics: a reference book of chemical and physical data*. chemical rubber Company: 1970; (b) Yagi, E.; Hasiguti, R. R.; Aono, M. Electronic conduction above 4 K of slightly reduced oxygen-deficient rutile TiO 2− x. *Physical Review B* **1996,** *54* (11), 7945; (c) Hayfield, P. *Development of a New Material: Monolithic Ti4O7 Ebonex Ceramic*. Royal Society of Chemistry: 2002.
234. Diebold, U.; Madey, T. TiO2 by XPS. *Surface Science Spectra* **1996,** *4* (3), 227-231.
235. Hayek, K.; Kramer, R.; Paál, Z. Metal-support boundary sites in catalysis. *Applied Catalysis A: General* **1997,** *162* (1), 1-15.
236. Singh, P.; Kaur, D. Room temperature growth of nanocrystalline anatase TiO 2 thin films by dc magnetron sputtering. *Physica B: Condensed Matter* **2010,** *405* (5), 1258-1266.
237. Bowker, M.; Bennett, R. A. The role of Ti3+ interstitials in TiO2 (110) reduction and oxidation. *Journal of Physics: Condensed Matter* **2009,** *21* (47), 474224.
238. Chambers, S. A.; Wang, C. M.; Thevuthasan, S.; Droubay, T.; McCready, D. E.; Lea, A. S.; Shutthanandan, V.; Windisch Jr, C. Epitaxial growth and properties of MBE-grown ferromagnetic Co-doped TiO 2 anatase films on SrTiO 3 (001) and LaAlO 3 (001). *Thin Solid Films* **2002,** *418* (2), 197-210.
239. Holzwarth, U.; Gibson, N. The Scherrer equation versus the'Debye-Scherrer equation'. *Nature Nanotechnology* **2011,** *6* (9), 534-534.
240. Sánchez-Sánchez, C.; Martín-Gago, J. A.; López, M. F. Small Pt nanoparticles on the TiO 2 (110)–(1× 2) surface. *Surface Science* **2013,** *607*, 159-163.
241. Eberhardt, W.; Fayet, P.; Cox, D.; Fu, Z.; Kaldor, A.; Sherwood, R.; Sondericker, D. Photoemission from mass-selected monodispersed Pt clusters. *Physical review letters* **1990,** *64* (7), 780.
242. Cheung, T. X-ray photoemission of small platinum and palladium clusters. *Surface Science* **1984,** *140* (1), 151-164.
243. Hammond, J.; Winograd, N. XPS spectroscopic study of potentiostatic and galvanostatic oxidation of Pt electrodes in H 2 SO 4 and HClO 4. *Journal of Electroanalytical Chemistry and Interfacial Electrochemistry* **1977,** *78* (1), 55-69.
244. Williams, L. J. Support and Particle Size effects in Electrocatalysis. *PhD Thesis* **2007**.
245. Markovića, N. M.; Sarraf, S. T.; Gasteiger, H. A.; Ross, P. N. Hydrogen electrochemistry on platinum low-index single-crystal surfaces in alkaline solution. *J. Chem. Soc., Faraday Trans.* **1996,** *92* (20), 3719-3725.
246. Maillard, F.; Eikerling, M.; Cherstiouk, O.; Schreier, S.; Savinova, E.; Stimming, U. Size effects on reactivity of Pt nanoparticles in CO monolayer oxidation: The role of surface mobility. *Faraday discussions* **2004,** *125*, 357-377.
247. Park, S. M.; Ho, S.; Aruliah, S.; Weber, M. F.; Ward, C. A.; Venter, R. D.; Srinivasan, S. Electrochemical Reduction of Oxygen at Platinum Electrodes in KOH Solutions - Temperature and Concentration Effects. *Journal of the Electrochemical Society* **1986,** *133* (8), 1641-1649.
248. Ramaswamy, N.; Mukerjee, S. Fundamental mechanistic understanding of electrocatalysis of oxygen reduction on Pt and non-Pt surfaces: acid versus alkaline media. *Advances in Physical Chemistry* **2012,** *2012*.
249. Prabhuram, J.; Manoharan, R. Investigation of methanol oxidation on unsupported platinum electrodes in strong alkali and strong acid. *Journal of power sources* **1998,** *74* (1), 54-61.
250. Pozio, A.; De Francesco, M.; Cemmi, A.; Cardellini, F.; Giorgi, L. Comparison of high surface Pt/C catalysts by cyclic voltammetry. *Journal of power sources* **2002,** *105* (1), 13-19.
251. Tammeveski, K.; Arulepp, M.; Tenno, T.; Ferrater, C.; Claret, J. Oxygen electroreduction on titanium-supported thin Pt films in alkaline solution. *Electrochimica acta* **1997,** *42* (19), 2961-2967.

252. Neufeld, O.; Toroker, M. C. Can we judge an oxide by its cover? The case of platinum over α-Fe 2 O 3 from first principles. *Physical Chemistry Chemical Physics* **2015,** *17* (37), 24129-24137.
253. Tammeveski, K.; Tenno, T.; Rosental, A.; Talonen, P.; Johansson, L. S.; Niinistö, L. The Reduction of Oxygen on Pt‐TiO2 Coated Ti Electrodes in Alkaline Solution. *Journal of the Electrochemical Society* **1999,** *146* (2), 669-676.
254. Svetzlozar, I. Platinised titanium dioxide electrodes for methanol oxidation and photo-oxidation. *Journal of The Electrochemical Society* **2012,** *2* (4), 155-169.
255. Wasmus, S.; Küver, A. Methanol oxidation and direct methanol fuel cells: a selective review. *Journal of Electroanalytical Chemistry* **1999,** *461* (1), 14-31.
256. Hamann, T. W. Splitting water with rust: hematite photoelectrochemistry. *Dalton Transactions* **2012,** *41* (26), 7830-7834.
257. Hirakawa, T.; Kamat, P. V. Photoinduced electron storage and surface plasmon modulation in Ag@ TiO2 clusters. *Langmuir* **2004,** *20* (14), 5645-5647.
258. Tilley, S. D.; Cornuz, M.; Sivula, K.; Grätzel, M. Light‐Induced Water Splitting with Hematite: Improved Nanostructure and Iridium Oxide Catalysis. *Angewandte Chemie* **2010,** *122* (36), 6549-6552.
259. Pflitsch, C.; Viefhaus, D.; Bergmann, U.; Kravets, V.; Nienhaus, H.; Atakan, B. Growth of thin iron oxide films on Si (100) by MOCVD. *Journal of The Electrochemical Society* **2006,** *153* (8), C546-C550.
260. Ostrikov, K. K.; Levchenko, I.; Cvelbar, U.; Sunkara, M.; Mozetic, M. From nucleation to nanowires: a single-step process in reactive plasmas. *Nanoscale* **2010,** *2* (10), 2012-2027.
261. Fujii, T.; De Groot, F.; Sawatzky, G.; Voogt, F.; Hibma, T.; Okada, K. In situ XPS analysis of various iron oxide films grown by NO2-assisted molecular-beam epitaxy. *Physical review B* **2001,** *59* (4), 3195-3202.
262. Cornell, R. M.; Schwertmann, U. *The iron oxides: structure, properties, reactions, occurrences and uses*. John Wiley & Sons: 2006.
263. Gota, S.; Guiot, E.; Henriot, M.; Gautier-Soyer, M. Atomic-oxygen-assisted MBE growth of α− F e 2 O 3 on α− A l 2 O 3 (0001): Metastable FeO (111)-like phase at subnanometer thicknesses. *Physical Review B* **1999,** *60* (20), 14387.
264. Klahr, B. M.; Martinson, A. B.; Hamann, T. W. Photoelectrochemical investigation of ultrathin film iron oxide solar cells prepared by atomic layer deposition. *Langmuir* **2010,** *27* (1), 461-468.
265. Jubb, A. M.; Allen, H. C. Vibrational spectroscopic characterization of hematite, maghemite, and magnetite thin films produced by vapor deposition. *ACS Applied Materials & Interfaces* **2010,** *2* (10), 2804-2812.
266. Graat, P. C.; Somers, M. A. Simultaneous determination of composition and thickness of thin iron-oxide films from XPS Fe 2p spectra. *Applied Surface Science* **1996,** *100*, 36-40.
267. Wang, H.; An, K.; Sapi, A.; Liu, F.; Somorjai, G. A. Effects of Nanoparticle Size and Metal/Support Interactions in Pt-Catalyzed Methanol Oxidation Reactions in Gas and Liquid Phases. *Catalysis Letters* **2014,** *144* (11), 1930-1938.
268. Hayden, B. E.; Suchsland, J. P. Support and particle size effects in electrocatalysis. *Fuel Cell Catalysis: A Surface Science Approach* **2009**, 567-592.
269. Perez, J.; Gonzalez, E.; Ticianelli, E. Oxygen electrocatalysis on thin porous coating rotating platinum electrodes. *Electrochimica Acta* **1998,** *44* (8), 1329-1339.
270. Gerischer, H. The impact of semiconductors on the concepts of electrochemistry. *Electrochimica Acta* **1990,** *35* (11), 1677-1699.
271. Frank, S.; Bard, A. J. Semiconductor electrodes. II. Electrochemistry at n-type titanium dioxide electrodes in acetonitrile solutions. *Journal of the American Chemical Society* **1975,** *97* (26), 7427-7433.
272. Horowitz, G. Capacitance-voltage measurements and flat-band potential determination on Zr-doped α-Fe 2 O 3 single-crystal electrodes. *Journal of electroanalytical chemistry and interfacial electrochemistry* **1983,** *159* (2), 421-436.
273. Sanchez, C.; Sieber, K.; Somorjai, G. The photoelectrochemistry of niobium doped α-Fe 2 O 3. *Journal of electroanalytical chemistry and interfacial electrochemistry* **1988,** *252* (2), 269-290.
274. Barroso, M.; Mesa, C. A.; Pendlebury, S. R.; Cowan, A. J.; Hisatomi, T.; Sivula, K.; Grätzel, M.; Klug, D. R.; Durrant, J. R. Dynamics of photogenerated holes in surface modified α-Fe2O3 photoanodes for solar water splitting. *Proceedings of the National Academy of Sciences* **2012,** *109* (39), 15640-15645.
275. Iandolo, B.; Hellman, A. The Role of Surface States in the Oxygen Evolution Reaction on Hematite. *Angewandte Chemie* **2014,** *126* (49), 13622-13626.
276. Neufeld, O.; Toroker, M. C. Platinum-Doped α-Fe2O3 for Enhanced Water Splitting Efficiency: A DFT+ U Study. *The Journal of Physical Chemistry C* **2015,** *119* (11), 5836-5847.
277. Ling, Y.; Wang, G.; Reddy, J.; Wang, C.; Zhang, J. Z.; Li, Y. The influence of oxygen content on the thermal activation of hematite nanowires. *Angewandte Chemie* **2012,** *124* (17), 4150-4155.

278. Le Formal, F.; Tétreault, N.; Cornuz, M.; Moehl, T.; Grätzel, M.; Sivula, K. Passivating surface states on water splitting hematite photoanodes with alumina overlayers. *Chemical Science* **2011,** *2* (4), 737-743.
279. Szánto, D.; Cleghorn, S.; Ponce‐de‐León, C.; Walsh, F. The limiting current for reduction of ferricyanide ion at nickel: the importance of experimental conditions. *AIChE journal* **2008,** *54* (3), 802-810.
280. Song, C.; Zhang, J. Electrocatalytic oxygen reduction reaction. In *PEM fuel cell electrocatalysts and catalyst layers*, Springer: 2008; pp 89-134.
281. Santhanam, K.; Sharon, M. Photoelectrochemical solar cells**1988**.
282. Karamdel, J.; Hadi, A.; Dee, C. F.; Majlis, B. Y. Effects of substrate on surface morphology, crystallinity, and photoluminescence properties of sputtered ZnO nano films. *Ionics* **2012,** *18* (1-2), 203-207.
283. Zandi, O.; Beardslee, J. A.; Hamann, T. Substrate Dependent Water Splitting with Ultrathin α-Fe2O3 Electrodes. *The Journal of Physical Chemistry C* **2014,** *118* (30), 16494-16503.
284. Elezovic, N.; Babic, B.; Radmilovic, V.; Vracar, L. M.; Krstajic, N. Nb–TiO 2 supported platinum nanocatalyst for oxygen reduction reaction in alkaline solutions. *Electrochimica Acta* **2011,** *56* (25), 9020-9026.
285. Watanabe, M.; Venkatesan, S.; Laitinen, H. Preparation of Dispersed Platinum on Conductive Tin Oxide and Its Catalytic Activity for Oxygen Reduction. *Journal of the Electrochemical Society* **1983,** *130* (1), 59-64.
286. Stevanović, S.; Tripković, D.; Kowal, A.; Minić, D.; Jovanović, V.; Tripković, A. Influence of surface morphology on methanol oxidation at a glassy carbon-supported Pt catalyst. *Journal of the Serbian Chemical Society* **2008,** *73* (8-9), 845-859.
287. Wang, H.; Zhang, M.; Cheng, F.; Xu, C. Pt supported on Ti for methanol electrooxidation by magnetron sputter method. *Int. J. Electrochem. Sci* **2008,** *3*, 946.
288. Jing, M.; Jiang, L.; Yi, B.; Sun, G. Comparative study of methanol adsorption and electro-oxidation on carbon-supported platinum in acidic and alkaline electrolytes. *Journal of Electroanalytical Chemistry* **2013,** *688*, 172-179.
289. Xia, X.; Iwasita, T.; Ge, F.; Vielstich, W. Structural effects and reactivity in methanol oxidation on polycrystalline and single crystal platinum. *Electrochimica Acta* **1996,** *41* (5), 711-718.
290. Iwasita, T. Electrocatalysis of methanol oxidation. *Electrochimica Acta* **2002,** *47* (22), 3663-3674.
291. Park, S.; Xie, Y.; Weaver, M. J. Electrocatalytic pathways on carbon-supported platinum nanoparticles: comparison of particle-size-dependent rates of methanol, formic acid, and formaldehyde electrooxidation. *Langmuir* **2002,** *18* (15), 5792-5798.
292. Ren, B.; Li, X.; She, C.; Wu, D.; Tian, Z. Surface Raman spectroscopy as a versatile technique to study methanol oxidation on rough Pt electrodes. *Electrochimica acta* **2000,** *46* (2), 193-205.
293. Beden, B.; Hahn, F.; Lamy, C.; Leger, J.; De Tacconi, N.; Lezna, R.; Arvia, A. Chemisorption of methanol on different platinum electrodes (smooth and rough polycrystalline, monocrystalline, and preferentially oriented), as studied by EMIRS. *Journal of electroanalytical chemistry and interfacial electrochemistry* **1989,** *261* (2), 401-408.
294. Beden, B.; Hahn, F.; Leger, J.; Lamy, C.; Perdriel, C.; De Tacconi, N.; Lezna, R.; Arvia, A. Electromodulated infrared spectroscopy of methanol electrooxidation on electrodispersed platinum electrodes: Enhancement of reactive intermediates. *Journal of electroanalytical chemistry and interfacial electrochemistry* **1991,** *301* (1), 129-138.
295. Mikhaylova, A.; Khazova, O.; Bagotzky, V. Electrocatalytic and adsorption properties of platinum microparticles electrodeposited onto glassy carbon and into Nafion® films. *Journal of Electroanalytical Chemistry* **2000,** *480* (1), 225-232.
296. Frelink, T.; Visscher, W.; Van Veen, J. Particle size effect of carbon-supported platinum catalysts for the electrooxidation of methanol. *Journal of Electroanalytical Chemistry* **1995,** *382* (1), 65-72.
297. Umeda, M.; Kokubo, M.; Mohamedi, M.; Uchida, I. Porous-microelectrode study on Pt/C catalysts for methanol electrooxidation. *Electrochimica Acta* **2003,** *48* (10), 1367-1374.
298. Xu, Y.; Schoonen, M. A. The absolute energy positions of conduction and valence bands of selected semiconducting minerals. *American Mineralogist* **2000,** *85* (4), 543-556.